Radiation Modelling in LES

For Hypersonic Flows and Combustion Systems

M. Brchnelova

under Prof. Dr. S. Hickel

Department of Aerodynamics
Faculty of Aerospace Engineering

TU Delft

Radiation Modelling in LES

For Hypersonic Flows and Combustion Systems

by

M. Brchnelova

to obtain the degree of Master of Science
at the Delft University of Technology,
to be defended publicly on Wednesday September 2, 2020 at 11:00.

Student number:	4443098	
Project duration:	February 1, 2020 – September 2, 2020	
Thesis committee:	Prof. Dr. S. Hickel,	TU Delft, supervisor
	Prof. Dr. R. Pecnik,	TU Delft
	Dr. Ir. L. Walpot,	TU Delft
	Dr. Ir. E. Mooij,	TU Delft

This thesis is not confidential.

An electronic version of this thesis is available at `http://repository.tudelft.nl/`.

Cover picture from Star Trek III: Search for Spock, 1984, Harve Bennett

Summary

Although typically neglected in aerodynamics, radiation can present the main heat transfer mechanism in some aerodynamic applications and cause significant changes in the behaviour of the flow. Such applications typically include very high temperature air, such as hypersonic flow during reentry and hot gas in combustion systems. In these cases, radiative heat transfer must be properly resolved and the divergence of this heat flux must be added as a source term to the energy budget of the flow. Additional modelling requirements may arise depending on the case of interest. In hypersonic plasma, local thermodynamic equilibrium oftentimes cannot be assumed, making efficient radiative modelling challenging. On the other hand, in combustion systems, radiation may interact with turbulence on small scales and result in large scale behaviour changes, requiring fine resolution. To that end, this thesis work focuses on the formulation and development of a radiation modelling method which could be used both for combustion systems as well as hypersonic plasma.

A literature study helped with a selection of the appropriate methods satisfying the requirements to accurately resolve the flow cases of interest. To solve radiative transfer, the emission reciprocity based Monte Carlo formulation was used. In order to generate the required spectral data, for combustion problems, a routine utilising the High Resolution Transmission Molecular Absorption (HITRAN) database was written. For hypersonic problems, the NASA Nonequilibrium Air Radiation (NEQAIR) code was adjusted and implemented.

Fourteen different validation cases were simulated to demonstrate the correct operation of the code in all three spectral regimes (grey/ HITRAN/ NEQAIR simulations). In the case of hypersonic flows, where the selected Monte Carlo formulation might not oftentimes be exact, the standard deviation for each validation case was also examined. It was found that an error of more than 10% might be sometimes present in regions close to high temperature spots. However, since this error is of the same order of magnitude as the expected error of the spectral generation by NEQAIR, this was still regarded as a sufficient performance.

Afterwards, several techniques were applied to accelerate the solution procedure. It was shown that the use of low discrepancy sequences such as the Sobol sequence here examined can reduce the requirements on the number of realisations for convergence by an order of magnitude in very anisotropic cases. It was also analysed how different spectral discretisation techniques can accelerate the solution time for both HITRAN and NEQAIR simulations. Thanks to the here developed approximate spectral representation used to handle HITRAN data, the time to generate a spectrum was reduced by up to two orders of magnitudes compared to the standard HITRAN library HAPI.

For hypersonic flows, two acceleration techniques were studied. Firstly, it was demonstrated how spectra can be effectively downsampled without significant loss of accuracy, resulting in a halving of the spectral size. The second method made use of spectral approximation. Another grid layer was added to the radiation solver for hypersonic problems, on which the spectra were resolved accurately. On the initial grid, the spectra were then estimated using the information from the coarser spectral grid. Various techniques ranging from a simple averaging to multi-dimensional regression were explored. In the end, it was found that the application of the analytic recalculation of the spectra with number densities and Planck function was the most reliable technique provided the flow was not too far from local thermodynamic equilibrium. If this technique was found to be inaccurate due to flow conditions, a two-point averaging of the nearest spectra was recommended.

Finally, the radiation solver was coupled with the INCA Computational Fluid Dynamics package. Some aspects and challenges of the coupling were discussed, mainly with regards to inaccurate NEQAIR solutions for cells of low temperatures. To further accelerate the calculation, the original radiation grid was kept separate from the INCA CFD grid, creating in total a system of two grid layers for HITRAN and grey simulations and three grid layers for NEQAIR simulations. It was shown that despite these attempts to accelerate the solution procedure, depending on the discretisation, 94% to 98% of the computation time of INCA was spent on resolving radiation (in the NEQAIR mode), which are unfortunately figures typical for this kind of problems.

From the analysis of the performance of various parts of the solver, the single most effective acceleration technique which should be applied in the future was the use of more approximate spectral methods, such as multi-band opacity binning for hypersonic plasma and k-distributions for combustion problems. In addition, an approach was also formulated for how the current solver could be parallelised further with Graphical Processing Units.

Acknowledgements

On a professional note, first and foremost, I must express my gratitude to my supervisor Prof. Dr. S. Hickel for his guidance and willingness to supervise my thesis. Despite his very busy schedule, he found some time for me every two weeks and responded whenever I needed help with INCA. He also did not openly protest against me handing in a 130 pages long literature study, which shows his dedication to this topic and his role as a supervisor.

Furthermore, I extend my gratitude to MSc. S. Silvestri and Prof. Dr. R. Pecnik from the Process and Energy department of TU Delft, who provided me with their own emission reciprocity based Monte Carlo implementation for inspiration and were willing to answer all my questions about the Monte Carlo methods.

In addition, firstly, I am grateful to Ir. K. Lemmens from the group of Mathematical Physics at TU Delft for providing me with advice regarding CPU and GPU parallelisation techniques and resulting challenges which I frequently faced. I must also thank Prof. Dr. J. Thijssen from the Kavli Institute of Nanoscience for providing me access to the Amsterdam Density Functional code with which I could recompute some of the databased NEQAIR transition factors for more accurate computation.

Finally, many thanks go to Dr. S. Karl from the German Aerospace Center's Institute of Aerodynamics and Flow Technology in Goettingen, who gave me very valuable advice regarding the use of grid layers and coupling with computational fluid dynamics; and to Dr. A. Brandis from NASA's Jet Propulsion Laboratory, whom I could contact regarding the NEQAIR code.

On a personal note, I must thank my partner Angelos for letting me complain to him about Fortran whenever I felt like it. I would also like to thank my friends Lenka, Daniella, Laura, Sam, Bart, Esmee, Juan, Hannah, Zyanya and Aaron for regularly going for a caffeine or wine dose with me and keeping me distracted when I needed it. Further thanks go to the rest of the Italian and aerodynamics basement cosa nostra for sharing the difficult Master times together with a cup of coffee. I also appreciate my good old friends back from Slovakia and Czech Republic for not forgetting about me despite the even-for-me-unusually high levels of asociality I displayed symptoms of during the last year. Peto, for example, was always there to show me wonderful photos from the hiking trips with his kids, which were a good reminder of why I should work hard to graduate on time and start having some actual life.

Of course, many thanks also to my family, without whom I would not be in this programme in the first place. Especially my wonder-sister Dominika helped me feel less alone whenever I felt like academia was not for me and wanted to quit, since she herself is enrolled in a doctoral programme and enjoying some of the effects of the good old impostor syndrome.

I would also like to thank to all my wonderful first year students I have mentored during the past two years, whose enthusiasm for basically anything that resembles an aircraft or spacecraft in some form, including a flying piece of foam and a metal box, helped remind me why I started with these studies in the first place.

Finally, I would like to thank *emergencycompliment.com* for helping me get through this thesis mentally.

M. Brchnelova
Delft, August 2020

Contents

Summary iii

List of Symbols and Abbreviations xi

List of Figures xvii

List of Tables xxiii

1 Introduction 1
- 1.1 Radiation in Flow Physics 1
- 1.2 Thesis Goal 2
- 1.3 Scope of This Text 3

2 Theoretical Background 5
- 2.1 Introduction to Radiation Definitions 5
- 2.2 Introduction to Radiation Physics 8
  - 2.2.1 Basic Theory of Matter-Radiation Interaction 8
  - 2.2.2 Basic Line Shapes and Broadening Mechanisms 11
  - 2.2.3 Atomic Lines, Rotational Lines, Rovibrational Bands and Vibronic Band Structures 13
  - 2.2.4 Radiation as a Larger Picture: The Radiative Transfer Equation 16
  - 2.2.5 Approaches to Spectral Approximation 19
- 2.3 Radiation in Hypersonics 23
  - 2.3.1 Historical Overview 23
  - 2.3.2 Modern Display of Hypersonic Radiation Modelling 28
  - 2.3.3 Modern Techniques of Hypersonic Radiation Modelling 32
- 2.4 Radiation in Combustion Systems 37
- 2.5 Turbulence Radiation Interaction 39
  - 2.5.1 TRI in Combustion Systems 40
  - 2.5.2 TRI in External Hypersonic Flows 42

3 Methodology 45
- 3.1 Method Selection 45
  - 3.1.1 Radiative Transfer Equation Solver 45
  - 3.1.2 Spectral Generation 45
  - 3.1.3 Further Spectral Processing 46
- 3.2 RTE Integration with Photon Monte Carlo 46
- 3.3 Spectral Generation with HITRAN and NEQAIR 48
  - 3.3.1 HITRAN / HITEMP 48
  - 3.3.2 NEQAIR 49

4 Implementation 61
- 4.1 Photon Monte Carlo 61
  - 4.1.1 Basic Logic 61
  - 4.1.2 Random Number Selection 62
  - 4.1.3 Discretization 63
  - 4.1.4 Basic Flow Diagram of ERMC 64
  - 4.1.5 Boundary Conditions 64
- 4.2 HITRAN 66
  - 4.2.1 Calculation of the Spectra from Database 66
  - 4.2.2 Approximation of the Total Internal Partition Function Sum 68
  - 4.2.3 Implementation Details 69
  - 4.2.4 HITEMP and Other Databases 73

4.3 NEQAIR . . . 73
4.3.1 NEQAIR Modifications and ADF . . . 74
4.3.2 Non-equilibrium Adjustments to Photon Monte Carlo Formulation . . . 75
4.3.3 NEQAIR Simulation Set-up Paramters . . . 75
4.4 INCA Implementation . . . 78
4.4.1 Required CFD Inputs. . . . 78
4.4.2 Implementation Principle . . . 78
4.4.3 Geometry and Flow Obstructions . . . 80
4.4.4 Flow Related Implementation Challenges . . . 80
4.4.5 Coupling Frequency . . . 82
4.4.6 Coupling with Nonequilibrium PMC . . . 84

5 Validation Results 85
5.1 Test Selection . . . 85
5.2 Discretisation and Convergence . . . 86
5.3 PMC Implementation and HITRAN Spectral Generation . . . 86
5.3.1 Case 1 and Case 2: Basic PMC Principles in 1D . . . 87
5.3.2 Case 3 and Case 4: Heat Transfer Mechanisms in 3D . . . 88
5.3.3 Case 5 and Case 6: HITRAN Implementation for H2O and Variable Domain . . . 89
5.3.4 Case 7 and Case 8: HITRAN Implementation for CO2 and Non-black Walls . . . 90
5.4 NEQAIR Verification and Validation Procedures . . . 91
5.4.1 CEV Entry . . . 91
5.4.2 FIRE II Entry . . . 94
5.4.3 Local vs Non-local Emission Wavelength Sampling . . . 96
5.4.4 Standard Deviations Compared to NEQAIR . . . 97
5.4.5 A Note on NEQAIR Accuracy and Convergence Requirements . . . 98
5.5 Results with INCA . . . 99
5.5.1 Case 1 Setup . . . 99
5.5.2 Case 2 Setup . . . 100
5.5.3 Case Results and Performance . . . 100

6 Further Acceleration Efforts 107
6.1 Acceleration using Sobol Sequences . . . 107
6.2 Acceleration by Optimising Discretisation Style . . . 112
6.3 Acceleration Using Three Grid Configurations . . . 114
6.3.1 Solution on a Coarser Mesh and IDW . . . 114
6.3.2 Spectral Interpolation and Regression . . . 115
6.3.3 Spectral Approximation and Regression . . . 115
6.3.4 Analytic Approach . . . 117
6.3.5 Performance Comparison . . . 121

7 Discussion 127
7.1 Performance of the Core of the RTE Solver . . . 127
7.2 Performance of the HITRAN Spectral Generator . . . 127
7.3 Performance of the NEQAIR-Based Spectral Generator . . . 128
7.4 Coupling and Performance with INCA . . . 129
7.5 Recommended Acceleration Methods . . . 129
7.5.1 On-the-Fly Calculation of QSS with Databasing Schemes . . . 129
7.5.2 Use of LBL Alternatives . . . 129
7.5.3 Other Recommended Acceleration Methods . . . 130
7.5.4 Recommendations for a Possible GPU Adaptation . . . 130

8 Conclusions and Outlook 133

Bibliography 137

A HITRAN Database 145

B Code Description 149
B.1 Brief Developer Guide . . . 149

B.2 Brief Description of Subroutines 154
B.3 Example Radiation Input File 161

List of Symbols and Abbreviations

List of Greek Symbols

α	Absorptivity
β	Extinction (attenuation) coefficient
Γ	Goulard number
γ_c	Collision half-width of a spectral line
γ_D	Doppler half-width of a spectral line
γ_L	Lorentz half-width of a spectral line
γ_s	Stark half-width of a spectral line
Δ	LES grid size
δ	DNS grid size, Dirac delta function, line pressure shift
ε	Emissivity, kinetic energy
ϵ_0	Permittivity of vacuum
η	Wavenumber
θ	Effective kinetic temperature, polar angle
κ	Absorption coefficient
κ_P	Planck mean absorption coefficient
κ_R	Rosseland mean absorption coefficient
Λ	Escape factor
λ	Wavelength
λ_k	Force constant in potential Hamiltonian
μ	Scattering coefficient, transition moment, reduced mass
μ_0	Permeability of vacuum
ν	Wavenumber
ρ	Density
σ	Stefan-Boltzmann constant, standard deviation, collision cross section, opacity
σ_s	Scattering coefficient
σ_{rot}	Number of distinguishable molecular rotational modes
τ	Optical thickness, transmissivity, time scale, relaxation time
ϕ	Scattering phase function, line function
$\underline{\phi}$	Gas state vector
ψ	Azimuthal angle, wavefunction
Ω	Domain, solid angle
ω	Angular frequency

List of Latin Symbols

A	Area
A_{ul}	Einstein coefficient for spontaneous emission
B	Planck black body emissive power, rotational constant
B_{lu}	Einstein coefficient for absorption
B_{ul}	Einstein coefficient for stimulated emission
C_1	First radiation constant in Planck's law
C_2	Second radiation constant in Planck's law
c	Speed of light
D	Diffusivity, diameter
E	Energy, Emissive power
E_n	Exponential integral of the n-th kind
E_b	Black-body emissive power
F	View factor, Herman-Wallis effect correction factor
G	Irradiation
g	Degeneracy, space of smoothly varying κ
$\overline{g}$	Gaunt factor
H	Hamiltonian, Heaviside step function
h	Planck constant, enthalpy
$\hbar$	Modified Planck constant
I	Intensity
I_b	Planck black body intensity
J	Radiosity, total angular quantum number
j	Rotational quantum number
K	Rate coefficient
k	Boltzmann constant, angular wavenumber
k^*	Reordered wavenumber distribution
k_b	Boltzmann constant
L	Length, Planck spectral emissive power distribution
l	Lower energy state
M	Heavy collision partner, vibrational transition dipole moment
m	Molar mass, mass, Sobol direction number
N	Total number, number density
n	Refraction coefficient, number density
$\boldsymbol{n}$	Normal
P	Power, pressure
P_n^m	Legendre polynomials
Pl	Planck number
p	Pressure, primitive polynomial
Q	Radiative power, partition function
q	Heat flux, Franck-Condon factor
$\mathscr{R}$	TRI correlation, dipole moment
R	Random number, probability of dipole transition, universal gas constant
R_y	Hydrogen ionisation potential (Rydberg's constant)
$\boldsymbol{r}$	Direction vector
r	Transition rate
S	Radiative source function, intensity
Sc	Schmidt number
$\boldsymbol{s}$	Direction vector
s	Path, path length
T	Temperature
t	Time, transmission coefficient
u	Upper energy state, scaling function
V	Potential energy Hamiltonian, volume
v	Vibrational quantum number, velocity, direction number
W	Band width, electron average kinetic energy
w	Specific width, weighting factor
x	Coordinate, mole fraction
Y	Mass fraction, spherical harmonics
y	Coordinate
z	Coordinate

List of Subscripts and Superscripts

∞	Freestream
$+$	Positive, ionic
$-$	Negative, electronic
0	Reference, initial
a	Atoms, atomic
abs	Absorption
avg	Average
$b-b$	Bound-bound
$b-f$	Bound-free
bb	Black body
c	Continuum, cold, chemistry, collisional
coup	Coupled
D	Doppler
Dis	Dissociation
E	Emission
e	Electrons, electron, electronic
η	At given wavenumber (spectral)
emi	Emission
f	Flow, filtered cells
$f-f$	Free-free
G	Absorption
g	In g space, gas
γ	Photon
H	Hydrogenic
i	Incoming
ion	Ionisation
k	At given wavenumber (spectral)
λ	At given wavelength (spectral)
L	Lower state
l	Lower state
lu	Lower to upper state
M	Heavy collision partner
mix	Mixture
ne	Nonequilibrium
ν	At given frequency
o	Outgoing
P	Planck
pred	Predissociation
rad	Radiative
r	Rotational, radiative
ref	At reference state
rl	Lower rotational state
ru	Upper rotational state
rot	Rotational
θ	Polar
T	Turbulent
t	Translational, total, thermal
tot	Total
U	Upper state
u	Upper state
ul	Upper to lower state
unc	Uncoupled
v	Vibrational
rv	Rovibrational
w	Wall
x	Mole fraction
ψ	Azimuthal

List of Acronyms and Abbreviations

ADF	Amsterdam Density Functional
ARMC	Absorption Reciprocal Monte Carlo
ASCII	American Standard Code for Information Interchange
b-b	Bound-bound
b-f	Free-bound
CEV	Crew Exploration Vehicle
CFD	Computational Fluid Dynamics
CK	Correlated-k
CPU	Central Processing Unit
CR	Collisional-Radiative
DNS	Direct Numerical Simulation
DOS	Discrete Ordinates Method
DPLR	Data Parallel Line Relaxation Code
DSMC	Direct Simulation Monte Carlo
EAST	Electric Arc Shock Tube
ERMC	Emission Reciprocal Monte Carlo
EWB	Exponential Wide Band
f-f	Free-free
FIRE	Flight Investigation Reentry Environment
FMC	Forward Monte Carlo
FSCK	Full Spectrum Correlated-k
FSSK	Full Spectrum Scaled-k
FVM	Finite Volume Method
GPU	Graphics Processing Unit
HAPI	HITRAN Application Programming Interface
HITRAN	High Resolution Transition Molecular Absorption Database
HITEMP	High-temperature Molecular Spectroscopic Database
HLF	Hoenl-London Factor
HOMO	Homogeneous
HSBN	Hybrid Spectral Narrow Band
HYPTBL	Hyperbolic tangent boundary layer stretching
ICBM	Inter-continental Ballistic Missile
IDW	Inverse distance weighting
IRBM	Inter-range Ballistic Missile
IR	Infrared
LBL	Line-by-line
LDS	Low Discrepancy Sequence
LES	Large Eddy Simulations
LORAN	Langley Optimized Radiative Nonequilibrium
LOS	Line-of-sight
LS	Least squares, LOS integration
LTE	Local Thermodynamic Equilibrium
LTNE	Local Thermodynamic Nonequilibrium
MBOB	Multi-band Opacity Binning
MC	Monte Carlo
MGFSCK	Multi-group Full Spectrum Correlated-k
MGFSK	Multi-group Full Spectrum k-Distribution
MGME	Multi-group Maximum Entropy
MSFSCK	Multi-scale Full Spectrum Correlated-k
MSFSK	Multi-scale Full Spectrum k-Distribution
MSL	Mars Science Laboratory
NBCK	Narrow Band correlated k-distribution
NEQAIR	Nonequilibrium Air Radiation
NIR	Near Infrared

List of Acronyms and Abbreviations Continued

NIST	National Institute of Standards and Technology
NNLS	Non-negative least squares
ODF	Opacity Distribution Function
OT	Optically thin
PARADE	ESA Plasma Radiation Database
PDE	Partial Differential Equation
PDF	Probability Density Function
PMC	Photon Monte Carlo
QMC	Quasi-Monte Carlo
QSS	Quasi-Steady State
RAM	Reentry Attenuation Measurement
RANS	Raynolds-Averaged Navier Stokes
RQMC	Randomized Quasi-Monte Carlo
RTMC	Ray-Tracing Monte Carlo
RT(M)	Ray Tracing (Monte Carlo)
RTE	Radiative Transfer Equation
SGS	Subgrid scale
SHM	Spherical Harmonics Method
SLWSGG	Spectral-line Based Weighted-sum of Grey Gasses
SNB	Statistical Narrow Band
SPARTAN	Simulation of Plasma Radiation in Thermodynamic Nonequilibrium
SPRADIAN	Structured Package for Radiation Analysis
SRB	Smeared Rotational Band
SSH	Schwartz, Slawsky and Hetzfeld
STDEV	Standard deviation
STRAP	Shock Tube Radiation Program
StS	State-to-State
TRI	Turbulence-Radiation Interaction
TS	Tangent Slab
V - e	Vibrational-electronic exchange
V - T	Vibrational-translational exchange
V - V	Vibrational-vibrational exchange
VUV	Vacuum-ultraviolet
VIS	Visible
WSGG	Weighted-sum of Grey Gasses
WSCK	Wide Spectrum Correlated-k

List of Figures

2.1 Variable definitions for the derivation of the 1D approximation of radiative heat transfer in Equation (2.9). From Ref. [68]. 6
2.2 Illustration of the possible collisional-radiative transition interactions, where b stands for collisional rates. Note that in this drawing, the second and third Einstein coefficients are denoted with C, not B as in the text. From Ref. [37]. 9
2.3 Illustration of the conditions where the Lorentz and the Doppler Broadening typically dominate. From Ref. [68]. 12
2.4 P, Q, and R branches in typical rovibrational spectral bands due to the -1, 0 and 1 changes in the rotational quantum number during transition. From Ref. [68]. 15
2.5 Definitions of the positive and negative direction variables for the derivation of the 1D radiative transfer Equations (2.63) and (2.64). From Ref. [68] 16
2.6 Demonstration that while the absorption coefficients of the gas at two different pressures do not look correlated at all, the resulting smooth $k(g)$ distributions do. This lead to the development of correlated-k and scaled-k models for non-homogeneous media. From Ref. [57]. 19
2.7 Demonstration of the reordering procedure of the absorption coefficient, from the original spectrum on the left to the reordered k-distribution (red) and cumulative k-distribution (black) on the right. From Ref. [68]. 20
2.8 Elsasser constant-line-strength and constant-line-spacing band model compared to a statistical band model assuming random spacing and random line strengths. From Ref. [68]. 22
2.9 The principle of frequency banding (left) based on the spectral location and opacity binning (right) based on the absorption coefficient. From Ref. [51]. 23
2.10 Kivel's diagram to emphasise the significance of radiation heat flux and consideration of nonequilibrium for (re)entry trajectories of ICBMs, Mars probes and re-entering satellites from Ref. [53]. 24
2.11 For the velocity vs. entry time profile shown on the left Figure, the right Figure shows the expected radiative heat flux compared to the convective heat flux for a Jovian entry, as computed by Moss et al. in 1976 further discussed in Ref. [70]. 25
2.12 Experimental data compared to Park's predictions of total nonequilirium radiation heat flux as a function of flight velocity based on NEQAIR, showing a relatively good agreement. From Ref. [80]. 27
2.13 Comparison between experimental spectra and NEQAIR spectral prediction at 10km/s and pressure of 13Pa by Park in 1989 showing a significant disagreement. However, due to under-prediction in shorter wavelengths and over-prediction in longer wavelengths, the integrated heat flux agreed well as shown in Figure 2.12. From Ref. [80]. 27
2.14 The disagreement between experimental data and a NEQAIR simulation at lower altitudes discovered by Levin et al. in 1993, leading to the development of NEQAIR96 two years later. From Ref. [60]. 28
2.15 Demonstration of the validity of the QSS assumption at 71km (left) and 80km (right) with the speed of 5.1km/s, including the N_2 QSS correction, performed by Levin et al. in 1994. From Ref. [62]. 28
2.16 The integrated convective, radiative and total heat flux along the stagnation line of Stardust computed by Olynick et al. in 1999 in Ref. [74]. 29
2.17 The radiative heat flux along the stagnation line at different trajectory points of Stardust computed by Olynick et al. in 1999 in Ref. [74]. 29
2.18 Comparison between the computed translational and vibrational temperatures when using 11, 12 and 17 species models using QSS (G) and Boltzmann (E) distributions at two different flight conditions computed by Liu et al. in 2010, showing a significant deviation due to the equilibrium distribution assumption (11G vs 12E), which is larger than the deviation when ablation is considered (12E vs 17E). From Ref. [64]. 30

2.19 Example of resolved spectra at the 51s trajectory point using the 11 species non-Boltzmann model in the direction inward (from the perspective of the vehicle) and outward (from the perspective of the observed of the reentry) computed by Liu et al. for the Stardust reentry. It is shown that at these conditions, majority of the radiation comes from the VUV atomic lines. From Ref. [64]. 30
2.20 Difference in the resolved radiative heat flux along the stagnation line depending on how many species are considered and whether Boltzmann distribution is assumed. Comparing the 12EB and 12EQ models, it is apparent that assumption of Boltzmann distributions at these flight conditions (≈ 62km, ≈ 11km/s) results in unphysical kinks, introducing more errors into the solution than neglecting ablation altogether (17EB vs 11GQ and 12EQ). 31
2.21 Spectrum of air at 8.33km/s and 10Pa showing the categorisation of the major spectral features. From Ref. [26]. 31
2.22 Simulation of the VUV portion of the spectrum by the original NEQAIR model, improved NEQAIR model, Johnston's model and experimental data. From Ref. [26]. 32
2.23 Simulation of the VIS portion of the spectrum by the original NEQAIR model, improved NEQAIR model, Johnston's model and experimental data. From Ref. [26]. 32
2.24 Simulation of the NIR and IR portion of the spectrum by the original NEQAIR model, improved NEQAIR model, Johnston's model and experimental data. From Ref. [26]. 32
2.25 The match between the zonal, view-factor based method (VF) and tangent slab (TS) method compared to assumed accurate solution by a ray tracing MC method (RTM), showing in general a very good agreement with better convergence for VR when computing the flux density of the RAM-C II probe reentry, at 61km and 7.5km/s, by Andrienko et al. from [7]. 33
2.26 Comparison between the LBL and FSCK approaches (left), and between the exact tangent slab (TS) method and SHM approximations (right) for Mars CEV entry. From Ref. [12]. 34
2.27 Results for stagnation point (a) and shoulder region (b) heat flux divergence at the maximum heat flux trajectory point of Orion CEV when using tangent slab (TS) and photon MC (PMC) approaches, with PMC already verified. It is observed that TS method can result in fair errors in shoulder regions (note that the scale is logarithmic). From Ref. [31]. 35
2.28 Behaviour of line strength of the strongest atomic N (left) and O (right) lines as a function of temperature, showing different trends according to which the lines could be grouped into scales by Bansal et al. from Ref. [10]. 35
2.29 Comparison between the LBL approach, the HSBN model developed by Soucasse et al. and the SRB model from LORAN for the spectral incident flux (left) and divergence of heat flux (right) of the Huygens probe entry to Titan. From Ref. [102]. 36
2.30 Wall directed heat flux for Martian entry from the CO 4-th positive band computed with LBL, SRB and MBOB models by Johnston et al. in Ref [49]. 37
2.31 Divergence of heat flux for Martian entry from the CO 4-th positive band computed with LBL, SRB and MBOB models by Johnston et al. in Ref [49]. 37
2.32 Mole fraction and internal energy development of Nitrogen undergoing internal excitation and dissociation at 10kK for various numbers of internal groups of the StS model and for the NEQAIR (Park) model. From Ref. [65]. 38
2.33 Accuracy comparison of various SHM approximations including P_1, SP_3 and SP_5 and the optically thin approximation (OT) compared to an accurate PMC LBL data in a hydrogen combustor shown at two x positions, 6cm (left) and 12cm (right). 38
2.34 Emission correlation due to TRI as a function of LES filter width Δ ratio to DNS grid size δ for 10%, 20% and 30% temperature fluctuations in a turbulent jet far field. From Ref. [87]. 41
2.35 Absorption correlation due to TRI as a function of LES filter width Δ ratio to DNS grid size δ for 10%, 20% and 30% temperature fluctuations in a turbulent jet far field. From Ref. [87]. 41
2.36 The magnitude of the emission (dash-dotted), absorption (dashed) and total TRI terms for optical thicknesses of 0.1 (a), 1 (b) and 10 (c) computed by Silvestri in Ref. [98]. It is obvious that absorption TRI term cannot be neglected for gasses which are not optically thin. 42
2.37 The TRI effects in hypersonic boundary layer on mean streamwise velocity (left) and turbulent kinetic energy (right) evolving in time t, considering 9.5km/s flight at 53km altitude with M_δ = 0.153. From Ref. [27]. 43

3.1 The principle of operation of the forward MC, emission based reciprocal MC and absorption based reciprocal MC by Tesse et al. from Ref. [108]. Optical path shown. 48

4.1 Visualisation of photon ray trajectories in a Cartesian 3D domain for illustration. The trajectories are shown at points in which a new cell is entered. 63
4.2 Illustration that wavenumber-based (k) discretization leads to more points located in the steep region of the Planck function unlike wavelength-based (λ) discretization, generally leading to a slightly better accuracy since majority of the radiation comes from the steep peak region. 64
4.3 Flow diagram of core of the Monte Carlo ray tracing code. 65
4.4 Illustration of some of the main transition parameters saved in HITRAN. S, the line strength, is the area under the line, γ is the line half width at half maximum and δ is the shift due to pressure (non-vacuum conditions). 66
4.5 Absolute relative error in the sum of the total partition function when evaluated using cubic splines developed in Equations (4.28), (4.29) and (4.30) for H_2O, CO_2 and H_2, respectively. 69
4.6 Visualisation of the discretization principle for fast HITRAN calculations of the emission spectra. Both the maximum absorption cross section as well as the area under the curve are preserved, leading to both accurate integral and κ_p as well as correct sampled emitting wavelengths. 70
4.7 Demonstration of the principle shown in Figure 4.6 applied to a real spectrum. The light grey + data represents the original spectrum whereas the dark x data shows the reduced, fast calculation. 70
4.8 A comparison between an accurate and simulated Planck mean absorption coefficient for CO_2 with the original and the reduced spectral technique, showing an excellent agreement in the range where HITRAN is accurate despite the use of the reduction technique. Validation data from [68]. 71
4.9 A comparison between an accurate and simulated Planck mean absorption coefficient for H_2O with the original and reduced spectral technique, showing an excellent agreement in the range where HITRAN is accurate despite the use of the reduction technique. Validation data from [68]. 71
4.10 Transition cross sections for H_2O and CO_2 at reference conditions for illustration of the typical cross-section spectra. 72
4.11 A depiction of the cumulative emissivity of H_2O and CO_2 for various temperatures to indicate the requirements for the minimum and maximum resolved wavelength. 73
4.12 A comparison between the Planck function defined as a ratio between the emissivity and the absorption coefficient for conditions close to an equilibrium (lighter blue + data) and in a high nonequilibrium (dark x data) for a Nitrogen mixture. 74
4.13 An illustration of a 100 selected wavelengths from a highly variable emission spectrum of hot air. 76
4.14 The integrated spectral radiance for two Earth reentry cases to indicate the necessary requirements on minimum and maximum wavelengths needed to be resolved to capture the essential spectral featured. 77
4.15 An illustration of the principle of detection of the end of a computational domain (EOD) from INCA. On the upper part of the Figure, a case of aligned grids is shown. The right radiation cell (in blue dashed lines) is outside of the INCA grid (black thin lines). This is detected by the comparison of the distance ds of the radiation cell centroid (blue) to the nearest INCA cell centroid (grey). Since this distance is larger than half of the dimension of the radiation cell in the axis where the nearest INCA cell is located (x-axis, dx), the radiation cell is considered outside of the domain. For the left radiation cell, the nearest centroid is less than $dx/2$ away, and thus this cell is a part of the domain. The same scenario is illustrated on the lower half for non-aligned grids, showing the source of the misalignment in the domain boundaries as a result. In case the nearest cell was located in the y axis, ds would be compared to $dy/2$. 81
4.16 Illustrations of the problematic results obtained when using NEQAIR for flow at low temperatures. The missing section for temperatures of 300K (grey x signs) and 400K (dark grey plus signs) represents the regions where the values which come from NEQAIR are undefined. The values for 500K (light blue squares) and 600K (dark blue stars) are resolved without errors. . . . 82
4.17 The effect of pressure broadening for H_2O at reference temperature (296K) for pressure levels of 0.2, 1.0 and 5.0 atmospheres. As can be seen, for small variations in pressure (10-100%), the spectra should not differ significantly and the absorption coefficient can be recomputed by the pressure ratio. 83

5.1 The radiative source term for the 1st test case: 1D domain with a constant absorption coefficient of 1 m^{-1} and black walls, linear profile. Validation data from Ref. [98]. 87
5.2 The radiative source term for the 2nd test case: 1D domain with a constant absorption coefficient of 1 m^{-1} and black walls, parabolic profile. Validation data from Ref. [98]. 87
5.3 The radiative source term for the 3rd test case: 3D domain with a constant absorption coefficient of 5 m^{-1} and black walls and sinusoid profile. Validation data from Ref. [98]. 88
5.4 The radiative source term for the 4th test case: 3D domain with a constant absorption coefficient of 0.5 m^{-1} and black walls and sinusoid profile. Validation data from Ref. [98]. 88
5.5 The radiative source term for the 5th test case: 1D domain filled with H_2O at constant 1000K and black walls. Validation data from Ref. [98]. 89
5.6 The radiative source term for the 6th test case: 1D, downsized domain filled with H_2O at constant 1000K and black walls. Validation data from Ref. [98]. 89
5.7 The radiative source term for the 7th test case: 1D domain filled with CO_2 with black walls at a linear profile. Validation data from Ref. [98]. 90
5.8 The radiative source term for the 8th test case: 1D domain filled with CO_2 with black wall and partly reflective at a linear profile. Validation data from Ref. [98]. 90
5.9 The radiative source term for the 1st NEQAIR case: A box of a N and O mixture at 8000K enclosed by black walls at 5000K. Validation data directly from NEQAIR. 91
5.10 The real spacing between the line-of-sight points of the NEQAIR test cases. Fire II spacing shown in red, CEV spacing in blue. 92
5.11 Profiles of translational, electron, vibrational and rotational temperatures through the LOS points of the Orion Crew Entry Vehicle stagnation line. 92
5.12 Species number density profiles through the LOS points of the Orion Crew Entry Vehicle stagnation line 93
5.13 A comparison between the 1D results for the radiative source term of the large scale CEV simulation produced by NEQAIR and by own radiation solver (grey squares and blue triangles, respectively). 93
5.14 A comparison between the 1D results for the radiative source term of the small scale CEV simulation produced by NEQAIR and by own radiation solver (grey squares and blue triangles, respectively). 93
5.15 Profiles of translational, electron, vibrational and rotational temperatures through the LOS points of the FIRE II stagnation line. 94
5.16 Species number density profiles through the LOS points of the FIRE II stagnation line. 94
5.17 A comparison between the 1D results for the radiative source term of the large scale FIRE II simulation produced by NEQAIR and by own radiation solver (grey squares and blue triangles, respectively). 95
5.18 A magnification of Figure 5.17 without the high temperature region to show the rest of the profile. 95
5.19 A comparison between the 1D results for the radiative source term of the large scale FIRE II simulation produced by NEQAIR and by own radiation solver (grey squares and blue triangles, respectively). 96
5.20 A magnification of Figure 5.19 without the high temperature region to show the rest of the profile. 96
5.21 A comparison between the results for the radiative source term of NEQAIR and own solver for a simple nonequilibrium case (grey squares and blue triangles, respectively). 97
5.22 Difference between the divergence of the heat flux for the large scale FIRE II case (see Figure 5.17 and 5.18) when using local (blue triangle) and global (light blue diamond) wavelengths sampling compared to validation data (grey squares). 97
5.23 An illustration of the INCA grid for the first case. The overall domain dimension is 0.5m x 0.3m x 0.1m. 99
5.24 An illustration of the INCA grid for the second case. The overall domain dimension is 0.03m x 0.03m x 0.01m. The step if 0.01m tall and 0.02m wide. 101
5.25 The temperature field of the INCA CFD test case 1 at 0.003s. The black lines show the spectral discretisation. Temperature in K. 101
5.26 The density field of the INCA CFD test case 1 at 0.003s. The black lines show the spectral discretisation. Density in kg/m^3. 102
5.27 The radiative source term of case 1 at 0.003s. The black lines show the spectral discretisation. The radiative source is given in W/m^3. 102

5.28 The temperature field of the INCA CFD test case 2 at 0.007s. The black lines show the spectral discretisation. Temperature in K. 103
5.29 The density field of the INCA CFD test case at 2 0.007s. The black lines show the spectral discretisation. Density in kg/m^3. 104
5.30 Emission and absorption spectra from case 2 from three different regions in the domain along the bottom line. The spectrum at point 9 (black) is from the hottest, highest density region close the the symmetry wall. The middle grey spectrum is roughly in the middle of the domain, and the light-grey spectrum comes from the left side of the domain with lowest temperatures and number densities. 104
5.31 The radiative source term of case 2 at 0.007s. The black lines show the spectral discretisation. The radiative source given in W/m^3. 105

6.1 A comparison between a 2D Sobol sequence for 10000 (top, left) and 1000 (top, right) realisations and a 2D random number sequence generated using a built-in generator for 10000 (bottom, left) and 1000 (bottom, right) realisations. 108
6.2 Convergence of PMC using Sobol and built-in random number generators for case 3 with number of realisations. 109
6.3 Convergence of PMC using Sobol and built-in random number generators for case 1 with number of realisations. 110
6.4 Convergence of PMC using Sobol and built-in random number generators for case 3, adjusted by the higher Sobol number generation time. 110
6.5 Convergence of PMC using Sobol and built-in random number generators for case 1, adjusted by the higher Sobol number generation time. 111
6.6 Photon loop times for a HITRAN case of H_2O at 1000K with Sobol direction and random direction generation, demonstrating that the effect of Sobol generation time is completely negligible when complex spectra are involved. 111
6.7 The relative error in spectral radiance (W/cm^2/sr) for various spectral bands as a function of line discretization. 112
6.8 Principles of the two downsampling methods adapted and investigated. 112
6.9 The performance of the regular downsampling technique in terms of the STDEV and spectrum size with tolerance. 113
6.10 The performance of the cumulative (integral) downsampling technique in terms of the STDEV and spectrum size with tolerance. 113
6.11 The setup of the primary, secondary and tertiary grid with illustration where the interpolation weights used for 2nd grid spectral approximation are defined. 115
6.12 Strong nonequilibrium Planck functions (dark and light grey) at two consecutive LOS points in the CEV Afterbody test case in a spectral region relatively far away from strong transitions. Equilibrium Planck functions (dark and light blue) shown for comparison, illustrating the Planck function ratio assumption. 118
6.13 Strong nonequilibrium Planck functions (dark and light grey) at two consecutive LOS points in the CEV Afterbody test case in a spectral region at strong transition lines showing that the Planck function ratio assumptions cannot be made. Equilibrium Planck functions (dark and light blue) shown for comparison, illustrating the Planck function ratio assumption. 118
6.14 A demonstration of the accuracy of the analytical approach when LTE can be assumed. The original spectrum is in bright blue x, the approximated result in grey * and the real spectrum for comparison in dark +. 119
6.15 A demonstration of the accuracy of the analytical approach around the region of strong atomic emission when LTE can be assumed. The original spectrum is in bright blue x, the approximated result in grey * and the real spectrum for comparison in dark +. 120
6.16 A demonstration of the inaccuracy of the analytical approach in nonequilibrium. The original spectrum is in bright blue x, the approximated result in grey * and the real spectrum for comparison in dark +. 120
6.17 A demonstration of the inaccuracy of the analytical approach in nonequilibrium around the region of strong atomic emission. The original spectrum is in bright blue x, the approximated result in grey * and the real spectrum for comparison in dark +. 121

6.18 Performance of the spectral regression methods for a 3rd grid adjusted from 78 cells to 30. LS stands for least square regression and NNLS for non-negative least squares regression. 122
6.19 The performance of spectral approximation methods for a 3rd grid adjusted from 78 cells to 30. 122
6.20 The performance of spectral regression methods for a 3rd grid adjusted from 78 cells to 15. LS stands for least square regression and NNLS for non-negative least squares regression. 123
6.21 the performance of spectral approximation methods for a 3rd grid adjusted from 78 cells to 15. . 123

7.1 The average number of cell crossings over the Orion CEV stagnation line. The higher number corresponds to the more transmissive boundary layer region. 131

B.1 Basic logic of the subroutine used for NEQAIR spectral generation. 151
B.2 The principle of spectral data preparation in the main radiation routine before photon loop is started, depending on the type of simulation. 153
B.3 Example radparam.inp file. 161

List of Tables

2.1 Emission and absorption correlation terms computed by Roger et al. for a turbulent jet far field at 20% temperature fluctuations. From Ref. [87]. 40
2.2 Emission TRI terms in a turbulent jet far field computed by Roger et al. for 20% temperature fluctuations after application of a box filter. From Ref. [87]. 41
2.3 Absorption TRI terms in a turbulent jet far field computed by Roger et al. for 20% temperature fluctuations after application of a box filter. From Ref. [87]. 41

3.1 Available HITRAN species ID list. 49
3.2 The most recent update to NEQAIR reaction rate parameters determined by Brandis and Cruden in Ref. [26]. 57

4.1 A comparison of the performance of the standard HITRAN processing library API and own implementation. The respective speedup thanks to the developed techniques is also shown. 72
4.2 A short overview of the contents of the HITEMP database. For accuracy at high (> 3000K) temperatures, it contains 25 times more lines for CO_2 and more than 500 times the lines for H_2O. . . 73
4.3 The pre-set automatic spectral discretization used for NEQAIR subroutines. 76
4.4 Differences in radiative surface heatflux on the CEV backshell when using various NEQAIR absorption methods. 78
4.5 The input dataset required for each type of radiation simulation. 79

5.1 The summary of the validation cases. 86
5.2 Standard deviation and average (absolute) heat flux for comparison, and the ratio of the two for the nonequilibrium cases evaluated using data from the 1D NEQAIR technique. For FIRE II, since majority of the STDEV came from the edge, shock region thanks to the boundary conditions, the figures are also stated not taking these boundary condition points into account. 98
5.3 Evolution of test case results with NEQAIR version. From Ref. [25]. 98
5.4 Thermodynamic parameters and number species densities of the hot, non-reacting Nitrogen flow case simulated with INCA. 100
5.5 An overview of the simulated cases with INCA and the performance of the radiation code for varying discretisation levels. 100
5.6 Contributions of various parts of the radiative solver to the total computation time, for the 3rd run from Table 5.5. 105

6.1 The specification of the spectral regions defined for the species considered for regression. 116
6.2 The summary of the gas conditions of the 4 LOS points selected for analysis of the analytic adjustment method. 119
6.3 A comparison of standard deviations of the radiative heat flux divergence for the different spectral approximation techniques tested. (NN)LS stands for (non-negative) least squares with the number of regression dimensions indicated. 122
6.4 The time required for the tested acceleration schemes for the two 3rd grid discretisation levels (N_f) with doubling in photon ray number N_γ. N is the number of the 2nd grid cells. 124
6.5 The time required for the tested acceleration schemes for two 3rd photon ray discretisation levels (N_γ) with refining the 3rd grid N_f. N is the number of the 2nd grid cells. 124
6.6 The time required for the tested acceleration schemes with increasing number of 2nd grid cells. N_f stands for the number of the cells on the 3rd grid and N_γ for the number of photon rays. . . 124

1

Introduction

> *"I admit, I'm getting a little gray, but radiation will do that to you."*
>
> — J. T. Kirk, June 2326

1.1. Radiation in Flow Physics

Next to convection and conduction, radiation is one of the basic means of heat transfer. However, unlike convection and conduction, it is usually neglected in the field of aerodynamics. In most aerodynamic applications, contribution of radiation to the overall energy balance is insignificant and neglecting it typically does not cause significant errors in the flow solution.

This, however, does not hold for highly radiating flows, such as those encountered in hypersonic aerodynamics (e.g. during reentry) or in combustion systems, where the temperature of the gasses is very high. In these cases, radiation must be corrected for by an additional term in the energy equation, $S_{\text{radiation}}$, which is the divergence of the radiative heat flux q_{rad}. The radiative heat flux is the integrated balance between emission and absorption. For a condition of local thermodynamic equilibrium, it can be defined as, as will be derived in the text:

$$-S_{\text{radiation}} = \nabla \cdot q_{\text{rad}} = \int_0^\infty \kappa_\eta \left(4\pi I_{b\eta} - \int_{4\pi} I_\eta d\Omega \right) d\eta = 4\kappa_P \sigma T^4 - \int_0^\infty \int_{4\pi} \kappa_\eta I_\eta d\Omega d\eta, \tag{1.1}$$

where, for a wavenumber η, κ_η is the absorption coefficient, $I_{b\eta}$ is the Planck function, I_η is the spectral radiative intensity and κ_P is the Planck mean absorption coefficient. From this formulation, it is obvious that spectral properties must be determined to resolve the radiative heat flux.

The general definition of the Planck function assumes local thermodynamic equilibrium (LTE), in which the Planck function at a given wavelength can be computed directly from the temperature of the medium. The emissivity at each wavelength can then be easily determined from the absorption coefficient multiplied by the LTE Planck function. This information is then sufficient for a complete spectral description of the gas.

However, in very high speed applications or applications involving ionised mixtures, such as atmospheric reentry, LTE oftentimes cannot be assumed and the nonequilibrium Planck function is then defined as the ratio of emissivity to the absorption coefficient. The emissivity and absorption coefficients must be determined separately, derived from the detailed balance of internal molecular and atomic states and the transition rates in-between them, as well as their interaction with the free electrons outside in the gas. The mean Planck absorption coefficient κ_P in Equation (1.1) then loses its meaning, and instead, it is the integrated emissivity and absorption coefficients at each wavelength which provide spectral description of the medium.

Finally, the last component of Equation (1.1) is the spectral radiative intensity I_η. It is computed from the so-called radiative transfer equation (RTE) along a vector of sight s, along which there is emission, absorption and scattering. The RTE takes form as (this will be derived later in the text):

$$\frac{dI_\eta}{ds} = \hat{s} \cdot \nabla I_\eta = \kappa_\eta I_{b\eta} - \beta_\eta I_\eta + \frac{\sigma_{s\eta}}{4\pi} \int_{4\pi} I_\eta \left(\hat{s}_i\right) \Phi_\eta \left(\hat{s}_i, \hat{s}\right) d\Omega_i, \tag{1.2}$$

where β_η is the so-called attenuation coefficient, which is the sum of scattering and absorption coefficients ($\beta_\eta = \kappa_\eta + \sigma_\eta$). The integral term on the right represents the amount of light scattered from other directions to the line of sight s, with a scattering probability phase function from direction s_i to s of $\phi(s_i, s)$. In this work, scattering is not considered, since it is typically important only for cases with particulate media such as sooting flames or hypersonics with very significant ablation. Without scattering, Equation (1.2) can be simplified to:

$$\frac{dI_\eta}{ds} = \kappa_\eta (I_{b\eta} - I_\eta). \tag{1.3}$$

From Equation (1.3), is it observed that radiation is both a local and a global problem. It is local in the sense that the overall heat flux balance is directly dependent on the amount of emission of the radiating cell, and global since the amount of radiative heat flux absorbed depends on the nature and intensity of radiation of the flowfield around. Moreover, since many media are fairly transmissive to radiation, the photon rays can propagate over long distances, resulting to the fact that the local heat flux might be readily affected by radiating cells on the other side of the domain. This already hints at the amount of required resources involved in the computation of the radiation field.

Finally, the last term which enters both Equations 1.1 and 1.3 not yet discussed is the spectral absorption coefficient. For a so-called grey medium, the absorption coefficient is constant over the entire spectrum, and thus the integration of the RTE and solution of the heat flux divergence is fairly simple. However, some gasses have very highly variable absorption coefficients due to electronic, vibrational and rotational transitions (so called bound-bound), as well as due to bound-free and free-free transitions in ionised media, where:

– Bound-bound (b-b) transitions: are transitions of the internal states of the atoms and molecules, such as electronic, vibrational and rotational excitation and de-excitation

– Bound-free / free-bound (b-f / f-b) transitions: are transitions in which an electron is either released due to an electron or heavy-particle impact, or in which an electron recombines with an ion

– Free-free (f-f) transitions: are transitions where radiation is released or absorbed due to the change in energy of predominantly electrons due to trajectories altered by the collision with other particles (also called Bremsstrahlung)

All these processes result in highly variable spectra of the gas species, dominated by mostly atomic lines in the ultraviolet, vibrational molecular band radiation in the visible and near infrared, and rotational-vibrational molecular band radiation in the far infrared parts of the spectra. The line and band strength heavily depends on the gas state, and the shapes of the lines and bands change due to effects such as the presence of a magnetic field, collisions, resonance or Doppler effects. All these factors must be considered to properly determine the absorption and emission coefficients of the gas species as functions of the wavenumber, and, as can be inferred from Equation 1.3, the intensity, then, in principle, has to be solved separately for each wavenumber η. For most practical applications, the resulting spectrum has to be simplified in a manner such that the spectral energy is not altered significantly, which will be from now on referred to as spectral processing or approximation.

Thus, the problem at hand is threefold: i) to determine the spectra of the gas species at the given gas condition, ii) to simplify the spectra such that the computation is affordable, and finally, iii) to use the simplified spectral information to solve the RTE with scattering excluded. This should be done in a way that the process can be used for both media in local thermodynamic equilibrium, as well as for ionized media and media in nonequilibrium. This is the expected scope of the thesis work.

All of the methods selected to solve the above stated challenges thus must be suitable both for general basic flow configurations, as well as for extreme flow cases, such as nonequilibrium hypersonic flows and combustion flows with species and temperature gradients.

1.2. Thesis Goal

With the above in mind, the thesis objective can be formulated. *The goal of this thesis is to implement and validate radiation modelling to into INCA capable of resolving hypersonic flows and combustion by programming a RTE solver coupled with radiation codes and spectral processing algorithms.* The thesis work is thus attempting to answer the following research question: *How can one implement radiation modelling to INCA* *to model hypersonic and combustion flows, such that optimum balance between the accuracy of the solution and the respective computational cost is achieved?*

Obviously, these efforts will lead to a development of a radiation modelling code which will be adapted to INCA and which is the focus of this thesis work. In addition to code development, for the search of the optimum balance between accuracy and computational demands, acceleration techniques should be also developed controlling the solver speed and expected error. With the thesis goal defined in the previous paragraph, the following primary requirements can be formulated on the solver to be developed:

- The developed solver shall be capable of handling nonequilibrium hypersonic radiation
- The methods of the developed solver shall be capable of sufficient sensitivity to resolve turbulence-radiation interaction in combustion systems
- The developed solver shall be capable of working with a wide variety of problems with minimum additional effort
- The solver shall be directly implementable into INCA CFD
- Solution acceleration techniques shall be developed to reduce the computational demands of the solver if needed

This thesis report aims to summarise the process of the development of this code and its testing.

1.3. Scope of This Text

This thesis provides a summarised introduction to the topics of radiation in hypersonic and combustion flows in Chapter 2. Historical perspectives are presented, along with further complications of such modelling, such as the determination of the internal states in nonequilibrium and the topic of radiation-turbulence interaction in turbulent systems. With the thesis goal in mind, afterwards, the modelling methods selected for the thesis work are justified and further presented in Chapter 3. Chapter 4 discusses how these methods are implemented in the radiation solver and presents both the challenges encountered, as well as some basic attempts to lower the computational demands by making the code more efficient. The validation and verification of the code is presented in Chapter 5. Chapter 6 then shows further acceleration attempts by using low-discrepancy sequences and smart spectral discretisation and approximation techniques. The outcomes of the thesis and recommendations for future work are discussed in Chapter 7 and concluded in Chapter 8.

2

Theoretical Background

Before diving into the analysis of available methods to solve for radiation, the basic theory behind radiative heat transfer and the generation of radiation should be introduced, as this will be necessary when assessing the applicability and error of existing methods. Apart from general introduction to the radiation physics and definitions, this Chapter will also provide a short overview of the history and modern state of radiation research in hypersonics and combustion flows, which are the focus of this thesis work.

2.1. Introduction to Radiation Definitions

Before submerging into the actual physics of radiative transitions, some basic definitions must be introduced. Here, Ref. [68] is followed. Every medium of a temperature higher than 0K emits electromagnetic (EM) radiation in all directions, and its intensity and nature depends on the temperature and material properties of said medium. Total emissive power can then be defined as the emitted energy per time and per area. The emissive power can be obtained from the so-called spectral emissive power, which is the emissive power at a given wavelength or wavenumber in the spectrum:

$$E(T) = \int_0^{\infty} E_v(T, v)dv, \tag{2.1}$$

in which T is the temperature and v is the frequency. Before continuing, a distinction should be made between the variables used to describe the frequency of a photon, i. e. its position in a spectrum. Depending on the field of application, the following variables are used to describe frequency:

- wavelength, λ in nm or Å (Ångstroms)
- wavenumber η in cm^{-1}, defined as $1/\lambda$
- angular wavenumber, k, in cm^{-1}, defined as $2\pi/\lambda$
- frequency v, in Hz, defined as $c/\lambda/n$

where n is the refractive index of the medium (1 for vacuum). The use of these variables is oftentimes historical and depends purely on practicality when it comes to magnitude of the resulting values. For example, when dealing with radiofrequency radiation, it is most common to use the conventional units of (M)Hz. For combustion applications, the radiation is mostly in the infrared or far infrared, meaning that expression in wavenumbers in cm^{-1} is suitable. In hypersonics, the majority of the radiation occurs in ultraviolet at very short wavelengths, and thus expressions using Ångstroms (10^{-10}m) are more appropriate. The spectral emissive power for a blackbody is described by Planck's law, which will be later also derived:

$$E_{bv}(T, v) = \frac{2\pi h v^3 n^2}{c^2 \left[e^{hv/kT} - 1\right]}, \tag{2.2}$$

and, if integrated, the blackbody emissive power is:

$$E_b(T) = \int_0^\infty E_{b\lambda}(T,\lambda)d\lambda = C_1 n^2 T^4 \int_0^\infty \frac{d(n\lambda T)}{(n\lambda T)^5\left[e^{C_2/(n\lambda T)}-1\right]} \rightarrow E_b(T) = n^2\sigma T^4, \tag{2.3}$$

in which σ is the Stefan-Boltzmann constant:

$$\sigma = \frac{\pi^4 C_1}{15 C_2^4} = 5.670\times 10^{-8}\frac{W}{m^2K^4}. \tag{2.4}$$

Note that this radiative source function expression only holds for black bodies and bodies in LTE. For nonequilibrium cases, the Planck function is rather defined as a ratio of emissivity to absorption coefficient (will be defined below) and does not have a trivial expression, as will be shown later.

Emissive power refers to the energy emitted everywhere. However, radiation from surfaces is typically not isotropic, and so a more useful definition of emitted energy is when it is considered in the direction normal to the photon rays instead of the surface area. This is a so-called radiative intensity, and similarly to the emissive power, it can be defined as total as well as spectral. Angularly integrated spectral radiative intensity then leads to the spectral emissive power:

$$E(\mathbf{r}) = \int_0^{2\pi}\int_0^{\pi/2} I(\mathbf{r},\theta,\psi)\cos\theta\sin\theta d\theta d\psi = \int_{2\pi} I(\mathbf{r},\hat{\mathbf{s}})\hat{\mathbf{n}}\cdot\hat{\mathbf{s}}d\Omega, \tag{2.5}$$

where Ω is the solid angle. For a black body, the outgoing intensity is completely independent of direction, and thus the relationship between spectral emissivity and intensity is straightforward:

$$E_{b\lambda}(\mathbf{r},\lambda) = \pi I_{b\lambda}(\mathbf{r},\lambda). \tag{2.6}$$

For an arbitrary surface with a certain normal $\hat{\mathbf{n}}$, the radiation coming along a path vector $\hat{\mathbf{s}}_i$ at angle θ_i (see Figure 2.1), the incoming heat flux is defined as negative.

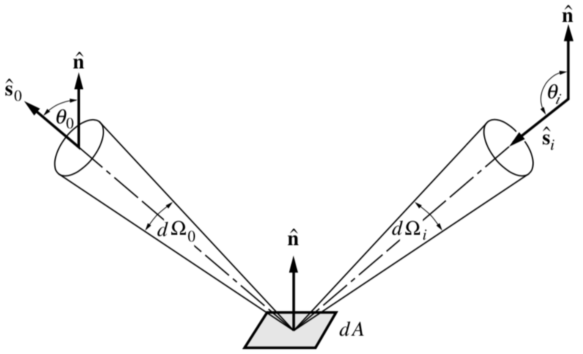

Figure 2.1: Variable definitions for the derivation of the 1D approximation of radiative heat transfer in Equation (2.9). From Ref. [68].

Integration over all possible directions for this arbitrary area leads to the total incoming heat flux of:

$$\left(q_\lambda\right)_{\text{in}} = \int_{\cos\theta_i<0} I_\lambda\left(\hat{\mathbf{s}}_i\right)\cos\theta_i d\Omega_i, \tag{2.7}$$

and similarly, since the situation is the opposite for the outgoing rays ($\cos\theta_o > 0$, see Figure 2.1), the integral of the outgoing radiation is:

$$\left(q_\lambda\right)_{\text{out}} = \int_{\cos\theta_o>0} I_\lambda\left(\hat{\mathbf{s}}_o\right)\cos\theta_o d\Omega_o, \tag{2.8}$$

resulting in the net heat flux, which is then integrated over the entire spectrum to give the so-called total radiative heat flux:

$$\left(q_\lambda\right)_{\text{net}} = \mathbf{q}_\lambda\cdot\hat{\mathbf{n}} = \int_{4\pi} I_\lambda(\hat{\mathbf{s}})\hat{\mathbf{n}}\cdot\hat{\mathbf{s}}d\Omega \quad\rightarrow\quad \mathbf{q}\cdot\hat{\mathbf{n}} = \int_0^\infty \mathbf{q}_\lambda\cdot\hat{\mathbf{n}}d\lambda = \int_0^\infty\int_{4\pi} I_\lambda(\hat{\mathbf{s}})\hat{\mathbf{n}}\cdot\hat{\mathbf{s}}d\Omega d\lambda. \tag{2.9}$$

The divergence of the above will be required when coupling radiation to computational fluid dynamics (CFD), since that is the radiative source term in the energy equation.

In addition to the spectral radiative intensity and the emissive power, a definition oftentimes also used in radiometry is the so-called radiosity, which can again be both total and spectral. Radiosity J is defined as a heat flux per unit area (and at a given wavelength for spectral radiosity):

$$J = \frac{\partial q_e}{\partial A}, \qquad J_\lambda = \frac{\partial J}{\partial \lambda}, \tag{2.10}$$

and it is used in various radiation transfer solution methods (such as the zonal method discussed later).

Finally, some definitions of characteristics of opaque surfaces should be given before proceeding into the actual physics of radiative transitions. The three fundamental properties of opaque surfaces are:

– Absorptance, α: ratio of absorbed amount of rays to the total amount of rays incident

– Reflectance, r: ratio of reflected amount of rays to the total amount of rays incident

– Transmittance, τ: ratio of transmitted amount of rays to the total amount of rays incident

where the sum of these three for any medium, from conservation of energy, is 1, $\rho + \alpha + \tau = 1$. In the present work, the majority of radiation is treated in semi-transparent gasses, where reflectance can be neglected (scattering is not considered) outside of the walls. The values of absorptance and transmittance then depend on the particular wavelength, and absorption along a certain path s at a given wavenumber can be shown to result in an exponential decay of transmissivity (spectral transmittance):

$$\tau_\eta = e^{-\kappa_\eta s} = 1 - \alpha_\eta, \tag{2.11}$$

in which κ is the so-called absorption coefficient and α_η is the absorptivity (spectral absorptance). If scattering was to be included, the exponential component would not only consist of κ, but also of the scattering coefficient μ_s, resulting in a so-called extinction (or also attenuation) coefficient β:

$$\beta_\eta = \kappa_\eta + \sigma_{s\eta}. \tag{2.12}$$

Finally, with all these definitions, the evolution of radiative intensity across a medium can be described in an integro-differential form. The change of spectral radiative intensity along a certain path (if considering LTE and thus emissivity represented using Planck function), including the effects of scattering, depends on the following components:

– Emission: $\kappa_\eta I_{b\eta}$

– Absorption: $-\kappa_\eta I_\eta$

– Scattering: $-\sigma_{s\eta} I_\eta$

– Net change of radiation scattered from other directions: $\frac{\sigma_{s\eta}}{4\pi} \int_{4\pi} I_\eta(\hat{\mathbf{s}}_i)\, \Phi_\eta(\hat{\mathbf{s}}_i, \hat{\mathbf{s}})\, d\Omega_i$

where Φ_η is the spectral scattering phase function, describing the probability of a ray being scattered from $\hat{\mathbf{s}}_\mathbf{i}$ to $\hat{\mathbf{s}}$. The so-called radiative transfer equation, RTE, is then given as:

$$\frac{dI_\eta}{ds} = \kappa_\eta I_{b\eta} - \kappa_\eta I_\eta - \sigma_{s\eta} I_\eta + \frac{\sigma_{s\eta}}{4\pi} \int_{4\pi} I_\eta(\hat{\mathbf{s}}_i)\, \Phi_\eta(\hat{\mathbf{s}}_i, \hat{\mathbf{s}})\, d\Omega_i. \tag{2.13}$$

If scattering is neglected and LTE is still assumed, the form of RTE is simplified to:

$$\frac{dI_\eta}{ds} = \kappa_\eta I_{b\eta} - \kappa_\eta I_\eta, \tag{2.14}$$

and this equation must be solved so that I_η can be integrated to obtain the total radiative heat flux (see Equation (2.9)). From the definitions above, it can be seen that the problem of radiation is very complex. The total radiative heat flux in a certain cell, even in case scattering is neglected, depends on how much radiation is emitted by other cells and thus how much radiation comes from all other directions; as well as how much of that radiation the cell in question absorbs. Thus, radiation problems are both local and global in nature. This is further complicated by highly variable spectra, which can make the problem more global on some frequencies and more local on others.

The most computationally challenging part when solving for the radiative heat flux in high temperature participating media is the actual determination of this spectral dependence - the computation of the absorption coefficient κ_η. The next section will thus elaborate on where this value comes from and how it can be derived from particle and quantum physics.

2.2. Introduction to Radiation Physics

From the previous section, it became clear that one of the most essential components to solving radiation problems is the so-called absorption coefficient, which, for LTE problems, also determines the spectral emission if weighted by the Planck function. To understand where this parameter comes from, however, the origin of radiation - the so-called radiative transitions in atoms and molecules - must be introduced.

2.2.1. Basic Theory of Matter-Radiation Interaction

The transitions in molecular states are a result of radiation, or vice versa. A photon may interact with a molecule or an atom in different ways - it might be either absorbed, scattered or emitted. Based on the initial and final states of the interacting molecule/ atom, the transitions are referred to as:

- Bound-bound transitions
- Bound-free transitions
- Free-bound transitions
- Free-free transitions

where "bound" refers to the bound states (electron remains bound to the atom), whereas "free" refers to free electrons.

As can be derived from quantum physics, for a photon to be either absorbed or emitted in bound - bound (b-b) transitions, the photons must have a specific energy to match the internal atomic or molecular energy level difference. Due to Heisenberg uncertainty principle and other effects discussed later (Doppler, Stark and collisional broadening), the resulting spectral line is not a simple delta function, but it is slightly spread out around the actual frequency of emission/ absorption. Bound-bound transitions are also transitions between various vibrational-rotational states (oftentimes also referred to as rovibrational, if both states are altered) in case of molecules. Since many combinations of these states exist close to each other, rovibrational transitions oftentimes create entire spectral bands, instead of a single spectral line. Entire band structures can be formed if these rovibrational transitions are coupled with electronic transitions.

Bound-free, b-f, transitions are present in case of high-temperature gasses where the energy of the molecule or atom is high enough such that the absorption of a photon causes a release in one of its electrons. Similarly, in the inverse fashion, free-bound transition can occur in the process of radiative recombination.

Other means of interaction with radiation is by the capture or release of photons by electrons in an electric field when interacting with ions, an effect also called braking radiation (Bremsstrahlung), which is an example of a free-free, f-f transition. Since the free electrons might have a continuous spectrum of energies unlike internal atomic or molecular states, both b-f and f-f radiation cause continua in the spectrum, simplifying their modelling.

In most applications with little dissociation and ionisation, b-b transitions are the most significant ones for radiative modelling, and in some conditions, b-f and f-f modelling can be ignored (see for example models of Pierrot et al. in Ref. [83] and Lemal in Ref. [58]). Thus, in most applications of interest, the most significant energy transitions that define matter-radiation interaction are those between the internal vibrational, rotational and electronic levels. These transitions can be due to collisional processes (defined by reaction rate coefficients, b) and radiation processes. This is shown in Figure 2.2.

The derivations following are in more detail elaborated on in Ref. [37]. Let there be n_u of atoms or molecules at a higher energy level u and n_l of atoms or molecules at a lower energy level l. The upper and lower (u, l) states of polyatomic molecules are connected via 5 different means denoted by Einstein (radiative) coefficients, A and B (shown as C in Figure 2.2), and b coefficients, called collisional transition coefficients. These coefficients indicate the rate of upper-to-lower transition. For spontaneous emission:

$$\left(\frac{dn_u}{dt}\right)_{u\to l} = -A_{ul} n_u. \tag{2.15}$$

Emission can be spontaneous, but is, according to conclusions of quantum mechanics, also more enhanced in the direction of the incoming radiation, resulting in a so-called stimulated (induced) emission:

$$\left(\frac{dn_u}{dt}\right)_{u\to l} = -n_u \left(A_{ul} + B_{ul} \int_{4\pi} I_\nu d\Omega\right), \tag{2.16}$$

from which the dependency on the incoming radiative intensity I_ν, causing the stimulated emission, is seen. The same dependency also holds for absorption:

$$\left(\frac{dn_l}{dt}\right)_{l\to u} = n_l B_{lu} \int_{4\pi} I_\nu d\Omega. \tag{2.17}$$

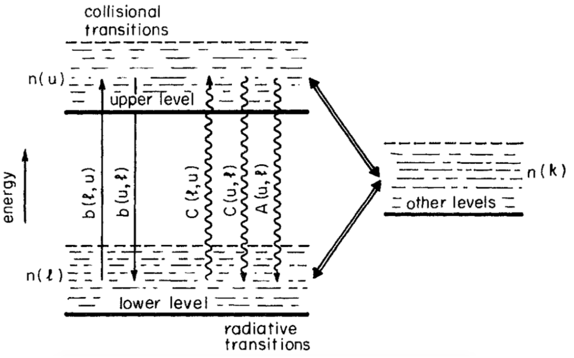

Figure 2.2: Illustration of the possible collisional-radiative transition interactions, where b stands for collisional rates. Note that in this drawing, the second and third Einstein coefficients are denoted with C, not B as in the text. From Ref. [37].

In case of thermodynamic equilibrium, a detailed balance might be written between the incoming and outgoing states. In addition, assuming that the equilibrium radiation occurs in a black isothermal enclosure, the radiative intensity everywhere is equal to the blackbody intensity. This means that the Einstein coefficients can be shown to be related to each other by assuming the net change in the levels to be zero:

$$g_u\left(\frac{dn_u}{dt}\right)_{u\to l} + g_l\left(\frac{dn_l}{dt}\right)_{l\to u} = -g_u n_u \left(A_{ul} + B_{ul}\int_{4\pi} I_{b\nu} d\Omega\right) + g_l n_l B_{lu} \int_{4\pi} I_{b\nu} d\Omega = 0, \tag{2.18}$$

where g_u and g_l refers to the degeneracy (multiplicity) of the upper and lower states, respectively. In addition, it was observed that in thermodynamic equilibrium, Boltzmann statistics holds for the distribution of the internal states (see Ref. [37] for proof):

$$\frac{\bar{n}(u)}{\bar{n}(l)} = \frac{g_u}{g_l}\exp\left(\frac{-h\nu_0}{kT}\right) \tag{2.19}$$

where, since the case of nonequilibrium will be discussed later, the equilibrium number densities are denoted with an overbar. Using Equation (2.18), the blackbody radiation intensity, which was already seen in Equation (2.2), can be actually obtained:

$$I_{b\nu} = \frac{1}{4\pi}\frac{A_{ul}/B_{ul}}{\left(g_l B_{lu}/g_u B_{ul}\right) e^{h\nu/kT} - 1}. \tag{2.20}$$

Substituting this relation into the three population rate Equations (2.15) to (2.17) and using the description for $I_{b\nu}$ above leads to so-called Einstein relations:

$$A_{ul} = \frac{8\pi h\nu^3}{c^2} B_{ul} \qquad\qquad g_u B_{ul} = g_l B_{lu}. \tag{2.21}$$

The Einstein coefficients are universal functions for all the transitions and thus can be also used in situations of thermodynamic nonequilibrium. They are provided in both NEQAIR and HITRAN - libraries which will be extensively used throughout this thesis.

To obtain the absorption coefficient at a given wavelength from these expressions, the theoretical propagation of this light in the form of a photon bundle travelling through an absorbing medium must be considered. Evaluating the number of induced transitions causing the number $\frac{d}{d\Omega}\left(g\frac{dn}{dt}\right)_{l\leftrightarrow u}$ of removed photons from a the initial bundle of rays in time yields:

$$\frac{d}{d\Omega}\left(g\frac{dn}{dt}\right)_{l\leftrightarrow u} = \left(g_l n_l B_{lu} - g_u n_u B_{ul}\right) I_\nu. \tag{2.22}$$

As each photon carries energy of $h\nu$, the radiative energy change is per unit solid angle per distance:

$$-h\nu\frac{d}{d\Omega}\left(g\frac{dn}{dt}\right)_{l\leftrightarrow u} = -\left(g_l n_l B_{lu} - g_u n_u B_{ul}\right) h\nu I_\nu. \tag{2.23}$$

Finally, the slight variation in frequencies must be also accounted for since, as will be discussed, broadening of the spectral lines is present for a multitude of reasons. Then, the intensity over some path s and over this frequency spread $\Delta\nu$ is:

$$\frac{d}{ds}\int_{\Delta\nu} I_\nu d\nu = -\left(g_l n_l B_{lu} - g_u n_u B_{ul}\right) h\nu I_\nu = -\int_{\Delta\nu}\left(g_l n_l B'_{lu} - g_u n_u B'_{ul}\right) h\nu I_\nu d\nu, \tag{2.24}$$

where, using a specified normalised spectral line shape function $\phi(\nu)$ (such that $\int_{\Delta\nu}\phi_\nu(\nu)d\nu = 1$) gives:

$$A'_{ul} = A_{ul}\phi_\nu, \quad B'_{ul} = B_{ul}\phi_\nu, \quad B'_{lu} = B_{lu}\phi_\nu. \tag{2.25}$$

The specific spectral line shapes will be discussed later. The change in the radiation intensity over a path s is then:

$$\frac{d}{ds}\int_{\Delta\nu} I_\nu d\nu = -\left(g_l n_l B_{lu} - g_u n_u B_{ul}\right)\int_{\Delta\nu} h\nu\phi_\nu I_\nu d\nu, \tag{2.26}$$

where the negative of the right hand side is referred to as the theoretical line intensity S_ν:

$$S_\nu = \left(g_l n_l B_{lu} - g_u n_u B_{ul}\right)\int_{\Delta\nu} h\nu\phi_\nu d\nu = \left(g_l n_l B_{lu} - g_u n_u B_{ul}\right) h\nu. \tag{2.27}$$

This leads to the definitions of the previously introduced absorption and emission coefficients. From the theoretical definition of the absorption coefficient, $S_\nu = \int_{\Delta\nu}\kappa_\nu d\nu$ and $\kappa_\nu = S_\nu\phi_\nu$ this gives:

$$\int_{\Delta\nu}\kappa_\nu d\nu = \left(g_l n_l B_{lu} - g_u n_u B_{ul}\right) h\nu, \tag{2.28}$$

which can be seen to incorporate both absorption and stimulated emission Einstein coefficients. Sometimes, to separate the effects of absorption and emission, the true absorption coefficient is defined as:

$$\int_{\Delta\nu}\kappa_{\nu,\mathrm{true}} d\nu = g_l n_l B_{lu} h\nu. \tag{2.29}$$

From the comparison with equilibrium distributions denoted with an overbar, the absorption coefficient can be also calculated with:

$$k_{\mathrm{v},\nu} = \frac{n(l)B_{lu}\phi_\nu}{c}\left[1-\frac{n(u)}{\bar{n}(u)}\frac{\bar{n}(l)}{n(l)}\exp\left(\frac{-h\nu}{kT}\right)\right], \tag{2.30}$$

which, in equilibrium (when the populations n_u and n_l equal $\bar{n}_u$ and $\bar{n}_l$) reduces to:

$$\hat{k}_{\mathrm{v},\nu} = \frac{\bar{n}(l)B(l,u)\phi_\nu}{c}\left[1-\exp\left(\frac{-h\nu}{kT}\right)\right]. \tag{2.31}$$

The emission coefficient can be also obtained by repeating the entire process while starting with the negatives of the transition rates. Multiplying by the energy $-h\nu$ and dividing by 4π considering isotropic emission, one arrives to the energy emitted per time, per unit area and per solid angle:

$$\frac{d}{ds}\int_{\Delta\nu} I_\nu d\nu = -h\nu\frac{d}{d\Omega}\left(\frac{dn}{dt}\right)_{u\to l} = g_u n_u A_{ul} h\nu/4\pi. \tag{2.32}$$

Evaluated across the frequencies $\Delta\nu$, the emission coefficient can be defined:

$$\frac{dI_\nu}{ds} = g_u n_u A'_{ul} h\nu/4\pi = \varepsilon_\nu, \tag{2.33}$$

and through the manipulation of the above expressions, this can be linked to the absorption coefficient by:

$$\varepsilon_\nu = \kappa_\nu\frac{2h\nu^3}{c^2}\frac{n_u}{n_l - n_u}. \tag{2.34}$$

Finally, considering the upper and lower state populations in case of equilibrium (following the Boltzmann distributions), it can be seen that Equation (2.34) reduces to:

$$\frac{dI_v}{ds} = \varepsilon_v = \kappa_v I_{bv}, \tag{2.35}$$

which justifies the conclusions made in the previous section. It also shows the definition of the "nonequilibrium Planck function" as being given by the ratio of the upper and lower states, $\frac{2hv^3}{c^2}\frac{n_u}{n_l - n_u}$.

Having defined the basic terms in radiative transitions, the focus can shift back to the molecular (and atomic) energies from which these transitions are further determined.

2.2.2. Basic Line Shapes and Broadening Mechanisms

The transitions defined above create spectral lines and, if a vast amount of narrow lines are present very close to each other in case of rovibrational transitions, spectral bands. The reason for these bands is the fact that the number of all of the rovibrational states are typically very high and close to each other in energies. Spectral bands are far more difficult to compute due to their complexity, and thus the discussion starts with a basic spectral line analysis.

The analysis here follows the texts of Goody [37] and Park [81]. Even the simplest of spectral lines caused by electronic state transitions (b-b or b-f) have a certain shape and are not just a simple delta function, which would have been the case for an emitted photon due to a transition with a change in energy of $\Delta E = hc/\lambda$. This is mainly due to four different so-called line broadening mechanisms causes:

- Natural broadening: due to the uncertainty in the energy levels as a result of the Heisenberg principle
- Collision broadening: due to possible perturbations of the energy levels by collisions
- Stark Broadening: due to the presence of external electric and magnetic fields
- Doppler broadening: due to thermal motion of the emitting species and the related Doppler effect

As for natural broadening (also called self-resonance), a very rough estimate on the spread in frequency of the emission line Δv as a function of the duration of emission Δt is given by:

$$\Delta t \Delta v \approx 1/2\pi, \tag{2.36}$$

as can be derived from Heisenberg uncertainty principle. The spread in frequencies due to collision broadening, Doppler broadening and Stark broadening typically far exceeds the natural broadening, and so natural broadening will not be considered further.

Two parameters are used to describe the shape of a spectral line - the area under the absorption coefficient $k - v$ curve, S (which can be also defined as line intensity as already seen in the previous subsection), and the line half-width, b, $\eta - \eta_0$ from the line center η_0 to η where the absorption coefficient has dropped to one half of its maximum value. The same notation for half-width is used in HITRAN and NEQAIR. A good approximation for a simple collision-broadened spectral line is given by the Lorentz dispersion formula:

$$\kappa_\eta = \frac{S}{\pi}\frac{\gamma_{\mathrm{col}}}{\left(\eta - \eta_0\right)^2 + \gamma_{\mathrm{col}}^2} = S\phi_{\mathrm{L}\eta}\left(\gamma_{\mathrm{col}}, \eta - \eta_0\right), \tag{2.37}$$

where the γ_{col} collision half-width can be approximated from the molecular kinetics for a molecule of mass m and diameter D, as follows (for derivation, see Ref. [37]):

$$\gamma_{\mathrm{col}} = \frac{2}{\sqrt{\pi}}\frac{D^2 p}{c\sqrt{mkT}} = \gamma_{\mathrm{col}}\left(\frac{p}{p_0}\right)\left(\frac{T_0}{T}\right)^n, \tag{2.38}$$

for a reference temperature, pressure and collision half-width. The exponent n is typically found from experiments or assumed to be 1/2. For a mixture, then:

$$\gamma_{\mathrm{col}} = \sum_i \gamma_{\mathrm{col},i}\left(\frac{p_i}{p_0}\right)\left(\frac{T_0}{T}\right)^{n_i}, \tag{2.39}$$

where σ_i is the effective collision diameter with species i. This is a greatly simplified approach which is not always accurate, but more accurate models are oftentimes very difficult to implement in practice. It is evident that collision broadening becomes significant at very high pressures and low temperatures. The combination of natural and collision broadening is sometimes referred to as Lorentz broadening. Lorentz broadening will be used when computing spectra from HITRAN.

Stark broadening occurs mainly in case of an electric field present during transition, such as the internal electric field in plasmas, which changes the energies of transition. The resulting width depends on the electron density n_e and electron temperature T_e. The half-width then is:

$$\gamma_s = \gamma_{s0}\left(\frac{T_e}{T_0}\right)^n\left(\frac{n_e}{n_0}\right), \tag{2.40}$$

and in case of very strong magnetic fields, Stark broadening can also cause a shift of the line. The effect of the γ_s can be incorporated in the same way as for the collision broadening discussed above.

For a Doppler-broadened line with negligible collision broadening:

$$\kappa_\eta = S\phi_{D\eta}\left(\gamma_D, \eta-\eta_0\right) = S\frac{\sqrt{\ln 2}}{\gamma_D\sqrt{\pi}}\exp\left[-(\ln 2)\left(\frac{\eta-\eta_0}{\gamma_D}\right)^2\right], \tag{2.41}$$

where the Doppler line half-width γ_D follows from the velocity distribution predicted from statistical mechanics:

$$\gamma_D = \frac{\eta_0}{c}\sqrt{\frac{2kT}{m}\ln 2}, \tag{2.42}$$

with k_b being the Boltzmann constant. It can be seen that Doppler broadening becomes dominant with increasing temperatures, unlike collision broadening. In addition, unlike Lorentz and Stark broadening, the extent of Doppler broadening depends on its spectral position.

The comparison of the broadening mechanisms discussed for H_2O and CO_2 at various temperatures and pressures is shown in Figure 2.3, from which it is obvious that Lorentz broadening is the most dominant mechanism unless the radiating gas is at very high temperatures and low pressures. In low-pressure plasma with large internal electric fields, Stark broadening should be also considered.

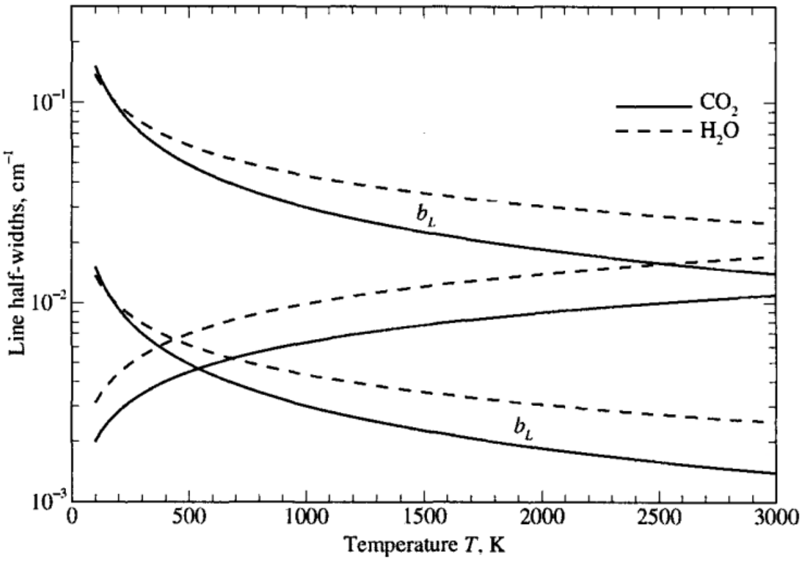

Figure 2.3: Illustration of the conditions where the Lorentz and the Doppler Broadening typically dominate. From Ref. [68].

The most common approach to model a combination of Doppler and collision broadening is to assume a collision-broadened profile displaced by the Doppler shift and averaged over its probability:

$$p(v) = \left(\frac{m}{2\pi kT}\right)^{1/2}\exp\left(-\frac{mv^2}{2kT}\right). \tag{2.43}$$

This leads to the so-called Voigt line profile (here the Lorentzian half-width is γ_L):

$$\kappa_\eta = \frac{S\gamma_L}{\pi^{3/2}} \int_{-\infty}^{+\infty} \frac{e^{-x^2}dx}{\left(\eta - \eta_0 - \frac{x\gamma_D}{\sqrt{\ln 2}}\right)^2 + \gamma_L^2} \quad \text{with} \quad x = v\sqrt{\frac{m}{2kT}}, \tag{2.44}$$

which is also used in NEQAIR calculations. So far, no closure formula has been obtained for the Voigt profile. However, FORTRAN subroutines exist to compute it iteratively.

2.2.3. Atomic Lines, Rotational Lines, Rovibrational Bands and Vibronic Band Structures

Finally, with basic knowledge about the theoretical line shape, the line intensity will be discussed next. This differs depending on the nature of the transition, and for the different cases, the theory is discussed further. Before that, however, the energy states of atoms and molecules should be first defined. This is typically done by expressing their Hamiltonian, composed of stationary and time-dependent terms:

$$H = H_1(q) + H_2(q,t), \tag{2.45}$$

where the first term is stationary and the second time-dependent. The stationary term is analysed to evaluate the existing energy states in the molecule, such as the energy levels at given vibrational and rotational quantum numbers. The time-dependent part is responsible for the transitions between these states. For atoms, this expression is the same, just without the vibrational and rotational contributions.

The stationary term consists of electronic energy, vibrational energy, rotational energy, translational energy and nuclear spin energy. Nuclear spin energy can be typically completely neglected due to its very low magnitudes, especially when compared to the others for reentry applications.

The translational energy does not have stationary states unlike the electronic and vibrational energies, but needs to be considered when establishing the equilibrium populations of energy levels. The typical wavenumbers of translational energies are around 400 cm^{-1}, which is much less than electronic energies, slightly less than vibrational energies and much more than rotational energies. This means that kinetic events such as collisions can affect rotational bands and, to an extent, vibrational bands, but have a typically negligible influence on electronic bands.

Since electronic energy is fairly straightforward to calculate, it will not be discussed further. The biggest simplifications which have to be made when computing molecular states and transitions are due the approximations in the vibrational and rotational energies, which will be discussed below further. The theory below will be presented for diatomic molecules only for simplicity, and follows the derivations in the books of Bernath (see Ref. [13]) and Goody (see Ref. [37]).

The potential curve within a molecule is usually described by the so-called Morse potential function, $U(r) = D_0\left[1 - \exp\left(-\alpha\left(r - r_0\right)\right)\right]^2$, where r_0, D_0 and α are Morse potential parameters. The vibrational levels are then described either considering harmonic oscillator model close to the nucleus where Morse potential holds well, or anharmonic model further away. In either case, the respective energy is described as a function of the so-called vibrational number v. For example, for the simpler, harmonic approximation:

$$E_\text{v} = \hbar\omega\left(\text{v} + \frac{1}{2}\right) \quad \text{with} \quad \omega = \alpha r_0\sqrt{\frac{2D_0}{I}}, \tag{2.46}$$

where I is the moment of inertia for a diatomic molecule.

When it comes to the rotational energy, the so-called rotational number is introduced for the same purpose as v. Considering the simplest assumption of a rigid rotator with intermolecular distance of r_0, this is:

$$E_\text{r} = \frac{\hbar^2}{2I}J(J+1) = BJ(J+1), \tag{2.47}$$

where J is the total angular momentum quantum number and B is referred to as a rotational constant.

The time-dependent Hamiltonian then represents any external interaction or transition between these states. For a molecule with a dipole moment, dipole transition can occur in case certain selection criteria are met (for more detailed discussion, refer to texts on quantum mechanics such as Ref. [13]). Then, with the probability of a dipole transition given by μ_{ij}, where subscripts i and j represent two quantum states, the line intensity can be shown to be:

$$S_n(i,j) = \frac{n_j}{n}\frac{8\pi^3 \nu_{ij}\left|\mu_{ij}\right|^2}{3hc}\left[1 - \exp\left(\frac{-h\nu_{ij}}{kT}\right)\right]. \tag{2.48}$$

The transition dipole moment (also just transition moment), usually denoted by the difference between an initial state and a final state i and j, is the electric dipole moment associated with the transition between the two states $i \rightarrow j$. Typically, it is a complex vector quantity that includes the phase factors connected with the two states i and j. The polarisation of the transition is given by its directions, which determines how the system will interact with an EM wave of a given polarisation, whereas the square of its magnitude gives the strength of the interaction thanks to the system's charge distribution. Equation (2.48) is also made use of in NEQAIR when computing line intensities, where, to express the dipole moment, the Franck-Condon factors and Hoenl-London factors are made use of.

Not all transitions are allowed as mentioned earlier, depending on the conservation of angular momentum and the so-called spin coupling. However, further discussion on this topic is beyond the scope of this text, and can be found in Ref. [13]. Having defined the line intensity in terms of dipole moments, the intensities of various transition mechanisms can be discussed.

Atomic Lines

In case of atomic lines, the only internal transitions occurring are electronic transitions. For a given transition from one quantum state with J' to another quantum state of J'', a relationship between the Einstein coefficient and line intensity at frequency υ can be expressed as:

$$A|_{\text{electronic}} = \frac{16\pi^3 \upsilon^3 S_{J'J''}}{3\varepsilon_0 hc^3 (2J'+1)}, \tag{2.49}$$

where $S_{J'J''}$ is the line intensity (strength). Since electronic transitions are fairly simple as only so many electronic states are present in a molecule or an atom, the line intensities are typically databased for each species along with the respective Einstein coefficients in libraries such as HITRAN or NEQAIR, as will be shown in Chapter 3.

Rotational Lines

In case of purely rotational transitions of molecules, the Einstein coefficient expression has the same form as in case of atomic transitions:

$$A|_{\text{rotational}} = \frac{16\pi^3 \upsilon^3 S_{J'J''}}{3\varepsilon_0 hc^3 (2J'+1)}. \tag{2.50}$$

The line intensity has in this case a slightly more complex expression as the nature of the rotational states may vary for molecules of different structures and number of atoms. In general, for a purely rotational transition:

$$S_{J'J''} = \mu_0^2 \text{HLF}, \tag{2.51}$$

where HLF stands for the so-called Hoenl-London factor. For linear and diatomic molecules, it can be shown that since this transition case is so simple, the Einstein coefficient can be directly expressed as:

$$A_{J+1\rightarrow J} = \frac{16\pi^3 \upsilon^3 \mu_0^2 (J+1)}{3\varepsilon_0 hc^3 (2J+3)}, \tag{2.52}$$

where the HLF was expressed simply as $J+1$. For symmetric and asymmetric top molecules, the expression for $S_{J'J''}$ is far more complicated, whereas for symmetric top molecules, it can be evaluated analytically, for asymmetric top molecules, it must be computed directly from the Hamiltonian matrix. For some simpler configurations, HLF for rotational lines can be databased, as it is done in NEQAIR.

Rovibrational Bands

In most cases in radiation coming from hypersonic flows, the transitions involve both rotational and vibrational states, resulting in so-called rovibrational transitions; and in most cases, also the electronic states, being thus denoted as rovibronic or vibronic transitions. The former is discussed first.

For a simple harmonic oscillator model introduced in Equation (2.46), the selection rules further discussed in, for example, Ref. [13], dictate that allowed transitions are of ΔJ of 0 and ± 1. There three types of transitions lead to separate branches in rovibrational bands; P: $\Delta J = -1$, Q: $\Delta J = 0$ and R: $\Delta J = 1$

These branches are visualised in a typical spectral band in Figure 2.4. The Q branch oftentimes lacks due to forbidden transitions of $\Delta J = 0$ in linear (anharmonic) molecules. Since these lines are broadened around their default frequencies, an entire spectral band is created across the span of the frequencies.

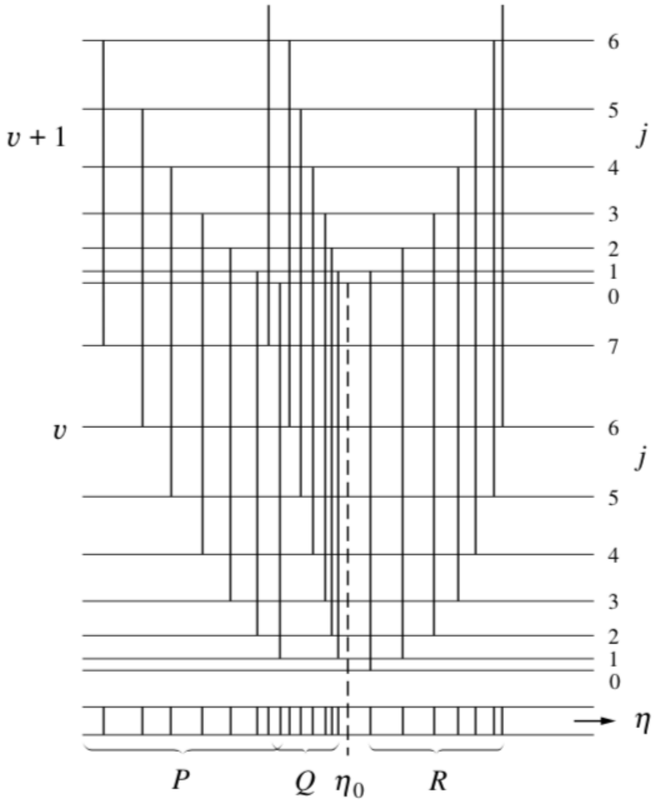

Figure 2.4: P, Q, and R branches in typical rovibrational spectral bands due to the -1, 0 and 1 changes in the rotational quantum number during transition. From Ref. [68].

To compute the shapes of all the lines in a band, the same relations as used for a single line emission (Equation (2.48)) can be applied, with a properly computed band strength $S_{J'J''}$ such that the Einstein first coefficient becomes:

$$A|_{\text{rovibrational}} = \frac{64\pi^4 v^3}{3hc^3 g_u} S_{J'J''}, \tag{2.53}$$

where this time, the degeneracy (multiplicity) g_u is not specifically stated, since energy levels of multiple types are involved. To adjust for these multiple types and differences, for a diatomic molecule, the line strength can be computed as a product of three contributions; the vibrational part, rotational part and a correction factor:

$$S_{J'J''} = \quad |M_{v'v''}|^2 F(m)\text{HFL}, \tag{2.54}$$

where $|M_{v'v''}|^2$ is the vibrational transition dipole moment integral (dipole moment from a quantum state with vibrational number v' to v''), HLF is the Hoenl-London factor and $F(m)$ is a Herman–Wallis effect correction factor, to compensate for the fact that rotational and vibrational modes are computed as decoupled. For a vibrational wavefunction ψ_{vib} (denoted by $'$ and $''$ for the two quantum states), the vibrational transition dipole integral can be computed from the electronic dipole moment μ:

$$M_{v'v''} = \int \psi'^*_{\text{vib}} \mu(r) \psi''_{\text{vib}} dr, \tag{2.55}$$

which could be further approximated with Taylor expansion to μ to arrive at simplified expressions (see Ref. [13]). NEQAIR computes the Hoenl-London factors directly from Hamiltonians. This line strength is evaluated for every rovibrational state transition, forming the rovibrational bands.

Vibronic Band Structures

Finally, the line stregth for vibronic (vibrational - electronic) transitions can be expressed in a similar way:

$$A|_{vibronic} = \frac{64\pi^4 v^3}{3hc^3 g_u} S_{J'J''}, \tag{2.56}$$

where the factor that again needs to be determined is the strength $S_{J'J''}$. For a transition of a molecule having electronic transition dipole moment magnitude $|\mu|^2$, analogously to Equation (2.54):

$$S_{J'J''} = q_{v'-v''} \left|\mu\right|^2 \mathrm{HLF}, \tag{2.57}$$

where in this case, apart from HLF, also the so-called Franck-Condon factor $q_{v'-v''}$ is required. This is due to the fact that electronic excitations in molecules, thanks to the large variation in masses between the nuclei and electrons, are ruled according to the Franck-Condon principle. This states that certain electronic transitions are far more likely to occur if the initial and final vibrational states overlap, and the larger the overlap, the more likely the transition is. This stems from the fact that electronic transitions are extremely fast compared to any nuclear motion. Thus, the transition rate coefficient between these two internal states, and hence also the Einstein coefficient, is directly proportional to the overlap of the wavefunctions of the states. Franck-Condon factors are typically databased since their calculation is very resource intensive, as it is also done in NEQAIR.

More information about how all these calculations are done in NEQAIR is in more detail discussed by Whiting and Nicholls in Ref. [111] (note that in case of Whiting and Nicholls, Hoenl-London factor denotes directly the line strength, not only the rotational contribution).

Note that this line strength is a direct input into the calculation of the absorption coefficient considering the specific desired line shape function, as for example seen in Equation (2.37). Thus, uncertainties in parameters such as HLF or q directly impact the accuracy of spectral calculations.

2.2.4. Radiation as a Larger Picture: The Radiative Transfer Equation

Now, with the knowledge on where the absorption coefficient originates from and how it can be described from parameters of quantum mechanics, it will be explained how the RTE presented (Equation (2.13)) can be solved knowing the absorption coefficients. There are several methods at hand, and the principles, advantages and disadvantages of each will be briefly outlined next. If not indicated otherwise, Ref. [68] is used as a reference.

Line-of-Sight Integration and 1D methods

The simplest and fastest RTE solution techniques are one dimensional. For definitions of optical paths and variables which will be used below, refer to Figure 2.5.

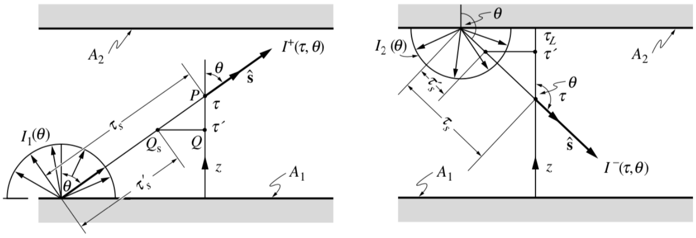

Figure 2.5: Definitions of the positive and negative direction variables for the derivation of the 1D radiative transfer Equations (2.63) and (2.64). From Ref. [68]

The divergence of the heat flux, required for coupling to the CFD solution, can be for this purpose expressed as a difference between the emitted energy and absorbed irradiation, G:

$$\nabla \cdot q_\eta = \kappa_\eta \left(4\pi I_{b\eta} - \int_{4\pi} I_\eta d\Omega\right) = \kappa_\eta \left(4\pi I_{b\eta} - G_\eta\right), \tag{2.58}$$

Along a 1D path, it is useful to apply the definition of optical depth τ based on the attenuation coefficient β. At a given path length s, the optical depth is then the integral $\tau_s = \int_0^s \beta ds$. For example, $\tau'_s = 0$ at one wall in Figure 2.5 and $\tau'_s = \tau_s$ at the other. Making use of the direction θ of the ray, from Figure 2.5, it can be seen that the following substitution can be made:

$$\frac{1}{\beta}\frac{dI}{ds} = \frac{dI}{d\tau_s} = \cos\theta\frac{dI}{d\tau}, \tag{2.59}$$

which will help simplify the resulting equations.

The intensity can then be split to negative − direction and positive + direction contributions, as shown in Figure 2.5. The positive and negative directions intensity contributions are then, if a substitution $\mu = \cos\theta$ is made:

$$I^{+}(\tau,\mu) = I_{b1} e^{-\tau/\mu} + \frac{1}{\mu}\int_0^{\tau} I_b\left(\tau'\right) e^{-(\tau-\tau')/\mu} d\tau' \quad \text{if} \quad 0 < \mu < 1 \tag{2.60}$$

and

$$I^{-}(\tau,\mu) = I_{b2} e^{(\tau_L-\tau)/\mu} - \frac{1}{\mu}\int_{\tau}^{\tau_L} I_b\left(\tau'\right) e^{(\tau'-\tau)/\mu} d\tau' \qquad \text{if} \quad -1 < \mu < 0. \tag{2.61}$$

With further definition of so-called exponential integral functions of order n, defined as:

$$E_n(x) = \int_1^{\infty} e^{-xt}\frac{dt}{t^n} = \int_0^1 \mu^{n-2} e^{-x/\mu} d\mu, \tag{2.62}$$

the total incident radiation can be derived to be:

$$G(\tau) = 2\pi\left[I_{b1}E_2(\tau) + I_{b2}E_2\left(\tau_L-\tau\right) + \int_0^{\tau} I_b\left(\tau'\right)E_1\left(\tau-\tau'\right)d\tau' + \int_{\tau}^{\tau_L} I_b\left(\tau'\right)E_1\left(\tau'-\tau\right)d\tau'\right], \tag{2.63}$$

resulting in the heat flux of:

$$q(\tau) = 2\pi\left[I_{b1}E_3(\tau) - I_{b2}E_3\left(\tau_L-\tau\right) + \int_0^{\tau} I_b\left(\tau'\right)E_2\left(\tau-\tau'\right)d\tau' - \int_{\tau}^{\tau_L} I_b\left(\tau'\right)E_2\left(\tau'-\tau\right)d\tau'\right]. \tag{2.64}$$

In one dimensional media, this technique is exact, and will be used for validation purposes as computed in Ref. [98]. It can be also applied to real 3 dimensional problems as long as the medium can be approximated as one dimensional. This is sometimes done to calculate the line-of-sight (LS) radiation between the shock and the nose of a reentry vehicle. Additional modifications can be derived from this technique (such as tangent-slab, TS, approximation or spherical-cap approximation which are available in NEQAIR). 1D methods have shown errors of more than 20% when compared to Monte Carlo for reentry application (see for example the work of Feldick et al. from 2011 in Ref. [30]) in 3D. While 1D evaluation can provide fair heat flux indications along the stagnation line (where the directions are approximately normal), it is not suitable when accurate solutions of radiative transfer are required in the entire flowfield. The performance of these methods will be discussed in the sections devoted to radiation modelling in hypersonic and combustion flows.

The Zonal Method

The zonal method is a technique in which an enclosure is split into several volume and surface zones with the same temperatures. The radiation exchange between these surfaces and volumes can be then calculated for all pairs of zones using the so-called exchange areas between them, which are pre-calculated from the view factors. This leads to a matrix system, which can be inverted to give the radiative transfer in each zone.

For black bodies of emissive power E_b, the radiative flux from zone $i \to j$ is given by:

$$Q_{i\leftrightarrow j} = -Q_{j\leftrightarrow i} = \overline{s_i s_j}\left(E_{bi} - E_{bj}\right), \tag{2.65}$$

in which, the exchange area $\overline{s_i s_j}$ is determined from the mutual view factors $F_{i\to j}$ or $F_{j\to i}$:

$$\overline{s_i s_j} = \overline{s_j s_i} = A_i F_{i\to j} = A_j F_{j\to i} = \int_{A_i}\int_{A_j} \frac{\cos\theta_i \cos\theta_j}{\pi s_{ij}^2} dA_j dA_i, \tag{2.66}$$

where in this case, θ refers to the orientation of the zones i and j (for example, surface normals). Then, the net heat flux at zone i is given by summation of all these N zone pairs:

$$Q_i = A_i q_i = \sum_{j=1}^{N} \overline{s_i s_j}\left(E_{bi} - E_{bj}\right) = A_i E_{bi} - \sum_{j=1}^{N} \overline{s_i s_j} E_{bj}, \quad i = 1,2,\ldots,N. \tag{2.67}$$

In case of non-black surfaces or cases with participating medium, the emissive power E_b is replaced by the radiosity J, accounting for the emissivity of the gas.

This approach works adequately for ordinary radiation problems with domains where radiation is dominated by hot walls. But while it can be extended to account for a participating medium, it does not allow for a medium that is not grey. It is thus not appropriate for hypersonic or high temperature combustion problems, where the medium has highly variable absorption spectra.

The Method of Discrete Ordinates, DOM

The method of discrete ordinates uses the logic of most flow solvers - transfer the RTE into a set of partial differential equations (PDEs), which can be solved using techniques such as finite differences or finite volumes - a so-called FVM DOM. The RTE in Equation (2.13) can be solved for n different direction vectors $\hat{s}$, and just like in flow solvers, the quadrature rule:

$$\int_{4\pi} f(\hat{s})d\Omega \simeq \sum_{i=1}^{n} w_i f(\hat{s}_i), \tag{2.68}$$

is used for integration with weights w_i associated with the directions $\hat{s}_i$. This technique is one of the modern state-of-art techniques for radiation problems. However, while its accuracy can be very high, as will be shown later in this Chapter, its convergence might be problematic for media with higher optical thickness, and proper convergence to solve the PDEs might be even impossible for very thick problems (such as some cases of hypersonic plasma).

The Method of Spherical Harmonics, SHM

The last method which is non-stochastic is similar to DOM in that it transfers the RTE into a set of PDEs. However, instead of solving the PDEs for different direction vectors, the radiative intensity field $I(r,\hat{s})$ at a given position vector r in the domain is approximated by Fourier series, for example in 2D:

$$I(r,\hat{s}) = \sum_{l=0}^{\infty}\sum_{m=-l}^{l} I_l^m(r)Y_l^m(s), \tag{2.69}$$

where $I_l^m(r)$ are location dependent coefficients and $Y_l^m(s)$ represent the spherical harmonics at polar and azimuthal angles θ and ψ:

$$Y_n^m(\theta,\psi) = \begin{cases} \cos(m\psi)P_n^m(\cos\theta), & \text{for } m \geq 0 \\ \sin(|m|\psi)P_n^m(\cos\theta), & \text{for } m < 0 \end{cases}. \tag{2.70}$$

In the SH expressions above, P_n^m are the Legendre polynomials defined as:

$$P_n^m(\mu) = (-1)^m \frac{\left(1-\mu^2\right)^{|m|/2}}{2^n n!} \frac{d^{n+|m|}}{d\mu^{n+|m|}} \left(\mu^2-1\right)^n. \tag{2.71}$$

Expression (2.69) is then used to represent the intensity field and is substituted back to the RTE. When then further expanding the RTE for l from 0 to ∞, infinitely many PDEs are obtained. As this would obviously be impractical, depending on the desired accuracy and application, the RTE is only expanded to a certain level, resulting in a so-called P_N-approximation. Especially for higher order approximations in 3D domains, this method becomes very complex and impractical for evaluation. The use of SHM for highly non-grey media has been widely researched with a varying degree of success (see for example the work of Andrienko in Ref. [5]).

Monte Carlo Methods, PMC

Finally, the most accurate method used to solve radiation problems is the stochastic method of Photon Monte Carlo (PMC). In its principle, PMC follows the actual radiation physics; photons are emitted in random directions with wavelengths corresponding to certain probability functions based on their spectra, and transmitted through the media until completely absorbed. Since this is the method of choice for the thesis work, more detailed description of principles and logic of PMC will be offered in Chapter 3.

2.2.5. Approaches to Spectral Approximation

Finally, before studying the radiation in hypersonic and combustion applications in more detail, one final aspect of radiation modelling should be discussed. As can be seen from the definition of the RTE (see Equation (2.13)), the radiative intensity has to be in theory solved separately for each wavenumber η. Spectra of gasses of interest span from high frequency ultraviolet to far infrared wavelengths, and since the absorption coefficient is highly variable, this means that the RTE would have to be solved for millions of wavenumbers / wavelengths. This is obviously an impractical approach. Thus, over the course of years, several approaches have been developed to approximate the absorption coefficient such that considering every single wavenumber is not necessary, here referred to as spectral approximation.

One exception to this problem is the Monte Carlo method. In PMC, the selection of wavelengths of the emitted photon follows a probability distribution, and thus the most significant wavelengths at which the medium emits will be automatically selected, meaning that all wavelengths do not have to be considered.

The most basic spectral discretization technique, where all wavelengths are considered and which is computed directly from radiative transition data is the line-by-line (LBL) spectrum. Other approaches to spectral approximation developed to alleviate the spectral computational demands will be discussed in the rest of this subsection.

k-Distributions and Homogenisation

The k-distribution method is one of the most accurate ways of modelling, and has several forms depending on the intended application.

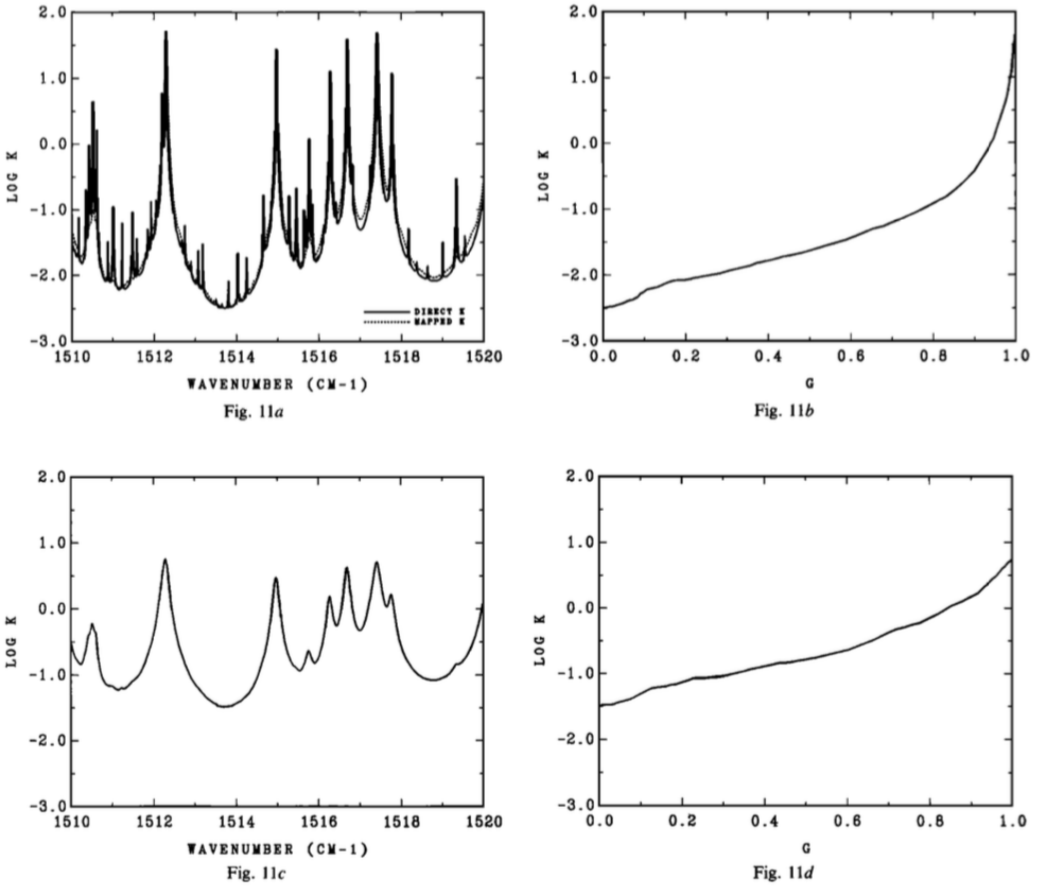

Fig. 11*a*

Fig. 11*b*

Fig. 11*c*

Fig. 11*d*

Figure 2.6: Demonstration that while the absorption coefficients of the gas at two different pressures do not look correlated at all, the resulting smooth $k(g)$ distributions do. This lead to the development of correlated-k and scaled-k models for non-homogeneous media. From Ref. [57].

The principle of k-distributions lies in the fact that while the absorption coefficient is highly variable, its values are repetitive (i. e. the absorption coefficient attains the same value many times in the spectrum across the wavenumbers). Thus, if we were to integrate the RTE at all these wavenumbers, the calculations would also repeat themselves each time the absorption coefficient has the same value. The idea behind k-distributions is thus to reorder the spectrum such that the absorption coefficients are, for example, ordered from the lowest to the highest value, ignoring the actual wavelengths at which these coefficients occur. This spectrum then forms a much smoother distribution, and the RTE is then integrated over this smoother spectrum. An example for this principle is shown in Figure 2.6.

Any parameter that directly depends on the absorption coefficient, such as the average transmissivity and intensity can be rewritten using the k-distribution $f(k)$ in the following manner:

$$\bar{\tau}_\eta(s) = \frac{1}{\Delta\eta}\int_{\Delta\eta} e^{-\kappa_\eta s} d\eta = \int_0^\infty e^{-ks} f(k) dk, \tag{2.72}$$

where the k-distribution $f(k)$ is a weighted sum of the number of points at which $k = \kappa_\eta$:

$$f(k) = \frac{1}{\Delta\eta}\sum_i \left|\frac{d\eta}{d\kappa_\eta}\right|_i = \frac{1}{\Delta\eta}\int_{\Delta\eta} \delta\left(k - \kappa_\eta\right) d\eta. \tag{2.73}$$

An example for CO_2 is shown in Figure 2.7. The behaviour of $f(k)$ is still very erratic (in red), but its cumulative distribution function $g(k)$ (in black) is not. Then, Equation (2.72) can be expressed in $g(k)$ as:

$$\bar{\tau}_\eta(X) = \int_0^\infty e^{-kX} f(k) dk = \int_0^1 e^{-k(g)X} dg. \tag{2.74}$$

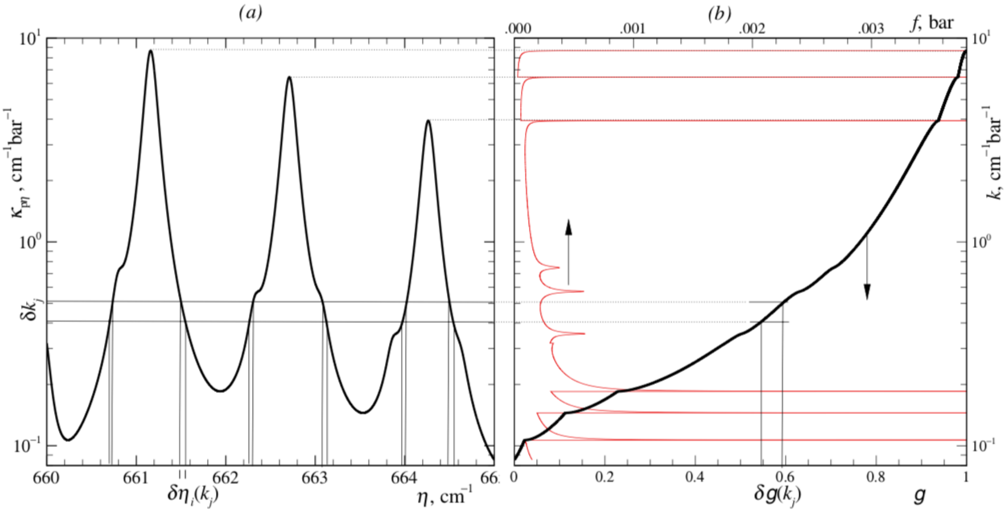

Figure 2.7: Demonstration of the reordering procedure of the absorption coefficient, from the original spectrum on the left to the reordered k-distribution (red) and cumulative k-distribution (black) on the right. From Ref. [68].

Thus, only the $g(k)$ distribution needs to saved and used when integrating RTE, and since it is smooth compared to the original κ distribution, its discretization when solving RTEs can be made far coarser.

In addition to the distribution being much smoother, looking at the Figure 2.6, it can be seen that even though the original κ spectra for the two conditions look very different, a certain correlation can be found between their $g(k)$ distributions. This correlation can be used to derive the $g(k)$ distribution of the gas at a different position from the reference, if it can be determined as a function of some state vector ϕ (for example containing pressure and temperature information). How this is dealt with results in two separate approaches - the so-called correlated- and scaled-k models.

The correlated k-distribution models look at the relationships between the $g(k)$ distributions of media at various conditions directly. The scaled k-distribution models attempt to separate the effects of the gas state from the effects of the wavelength reordering. The correlated k-distribution of the absorption coefficient at some reference state ϕ_0, $k_\eta = \kappa_\eta(\eta, \phi_0)$ can be then formulated as:

$$\kappa_\eta(\eta, \phi)_{\text{correlated}} = k^*_\eta(\phi, k_\eta), \tag{2.75}$$

while the scaled k-distribution model is expressed separately for the wavenumber reordering and the gas state vector ϕ with some scaling u:

$$\kappa_\eta(\eta,\phi)_{\text{scaled}} = k_\eta(\phi)\,u(\phi,\phi_0). \tag{2.76}$$

Clearly, with the loss of the information about the actual wavenumber, the emissivity cannot be properly calculated either (from the product of absorption coefficient and the Planck function in LTE) as the Planck function depends on the wavelength. To deal with the loss of the data on the wavelength, depending on the scope at which the reordering is performed, the k-distributions can be classified as:

- Narrow band /wide band k-distributions
- Full spectrum k-distributions

In case of the former, the k-distributions are only created for separate bands of the spectrum. These bands are relatively narrow in the spectrum, meaning that in general, the approximation can be made that the Planck function over these narrow regions varies only insignificantly. The location of these bands is still retained, and the Planck function for these bands is computed at their central wavelength.

For the latter, the approximation of a constant Planck function can be no longer made. Thus, the k-distributions are also generated using the Planck functions as a weight. For example, for the scaled-k full spectrum model (FSSK) for a non-homogeneous medium, the k-distribution is defined with Planck weighing as:

$$f(T,\phi,k) = \frac{1}{I_b}\int_0^\infty I_{b\eta}(T)\delta\left(k-\kappa_\eta(\eta,\phi)\right)d\eta = \frac{1}{I_b(T)}\sum_i I_{b\eta i}(T)\left|\frac{d\eta}{d\kappa_\eta}\right|_{\kappa_1(\eta_i,\phi_0)=k}. \tag{2.77}$$

Similarly, for the correlated k-distribution k^* (FSCK) at the local state:

$$f(T,\phi,k^*) = \frac{1}{I_b}\int_0^\infty I_{b\eta}(T)\delta\left(k^*-\kappa_\eta(\eta,\phi)\right)d\eta = \frac{1}{I_b(T)}\sum_i I_{b\eta i}(T)\left|\frac{d\eta}{d\kappa_\eta}\right|_{\kappa_1(\eta_i,\phi_0)=k^*}. \tag{2.78}$$

While these approaches are very accurate and computationally beneficial, the knowledge of the Planck function is still necessary for the full spectrum models as seen in Equations (2.77) and (2.78). Similarly, for the narrow and wide band models, the assumption that the Planck function has roughly the same value within the bands must be made. Both of these assumptions do not hold for nonequilibrium plasma, where the Planck function behaves rather erratically and cannot be expressed as a simple function.

Attempts have been made to create such models also for hypersonics. For example, it has been attempted to separate the wavelength regions depending on how they scale with temperature (such as separation of lines of different elements and molecules), and create separate correlations for these groups, resulting in multi-group / multi-scale full spectrum correlated / scaled k-distributions, MGFSCK/ MSFSSK (see e.g. Ref. [120]). These, however, require significant pre-processing to correctly separate the groups / scales in the spectra, and are thus fairly inflexible.

Similar to the k-distribution theory is the homogenisation approach developed already in 1966 by Strom and Kurucz in Ref. [103]. This procedure was created for blanketed spectra of stars, which are spectra where lines are heavily shadowed by the continuum due to the very high temperatures of stars. The procedure involved computing the equivalent absorption coefficient by diving the actual coefficient of the line by the absorption coefficient of the continuum and determining its weight based on its frequency of occurrence in the examined spectral band. Homogenisation was, however, developed and validated for hot stars, not atmospheric (re-)entry and never applied to atmospheric entry flows, to author's knowledge. Hence, since k-distribution techniques are similar in their nature, homogenisation will not be considered further.

Wide and Narrow Band Models

Next to wide and narrow band k-distributions, separate models exist which assume that in small specral bands, the absorption coefficient can be averaged or modelled in a simple way. The most widely used models from this category include:

- Elsasser (narrow band) model
- Statistical narrow band model (SNB)
- Box (wide band) model

- Exponential wide band model (EWB)

For example, the Elssaser model assumes constant line strength and line spacing within these narrow bands, while the statistical narrow band model assumes random line intensity and random line spacing, as shown in Figure 2.8. The box wide band model uses LBL data to find the average band absorption coefficient and approximates spectral bands as a collection of these regions (which resemble boxes due to the constant κ value). The EWB model is meant to be a more sophisticated version of such an approach, where the bands are modelled using different exponential functions to resemble the actual rovibrational band features also at the band edges. The coefficients of these exponential functions are then computed from the actual gas state and scale with temperature and pressure.

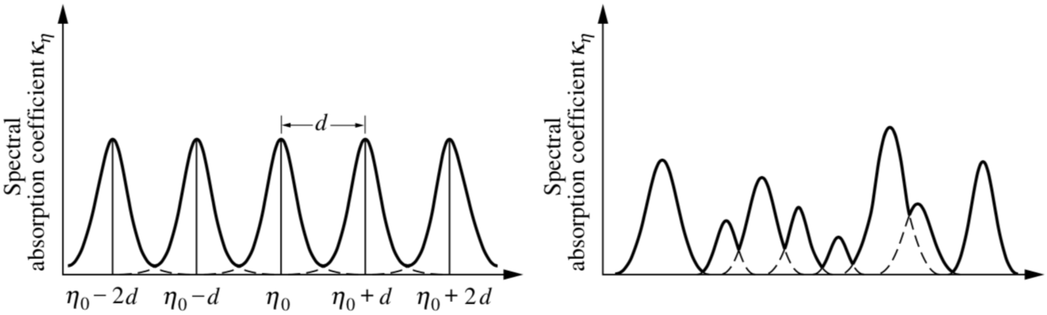
Spectral absorption coefficient κ_η
d
$\eta_0 - 2d$
$\eta_0 - d$
η_0
$\eta_0 + d$
$\eta_0 + 2d$
Spectral absorption coefficient κ_η

Figure 2.8: Elsasser constant-line-strength and constant-line-spacing band model compared to a statistical band model assuming random spacing and random line strengths. From Ref. [68].

While these models can be accurate, they are generally very difficult to apply in non-homogeneous media. In addition, these models provide a good description of the absorption coefficient, but to calculate the emissivity, the Planck function is still needed. They thus offer no significant advantage for calculation of media in nonequilibrium compared to direct use of LBL, unless Planck function or emissivity can also be approximated this way.

Full Spectrum Models

Finally, full spectrum (global) models besides the FSSK and FSCK techniques also exist. In global models, the total radiative fluxes are calculated directly from spectrally integrated properties. The following global models are frequently in use and will be briefly discussed:

- Weighted-sum-of-grey-gasses model (WSGG)
- Spectral-line based weighted-sum-of-grey-gasses model (SLW/ SLWSGG)
- Opacity binning and opacity banding models

The WSGG and SLWSGG models are based on the principle that the total gas emittance can be expressed as a weighted sum of grey gas (κ = const.) emittances. The emission weighting factors and the absorption coefficients are obtained from a fit of total emittance measurements of isothermal and homogeneous columns. This model is suitable mainly for gasses close to the grey conditions, but Modest in Ref. [67] has shown that this model can be used also for non-grey gasses, if certain adjustments to weighting and summation are made. The radiative heat flux is computed for each gas and then the resulting heat fluxes are added together to represent the entire system. However, these techniques are definitely not sophisticated enough for highly non-grey, non-homogeneous media such as reentry plasma.

Similar to the origin of the homogenisation method, other methods currently applied to reentry flows were initially developed for modelling of stellar atmospheres in the 1980s. These are based on the division of the spectra into multiple sections, either based on the spectral position (so-called frequency banding) or the absorption coefficient (so-called opacity binning). These methods might be more primitive than the complex techniques such as wavelength reordering, but nonetheless they were found to yield very accurate results as will be shown later.

The first of these methods, frequency/ spectral banding, typically requires a large number of wavelength bands to reach high accuracy, especially for very non-homogeneous flows (see Ref. [116]). The second one, opacity binning (also sometimes referred to as opacity sampling) is more powerful in that it offers similar accuracy at much lower number of samples. It has been widely applied in the studies of stellar atmospheric radiation (see Ref. [44]). The principle of these two methods is shown in Figure 2.9. In case of opacity binning, the RTE is evaluated for each separate frequency bin.

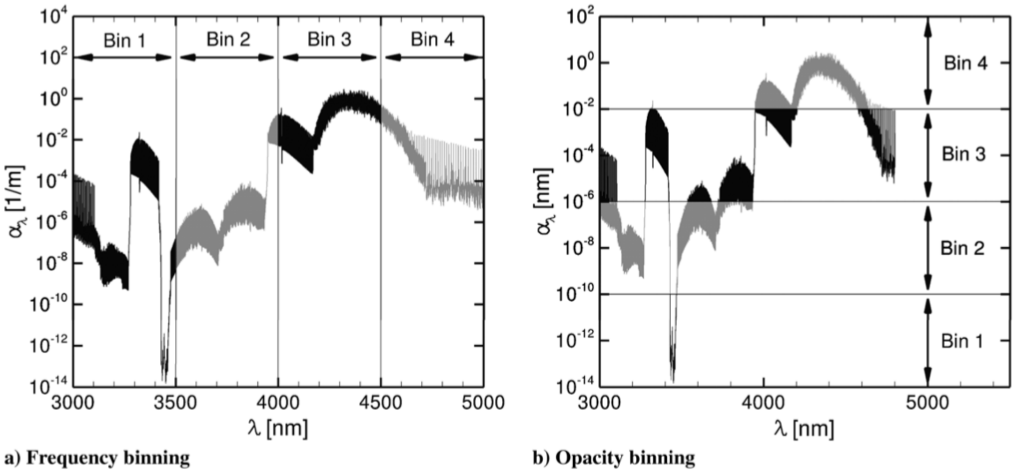

Figure 2.9: The principle of frequency banding (left) based on the spectral location and opacity binning (right) based on the absorption coefficient. From Ref. [51].

A k-distribution version of spectral banding and opacity binning exists, where probabilities of certain opacities in discrete spectral bands are evaluated and fitted with a probability density function, PDF. These are then integrated to find the total opacity of the media; an approach which is very similar to the developed wide-band and narrow-band cumulative k-distribution function. In astrophysics, this method is often referred to as the Opacity Distribution Function method, ODF and is further described by, for example, Cernetic et al. in their work in Ref. [21] from 2019. Since this approach is very similar to the already discussed k-distribution and since it is typically used for stellar atmospheres, only the discrete equivalent, opacity binning, which has been applied to hypersonic flows will be considered.

This concludes the introduction to the spectral processing methods available. Having defined these various RTE solutions and spectral processing methods, as well as having introduced the basic theory behind radiation, an overview of hypersonic radiation research over the last half a century will be presented in the next Section.

2.3. Radiation in Hypersonics

The main requirement for the radiation solver to be developed within this thesis work is that it shall be capable of resolving hypersonic radiation. To outline the difficulties of this process and illustrate the modern state-of-art, this section presents the necessary historical concepts and evolution of hypersonic radiation modelling starting from the mid of 20th century. The arguments from this section will then also be used when justifying the selection of the methods for this thesis work.

2.3.1. Historical Overview

The attempts to model reentry radiation date back to late first and mostly the second half of the 20th century. In the 40's and 50's, the focus was placed mostly on military applications, such as the effects of radiation on the design of ICBM's. In the 60's, the focus shifted towards the atmospheric reentry upon return from Moon missions and, in the 70's and 80's, towards the entry to atmospheres of other planets and celestial bodies. As the computational technology evolved, so did the accuracy of these calculations, starting from simple grey, LTE assumptions in the 40's and 50's to the development of complex nonequilibrium codes in 80's and 90's. This progress will be elaborated on in more detail in the subsections following.

Early Investigations of Shock Radiation

After the end of the World War II and the development of intercontinental and intermediate-range ballistic missiles (ICBMs and IRBMs), hypersonic radiation started to be of prime focus when it came to their development to ensure survival during atmospheric descent and delivery. Some of the first papers published on the analysis of radiation were written by Sachs in 1946 (see Ref. [89]), where only 1D plane analysis with Rankine-Hugoniot relations was performed. In the 50's, it was typical to make the so-called diffusion approximation, where the radiative heat flux was determined using an estimated Rosseland mean absorption coefficient (inverse of a weighted mean of the transmission coefficient over all frequencies) and the temperature gradient (see for example the work of Sen and Guess in Ref. [96]). A comprehensive overview of the approaches of radiation modelling in the 50's and 60's is provided in the paper of Anderson from 1969 in Ref. [4].

One of the first attempts to actually numerically solve the RTE was made by Pomerantz in 1961 (see Ref. [85]). He used what could be considered as a primitive version of DOM (which was possible with the technology from that time), assuming LTE for a geometry of a shock tube filled with Argon. His findings underlined the fact that at some conditions, the presence of radiation changes the shock profile and composition significantly. Other simplified one dimensional LTE efforts continued to show strong effects of radiation on the temperature and velocity ratios across the shocks (see for example the work of Pai and Speth in Ref. [77]), which motivated further, more complex analyses.

The significance of radiation on the flow was more formally defined by Goulard in 1961 in Ref. [39], who introduced the Goulard number to express the radiation-flow coupling. This variable is, to date, used to express the effects of radiation on the energy budget, and it is of importance when estimating how frequently the radiation solution should be updated during CFD iterations. For example, loose CFD coupling can be chosen if the Goulard number is low (< 0.01), as will be discussed in the next Chapter.

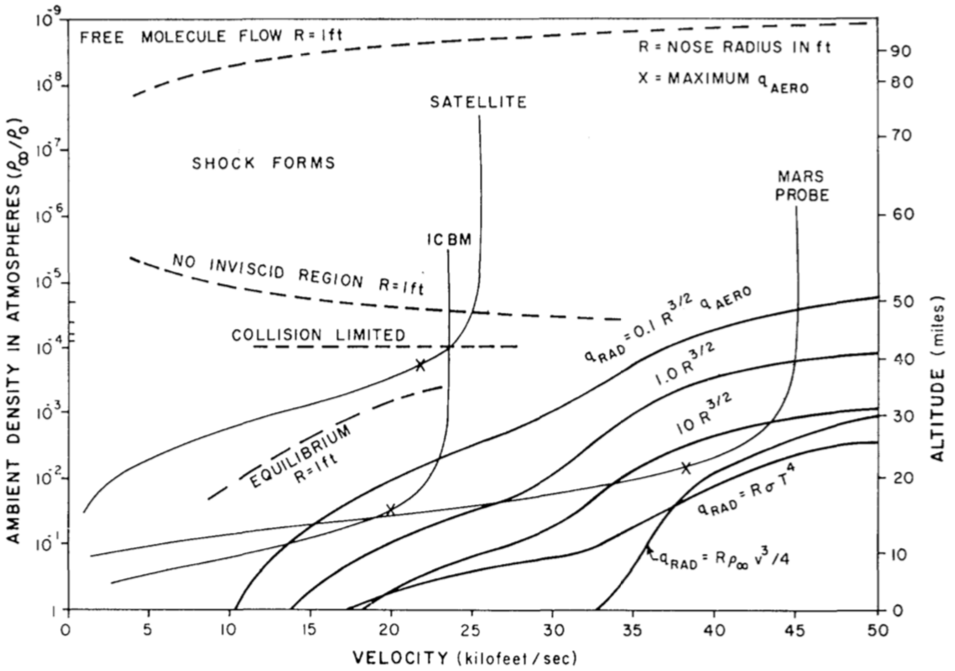

Figure 2.10: Kivel's diagram to emphasise the significance of radiation heat flux and consideration of nonequilibrium for (re)entry trajectories of ICBMs, Mars probes and re-entering satellites from Ref. [53].

One of the first researchers to emphasise the effects of nonequilibrium was Kivel in 1961. His experimental research work from 1959 in shock tubes allowed him to formulate many semi-empirical relations to estimate radiative heat transfer as a function of speed, gas composition, altitude and nose radius. He then used these expressions to carry out conceptual calculations for a hypothetical Mars probe entry, satellite reentry and ICBM flight and discussed the conditions in which nonequilibrium prevails in Ref. [53]. He was also one of the first researchers to correctly speculate the potency of NO when it comes to radiation despite its low content in the atmosphere. With the estimated uncertainty of 30% from his experimental data, he estimated and plotted the radiative transfer as a function of aerodynamic heat transfer and nose radius, which is shown in Figure 2.10. The Figure shows the expected equilibrium limits (the dashed equilibrium curve) and that for a typical reentry, for the majority of the trajectory, equilibrium cannot be assumed. This was confirmed also by other analysis efforts and experimental work from that time, such as those by Wrey and coworkers in 1961 (see Ref. [116]) and Camm et al. (see Ref. [18]), which further stimulated the development of proper nonequilibrium solution techniques.

The definitive proof that LTE cannot be assumed for a majority of reentry calculations and that more complex description of the absorption spectrum is required instead of the diffusion approximation was given by the data from the FIRE II mission, which flew in 1964 and 1965, with its purpose to provide validation data for reentry radiation calculations. The geometry of it matched the Apollo forebody, and it utilised several instruments to measure radiation; a spectral calorimeter for measurements of spectral heat flux, a total radiometer for measurements of total radiative intensity and a calorimeter for the determination of the sum of convective and radiative heat flux (see Ref. [86] for details about the trajectory and instrumentation). FIRE II data is to date used for validation of radiation solvers, and will also be used in this thesis work for the same purpose. The data from FIRE II and comparison to various numerical approximations made at the time (such as grey gas approximation) were analysed by Olstadt in Ref. [73], showing the general unsuitability of these assumptions when computing reentry radiation.

One of the first sophisticated models to represent the spectral absorption coefficient variations was developed by Hoshizaki and Wilson utilising solutions of quantum statistics in 1966 (see Ref. [45]).

In the 70's, the focus shifted from radiation for ICBMs and IRBMs and Lunar missions to radiation during entry to other planetary atmospheres; mostly Mars, Venus and Jupiter. The Pioneer space mission's entry into Venus's atmosphere was studied by Sutton in his PhD thesis in Ref. [106]. The Jovian entry radiation for the Galileo mission was analysed by, for example, Moss and his coworkers in Ref. [70].

Technology was becoming more capable with each year, and so the radiation solution techniques were becoming more sophisticated. In the 70's, the first numerical solvers thus became available - RATRAP from Lockheed (original publication not available, mention in Ref. [47]) and MDAC from McDonnell Douglas (Ref. [3]). Besides these two, in 1970, Nicolet in Ref. [72] developed a code that soon became the predecessor to many modern solvers such as NEQAIR, which could also compute radiation transport in hypersonic flows along with the effects of ablation. This code was called RAD/EQUIL, with its name implying that thermal and chemical equilibrium was still assumed. Nevertheless, it featured an advanced spectral description with atomic LBL data, and for molecular bands, smooth fit was used (similar to what is now referred to as narrow band spectral modelling). Compared to RATRAP and MDAC, RAD/EQUIL was far more accurate (see for example the analysis of Suttles in Ref. [105]), and soon became the standard for (re)entry design.

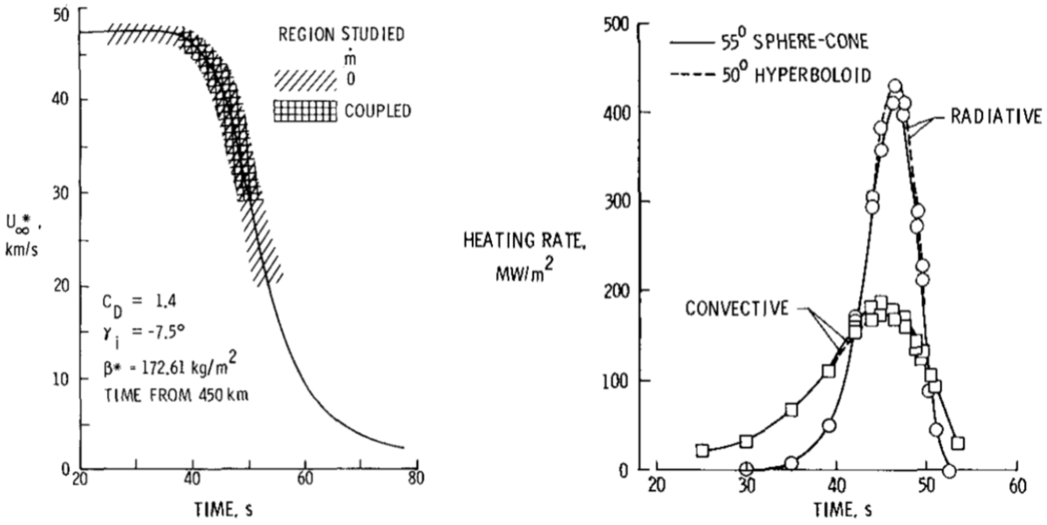

Figure 2.11: For the velocity vs. entry time profile shown on the left Figure, the right Figure shows the expected radiative heat flux compared to the convective heat flux for a Jovian entry, as computed by Moss et al. in 1976 further discussed in Ref. [70].

Over the course of the early 70's, minor corrections were made to the RAD/EQUIL solver. The suitability of its basic building blocks (LTE and chemical equilibrium), however, started to be seriously questioned when in 1975, Grose and Nealy recomputed the entry to Venus assuming both chemical equilibrium and nonequilibrium and showed that the radiative heat flux might be double for the case chemical nonequilibrium (see Ref. [40]). Especially for Jovian entry, radiation was considered to be the primary source of heating (see for example Ref. [70]), thus motivating further development of tools which would handle nonequilibrium radiation, leading to the origin of NEQAIR.

RAD/EQUIL was still maintained and developed next to the nonequilibrium codes, and was still used for cases when nonequilibrium was not too heavy. For example, in 1989, Carlson applied an approximate correction for nonequilibrium to RAD/EQUIL from Ref. [20], nowadays referred 1st order local thermodynamic nonequilibrium, LTNE. The second order approximation was developed and implemented to RAD/EQUIL by Gally et al. in Ref. [35]. However, since the resulting version of RAD/EQUIL, even when accounting for nonequilibrium with the 1st and 2nd LTNE approximations, still resulted in over 10% errors in wall intensity when validating against the FIRE II data (see Ref. [47]), this software is rarely used nowadays and is not further discussed here.

Development of NEQAIR and Other Modern Solvers

Besides planetary entry, from the 80's onwards, the research also started to focus on concepts such as the aeroassisted orbital transfer vehicle and aeroassisted flight experiments. The trajectory of these vehicles meant high deceleration at high altitudes, making nonequilibrium unavoidable. Despite the fact that these vehicles never existed, their design inspired and supported development of many tools which, in their modern versions, are still used for entry vehicle design to date, including NEQAIR.

The very first version of NEQAIR was developed in 1984 by Park (see Ref. [79]). Initially, NEQAIR computed with a three temperature model; vibrational temperature T_v, translational temperature T_t and electronic temperature T_e, with the approximation that $T_t = T_r$ (rotational). Nowadays, it is typical to either use a full 4 or 5 temperature model (T_t, T_e, T_v, T_r and possibly electronic T_{el}) or a 2 temperature model, which is also considered in this thesis ($T_t = T_r$, $T_v = T_e = T_{el}$). The operation and logic of NEQAIR will be discussed frequently in this text, mainly in Chapter 3, since its subroutines are also made use of in this thesis work.

To model the non-Boltzmann distribution, Park introduced the so-called Quasi-Steady-State (QSS) assumption. As discussed in the previous section, in LTE, one can compute the population state of the energy levels with the Boltzmann distribution. In nonequilibrium, the populations have to be computed separately from each level by considering all the neighbouring levels and the respective transitions rates between these levels. The QSS assumption, in short, states that the rate of change of the population of these levels is much smaller than these transition rates themselves. This will be discussed in more detail in the next Chapter.

Since the initial development of NEQAIR, several corrections have been introduced to improve its accuracy. For example, Candler et al. noticed that far away from thermochemical equilibrium, the QSS assumption over-predicted the number of N_2^+ species, causing substantial errors as N_2^+ has a very large contribution to the overall radiative transfer. A correction described in Ref. [19] was thus introduced. One dimensional techniques were (and still are) employed by NEQAIR not only to solve for the absorption and emission spectra, but also to integrate the RTE. The TS method, most widely used when using NEQAIR, is described by Wilson in Ref. [113]. Other discrepancies noticed by Park were for example due to chemi-luminiscence of NO in presence of atomic oxygen at around 0.6 μm, also later corrected for.

In 1989, Park attempted to accurately evaluate the spectral errors of NEQAIR when compared to the experimental data from the Shock-Tube Radiation Program (STRAP). The total radiative heat flux was found to be in a relatively good agreement even in nonequilibrium conditions, see Figure 2.12, but the spectral representation left much to be desired as shown in Figure 2.13. Indeed it could be even argued, judging from the fit on Figure 2.13 that the match of the radiative heat fluxes was purely coincidental, with the under-prediction at lower wavelengths and over-prediction at higher wavelengths cancelling each other out.

Due to this complete lack of spectral agreement, the lack of flexibility when handing the species and the poor computational efficiency, in 1992, Moreau and colleagues presented a new version of NEQAIR, NEQAIR2 (see Ref. [69] for details). NEQAIR2 included more species and spectral bands, had new expressions for partition functions and more up-to-date databases, all of which resulted in superior accuracy and 20 times speedup.

Further corrections were motivated by the studies of Levin et al. from 1993 (see Ref. [60]), which found significant disagreement with the spectral data for regimes at which molecular species were the dominant radiator instead of the atomic lines, such as at lower altitudes. This was expected, since NEQAIR was, during its development, validated mainly against Earth reentry flights were atomic lines dominate. Comparison with experimental data published by Levin et al. are shown in Figure 2.14. In 1994 in Ref. [61] and in Ref. [62], changes were proposed to improve this match (which originated mainly from incorrectly computed excited

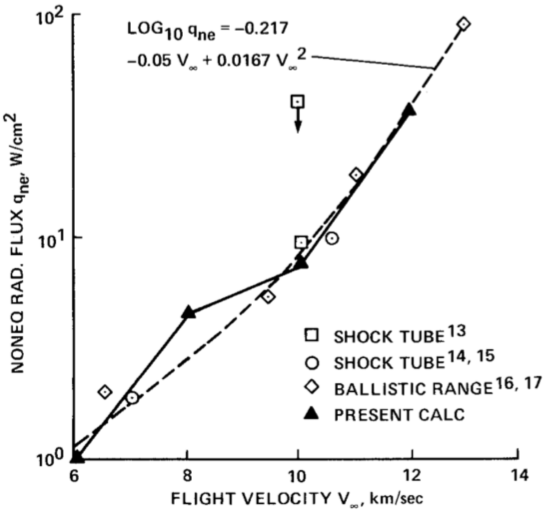

Figure 2.12: Experimental data compared to Park's predictions of total nonequilirium radiation heat flux as a function of flight velocity based on NEQAIR, showing a relatively good agreement. From Ref. [80].

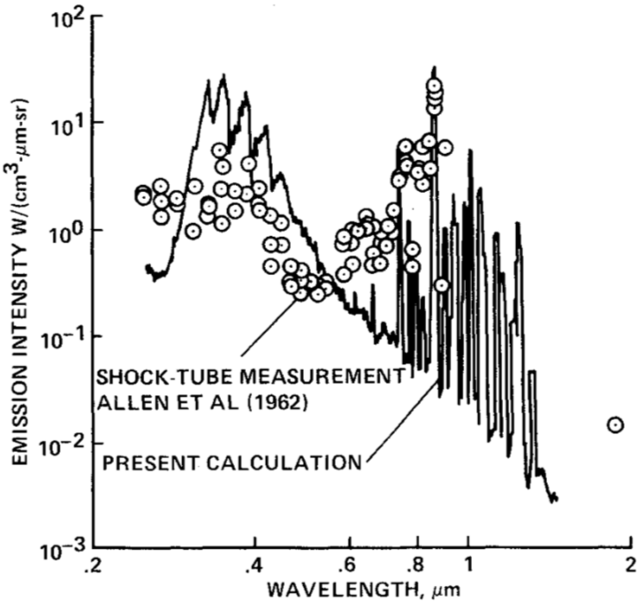

Figure 2.13: Comparison between experimental spectra and NEQAIR spectral prediction at 10km/s and pressure of 13Pa by Park in 1989 showing a significant disagreement. However, due to under-prediction in shorter wavelengths and over-prediction in longer wavelengths, the integrated heat flux agreed well as shown in Figure 2.12. From Ref. [80].

NO states).

In the same report by Levin et al., it is also investigated to what extent QSS is applicable depending on the gas conditions. For two different flow cases at 5.1km/s at 71km and 80km altitude, the error due to the QSS approximation is shown in Figure 2.15.

All these corrections led to the introduction of NEQAIR96 (see for example Ref. [112]). Spectral accuracy was improved and NEQAIR was turned more into a user friendly software. Further adjustments then led to the update of NEQAIR every couple of years, with the current version being NEQAIRv15.0, used in this thesis.

Other alternatives also became available besides NEQAIR, first of which was the so-called LORAN code developed at the Langley Research Center by Hartung and Chambers in 1991 (see for example Ref. [43]). However, its spectral description used smearing of vibrational bands (SRB) to reduce computational costs, which turned out to be fairly inaccurate for some applications. NEQAIR thus remained the standard.

This brings us to the 21st century research efforts, in which the accuracy has been further improving

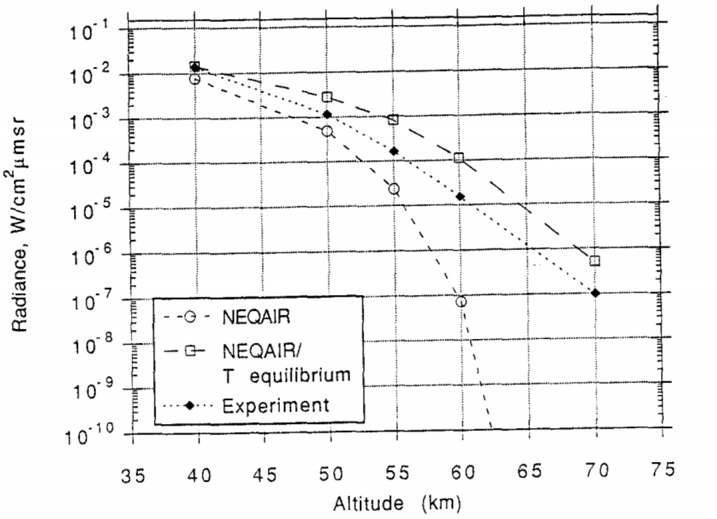

Figure 2.14: The disagreement between experimental data and a NEQAIR simulation at lower altitudes discovered by Levin et al. in 1993, leading to the development of NEQAIR96 two years later. From Ref. [60].

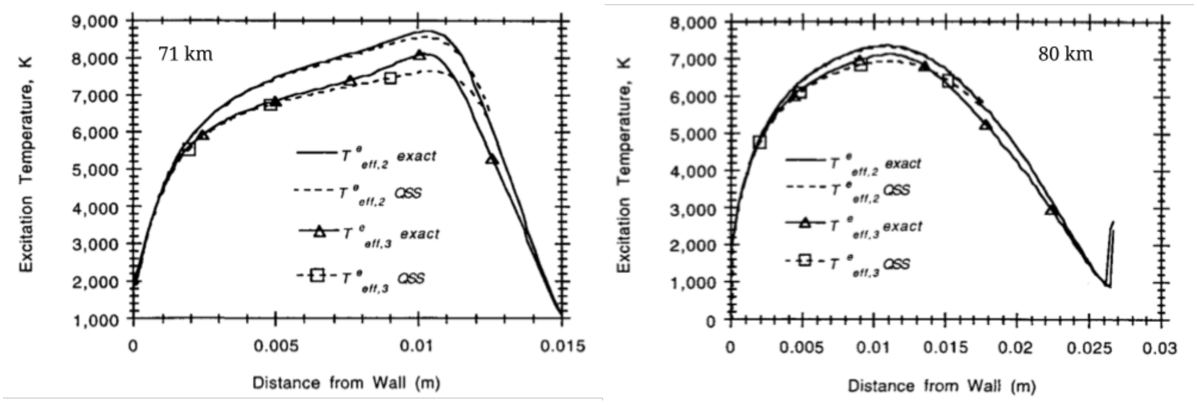

Figure 2.15: Demonstration of the validity of the QSS assumption at 71km (left) and 80km (right) with the speed of 5.1km/s, including the N_2 QSS correction, performed by Levin et al. in 1994. From Ref. [62].

mainly thanks to better computational resources and experimental facilities allowing for more rigorous validation routines.

2.3.2. Modern Display of Hypersonic Radiation Modelling

The era of modern research in applied hypersonics in this text is assumed to have started once proper nonequilibrium description of the flow became available and relatively accurate, roughly with NEQAIR96. Radiation became a routine part of aerothermodynamic design of most (re)entry vehicles since then. While a complete overview of the research done on hypersonic radiation in the 21st century on this topic is believed to be neither practical nor necessary, some interesting developments and applications will be presented nevertheless to formulate expectations on the thesis work.

Right before the onset of the 21st century, a very interesting radiation event took place in the form of the Stardust capsule reentry, which was the fastest man made object to ever reenter (at 12.6 km/s). The radiation predictions using LORAN were computed by Olynick, Chen and Tauber in Ref. [74]. They predicted that less than 10% of the total heat flux should come from radiation due to the trajectory and geometry characteristics of Stardust (a very small shock stand-off distance due to small dimensions), as can be seen on Figure 2.16. The development of the radiative heat flux over the course of reentry is shown in Figure 2.17. While Stardust did not have any instrumentation similar to that aboard FIRE II, the radiation data was obtained by observation of the reentry from the DC-8 Airborne observatory.

This mission was revisited in 2010 by Liu and coworkers, who simulated the Stardust radiation with NEQAIR and compared it to the measured data in Ref. [64]. This study is of great interest to modern mod-

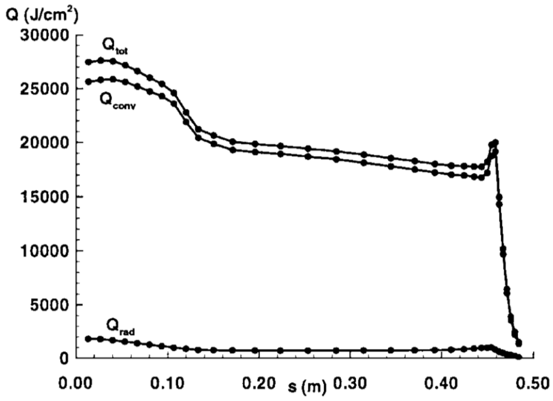

Figure 2.16: The integrated convective, radiative and total heat flux along the stagnation line of Stardust computed by Olynick et al. in 1999 in Ref. [74].

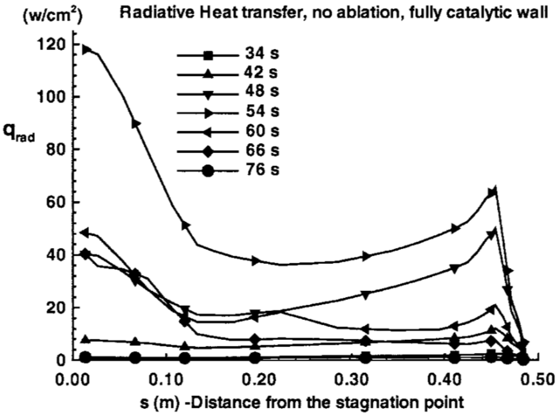

Figure 2.17: The radiative heat flux along the stagnation line at different trajectory points of Stardust computed by Olynick et al. in 1999 in Ref. [74].

elling, since it shows the effects of using various thermochemical model options on the result accuracy. Liu et al. explored the effects of using 11, 12 (+ Ar) and 17 species air models as well as models assuming electronic excitation or ground states only (labelled as E and G, respectively). The 17 species model also included carbon bearing species CO_2, CN, CO, C_2 and C. In addition, since the NEQAIR version back at that time did not support QSS for all 17 species, the 17 species model assumed Boltzmann distribution. To evaluate the effect of this effect, the 12 species model was computed using both Boltzmann and non-Boltzmann modelling.

Since this study shows both the integrated values as well as spectral distributions and spectral contributions of various groups of radiators, it will be used in this text to illustrate the typical trends observed in modern hypersonic radiation modelling. The freestream conditions at the the Stardust's trajectory points which were analysed and which will be presented in the next Figures are:

- 42s: 71.19km, 12062.73m/s, 5.5520E-05kg/m^3 and 221.82K
- 51s: 61.76km, 10871.38m/s, 2.1100E-04kg/m^3 and 234.95K

The differences in the predicted vibrational and translational temperatures along the stagnation line between the different modelling settings are shown in Figure 2.18. As expected, exclusion of the electronic excitation leads to overestimation of temperature. This follows since electronic excitation allows for some energy to be stored in the internal states. Currently, NEQAIRv15 does correct for that (but its original versions NEQAIR to NEQAIR96 did not).

The specific intensity (which here is equivalent to emissivity) is shown in Figure 2.19 for the model 11GQ. "Inward" refers to the radiation directed towards the vehicle wall and "outward" to the radiation directed to the DC-8 platform. Even though these measurements were not validated experimentally, they show some of the consensus of modern hypersonic radiation research - that the dominant contributions during reentry come from the vacuum ultra-violet (VUV) radiation due to the atomic species' electronic transitions. Similar spectra are also expected to be obtained for hypersonic cases studied in this thesis work.

The match between the radiative heat fluxes along the stagnation line in different spectral windows are compared in Figure 2.20 at 51s of flight. Clearly, the Boltzmann models show nonphysical behaviour at 0.1m to 0.25m, confirming the importance of including QSS calculations to resolve the population states. Liu et al. also investigated the fit between the actual observations of the radiative flux from the Oxygen and Nitrogen lines. In these, they found that NEQAIR under-predicted the Oxygen lines significantly with all models, while in general the Nitrogen lines were computed well. It was hypothesised by the authors that this under-prediction could be due to inaccurate Einstein coefficients used in NEQAIR, since the newly published Einstein coefficients by NIST were by 9% higher. Another possibility presented was that the predicted populations of the upper states of Oxygen were too low. New versions of NEQAIR with updated transition data has been since released.

The most recent study documenting the spectral accuracy of NEQAIR, this time for the visible (VIS) to infrared (IR) wavelengths not yet so heavily studied, was published by Brandis and Cruden who are currently responsible for NEQAIR maintenance and development in Ref. [26]. They recognised the poor fit of NEQAIR

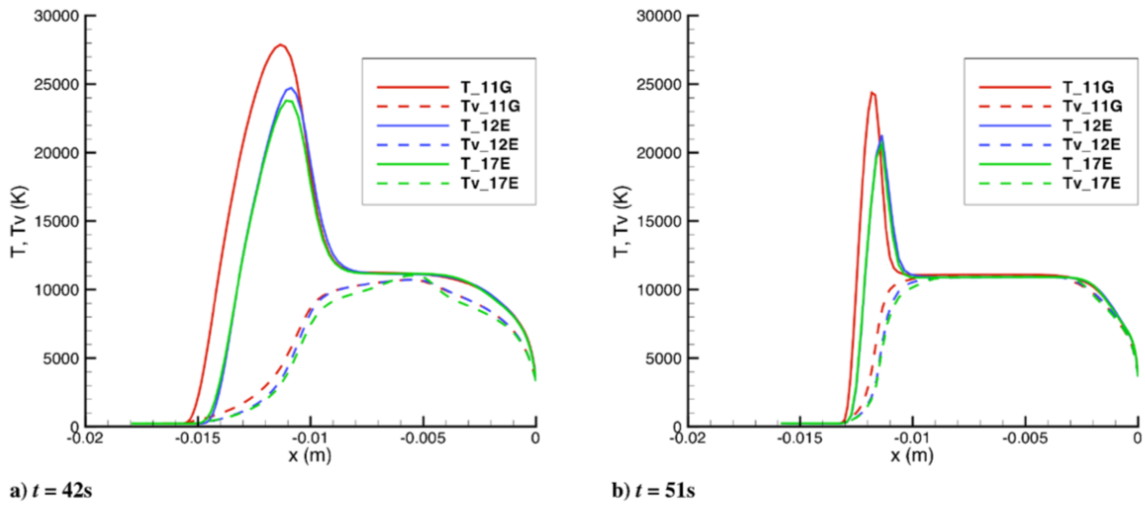

Figure 2.18: Comparison between the computed translational and vibrational temperatures when using 11, 12 and 17 species models using QSS (G) and Boltzmann (E) distributions at two different flight conditions computed by Liu et al. in 2010, showing a significant deviation due to the equilibrium distribution assumption (11G vs 12E), which is larger than the deviation when ablation is considered (12E vs 17E). From Ref. [64].

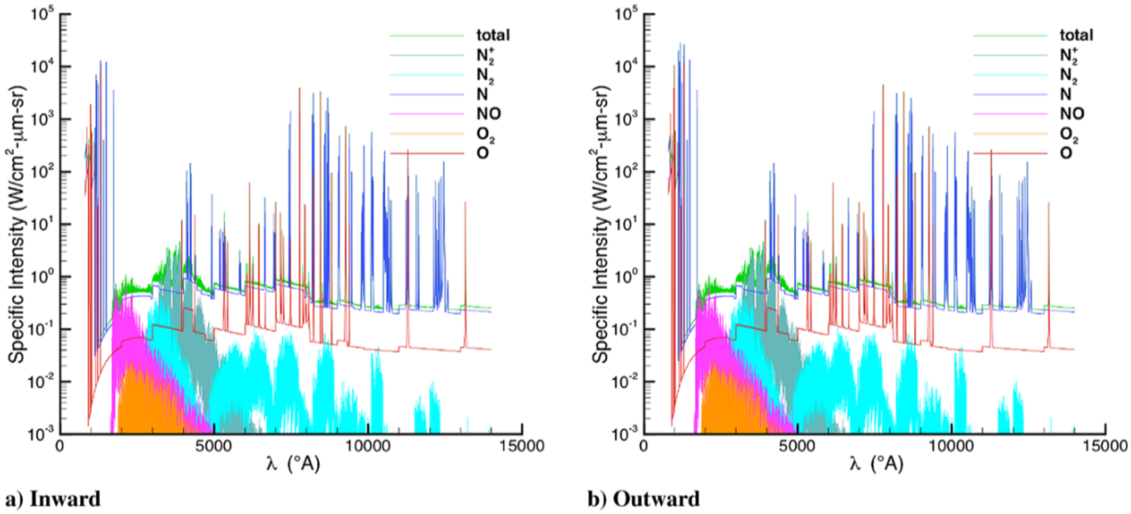

Figure 2.19: Example of resolved spectra at the 51s trajectory point using the 11 species non-Boltzmann model in the direction inward (from the perspective of the vehicle) and outward (from the perspective of the observed of the reentry) computed by Liu et al. for the Stardust reentry. It is shown that at these conditions, majority of the radiation comes from the VUV atomic lines. From Ref. [64].

in these regions when compared to the EAST data. This fit with EAST data was shown for the original NEQAIR (Park 90), for the NEQAIR2 (Park93), for a CR solver with improved reaction rates which were completely up to date and later implemented to NEQAIR (Johnston14), for various pressures. Example data at 40Pa for various portions of the spectrum are shown in Figures 2.22 for the VUV section, 2.23 for the VIS section and 2.24 for the near-IR and IR sections. In addition, the dotted lines in Figures 2.23 and 2.24 show the integrated spectral emissivity (which can be said to dictate the error of the heat flux calculations as will be explained later). To allow for faster evaluation and to provide intuition when reading these spectra, Figure 2.21 shows the species responsible for the observed transitions. From the data, Brandis and Cruden formulated several conclusions about the, at that date, most recent NEQAIRv14 version:

- The NO radiation in VUV is significantly under-predicted by all models and at all pressures
- The radiation of the N_2 second positive bands is significantly under-predicted by all models and at all pressures

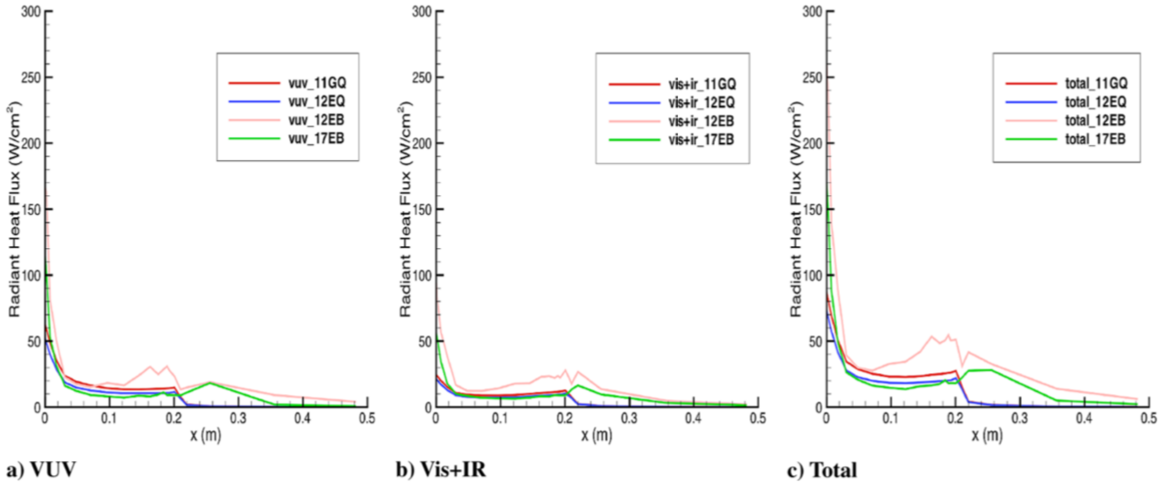

a) VUV **b) Vis+IR** **c) Total**

Figure 2.20: Difference in the resolved radiative heat flux along the stagnation line depending on how many species are considered and whether Boltzmann distribution is assumed. Comparing the 12EB and 12EQ models, it is apparent that assumption of Boltzmann distributions at these flight conditions (≈ 62km, ≈ 11km/s) results in unphysical kinks, introducing more errors into the solution than neglecting ablation altogether (17EB vs 11GQ and 12EQ).

- The N_2^+ radiation is predicted well by current models at pressures higher than 10Pa
- The 1st positive band of N_2 in VIS (500 - 800nm) is not predicted by any of the models
- Several lines from higher states of atomic N are predicted in the 500 - 800nm range, but not observed - likely due to over-prediction of the upper energy state densities of N
- Both atomic O lines in VIS are under-predicted, likely due to inapplicability of QSS
- Atomic N lines in VIS are generally well matched
- Atomic O lines in NIR/IR are generally substantially over-predicted at all pressures

While some of the inaccuracies have been corrected by modification of the reaction rates in NEQAIR (with the modifications discussed in Ref. [26]), not all of them can be resolved without more complex modelling strategies (such as proper CR models without the QSS assumptions, which will be discussed later). Thus, the observed performance in Figures 2.22 through 2.24 can be expected to be roughly indicative of the error that still exists in the current NEQAIR version.

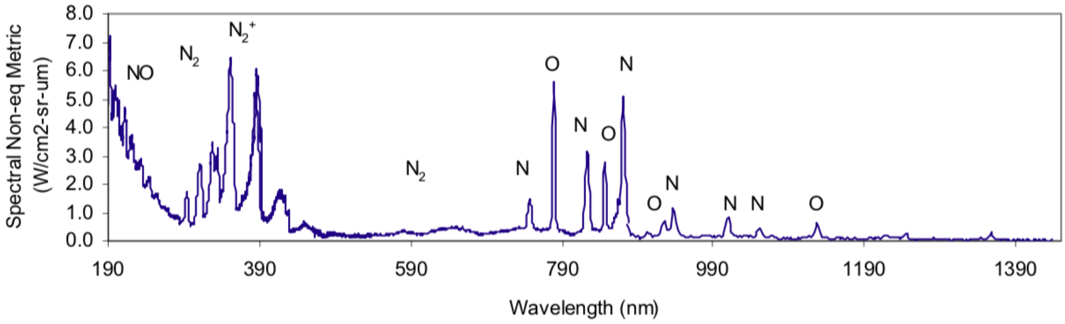

Figure 2.21: Spectrum of air at 8.33km/s and 10Pa showing the categorisation of the major spectral features. From Ref. [26].

While other libraries similar to NEQAIR exist, such as SPARTAN or PARADE, they are based on principles similar to NEQAIR and thus a similar accuracy can be expected. A short trade-off among these libraries will be performed in the next Chapter.

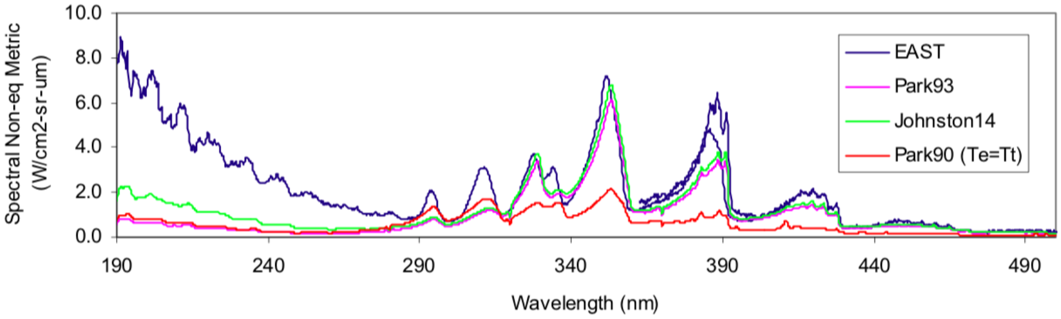

Figure 2.22: Simulation of the VUV portion of the spectrum by the original NEQAIR model, improved NEQAIR model, Johnston's model and experimental data. From Ref. [26].

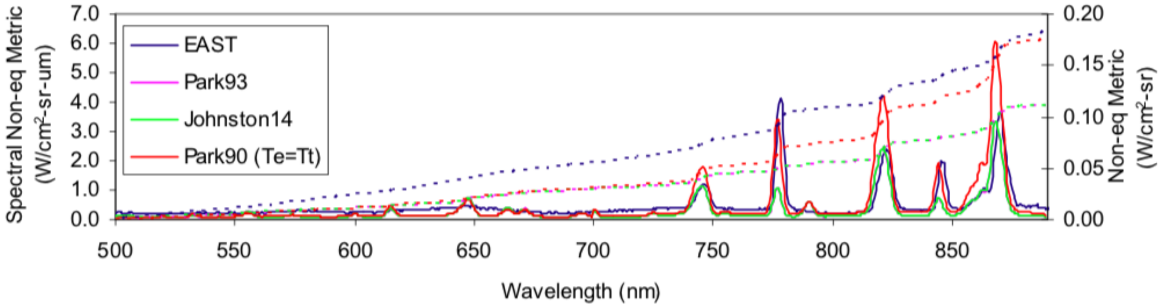

Figure 2.23: Simulation of the VIS portion of the spectrum by the original NEQAIR model, improved NEQAIR model, Johnston's model and experimental data. From Ref. [26].

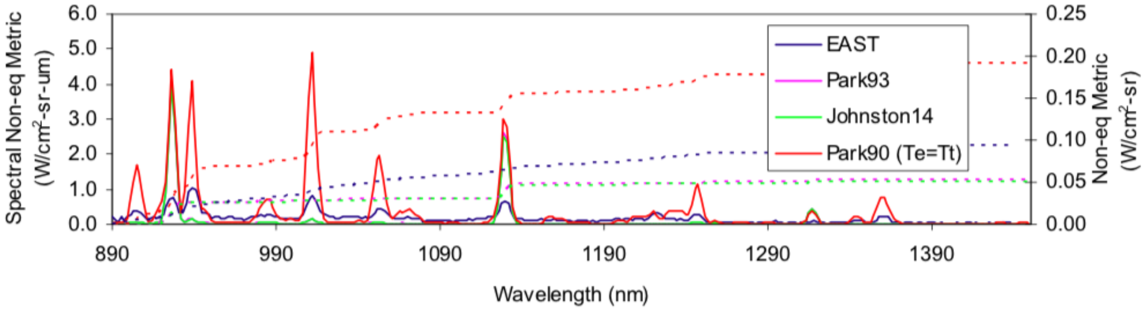

Figure 2.24: Simulation of the NIR and IR portion of the spectrum by the original NEQAIR model, improved NEQAIR model, Johnston's model and experimental data. From Ref. [26].

With the capabilities of the modern nonequilibrium solvers discussed, next, the RTE solution methods and spectral approximation techniques presented in the previous Section will be evaluated from the hypersonic modelling standpoint and compared to accurate calculations. This will allow for a selection of the most appropriate one for the thesis work.

2.3.3. Modern Techniques of Hypersonic Radiation Modelling

In addition to more accurately determining the population states and thus the actual absorption and emission spectra, the modern attempts in radiation modelling have also focused on solving the RTE effectively and accurately while minimising the computational efforts. This subsection thus briefly mentions the observed performance of various RTE solution methods for hypersonics as well as spectral approximation methods, which were already outlined in the previous Section.

Attempts of Alternative RTE Methods

For applications of any kind, PMC has been shown to produce the best accuracy if properly converged, for any gas conditions (multi-species gasses including very high temperature and concentration gradients), see e.g. Ref. [68]. It is also, however, the method which has the highest computational cost. This section will compare other RTE integration possibilities and uses PMC results as benchmark.

One of the most straightforward 1D methods used to date for some approximate calculations is the TS method. It is simple and has a low computational cost. However, when it comes to its accuracy for three dimensional problems, its applicability is questionable and depends on the specific case. For 3D flows, a type of a zonal method was developed by Wright and Bose in 2000 (see Ref. [15]). Even though it was shown to be superior to TS for optically thin cases, its computational cost increased drastically for thick problems with convergence being sometimes impossible. This method was adjusted by Andrienko et al. in 2016 in Ref. [7], who investigated the radiation around the RAM-C II reentry probe. Errors of up to 7% were found, and the results (denoted by VF), compared to the TS method and the accurate Monte Carlo results (here denoted as RTM - ray tracing Monte Carlo) are shown in Figure 2.25. The trajectory point shown in Figure 2.25 is at 61km, 7.5km/s. Since this was the case for 1D media, much higher errors are expected for a full 3D flowfield.

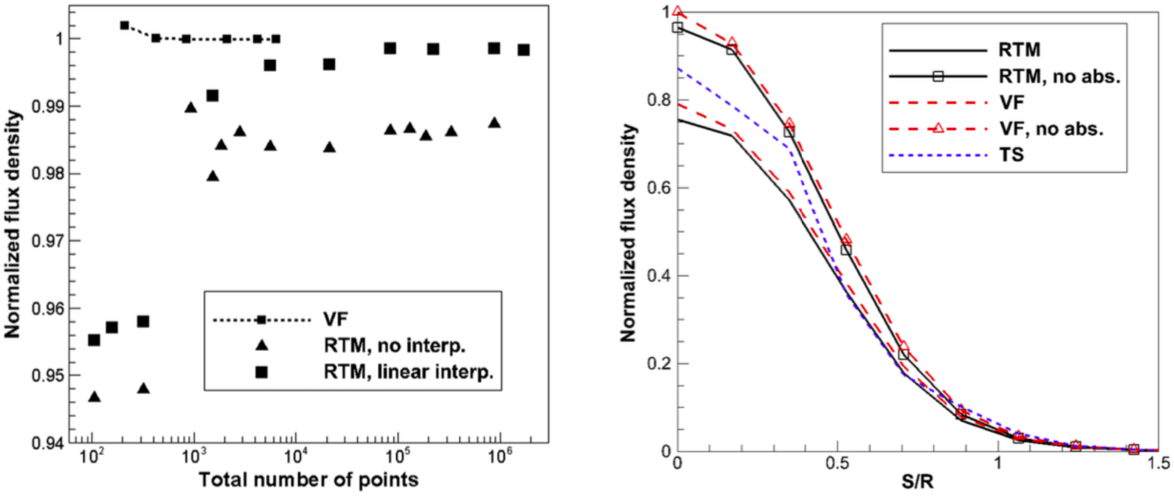

Figure 2.25: The match between the zonal, view-factor based method (VF) and tangent slab (TS) method compared to assumed accurate solution by a ray tracing MC method (RTM), showing in general a very good agreement with better convergence for VR when computing the flux density of the RAM-C II probe reentry, at 61km and 7.5km/s, by Andrienko et al. from [7].

The SHM for hypersonic flows was put to the test in 2012 by Bansal, Feldvick and Modest, who made the radiation calculation possible with OpenFOAM in Ref. [12]. As discussed in the previous Section, various degrees of SHM are possible, and the approaches tested here were the P_1 and SP_3 models coupled with a emission-weighted FSCK method. The "S" in SP_3 refers to the third order SHM being simplified, since the original version was too complex to solve with OpenFoam. The errors of SHM were evaluated in 1D, where the TS method was used, which is exact in 1D. The results are shown in Figure 2.26. The spectral modelling technique (FSCK) proved to be accurate enough to replace the LBL spectra, but the SHM showed to yield relatively large errors at the nonequilibrium region of more than 20%. The simulated conditions were Mars entry at 6.5km/s at 10Pa, 140K and 3.7E-4kg/m^3.

The same conclusions about SHM were reached by Andrienko and coworkers in 2013 (see Ref. [5]), who implemented P_1 approximation, also for Mars entry at 3.842km/s, the density of 1.186E-3kg/m^3 and pressure of 35.28Pa. The fit with PMC was very good for optically thick problems, but errors of more than 30% were observed otherwise, again mostly at the shock.

Photon/ Ray-Tracing Monte Carlo Applications

Since the other techniques were demonstrated to often result in significant errors at the radiatively most active parts of the flow, PMC remained the standard. For that reason, the effort of many researchers has shifted towards making PMC more computationally affordable and more easily coupled with CFD.

For example, in 2012, Feldick and Modest implemented a PMC method for hypersonic flows and coupled it with CFD in Ref. [31]. They noticed that due to the stochastic nature of PMC, the solution returned to CFD

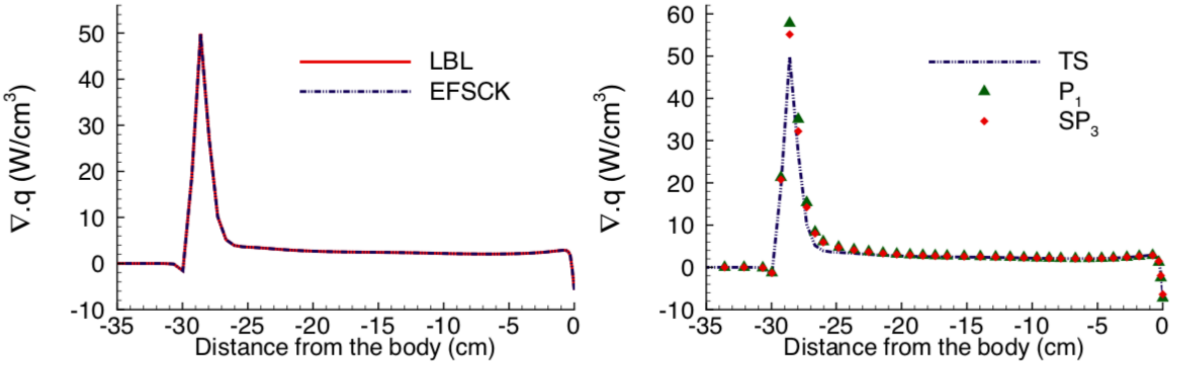

Figure 2.26: Comparison between the LBL and FSCK approaches (left), and between the exact tangent slab (TS) method and SHM approximations (right) for Mars CEV entry. From Ref. [12].

(the source term) is slightly different each time, creating convergence challenges if radiation and CFD were tightly coupled. Therefore, instead of the actual solution, they used $\nabla \cdot q_r = \alpha \nabla \cdot q_{\text{new}} + (1-\alpha)\nabla \cdot q_{\text{old}}$, where α is a relatively small number. They observed that while this method improved convergence in quasi-steady time marching simulations, it led to convergence issues in steady flows. Thus, this approach will not be used in this thesis work.

In addition, they also attempted to couple TS with PMC. The solution by PMC would be only obtained every tens to hundreds of iterations, and otherwise, the TS method would provide an approximate estimate. The stagnation region and shoulder region energy source term along the LOS are shown in Figure 2.27. Figure 2.27 demonstrates that TS is somewhat insufficient in the shoulder region, but it still proved to be a good approximation, especially when the Goulard number (flow/ radiation coupling) is small ($\Gamma = 0.02$ in this case). When evaluating the total heat flux, errors of 10% were observed for TS, but the divergence of this heat flux was still predicted sufficiently well.

Similar hopeful findings about TS were made by Ozawa et al. in 2010 (see Ref. [76]). They, however, emphasised that the most likely reason for these promising observations was the fact that only the stagnation region was evaluated, not the other parts of the flow. The stagnation region between the nose and the shock is the closest that the hypersonic flow gets to 1D, and thus the observed errors when using a 1D technique would be the smallest. Johnston and Mazahari also attempted a similar method by combining PMC and TS in Ref. [48]. They also note that while this approach works well for the stagnation line, the error would be much greater for curved and convex surfaces or grids, and it is not appropriate for general purpose simulations for which the use of TS is not validated.

Acceleration techniques for MC have also been in development. For example, in 2014, Shang and coworkers partially optimised a PMC code using a space partitioning algorithm for nearest neighbour search and a Gauss–Lobatto polynomial refinement technique while ray-tracing in Ref. [6]. Shang et al. reported order of magnitude increase in computational speed, with 44x faster computation for dense grids and 20x faster computation for sparse grids. However, since in this thesis Cartesian grids will be used only, this technique is not necessary.

Use of parallel programming was also made by Santos and Lani in 2016 discussed in their paper on the radiation solver of the COOLFluid package in Ref. [93]. Instead of NEQAIR, they used the PARADE 3.1 library from the von Karman Institute. Mesh decomposition was made to make parallelisation the most efficient, reaching the parallel efficiency close to its ideal limit. Use of the massage passing interface (MPI) parallel programming is also intended for this thesis work.

The technique of PMC combined with the opacity binning approach (see Ref. [114] and [115]) has been also implemented in DLR's TAU code, as discussed by Karl et al. in Ref. [51]. Example results of TAU for Viking afterbody are shown in Ref. [50]. Karl et al. used their own ray tracing module already implemented in TAU to ray trace photons in their MC implementation, significantly reducing the development time. Finally, parallelisation for the purposes of accelerating PMC has been widely studied by Silvestri and Pecnik in Ref. [97]. However, since their application regarded equilibrium flows, their work will be discussed in the next Section. Before proceeding to the next section, however, a short discussion will be made regarding the spectral processing techniques for hypersonic applications.

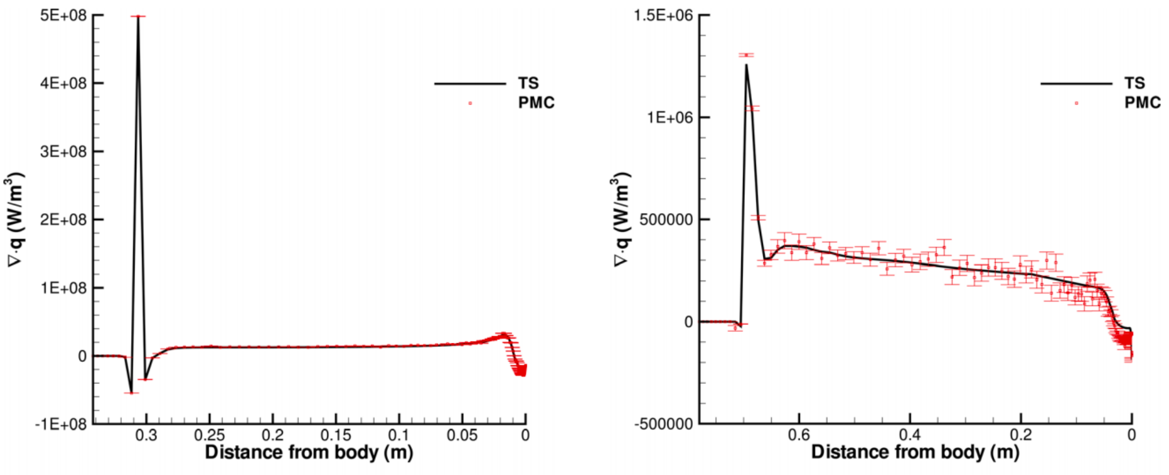

(a)

(a)

Figure 2.27: Results for stagnation point (a) and shoulder region (b) heat flux divergence at the maximum heat flux trajectory point of Orion CEV when using tangent slab (TS) and photon MC (PMC) approaches, with PMC already verified. It is observed that TS method can result in fair errors in shoulder regions (note that the scale is logarithmic). From Ref. [31].

Development of Spectral Approximation Techniques for Nonequilibrium

Besides the application of alternative RTE techniques, a considerable speedup could be achieved by spectral approximation methods simplifying the LBL data.

In 2002, Zhang and Modest demonstrated the capability of the extended FSCK for highly nonhomogeneous media in equilibrium, dominated by atomic radiation in Ref. [120]. For this purpose, the multi-scale full spectrum, MSFSCK approach was developed (splitting the lines according to their temperature dependence), where one scale was considerably more intense at low temperatures than the other one. Already considering 2 scales provided almost LBL accuracy. Without the use of the multi-scale formulation, however, the errors exceeded 20%.

A similar approach, MG/MS FSCK, was in 2009 developed for nonequilibrium media by Bansal and coworkers in Ref. [10] to model the emission by N and O species in hypersonic flows using data from NEQAIR. Four groups in total were established. To illustrate this principle, the behaviour of these separate groups for N and O with increasing electron temperature is shown in Figure 2.28. Group 1 is in red, group 2 in blue, group 3 in green and group 4 (only present for O) in dark green. Despite the definition of so many groups, near the shock, errors of over 20% were still observed (even though this was lowered from 40% when ordinary FSCK was used). An extension for molecular radiation, with 2 additional scales was provided in Ref. [11]. For molecular radiation, the predictions of the 2-scale model were highly accurate, with errors below 3%.

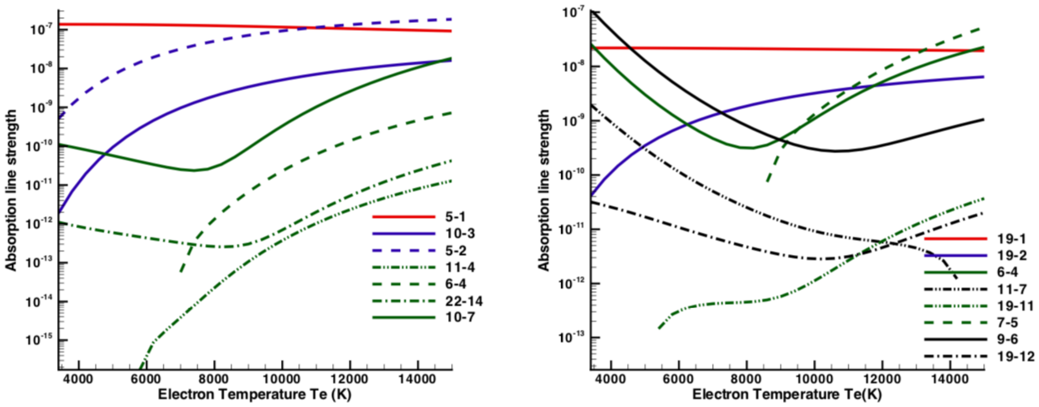

Figure 2.28: Behaviour of line strength of the strongest atomic N (left) and O (right) lines as a function of temperature, showing different trends according to which the lines could be grouped into scales by Bansal et al. from Ref. [10].

To accelerate the spectral generation for hypersonic flows in nonequilibrium, in 2010, Sohn and coworkers developed a databasing scheme in Ref. [101]. In this approach, they split some of the parameters for atomic and molecular radiation which remained constant for any temperature or pressure. For example, for b-b radiation, the "specific" absorption coefficient (normalised by atom number density) was separated into:

$$\kappa_\lambda^* = \frac{\kappa_\lambda}{N_a} = \kappa_\lambda^c \left(\frac{N_L}{N_a} - \frac{N_U}{N_a} \right) \phi_\lambda \tag{2.79}$$

in which κ_λ^c could be databased as it is an independent parameter. The number densities of the upper and lower states were then separately computed from a numerically much more simplified QSS formulation:

$$\frac{N_i}{N_a} = F_i \left(T_e, N_e \right) \frac{N_+}{N_a} + G_i \left(T_e, N_e \right), \tag{2.80}$$

where $F_i \left(T_e, N_e \right)$ and $G_i \left(T_e, N_e \right)$ contained all the effects of radiative transitions and could be databased for various electron temperatures and electron number densities a priori. This technique proved to be more challenging for molecular radiation due to the fact that rotational and vibrational states must also be taken into account. Thus, the QSS had to be properly computed on the fly, meaning that, while for atomic radiation a speedup of 23x was measured, this was only 3.5x for diatomic species.

Other approaches next to FSCK extensions also continued to develop. As already touched upon, occasionally, use was made of the so-called Smeared Rotational Band model, SRB, which was also used in the LORAN code (see Ref. [22]). While it can perform admirably for Earth entries, for optically thick atmospheres such as Titan, SRB was found to result in errors of 40% in the heat flux.

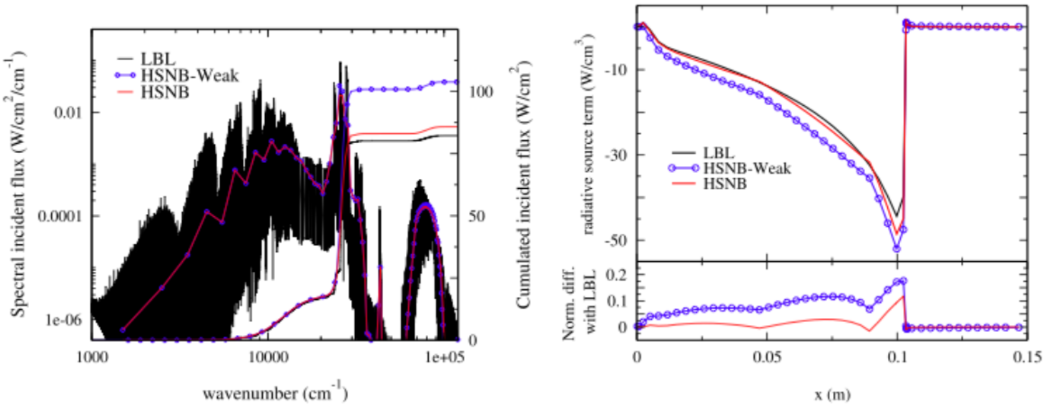

Figure 2.29: Comparison between the LBL approach, the HSBN model developed by Soucasse et al. and the SRB model from LORAN for the spectral incident flux (left) and divergence of heat flux (right) of the Huygens probe entry to Titan. From Ref. [102].

An extension to the SNB model, the Hybrid Statistical Narrow Band (HSBN) was provided by Soucasse and coworkers in 2016 (in Ref. [102]), in which they combined the SNB for optically thick molecular systems, the box model for optically thin systems and the LBL spectra for atomic lines. The errors, compared to purely LBL spectra, were generally within 5%, with the computational requirements dropping by two orders. An example comparison between the SRB (denoted by HSNB-Weak) and the HSBN developed by Soucasse et al. for Titan entry is shown in Figure 2.29. Errors of roughly 10% are, however, still observable even for HSBN in some places.

The opacity binning approach was extended to nonequilibrium flows in Ref. [49] by Johnston and coworkers in 2018, resulting in multiband opacity-binning (MBOB). The "multiband" attribute refers to the fact that the bins are separately defined for each spectral band. A comparison between the performance of a classical SRB and MBOB for Mars entry (7km/s and 2E-4kg/m^3) is shown in Figure 2.30 for wall-directed heat flux and Figure 2.31 for the divergence of the heat flux.

This approach was further modified by Sahai et al. in 2020 (see Ref. [91]), who suggested a different grouping strategy for the bins by considering the local Planck function. The paper of Sahai et al. also serves as a very good overview and categorisation of the modern methods, and their respective errors.

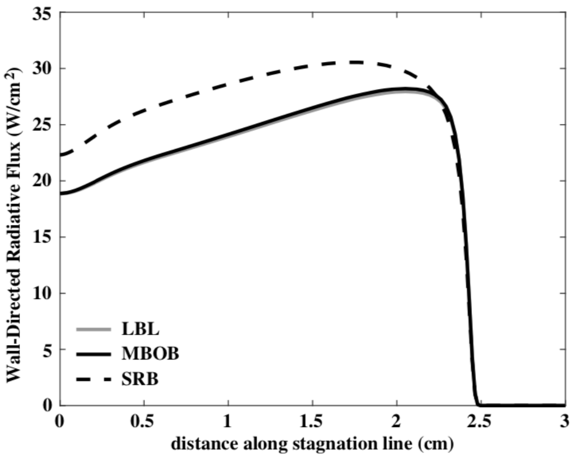

Figure 2.30: Wall directed heat flux for Martian entry from the CO 4-th positive band computed with LBL, SRB and MBOB models by Johnston et al. in Ref [49].

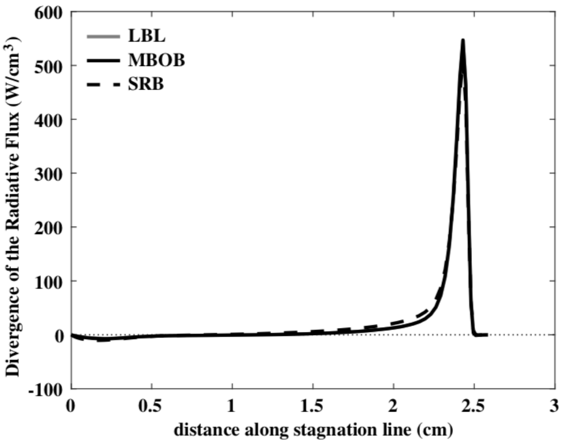

Figure 2.31: Divergence of heat flux for Martian entry from the CO 4-th positive band computed with LBL, SRB and MBOB models by Johnston et al. in Ref [49].

Shifts in Thermochemical Modelling towards State-to-State

Finally, while the errors of the extended spectral methods and RTE integration schemes were falling below 5%, the factor mostly contributing to the radiative heat flux error remained the actual resolution of the population states, and thus the accuracy of the LBL spectra, as could be seen from the recent paper by Brandis and Cruden (see Ref. [26]). Already from the times of the late 90's, it was becoming obvious that the QSS assumption might need replacement for some entry environments.

More sophisticated CR models thus entered development, in which the QSS assumption is either not made or at least more reactions are considered. For reference and details on the principle of operation, see for example the CR models described by Johnston in Ref. [47], Lemal in Ref. [58] and Pierrot et al. in Ref. [83]. While these models still include some approximations to be computationally feasible, they are the first steps in the transition to full so-called State-to-State (StS) modelling. In StS, for a collisional reaction for example, the reaction rates should not be simply approximated using controlling temperatures and parameters with the Aarhenius form (as it is done in NEQAIR), but all possible internal states of the two colliding species should be evaluated to yield the most probable result of the transition. Needless to say, this approach is extremely demanding when it comes to computational resources and not yet practical for real flow calculations. In addition, StS models also do not employ 2T or 4T models, since multi-temperature models, in principle, force separation of the internal states, which is too nonphysical for StS modelling. Thus, they are not properly compatible with the usual CFD solvers, which typically do operate based on 2T/ 4T or 5T internal state separation principle.

One such StS solver was developed in Urbana-Champaign, based on first principle modelling of quantum states, referred to as multigroup maximum entropy method, MGME (see for example Ref. [65]). While the principle behind this method is not relevant for this thesis, only to outline the differences with the conventional approach (referred to as "Park"), Figure 2.32 shows Nitrogen undergoing excitation and dissociation at 10kK. It is clear from Figure 2.32 that the QSS model is completely inaccurate in some environments compared to even the simplest (1 group) StS calculations. The MGME model was further improved in 2019 by Sahai et al. (see Ref. [90]) for some molecular species (tested for CO_2 in the paper cited). Errors of up to 30% were seen when compared to NEQAIR predictions.

While StS modelling is promising from the perspective of spectral accuracy, it is still impractical for daily use when calculating radiation. The take away lesson from this subsection should thus be to remain aware of the possible errors and inaccuracies in NEQAIR-like solvers, especially if used for design purposes, rather than suggest shifting towards StS before significant leaps in its computational efficiency are achieved.

2.4. Radiation in Combustion Systems

The second intended use for the thesis work is to study combustion systems, with focus on hydrogen combustion. Since in general, LTE can be assumed in such systems compared to hypersonic flows, the requirements on the RTE solution techniques or spectral modelling are much smaller and do not drive the method selec-

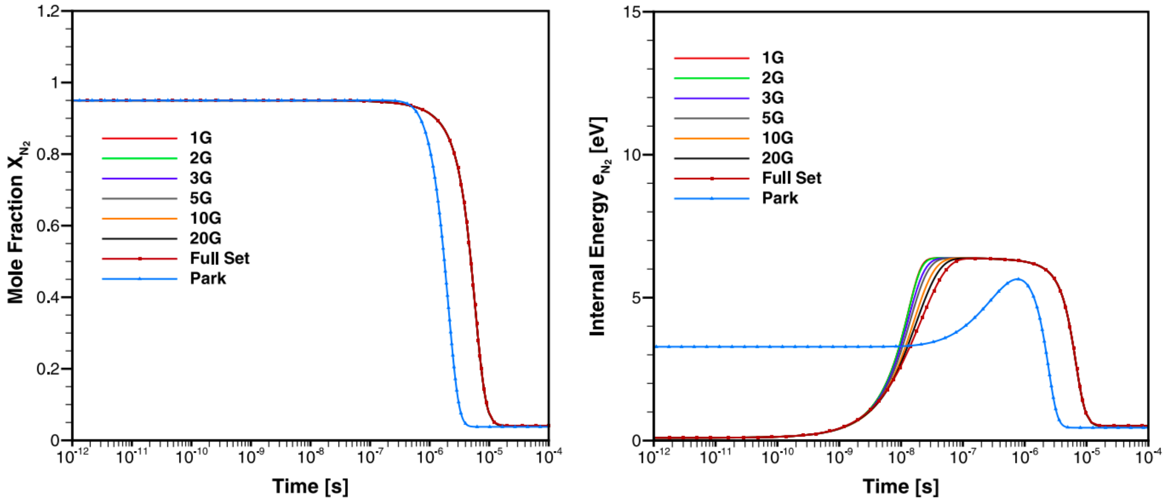

Figure 2.32: Mole fraction and internal energy development of Nitrogen undergoing internal excitation and dissociation at 10kK for various numbers of internal groups of the StS model and for the NEQAIR (Park) model. From Ref. [65].

tion process for this thesis work. For this reason, this section will be significantly shorter than the previous one as extensive critical discussion of methods is not required.

A wide variety of techniques has been investigated for combustion systems. For example, the P_1 SHM has been successfully implemented to model hydrogen combustion in Ref. [82] and Ref. [63]. The global WSGG model combined with DOM was applied in Ref. [118] by Yang and coworkers. For other gasses such as laminar air/ammonia flames, even the optically thin, OT, approximation can be used (see Ref. [71]). OT refers to the method in which the integrals in Equations (2.63) and (2.64) are evaluated only up to $\mathcal{O}(\tau)$ and terms of $\mathcal{O}(\tau^2)$... are neglected.

A comparison of some of these methods for hydrogen systems with high temperature and pressure gradients was carried out by Cai et al. in 2014 (see Ref. [17]). The results for the SHM methods (classical P_1 order and simplified SP_3 and SP_5) with full spectrum k-distribution and OT approximation are compared in Figure 2.33. Figure 2.33 shows that some errors of less than 5% are still present for nonstochastic methods, especially close to the combustor wall.

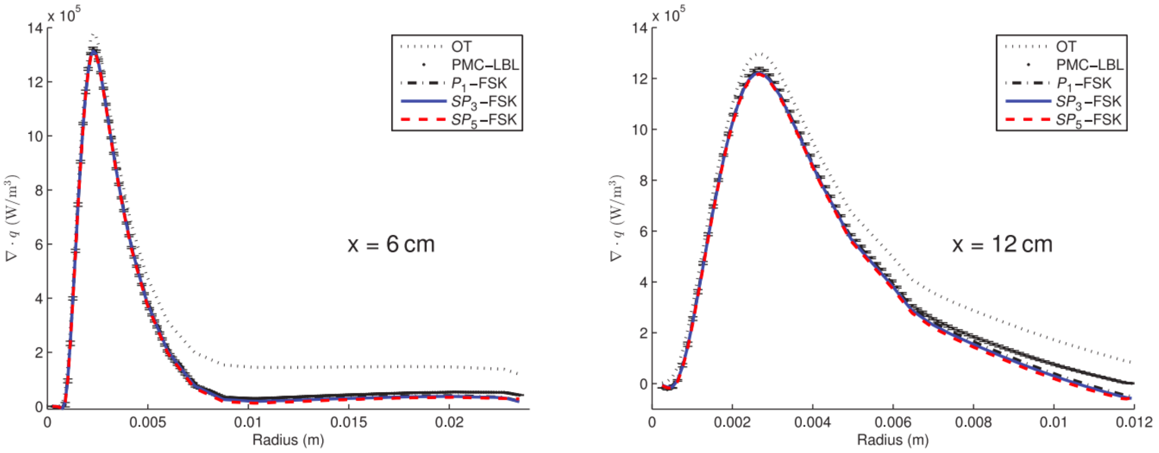

Figure 2.33: Accuracy comparison of various SHM approximations including P_1, SP_3 and SP_5 and the optically thin approximation (OT) compared to an accurate PMC LBL data in a hydrogen combustor shown at two x positions, 6cm (left) and 12cm (right).

Similarly to hypersonics, a lot of the research focus recently shifted towards acceleration techniques. A notable attempt to achieve faster PMC convergence was made in Ref. [28] by Farmer, who utilised low discrepancy sequences, LDS, (the Sobol sequence in particular) instead of ordinary random numbers for photon ray direction generation. This is sometimes referred to as Quasi PMC, QMC. This approach was then revisited by Farmer and Roy in Ref. [29]. They concluded, though, that more research is still needed to confirm the efficiency of this technique, depending on the optical properties of the intended application case. Use of the Sobol LDS and evaluation of its performance benefits will also be a subject of this thesis work. The principle of the Sobol sequence generation is outlined in Chapter 6.1.

A modification to QMC was offered by Paluotto et al. in 2019 in Ref. [56], where they randomised the applied LDS, resulting in what they refer to as Randomized-QMC, RQMC. In the applications they investigated, they managed to halve the time required for convergence, which implies that RQMC or QMC could be promising means of acceleration.

Parallelisation and Graphical Processing Units (GPU) implementation of PMC for combustion flows was performed and documented in Ref. [97] in 2019 by Silvestri and Pecnik. They discuss that parallelisation could be achieved either by ray or by domain parallelisation, and chose the latter for their own PCM implementation. This can be especially efficient for the emission reciprocity based MC formulation (ERMC) which they then also adjusted for the use of GPUs. The ERMC formulation will be discussed in Chapter 3 and Chapter 4 in more detail. In the results, Silvestri and Pecnik showed that GPU implementation can increase the speed by up to 50 times compared to CPU implementation.

They also outlined further techniques to accelerate the PMC solution. Since GPU was used, they showed that the use of texture memory (a type of a GPU memory) can significantly accelerate the computation. In addition, they also analysed the benefits of using multiple grid layers and wavelength sorting to equalise the thread load when ray tracing the photons.

GPU parallelisation has been also implemented by Bonin and Mundt in Ref. [14] in 2019 in their development of a 3D PMC code StaRad. While Pecnik and Silvestri used ERMC with a correlated-k model, Bonin and Mundt developed a forward MC with LBL accuracy.

It should be noted that while GPU parallelisation can definitely be very beneficial for the performance of the radiation solver, it can also cause net performance decrease if too much memory needs to be sent back and forth between CPU and GPU. Thus, if GPU parallelisation is implemented, it should be arranged in a way to minimise memory transfer. The recommended approach how this could be done for hypersonic flow in the presently developed solver is touched upon in Chapter 7.

2.5. Turbulence Radiation Interaction

Due to the fact that this thesis work concerns LES, it should be determined to what extent the unresolved turbulent scales affect the radiation results and vice versa, in order to estimate the error due to TRI for a given grid refinement or filter width. Strong interactions between the turbulent temperature fluctuations, species concentrations and the radiation field have been observed in turbulent participating flows, resulting in significantly enhanced radiative heat transfer (see for example Ref. [38] and Ref. [55]). If this phenomenon was to occur at the subgrid non-resolved scales, large errors could be introduced to the final solution regardless of properly converged MC with a close-to-exact spectral model.

TRI in itself is an extensive, dynamic research area and capturing it in its entirety would not be practical for this text. The focus of this Section is thus to discuss the basic description of TRI from both the perspectives of RANS and LES, analyse how TRI affects the fidelity of radiation modelling in the context of LES and, from the perspective of this thesis work, what requirements proper resolution of TRI in turbulent combustion system introduces.

Historically, TRI is a concept from Reynolds-Averaged Navier Stokes (RANS) modelling, where all turbulent scales are modelled. The Reynolds averaging can be performed on the emitted energy to give:

$$Q_{\text{emi}} = 4\pi \int_0^\infty \kappa_\eta I_{b\eta} d\eta = 4\pi \kappa_P \left(T, p_\alpha\right) I_b(T) \xrightarrow{\langle Q \rangle} \langle Q_{\text{emi}} \rangle = 4\pi \langle \kappa_P I_b \rangle = 4\pi \langle \kappa_P \rangle \langle I_b \rangle + \left\langle \kappa'_P I'_b \right\rangle, \tag{2.81}$$

which clearly shows that the correlation is composed of κ, I_b and κI_b, leading to the definition of the total emission TRI parameter:

$$\mathscr{R}_{\text{emi}} = \mathscr{R}_\kappa \mathscr{R}_{I_b} \mathscr{R}_{\kappa I_b}, \tag{2.82}$$

with

$$\mathscr{R}_\kappa = \kappa_P \left(\langle T \rangle, \left\langle p_\alpha \right\rangle\right) / \left\langle \kappa_P \left(T, p_\alpha\right)\right\rangle \qquad \mathscr{R}_{I_b} = I_b(\langle T \rangle) / \langle I_b(T) \rangle = \langle T \rangle^4 / \left\langle T^4 \right\rangle \qquad \mathscr{R}_{\kappa I_b} = (\langle \kappa_P \rangle \langle I_b \rangle) / \langle \kappa_P I_b \rangle . \tag{2.83}$$

Table 2.1: Emission and absorption correlation terms computed by Roger et al. for a turbulent jet far field at 20% temperature fluctuations. From Ref. [87].

Parameter	Filter	$\Delta = 2\delta$	$\Delta = 4\delta$	$\Delta = 8\delta$	$\Delta = 16\delta$	$\Delta = 32\delta$
Emission term ratio, $\mathscr{R}_{\kappa_P I_b}$, %	Box	0.205	0.92	2.87	6.56	11.6
Emission term ratio, $\mathscr{R}_{\kappa_P I_b}$, %	Cut-off	9.00E-05	0.108	1.25	4.32	8.82
Absorption term ratio, $\mathscr{R}_{\kappa_G I}$, %	Box	0.00564	0.0276	0.101	0.377	1.03
Absorption term ratio, $\mathscr{R}_{\kappa_{G},I}$, %	Cut-off	9.00E-05	9.00E-05	0.00382	0.0781	0.53

For the illustration of typical magnitudes of these correlations in methane flames in RANS, refer to for example the work of Coelho from 2013 in Ref. [24].

In the concept of LES, these correlations can also be treated and categorised in a fashion similar to subgrid stresses. Following the approach by Roger et al. in 2009 (see Ref. [87]), the LES filtered RTE without scattering (see Equation (1.3)), assuming LTE yields:

$$\frac{d\bar{I}_\eta}{ds} = -\overline{\kappa_\eta I_\eta} + \overline{\kappa_\eta I_{b\eta}} = -\bar{\kappa}_\eta \bar{I}_\eta - \left(\overline{\kappa_\eta I_\eta} - \bar{\kappa}_\eta \bar{I}_\eta\right) + \bar{\kappa}_\eta \bar{I}_{b\eta} + \left(\overline{\kappa_\eta I_{bv}} - \bar{\kappa}_\eta \bar{I}_{b\eta}\right), \tag{2.84}$$

in which the filtered variables are denoted by an overbar. The Planck mean absorption coefficient κ_P and incident mean absorption coefficient κ_G, for isotropic radiation ($G_v \rightarrow 4\pi I_v$) can be assumed to be given by:

$$\kappa_P = \frac{\int_0^{+\infty} \kappa_\eta I_{b\eta} d\eta}{\int_0^{+\infty} I_{b\eta} d\eta} \qquad \kappa_G = \frac{\int_0^{+\infty} \kappa_\eta G_\eta d\eta}{\int_0^{+\infty} G_\eta d\eta} \approx \frac{\int_0^{+\infty} \kappa_\eta I_\eta d\eta}{\int_0^{+\infty} I_\eta d\eta}, \tag{2.85}$$

and splitting the κ_G, κ_P, I_b and I into the resolved and unresolved components:

$$\kappa_G = \overline{\kappa}_G + \kappa''_G \qquad \kappa_P = \overline{\kappa}_P + \kappa''_P \qquad I_b = \overline{I}_b + I''_b \qquad I = \overline{I} + I'', \tag{2.86}$$

gives:

$$\frac{d\bar{l}}{ds} = -\overline{\overline{\kappa}_{\mathrm{G}} \bar{l}} - (\overline{\kappa''_{\mathrm{G}} \bar{\mathrm{I}}} + \overline{\overline{\kappa}_G l''} + \overline{\kappa''_{\mathrm{G}} l''}) + \overline{\kappa}_P \overline{I}_b + (\overline{\kappa''_P \overline{I}_b} + \overline{\overline{\kappa}_P I''_b} + \overline{\kappa''_P I''_b}). \tag{2.87}$$

Analogously to turbulent stresses in LES nomenclature, the terms $\overline{\kappa''_{\mathrm{G}} l''}$ and $\overline{\kappa''_P I''_b}$ are denoted as SGS Reynolds absorption and emission terms, respectively, while the other partially unresolved components, $\overline{\kappa''_{\mathrm{G}} \bar{\mathrm{I}}}, \overline{\overline{\kappa}_G l''}, \overline{\kappa''_P \overline{I}_b}$ and $\overline{\overline{\kappa}_P I''_b}$ are referred to as cross SGS absorption and cross SGS emission terms. These definitions will be used throughout the rest of this section.

2.5.1. TRI in Combustion Systems

One of the first mentions of significant TRI was made by Gore, Jeng and Faeth in the 80's in Ref. [38] and Ref. [55]. In hydrogen-air combustion modelling with temperature gradients between 400K to 2000K, they observed up to 110% increase in spectral radiation intensity due to TRI. In 1999, Mazumder and Modest arrived to the conclusion that for TRI to be of a significance, the concentration and temperature fluctuations must be correlated, see Ref. [66]. This was investigated within RANS simulations, but similar findings were obtained by Gupta and coworkers in 2009 in Ref. [42] for LES. They also added that absorption TRI seemed to be non-negligible only for high optical thickness media, while the emission TRI was significant at all optical thicknesses.

The Leonard, Cross and Reynolds emissions and absorption terms were in detail investigated by Roger et al. in Ref. [87] in a statistically stationary forced isotropic velocity field using DNS. This was supposed to be representative of a turbulent jet farfield with 10%, 20% and 30% temperature turbulent intensities $\sqrt{\langle T'^2 \rangle}/\langle T \rangle$, with temperatures varying between 300K and 2500K and with an average temperature of 1500K.

For illustration of typical magnitude of these values, the resulting values of these emission and absorption terms for a box and a cut-off filter utilising various filter widths (Δ compared to the DNS grid size, δ) is shown in Tables 2.1, 2.2 and 2.3 for 20% temperature turbulent intensity.

How the ratio of the SGS emission and absorption terms to the total emission and absorption depends on both the temperature level and mesh size is shown in Figures 2.34 and 2.35, respectively, where crosses show 30%, circles 20% and squares 10% temperature turbulence level. From the results of Roger and coworkers, it

Table 2.2: Emission TRI terms in a turbulent jet far field computed by Roger et al. for 20% temperature fluctuations after application of a box filter. From Ref. [87].

Parameter	$\Delta = 2\delta$	$\Delta = 4\delta$	$\Delta = 8\delta$	$\Delta = 16\delta$	$\Delta = 32\delta$
Leonard emission, $\langle\overline{\overline{\kappa}_P \overline{I}_b}\rangle / \langle\overline{\kappa_P I_b}\rangle$	1.00206	1.00929	1.0296	1.0702	1.131
Cross emission, $\left\langle\overline{\kappa''_P \overline{I}_b}\right\rangle / \langle\overline{\kappa_P I_b}\rangle$	-1.4e-5	-0.00342	-0.0111	-0.0209	-0.0290
Cross emission, $\left\langle\overline{\overline{\kappa}_P I''_b}\right\rangle / \langle\overline{\kappa_P I_b}\rangle$	-2.04e-5	-0.00344	-0.0111	-0.0209	-0.0291
Reynolds SGS emission, $\left\langle\overline{\kappa''_P I''_b}\right\rangle / \langle\overline{\kappa_P I_b}\rangle$	-0.00202	-0.00243	-0.00733	-0.0284	-0.0734

Table 2.3: Absorption TRI terms in a turbulent jet far field computed by Roger et al. for 20% temperature fluctuations after application of a box filter. From Ref. [87].

Parameter	$\Delta = 2\delta$	$\Delta = 4\delta$	$\Delta = 8\delta$	$\Delta = 16\delta$	$\Delta = 32\delta$
Leonard absorption, $\langle\overline{\overline{\kappa}_G \overline{I}}\rangle / \langle\overline{\kappa_G I}\rangle$	1.0000564	1.000276	1.00110	1.00379	1.0104
Cross absorption, $\left\langle\overline{\kappa''_G \overline{I}}\right\rangle / \langle\overline{\kappa_G I}\rangle$	-2.51e-4	-3.53e-4	-7.26e-4	-0.00179	-0.00367
Cross absorption, $\left\langle\overline{\overline{\kappa}_G I''}\right\rangle / \langle\overline{\kappa_G I}\rangle$	-2.46e-4	-1.31e-4	-2.78e-4	-0.00143	-0.00345
Reynolds SGS absorption, $\left\langle\overline{\kappa''_G I''}\right\rangle / \langle\overline{\kappa_G I}\rangle$	-5.14e-5	-5.42e-5	-9.85e-5	-5.7e-5	-0.00327

can be concluded that in order to avoid errors larger that 2-5% in the simulations, the expected magnitude of temperature fluctuations should be known a priori to select a proper filter width. For example, for the average 20% fluctuations, to keep the errors in TRI computation below 10%, the mesh size should be lower than 32δ for this particular low Re flow. Figures 2.34 and 2.35 are presented in this overview, since they give a good indication of the errors that can be expected if radiation is not computed with sufficient coupling and with a sufficiently small filter width.

Follow-up studies on TRI were performed by, for example, Ghosh et al. in Ref. [88] in supersonic turbulent channels, by Vicquelin et al. in 2014 in Ref. [110] in channels with varying optical thicknesses and again by Gosh at coworkers in 2015 in Ref. [36] for inert and reacting mixing layers.

Finally, research on TRI has also been conducted at Delft University of Technology by Silvestri and Pecnik in the department for Process and Energy Engineering. In Ref. [98], they coupled DNS with PMC and modelled channel flow for optical thicknesses ranging from 0.1 to 10. They showed that while it is true that the majority of the TRI contribution at low optical thicknesses comes from the emission term, this changes as the medium is able to absorb more energy. The results of the absorption, emission and total terms $\mathscr{R}_e$, $\mathscr{R}_a$ $\mathscr{R} = \mathscr{R}_e + \mathscr{R}_a$ are shown in Figure 2.36.

They also showed that with increasing optical thickness, as the TRI grows, the effect of radiation on the statistics of temperature virtually replaces the role of the viscous terms and acts to dissipate and redistribute

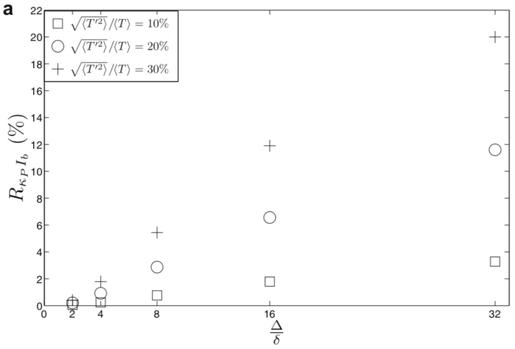

Figure 2.34: Emission correlation due to TRI as a function of LES filter width Δ ratio to DNS grid size δ for 10%, 20% and 30% temperature fluctuations in a turbulent jet far field. From Ref. [87].

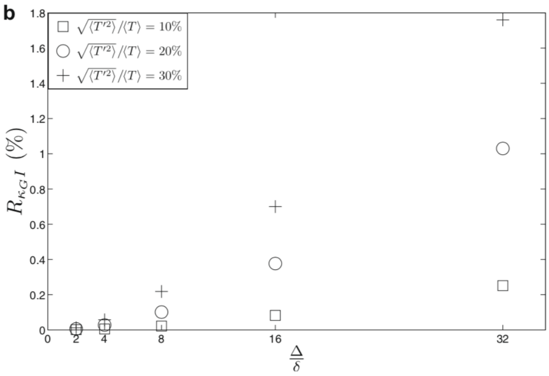

Figure 2.35: Absorption correlation due to TRI as a function of LES filter width Δ ratio to DNS grid size δ for 10%, 20% and 30% temperature fluctuations in a turbulent jet far field. From Ref. [87].

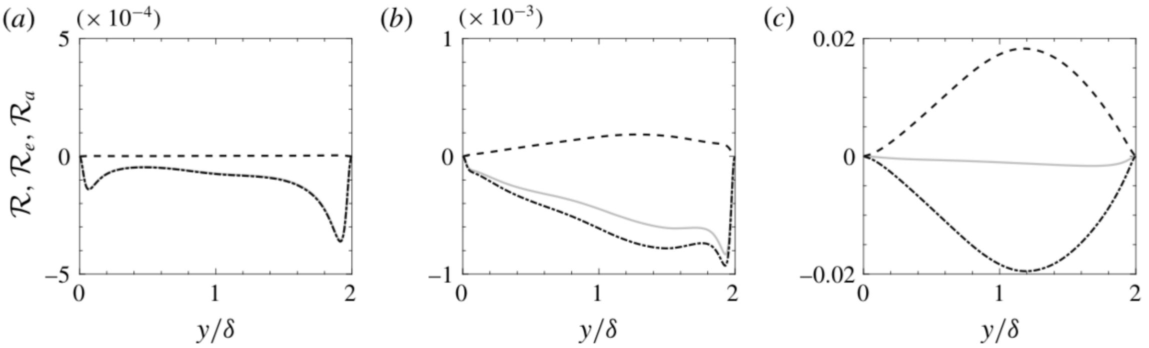

Figure 2.36: The magnitude of the emission (dash-dotted), absorption (dashed) and total TRI terms for optical thicknesses of 0.1 (a), 1 (b) and 10 (c) computed by Silvestri in Ref. [98]. It is obvious that absorption TRI term cannot be neglected for gasses which are not optically thin.

the temperature variance. This causes a redistribution of temperature fluctuations over most of the temperature scales.

The research was then extended to non-grey, participating media in Ref. [99]. They showed the TRI in non-reacting flows can be accounted for by the variation of the mean absorption coefficient alone and that for non-grey gas cases, it is the variability of the absorption spectra in the media that heavily affects the interactions between the temperature and radiative field. They defined a spectrally averaged absorption coefficient to predict TRI for non-grey gases.

2.5.2. TRI in External Hypersonic Flows

Since it was found in combustion TRI research that the extent of TRI increases with temperature and concentration gradients, it was hypothesised that TRI would also be significant in hypersonic, reacting boundary layers, where both strong temperature and concentrations gradients are present. In addition, many regions of the hypersonic plasma are also optically thick. TRI was thus also studied in the context of hypersonic boundary layers by Feldick and coworkers in Ref. [32] in 2010. Since the inter-relationship between turbulence and radiation cannot be well captured with RANS modelling without properly DNS-validated adjustments to the turbulence models, LES (in NASA's DPLR) was used to study this interaction at the vehicle velocity of 9.5km/s at 53km Earth altitude. The LES was run only with a 1-temperature model, thus effectively assuming LTE (which should be, however, applicable for boundary layers). Top hat filter with 8 x 4 x 2 DNS width was used such that 20% of the turbulent kinetic energy remained in the SGS stress.

Feldick and coworkers computed intensity from average flow values $I_w(\langle T\rangle, \langle \underline{n}\rangle)$ and intensity based on the fluctuating flow field ($\langle I(T, \underline{n})\rangle$) and the standard deviation between these two, σ. They evaluated these at 11 different locations on the wall, and saw that the σ due to TRI was 3 orders of magnitude lower than the resolved intensities, indicating TRI to be almost completely insignificant.

The full results of this work were then presented in 2011 by Duan et al. in Ref. [27]. They hypothesised that the reason why TRI seemed not to be of significance for hypersonic boundary layers compared to combustion systems lies in the fact that it is mostly the atomic species N and O radiating instead of molecular species. To create these species from chemical reactions, very high temperatures and thus very high flow enthalpies are required, which then overshadows the heat loss due to TRI. This is supported by the fact that the TRI effects were visible in the profiles in the turbulent kinetic energy, but not the velocity, as shown in Figure 2.37.

Feldick and coworkers have, however, studied only one set of flight conditions, and thus multiple simulations should be performed to confirm this hypothesis to allow for extension of the conclusions to any hypersonic boundary layers. If it is indeed true that the effects of TRI overshadowing are present due to the very high flow enthalpy, TRI might be still relevant in hypersonic boundary layers at lower speeds. This might significantly complicate the simulations since to resolve TRI, fully coupled radiation simulations are required, which are very computationally demanding for hypersonic flows.

Since performing research on TRI in hypersonic boundary layers was not possible within the scope of this thesis, CFD cases where radiation heat flux was very small compared to convective heat flux were run only to avoid large effects on the flowfield. In the future, if cases are simulated with the developed thesis radiation solver, it is important to note that mesh refinement might give different results not necessarily only due to

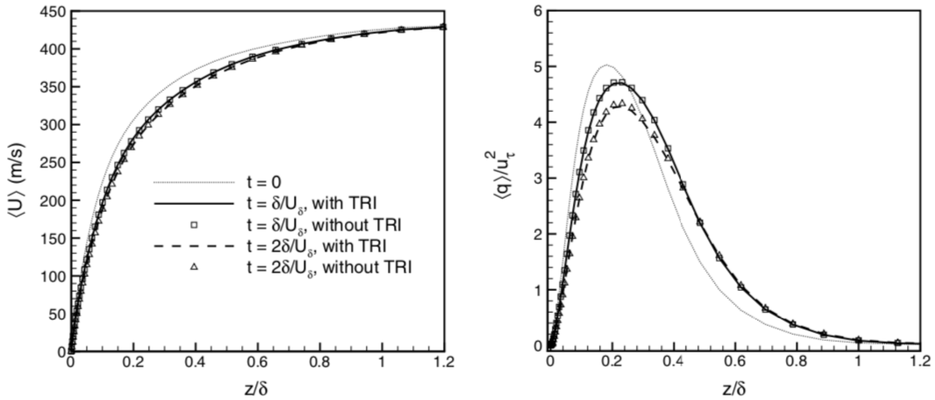

Figure 2.37: The TRI effects in hypersonic boundary layer on mean streamwise velocity (left) and turbulent kinetic energy (right) evolving in time t, considering 9.5km/s flight at 53km altitude with $M_\delta = 0.153$. From Ref. [27].

insufficient PMC or CFD convergence, but also due to the possible effects of TRI.

Having discussed the accuracy of various modelling techniques for hypersonic flow radiation and combustion radiation in the previous section and having shortly analysed additional requirements on the code due to the effect of TRI, decisions regarding the most appropriate modelling strategy can be formulated. The final methods chosen for this thesis work will thus be discussed in the following Chapter.

3

Methodology

In the previous Chapter, various radiation solution methods were presented, and their suitability was discussed for the applications of interest. This Chapter uses this information to justify the decisions made regarding the selection of the methods for this thesis work. Firstly, the combination of the solution methods chosen is presented, the theories and principles behind which are then described in further detail.

3.1. Method Selection

Firstly, the aim is to use the literature study findings in conjunction with the formulated thesis requirements to select the most appropriate techniques for the thesis work. The rationale behind the choices made is described below.

3.1.1. Radiative Transfer Equation Solver

As demonstrated in the previous Chapter, several techniques can be utilised to solve the RTE with relatively small errors for both external hypersonics (see e.g. Ref. [12]) as well as combustion systems (see Ref. [17]). If TRI is, however, to be possibly studied with the code in the future for which a very high accuracy and sensitivity is required to resolve the species and temperature gradients exactly, the Monte Carlo method is the only 3D universally reliable method available (as for example mentioned in Ref. [68]). It is also the only method the accuracy of which does not significantly depend on the nature of the problem (as, for example, the presence of multiple species or very high temperature gradients). The stochastic PMC was thus selected. Since the ERMC formulation has a potential of being efficiently accelerated using GPU as shown by Silvestri and Pecnik in Ref. [98], the ERMC formulation was also chosen for this thesis work. The ERMC formulation will be outlined in the next Section. Before proceeding there however, it should be discussed which method will be used to generate the spectra for the integration of the RTE.

3.1.2. Spectral Generation

Combustion gas spectra at LTE can be resolved using various databases with transition data. One of the largest databases existing to date is HITRAN (High-Resolution Transmission Molecular Absorption Database). HITRAN has now, for over half a century, been considered the international standard for spectroscopy, and the data in it is regularly checked, validated and updated. For higher temperature applications, its extension HITEMP can be also used. It is thus the obvious choice for problems in LTE.

For problems in which LTE cannot be assumed, a library capable of computing the QSS must be used instead. Examples of such libraries currently or historically used in research include:

- NEQAIR (NASA, restricted access)
- LORAN (NASA, not available, obsolete)
- RAD/EQUIL (NASA, not available, obsolete)
- PARADE (VKI, restricted access)
- SPARTAN (TU Lisbon, open access)

- SPECAIR (SPECAIR, for purchase)

The most suitable option to ensure open distribution of the final thesis code would be the use of SPARTAN which is open access. However, SPARTAN is not parallelised and is written in MATLAB, resulting in extremely long computational times, and is thus not suitable. SPARTAN was used once in the beginning of the thesis work for trial, and the generation of the spectrum took more than 30 minutes, which is unacceptable. From the other two options, NEQAIR and PARADE, NEQAIR was selected. Even though NEQAIR has still many limitations and inaccuracies in spectral solutions as seen in Chapter 2, since it is frequently used in research, the documentation on its performance is fairly abundant. Thus, the magnitude of the expected errors and conditions in which such erroneous results are typically obtained are relatively well known. In addition, NEQAIR is parallelised and written in Fortran, which means that it is most likely the fastest and most INCA-compatible library. Inclusion of the restricted-distribution NEQAIR code in the thesis work means that the entire thesis code cannot be open access and only its parts without NEQAIR subroutines can be distributed freely.

3.1.3. Further Spectral Processing

Finally, the last selection should be made regarding the technique in which the spectra are processed or approximated. Examples of such techniques mentioned in the previous Chapter include the narrow and wide band models (Elsasser, SNB, HSNB, EWB), MG/MF FSCK/FSSK, narrow band correlated/ scaled k-distributions, (multiple band) opacity binning, WSSG and others.

As shown in Chapter 2, each of these approaches can be very accurate for some applications. Elsasser, box or exponential models are a good approximation for relatively homogeneous, single species media without significant gradients and without any departure from LTE. The k-distributions are even more accurate, but their efficient formulation relies on simple expression for the Planck function, which is not possible for nonequilibrium simulations. In nonequilibrium conditions, the opacity binning approaches have been in frequent use, instead.

The optimum solution for this solver would be a combination of all these methods depending on the application and desired accuracy - opacity binning or MBOB for hypersonic flows, k-distribution for LTE problems when accuracy is of prime importance (TRI studies) and simple box or EWB models for other combustion problems. This is, however, impossible in the scope of this thesis work, since most of these models require different coupling to the RTE solver and also vast pre-databasing effort. One of the requirements on this solver is to be universally applicable to a wide variety of problems, which would not be satisfied if each reentry or combustion case required hours of pre-databasing.

As mentioned already, for methods such as SHM and DOM, LBL spectra demand that the RTE has to be integrated for each wavelength separately, making LBL spectral description very impractical. However, for MC simulations, since the selection of the wavenumbers/ wavelengths is stochastic, this is not required, significantly lowering the computational requirements when using LBL description. The LBL description is the most accurate method for both LTE and non-LTE problems as the spectra are represented exactly as computed from the transitions data and possibly QSS. Since its coupling to PMC means that its required computational effort and desired accuracy can be balanced by selecting a suitable number of photon rays at different wavelengths, it was this method which was chosen for further thesis work. It is, however, recommended that for future attempts to accelerate the code, the other avenues such as MBOB and k-distributions are also explored if pre-databasing is feasible.

3.2. RTE Integration with Photon Monte Carlo

Next, the principle of PMC will be outlined. For full derivation, refer to the book of Modest in Ref. [68]. Consider integral $\int_a^b f(x)dx$. The most straightforward way how this integral can be estimated numerically is by the quadrature:

$$\int_a^b f(x)dx \simeq \sum_{i=1}^{N} f\left[x_i = \left(i - \frac{1}{2}\right)\Delta x\right]\Delta x, \quad \Delta x = \frac{b-a}{N}, \tag{3.1}$$

where for large enough N, the result of Equation (3.1) converges to the true value of $\int_a^b f(x)dx$. The values of x_i are, in case of Equation (3.1), equally distributed between the integral bounds a and b. Thus, in a statistical sense, we would converge to the same result if N random locations were to be drawn and used instead if equally distributed between a and b. This is the principle of integral evaluation by photon Monte Carlo:

$$\int_a^b f(x)dx \simeq \sum_{i=1}^{N} f\left[x_i = a + (b-a)R_i\right]\Delta x, \Delta x = \frac{b-a}{N}, \tag{3.2}$$

where R_i is a random number. If $f(x)$ varies by orders of magnitude, however, which is oftentimes the case for e.g. absorption coefficients, Equation (3.2) would place equal emphasis on low importance regions as it would on the high importance ones, leading to large errors and slow convergence. Thus, for a stochastic integration, it is far more reasonable to evaluate x_i from a PDF:

$$\int_a^b f(x)dx = \int_a^b \frac{f(x)}{p(x)} p(x)dx = \int_0^1 \frac{f(x(\xi))}{p(x(\xi))} d\xi, \tag{3.3}$$

in which:

$$\xi(x) = \int_a^x p(x)dx, \quad \int_a^b p(x)dx \equiv 1. \tag{3.4}$$

If $f(x)/p(x)$ remains relatively constant across the interval a to b, then the integral can be stochastically evaluated as:

$$\int_a^b f(x)dx \simeq \frac{b-a}{N} \sum_{i=1}^{N} \frac{f(x_i)}{p(x_i)}, \quad x_i = \xi^{-1}(R_i), \tag{3.5}$$

and this method is used to solve the RTE in PMC. The radiative heat exchange between two volumes in a grey medium assuming LTE, where cell i is emitting and cell j is absorbing is given as (see Ref. [98]):

$$Q^R_{i\to j} = \int_0^\infty \kappa_\nu(T_i) I_{b\nu}(T_i) \int_{V_i} \int_{4\pi}^{N_c} \tau_\nu(i\to j, m) \left[\int_0^{l_{l,m}} \kappa_\nu(T_j) e^{-\kappa_\nu(T_j)s_{j,m}} ds_{j,m}\right] d\Omega dV_i d\nu, \tag{3.6}$$

which, for an isothermal cell j case, has a solution of:

$$\alpha_{\nu j,m} = 1 - e^{-\kappa_\nu(T_j)l_{j,m}}. \tag{3.7}$$

While clearly hypersonic plasma is not an isothermal grey domain, it can be split into a large number of isothermal cells and Equation (3.7) can be applied across each cell, and integration for various absorption coefficients $\kappa \neq \kappa_{\text{const.}}$ can be carried out by repeated realisation. The spectral transmissivity is the result of the absorption by the finite volumes and surfaces crossed by path m, and can be calculated as:

$$\tau_\nu(i\to j, m) = \prod_{k=i}^{j-1} \left(1 - \alpha_{\nu k,m}\right) \times \prod_{c=1}^{N_r} (1 - \varepsilon_w). \tag{3.8}$$

The complete PMC implementation and logic as employed in the code will be shown in the next Chapter, along with the necessary adjustments to Equation (3.6) to account for nonequilibrium.

Three different formulations of PMC were defined by Tesse, see also Tesse et al. [108]. Depending on how the optical transfer path between different cells is computed, he distinguished forward and reciprocal MC formulations:

- Forward Monte Carlo, FMC
- Emission Reciprocity Monte Carlo, ERMC
- Absorption Reciprocity Monte Carlo, ARMC

In FMC, the optical path, which is computed stochastically from a point A to a point B, is used only for the transport of radiation from point A to point B in one direction. The radiation flux coming from point B back to point A is completely independent of the flux from A to B. In reciprocal MC, on the other hand, the same optical path is used to compute the exchange from B back to A. ARMC then determines the emission of the cell from stochastic estimation of the absorbed heat flux or absorbed power, while ERMC estimates the absorption based on the emitted heat flux or emitted power. The illustration of the differences between these three methods is shown in Figure 3.1.

Tesse et al. [108] showed that the suitability of each of these formulations depends on the intended application. In general, ARMC results in lower errors in low temperature absorption-dominated zones, whereas

ERMC should be used in high temperature zones with significant emission. ERMC implementation is, however, easier to parallelise since only limited communication between cells is necessary while solving the domain. As the acceleration potential is one of the main focuses when developing the radiation solver in this thesis work, ERMC was chosen from these methods.

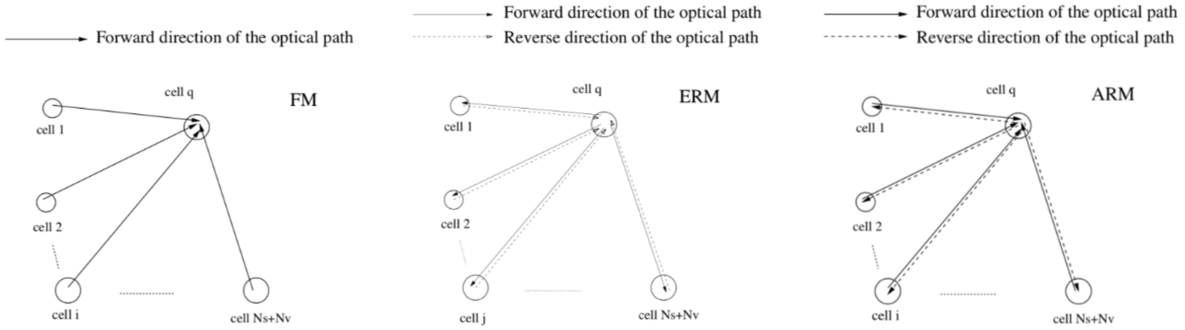
Forward direction of the optical path
FM
cell q
cell 1
cell 2
cell i
cell Ns+Nv
Forward direction of the optical path
Reverse direction of the optical path
ERM
cell q
cell 1
cell 2
cell j
cell Ns+Nv
Forward direction of the optical path
Reverse direction of the optical path
ARM
cell q
cell 1
cell 2
cell i
cell Ns+Nv

Figure 3.1: The principle of operation of the forward MC, emission based reciprocal MC and absorption based reciprocal MC by Tesse et al. from Ref. [108]. Optical path shown.

According Ref. [108], ERMC can under-perform in cold, absorptive regions in transmissive problems (as will also be shown in Chapter 5). This is due to the fact that the original formulation had the wavelengths to be sampled from the local cell (the one from optical paths are being determined). However, from the perspective of physics, in highly transmissive media with very hot and cold regions, it is likely that the majority of the photons in the domain will originate from the hottest regions, meaning that sampling the wavelengths from the hottest regions in the domain is more physically sound. This approach was also adopted in the work of Silvestri et al. in Ref. [98] and Ref. [97], and can be employed by adding an additional factor in the radiative heat transfer equation, as will be shown in Chapter 4.

This correction is, however, not always necessary or desired. In problems with high optical thickness where the propagation of photons is very limited and thus radiation is more local, such as some cases of hypersonic plasma, this global wavelength sampling leads to wrong results. For some problems, a combination of the two approaches might be even required. This will be discussed in the Chapter 5.

3.3. Spectral Generation with HITRAN and NEQAIR

3.3.1. HITRAN / HITEMP

For LTE applications, databases such as HITRAN and HITEMP contain transition data for a large number species and their respective isotopologues (molecules with the same formula but with the atoms having different number of neutrons, so-called isotopic composition). The following data is provided by the HITRAN 2012 database for each transition:

- The molecular species identification (ID) number
- The isotopologue ID number
- The wavenumber of the spectral line transition in vacuum, ν_{ij}
- The spectral line intensity at $T_{\text{ref}} = 296\text{K}$, S_{ij}
- The Einstein-A coefficient of a transition, A_{ij}
- The air-broadened half width at half maximum at $p_{\text{ref}} = 1\text{atm}$ and T_{ref}, γ_{air}
- The self-broadened half width at half maximum at $p_{\text{ref}} = 1\text{atm}$ and T_{ref}, γ_{self}
- The lower-state energy of the transition, E''
- The coefficient of T dependence of the air-broadened half width, n_{air}
- The pressure shift at p_{ref} and T_{ref}, δ

Table 3.1: Available HITRAN species ID list.

1	H_2O	8	NO	15	HCl	22	N_2	29	COF_2	36	NO+	43	C_4H_2
2	CO_2	9	SO_2	16	HBr	23	HCN	30	SF_6	37	HOBr	44	HC_3N
3	O_3	10	NO_2	17	HI	24	CH_3Cl	31	H_2S	38	C_2H_4	45	H_2
4	N_2O	11	NH_3	18	ClO	25	H_2O_2	32	HCOOH	39	CH_3OH	46	CS
5	CO	12	HNO_3	19	OCS	26	C_2H_2	33	HO_2	40	CH_3Br	47	SO_3
6	CH_4	13	OH	20	H_2CO	27	C_2H_6	34	O	41	CH_3CN	48	C_2N_2
7	O_2	14	HF	21	HOCl	28	PH_3	35	$ClONO_2$	42	CF_4	49	$COCl_2$

- The lower and upper state statistical weights g' and g''

The species for which HITRAN databases exist and their official identification numbers in HITRAN data are presented in Table 3.1.

The parameters ν, S, γ and δ as shown in Figure 4.4 for a line measured and databased in vacuum (dotted) and actual line that is computed in air (solid). The meaning of the Einstein coefficient, upper and lower statistical weights and line intensity from the theoretical standpoint was given in Chapter 2. Additional transition data for more detailed calculations, such as the upper and lower vibrational number, are also available but not required for a simple spectral generation.

The transition wavenumber, line width and spectral line intensity depend on pressure and temperature. In HITRAN, all these parameters are given at reference conditions (reference pressure and temperature of 296K and 1 atmosphere). Therefore, these parameters must be converted to local environment. The procedure in which this is done and how the resulting data is converted into absorption spectra in the code, along with the underlying assumptions and approximations, will be elaborated on in Chapter 4.

While a standard HITRAN library HAPI exists and is available as open source, as will be shown in Chapter 4, it is also relatively slow. Since the goal of this thesis is to design a code which will be practical for real simulations coupled with CFD, a much faster implementation was formulated instead.

3.3.2. NEQAIR

Since the internal states of molecules and atoms are not known apriori in nonequilibrium, providing a dataset from which the absorption and emission spectrum could be determined in the same way as shown above is impossible. Below, a short description will be given how nonequilibrium codes, such as NEQAIR, compute the state populations and how this translates to generation of emission and absorption spectra.

The theory behind "proper" CR modelling is very exhaustive and impractical to describe in detail. However, at least a brief outline should be provided to understand the logic behind NEQAIR's QSS and limitations when modelling the collisional and radiative transitions. Not all processes defined below are actually simulated in NEQAIR, but their discussion is presented to show where NEQAIR still lacks in its physical formulation. Specifically the processes from NEQAIRv15 will be discussed (see release notes for v15 in Ref. [16]). Note that this text will not focus on StS modelling, only a more detailed CR modelling still considering separation of internal states with multi-T models.

The theory below presented, apart from the book of Park (see Ref. [81]) come from two CR models. The first one was developed by Lemal in his dissertation from 2013, discussed in Ref. [58]. The second CR model was introduced by Pierrot et al. in Refs. [83], [84] and [119], focused on modelling of nonequilibrium Nitrogen plasma.

All nonequilibrium codes are based on solving for the state population number densities for each species using a so-called Master Equation. The transition between these states then serves as input to radiation calculation. To express the population number density changes in time as a result of thermochemical processes, the following major processes are typically simulated and accounted for:

- Electron-impact (de-)excitation

- Electron-impact ionisation (recombination)

- Heavy-particle-impact (de-)excitation

- Electron-impact dissociation (recombination)

- Heavy-particle-impact dissociation (recombination)
- V-T-e energy exchange processes
- Predissociation
- Radiative processes

The frequency of these processes is defined by its respective rate coefficient. The determination of the rate coefficients is the most complex part of the calculation, where semi-empirical and empirical models are used when quantum mechanical approximations are either nonexistent or too simplistic. Adjustments to these rate coefficients are then the main means by which improvements of the match with the experimental data is reached.

Typically, for simple cases of collisional rate constants between two species states A and B characterised by Maxwellian translational energy distribution functions at an effective kinetic temperature, which can be defined as $\theta_{AB} = (m_A T_A + m_B))\, T_B / (m_A + m_B)$ and (collisional) kinetic energy ε, it is assumed that the collisional rate coefficient can be directly integrated as:

$$K(\theta_{AB}) = \frac{8\pi}{\sqrt{\mu_{AB}}}(2\pi k\theta_{AB})^{-\frac{3}{2}} \int_0^\infty \sigma(\varepsilon) e^{-\frac{\varepsilon}{k\theta_{AB}}} \varepsilon d\varepsilon, \tag{3.9}$$

where μ_e is the reduced mass, $\mu_{AB} = m_A m_B / (m_A + m_B)$, and where σ is the elementary cross section of the respective reaction/ transition process. Maxwellian velocity distribution is a practical assumption for all regimes of interest in aerospace applications according to the cited authors of the CR models. For example, for a two-temperature model, the heavy-particle impact rate constant K_M and electron-impact rate constant K_e are given by:

$$K_M(T_e) = \frac{8\pi}{\sqrt{\mu_{AB}}}(2\pi k T_M)^{-\frac{3}{2}} \int_0^\infty \sigma_M(\varepsilon) e^{-\frac{\varepsilon}{kT_M}} \varepsilon d\varepsilon, \tag{3.10}$$

$$K_e(T_e) = \frac{8\pi}{\sqrt{\mu_{AB}}}(2\pi k T_e)^{-\frac{3}{2}} \int_0^\infty \sigma_e(\varepsilon) e^{-\frac{\varepsilon}{kT_e}} \varepsilon d\varepsilon. \tag{3.11}$$

The cross section σ then depends on the exact process and sometimes even specific atoms and molecules. Cross sections can be determined from experimental measurements, semi-empirical models or derived directly from quantum mechanics. For example, electron-impact rates can be determined analytically for Hydrogen, assuming classical mechanics and inelastic collisions for most cases, and collisions for other atoms and molecules can then be corrected by the so-called Gaunt factor $\bar{g}$, introduced in Chapter 2. How these cross sections or total rate coefficients are computed for the various processes will be discussed in the following paragraphs.

Electron-Impact (De-)Excitation

Excitation is a basic process by which an atom or a molecule collides with another partner, transferring energy to its electrons and raising their orbits from the classical mechanics perspective as a result. Electron impact is, however, the most effective means of both excitation and ionisation (discussed later), since from elementary mechanics, it is known that the kinetic energy of the colliding particle is transmitted efficiently only when the masses of the two particles involved are of a similar order of magnitude. For an atom or a molecule X, the electron impact excitation is given by:

$$X(l) + e^- \xrightarrow{K_e(l,u)} X(u) + e^-, u > l, \tag{3.12}$$

and for the reverse process, de-excitation:

$$X(u) + e^- \xrightarrow{K_e(u,l)} X(l) + e^-, u > l, \tag{3.13}$$

which are the b-b transitions (along with V-V, V-T, V-e etc. transitions in molecules). The relation between the two rate constants can be derived from the so-called principle of detailed balance with the respective upper and lower partition functions Q:

$$K_e(u,l) = K_e(l,u)\frac{Q_l}{Q_u} = K_e(l,u)\frac{g_l}{g_u} e^{-\frac{E_l - E_u}{kT_e}}, \tag{3.14}$$

with the resulting species balance for all m atomic or molecular levels considered:

$$\left.\frac{\partial n_u}{\partial t}\right|_{Ex,e} = \sum_{k=1}^{m} K_e(k,u) n_k n_e - \sum_{k=1}^{m} K_e(u,k) n_u n_e. \tag{3.15}$$

These transitions are allowed only if they are spin-conserved. If the transition requires spin change, it is typically achieved by a complete electronic substitution, where the impacting electron replaces the original electron in a higher energy orbital and the original electron is freed (see the selection rules for transitions for example in Ref. [13]).

In the NEQAIR model, electron-impact excitation rate coefficients for atoms are expressed simply with the Arrhenius form:

$$K_e|_{\text{NEQAIR, atoms}} = A T_{\text{control}}^{n} \exp\left(-E_a / T_{\text{control}}\right), \tag{3.16}$$

where the parameters A and n are either determined from quantum mechanical solutions for the higher quantum number states (when most atoms and molecules can be considered to behave hydrogenically) or determined experimentally for the lower quantum number states. E_a is in theory the reaction activation energy, but optimisation to match experimental data can be further made by adjusting any of these rate coefficient parameters. For molecules, the process is more complex due to the fact that electronic transition in molecules is accompanied by vibrational and rotational transitions (the vibronic transitions mentioned in Chapter 2) and will be discussed a couple of paragraphs later.

In the modern, more accurate CR models, to remove the semi-empiricism with controlling temperatures, for atomic (de-)excitation, semi-empirical cross-section models are in use, derived directly from quantum mechanics and experimental data. For both optically allowed and forbidden transitions, several models have been proposed by for example Gryzinsky (1958 in Ref. [41]), Seaton (1962) in Ref. [95], Drawin (1966, original publication not available) and Frost et al. (1998 in Ref. [33]). One of the simplest expressions is the one from Drawin, for optically allowed transitions:

$$\sigma_{lu}|_{\text{CR, atoms, allowed}} = 4\pi a_0^2 \left(\frac{R_y}{E_u - E_l}\right)^2 \alpha_{lu} \frac{u_{lu}-1}{u_{lu}^2} f_{lu} \ln\left(\beta_{lu} u_{lu}\right) \qquad f_{lu} = \frac{1+\sqrt{1+\frac{1}{u_{lu}}}}{1-\sqrt{1-\frac{1}{u_{lu}}}}, \tag{3.17}$$

where a_0 stands for the Bohr radius, $\beta = 1.25$ and $\alpha = 1.0$, with the parameters made to match experimental data, and the upper-to-lower level index is defined as $u_{lu} = \varepsilon/(E_u - E_l)$. For optically forbidden transitions:

$$\sigma_{lu}|_{\text{CR, atoms, forbidden}} = 4\pi a_0^2 \left(\frac{R_y}{E_u - E_l}\right)^2 \alpha_{lu} \frac{u_{lu}-1}{u_{lu}^2}, \tag{3.18}$$

with R_y being the Rydberg constant (ionisation potential of H) and α again yields the best match if set to 1.

For molecules, the electronic excitation process is coupled with the changes in the rovibrational state as well. For that reason, the transition rates must be computed for all possible rotational and vibrational states at the given lower and upper electronic levels between which the excitation occurs. In both NEQAIR and the presented CR models of Pierrot et al. and Lemal, this is done in a similar way, originally derived by Park in Ref. [81]. Since large amount of combinations of the electronic levels with different rotational and vibrational states can exist for an electronically excited molecule and all must be accounted for, the overall transition rate $\overline{K}(e,e')$ is expressed by the summation of the possible rate coefficients and their averaging. The derivation of this total transition rate by Park results in:

$$\overline{K}(e,e')|_{\text{NEQAIR and CR, mol.}} = \frac{\text{HLF}_t \sum_v \sum_{v'} q(v,v') \exp\left[-G(v)/(kT_v)\right]}{(kT_r/B_e) Q_m^v}, \tag{3.19}$$

in which $G(v)$ is the vibrational energy for the considered state v, parameter B_e is a function of the sum of all possible rotational energy levels, and a lengthy, but analytic expression exists for the term HLF_t, which can be also databased as a total Hoenl-London factor. The Franck-Condon factors $q(v,v')$ are databased for each species as well. In addition, use is made of experimental excitation cross sections at room temperature, and all models apply some version of Equation 3.19 to extrapolate the room temperature data to higher temperatures.

While NEQAIR uses this formulation for all molecular electronic excitations (X → A, A → B etc.), the more accurate CR models use other semi-empirical relations when the transition does not happen from the ground state (such as A → B, A → C etc.), such as the relations developed by Bacri and Medani in Ref. [9], as Park's formulation was not found to fit very well for non-ground state transitions.

Electron-Impact Ionisation (Recombination)

Similarly, ionisation might occur due to electron collision if the energy of the impacting electron is large enough, resulting in another electron being freed, in turn resulting in a b-f transition:

$$X(u) + e^- \xrightarrow{K_e(u,c)} X^+ + 2e^-, \tag{3.20}$$

where the state of c is used to denote continuum. Similarly, the reverse process, three-body f-b recombination might occur:

$$X^+ + 2e^- \xrightarrow{K_e(c,u)} X(u) + e^-, \tag{3.21}$$

where the the third body (in this case electron) is always needed next to the two interacting, recombining particles. For example, if two atoms were to form a molecule without the presence of a third body, provided that they attract each other, they could never truly merge so as to conserve energy. A third body must be present to, in some way, drain the energy from the system, such that a molecule with total energy lower than the initial two atoms can be formed. Thus, all the recombination processes also further mentioned must be defined as a three-body recombinations.

In this case, from the principles of detailed balance, it is derived that the ionisation and recombination rate constants are related through:

$$K_e(c,u) = K_e(u,c)\frac{g_u}{2Q^+}\left(\frac{h^2}{2\pi m_e k T_e}\right)^{\frac{3}{2}} e^{-\frac{E_u - E'_{ion}}{kT_e}}, \tag{3.22}$$

in which E'_{ion} is the ionisation energy and Q^+ is the ion total partition function. Then, the overall balance reads, with n^+ being the ion number density:

$$\left.\frac{\partial n_u}{\partial t}\right|_{Ion,e} = K_e(c,u)n^+ n_e^2 - K_e(u,c)n_u n_e. \tag{3.23}$$

In NEQAIR, the same relationship as for atomic electronic excitation is used (Equation (3.16)), with tweaked coefficients T_{control}, A and n or activation energy E_a to achieve match with experimental data.

On the other hand, in both Lemal's CR and the CR of Pierrot et al., the Binary-Encounter Bethe (BEB) model is typically used instead to express ionisation rates. The cross section is then determined from:

$$\sigma_{u,c}|_{\text{CR}} = 4\pi a_0^2 \left(\frac{R_y}{E_u^s}\right)^2 N_u^s \zeta_6, \tag{3.24}$$

in which R_y is the Rydberg constant, E_u^s is the energy required to remove the electron from the shell, N_u^s is the number of electrons in that shell and ζ_6 is a function of $u = \varepsilon / E_u^s$ and $w = W / E_u^s$:

$$\zeta_6 = \frac{1}{1+u+w}\left[\frac{\ln u}{2}\left(1-\frac{1}{u}\right)^2 + 1 - \frac{1}{u} - \frac{\ln u}{u+1}\right], \tag{3.25}$$

where W is the average kinetic energy of the electron in the shell. The complex theory of the BEB model is beyond the scope of this text and will not be further discussed.

Heavy-Particle-Impact (De-)Excitation

Where electrons are scarce in the shock layer, heavy particle impact (de-)excitation is significant. For a heavy collision partner M, this can be written as:

$$X(l) + M \xrightarrow{K_M(l,u)} X(u) + M, u > l, \tag{3.26}$$

with the corresponding de-excitation given by:

$$X(u) + M \xrightarrow{K_M(u,l)} X(l) + M. \tag{3.27}$$

Similarly to the case of electron-impact electronic excitation, the rate constants are coupled through the degeneracies and energy level difference:

$$K_M(u,l) = K_M(l,u)\frac{g_l}{g_u}e^{-\frac{E_l-E_u}{kT_e}}, \tag{3.28}$$

resulting in the overall balance contribution:

$$\left.\frac{\partial n_u}{\partial t}\right|_{E_{xx},M} = \sum_{k=1}^{m} K_M(k,u)n_k n_M - \sum_{k=1}^{m} K_M(u,k)n_u n_M. \tag{3.29}$$

In NEQAIR, the model employed for all these cross sections is, if $u = \varepsilon/(E_u - E_l)$, with ε being the heavy particle impact energy, given by:

$$\sigma_{l,u}|_{\text{NEQAIR, CR atom-mol}} = 10^{-16}\frac{\ln u}{u}. \tag{3.30}$$

The cross section integrated from this is approximated, if $x(T_t) \equiv \Delta E_i/kT_t$ with ΔE being the change in state energy coming from upper state to lower state:

$$K_{M,lu}|_{\text{NEQAIR, mol.}} = 4057\cdot10^{-16}\frac{\Delta E}{\sqrt{T_t}}q[x(T_t)] \qquad q(x) \equiv \frac{x^2+2.33x+0.25}{x^2+3.33x+1.68}e^{-x}, \tag{3.31}$$

which was an approximation developed by Park in Ref. [81] to fit experimental data. On the other hand, if the excited species are ionised, the following rate coefficient is used:

$$K_{M,lu}|_{\text{NEQAIR, ions}} = \frac{5837\cdot10^{-17}}{x}(\Delta E)^2\frac{e^{-x}}{T_t\sqrt{T_t}}. \tag{3.32}$$

The CR model of Lemal in Ref. [58] uses the same relation as Park for atom-molecule collisions, and for atom-atom collisions, in contrast, he uses the model of Surzhikov derived in Ref. [104]:

$$K_{M,lu}|_{\text{CR}} = 32\pi a_0^2\left(\frac{R_y}{E_{ion}-E_u}\right)^2 f_{ul}\sqrt{\frac{kT_g}{\pi m_M}}\zeta_9 \qquad \xi_9 = \frac{m_M m_e}{m_h(m_M+m_e)}\left(1+\frac{1}{\rho}\right)\frac{e^{-\rho}}{1+\left(\frac{2m_e}{(m_M+m_e)\rho}\right)^2} \tag{3.33}$$

,
where $\rho = (E_u - E_l)/kT_g$, m_h is the molar mass of hydrogen and the upper-to-lower state function f_{ul} has been already defined in Equation (3.17).

Electron-Impact Dissociation (Recombination)

A molecule XY composed of species X and Y may experience dissociation as a result of an electron impact, written as:

$$XY(u) + e^- \overset{K_e(u,d)}{\longrightarrow} X + Y + e^-, \tag{3.34}$$

and in a reverse fashion, a three-body recombination may occur, where a free electron acts as an energy sink:

$$X + Y + e^- \overset{K_e(d,u)}{\longrightarrow} XY(u) + e^-. \tag{3.35}$$

The rate coefficients $K_e(u,d)$ and $K_e(d,u)$ from detailed balance are related as, analogously to the process of electron-impact ionisation:

$$K_e(d,u) = K_e(u,d)\frac{Q_u^{XY}}{Q^X Q^Y}\left(\frac{h^2}{2\pi m_e kT_e}\right)^{\frac{3}{2}} e^{-\frac{E_u^{Dis}}{kT_e}}, \tag{3.36}$$

in which Q^X and Q^Y are total atomic partition functions, Q_u^{XY} is the molecule's rovibrational partition function in its upper excited electronic state u, and E_u^{Dis} is the dissociation energy required for the molecule XY. The following balance contribution is then obtained:

$$\left.\frac{\partial n_u}{\partial t}\right|_{Dis,e} = K_e(d,u)n_X n_Y n_e - K_e(u,d)n_u n_e. \tag{3.37}$$

In NEQAIR, electron-impact dissociations are treated again using Equation 3.16 and calibrating the parameters A, T_{control} and n to obtain the best match with the experimental data.

The electron-impact dissociation rate coefficients in the CR model of Lemal and Pierrot et al. were determined according to the work of Yu et al. from 2001 (see Ref. [119]):

$$\sigma_Y(\varepsilon) = 4\pi a_0^2 \alpha \left(R_y/\Delta E_Y\right)^2 (u-1)/u^2 \ln(1.25u), \tag{3.38}$$

which is a formulation directly taken from the work of Drawin from 1966, the original publication of which was not. In Equation (3.38), ΔE_Y is the ionisation level for level Y. For collisional impact energy of ε, u is now the reduced impact energy given by $\varepsilon/|\Delta E_{Y,v,j}|$, where the denominator is the dissociation energy of the state in question and was set to be $\alpha = 2\cdot 10^{-3}\mathrm{cm}^6/\mathrm{s}$ to match experimental data.

Heavy-Particle-Impact Dissociation (Recombination)

Similar to the case with the electron, dissociation of a molecule due to collision with a heavy particle M such as atom or an ion is defined as:

$$XY(u) + M \xrightarrow{K_M(u,d)} X + Y + M, \tag{3.39}$$

with the reverse three body recombination process:

$$X + Y + M \xrightarrow{K_M(d,u)} XY(u) + M, \tag{3.40}$$

and with the rate coefficients related in the same fashion as in the case of electron-impact dissociation in the previous paragraphs:

$$K_M(d,u) = K_M(u,d)\frac{Q_u^{XY}}{Q^X Q^Y}\left(\frac{h^2}{2\pi m k T_t}\right)^{\frac{3}{2}} e^{-\frac{E_t^{Dis}}{kT_t}}. \tag{3.41}$$

The overall balance is given by:

$$\left.\frac{\partial n_u}{\partial t}\right|_{Dis,M} = K_M(d,u) n_X n_Y n_M - K_M(u,d) n_u n_M. \tag{3.42}$$

In NEQAIR, heavy particle three body recombinations and dissociations are treated the same way as electron-impact excitations, ionisations and dissociations, by using Equation 3.16 and calibrating the parameters A, T_{control} and n to obtain ideal match.

In the CR models employed by Lemal and Pierrot et al., a semi-empirical expression is derived and tweaked such that it matches the experimental results which were measured by Park and first presented in Ref. [81] (see Ref. [119]):

$$\sigma^{\mathrm{h,dis}}_{Y,\mathrm{v},J}(\varepsilon)|_{\mathrm{CR}} = \alpha\pi a_0^2 \left(\Delta E_{Y,0,0}/\Delta E_{Y,\mathrm{v},J}\right)^n (\ln u)/u, \tag{3.43}$$

where $\Delta E_{Y,\mathrm{v},J}$ and $\Delta E_{Y,0,0}$ correspond to the dissociation energy of the rovibronic level given by the vibrational number of v, the rotational number J and the rovibronic base level with $v, J = 0$.

It was found that n =1 provides the best agreement with empirical data with α = 1, in case the impactor is Nitrogen atom, or α = 0.3, in case the impactor is N_2 (see Ref. [119]). This is the most significant process affecting the population of the N_2 molecule.

V-V, V-T, V-e Exchange Energy Processes

Since molecules consist also of vibrational and rotational internal states, further transitions can occur as a result of an encounter with another particle. First, the vibrational excitation due to an electron impact formally occurs via a generation of an unstable ion of that molecule, AB$^-$, which then decomposes back into the electron and molecule AB at a different vibrational state:

$$AB(X, v_l) + e^- \xrightarrow{K_{V-e}(v_u;v_l)} AB^-(X, v_l) \rightarrow AB(X, v_u) + e^-. \tag{3.44}$$

In the next case of a potential vibrational excitation due to a heavy-particle M impact, the vibrational excitation might result in the vibrational energy of M changing as well, such that the states evolve in opposite fashion (AB: l → u, M: u → l and vice versa):

$$AB(X, v_u) + M(Z, w_l) \xrightarrow{K_{V-V}(v_u,w_l;v_l,w_u)} AB(X, v_l) + M(Z, w_u). \tag{3.45}$$

Note that the X and Z refer to electronic states. Vibrational excitation by other heavy particles is especially significant in electron-depleted parts of shock waves. Finally, for a vibrational - translational excitation due to a heavy impact with M:

$$AB\left(X, v_u\right) + M\left(Z, w_l\right) \xrightarrow{K_{V-T}\left(v_u, w_l; v_l, w_u\right)} AB\left(X, v_l\right) + M\left(Z, w_u\right), \tag{3.46}$$

where the electron induced V-T transition is not considered due to the inefficient kinetic energy exchange between particles of such different masses. These processes combined change the overall state balance by:

$$\left.\frac{\partial n_u}{\partial t}\right|_{V-e} = K_{V_l-e} n_l n_e - K_{V_u-e} n_u n_e, \tag{3.47}$$

$$\left.\frac{\partial n_u}{\partial t}\right|_{V-V} = K_{V_l-V} n_l n_{M_u} - K_{V_u-V} n_u n_{M_l}, \tag{3.48}$$

$$\left.\frac{\partial n_u}{\partial t}\right|_{V-T} = K_{V_l-T} n_l n_M - K_{V_u-T} n_u n_M. \tag{3.49}$$

NEQAIR does not consider population state changes due to these V-V, V-T, V-e processes. However, it does simulate the radiation (mostly the rovibrational bands in IR) coming from these processes as if they happened using their respective Einstein factors:

$$A_{ul} = \frac{64\pi^4 \mu_{ul}^2}{3\varepsilon_0 h \lambda_{ul}^2}, \tag{3.50}$$

where the respective μ_{ul}^2 (the square of the transition dipole moment) is fitted by a polynomial and databased and used to compute the molecular band line radiation in IR.

In the majority of the CR models, the so-called SSH theory (Schwartz—Slawsky—Herzfeld) is used to determine the V-V, V-T and V-e transitions. To be able to solve these interactions, the SSH theory assumes that many vibrations occur during the course of the collision, that the vibrational amplitude is small compared to the range of intermolecular forces and that the relative kinetic energy for effective collisions is much greater than the transferred quantum of energy. These assumptions are not necessarily always correct, but small adjustments to the expressions in SSH have been shown to improve the fit match with the experimental data (see for example Ref. [109]).

Predissociation

Predissociation is a process in which a molecule at certain vibrational levels decays into two separate atoms in ground states:

$$AB(X, v \in V) \xrightarrow{K_{\text{pred}}} A + B. \tag{3.51}$$

In quantum mechanics, this occurs due to the crossing of the electronic state's stable potential curve with unstable curves. Park's NEQAIR uses databased predissociation rates. However, the only databased rates are for 3 vibrational states for NO and one state of O2, other molecules and states are completely neglected.

In the two CR models, use of the predissociation rate experimentally fitted by Pierrot et al. in 1998 for predissociation occuring from a particular vibrational level v (see Ref. [83]) was made:

$$K_{\text{pred}}(v)|_{\text{CR}} = \gamma_1(v) + \gamma_2(v) j(j+1), \tag{3.52}$$

where γ_1 and γ_2 are fitting parameters depending on the vibrational quantum number and j is the rotational quantum number.

Radiative Processes

Finally, the species causing the change in the internal states do not have to be electrons and heavy particles, but also photons, which are abundantly present in the radiating plasma flow. For example, spontaneous emission of a molecule or an atom might occur from the upper state to a lower state:

$$X(u) \xrightarrow{A_{ul} n_u}, u > l, \tag{3.53}$$

where A_{ul} is the first Einstein coefficient for spontaneous emission, in this case being analogous to a reaction rate constant. On the other hand, photo-excitation can occur if a molecule or an atom absorbs a photon of a certain energy:

$$X(l) + h\nu \xrightarrow{(1-\Lambda_{ul})A_{ul}n_u} X(u), u > l, \tag{3.54}$$

where Λ_{ul} is typically denoted as an "escape factor", which assumes that the depletion of some energy level u due to absorption can be approximated to be a fraction of the re-population rate of lower energy level l due to emission. This assumption comes from the fact that the second Einstein coefficient B_{lu}, denoting absorption, is dependent on the incoming radiative intensity, which is, generally, not known by the radiation code/ CR model during calculation. This has significant effects on the outcomes and will be discussed in Chapter 4. Then, the balance reads:

$$\frac{\partial n_u}{\partial t}|_{\text{rad}} = \sum_{k>u}^{m} \Lambda_{ku} A_{ku} n_k - \sum_{k=1}^{m} \Lambda_{uk} A_{uk} n_u. \tag{3.55}$$

In this case, the implementation in NEQAIR (nonequilibrium case) is the same as in CR models. If LOS data is provided, NEQAIR can also in principle include estimation of the respective photo-ionisation process, in which case the $X(u)$ is replaced by the respective positive ion. Lemal in his CR model equated the escape factor to 1cm, while the escape factor in NEQAIR is a user input, or a complete non-local calculation can be run. The value of this escape factor suggested by the NEQAIR manual (see Ref. [16]) is that it should be roughly the order of the shock stand-off distance further, which is also recommended by Whiting et al. in Ref. [112].

Other Processes not Considered

Other processes which can occur in plasma, and which are not covered by neither NEQAIR based codes nor the cited CR models are:

- Electron-impact molecular ionisation
- Heavy-particle-impact ionisation
- R-e, R-R, R-V and R-T transitions

The reason why these transitions are not included is due to their very minimum impact on the resulting integrated spectral intensity or population states dynamics. The dissociation of molecules typically requires far less energy than ionisation and thus is not treated, as the likelihood of such an event prior to dissociation is very low. Heavy-particle-impact ionisation is even less likely, due to the extremely inefficient kinetic energy transfer between a heavy particle to an electron (due to their very large mass difference). As for rotational transitions, R-e transitions are especially insignificant due to the same reason of ineffective energy transfer. Finally, the rotational R-R and R-T transitions do occur, however, they typically result in fairly weak lines far in IR, and would thus only add a significant computational cost, while not adding much to the accuracy of the calculation.

Resulting Master Equations

Combining all the contributions from the paragraphs above yields, for atoms, the following Master Equation:

$$\begin{aligned}\frac{\partial n_u}{\partial t}|_{\text{atoms}} = \sum_{k=1}^{m} K_e(k,u) n_k n_e - \sum_{k=1}^{m} K_e(u,k) n_u n_e + \sum_{k=1}^{m} K_M(k,u) n_k n_M - \sum_{k=1}^{m} K_e(u,k) n_u n_M \\ + K_e(c,u) n^+ n_e^2 - K_e(u,c) n_u n_e + \sum_{k>u}^{m} \Lambda_{ku} A_{ku} n_k - \sum_{k=1}^{m} \Lambda_{uk} A_{uk} n_u\end{aligned} . \tag{3.56}$$

For molecules, the vibrational excitations, dissociations and predissociations must be also included, and so the molecular Master Equation yields:

$$\begin{aligned}&\tfrac{\partial n_u}{\partial t}|_{\text{mol}} = \tfrac{\partial n_u}{\partial t}|_{\text{atoms}} + K_e(d,u) n_X n_Y n_e - K_e(u,d) n_u n_e + K_M(d,u) n_X n_Y n_M - K_M(u,d) n_u n_M \\ &+ K_{V_l-e} n_l n_{M_u} - K_{V_u-e} n_u n_{M_l} + + K_{V_l-T} n_l n_M - K_{V_u-T} n_u n_M + K_{V_l-e} n_l n_e - K_{V_u-e} n_u n_e\end{aligned} . \tag{3.57}$$

Table 3.2: The most recent update to NEQAIR reaction rate parameters determined by Brandis and Cruden in Ref. [26].

Reaction	M	A (cm^3/mol/s)	n	E_a (K)	Controlling T
$N_2 + M \rightarrow 2N + M$	Molecule	$7.0 \times$ 10E21	-1.6	113,200	$\sqrt{TT_{ev}}$
	Atom	$3.0 \times$ 10E22			$\sqrt{TT_{ev}}$
	Electron	$1.2 \times$ 10E7	2.69		T_e
$O_2 + M \rightarrow 2O + M$	Molecule	$2.0 \times$ 10E21	-1.5	59,500	$\sqrt{TT_{ev}}$
	Atom	$1.0 \times$ 10E22			$\sqrt{TT_{ev}}$
$NO + M \rightarrow N + O + M$	Molecule	$1.5 \times$ 10E15	0	74,570	$\sqrt{TT_{ev}}$
	Atom	$7.3 \times$ 10E15			$\sqrt{TT_{ev}}$
	Electron	$5.7 \times$ 10E18			T_e
$N + e^- \rightarrow N^+ + 2e^-$		$2.5 \times$ 10E34	-3.82	168,600	T_e
$O + e^- \rightarrow O^+ + 2e^-$		$3.9 \times$ 10E33	-3.78	158,500	T_e
$N_2 + O \rightarrow NO + N$		$1.8 \times$ 10E14	0	38,249	T_t
$O_2 + N \rightarrow NO + O$		$9.0 \times$ 10E9	1	3,270	T_t
$N + O \rightarrow NO^+ + e^-$		$8.8 \times$ 10E8	1	31,900	T_e
$N + N \rightarrow N_2^+ + e^-$		$4.4 \times$ 10E7	1.5	67,500	T_e
$O + O \rightarrow O_2^+ + e^-$		$7.1 \times$ 10E2	2.7	80,600	T_e
$N^+ + N_2 \rightarrow N2^+ + N$		$7.0 \times$ 10E6	1.47	13,130	T_t
$O^+ + N_2 \rightarrow N2^+ + O$		$9.1 \times$ 10E11	0.36	22,800	T_t
$O_2^+ + O \rightarrow O^+ + O_2$		$4.0 \times$ 10E12	-0.09	18,000	T_t
$O^+ + NO \rightarrow N^+ + O_2$		$1.4 \times$ 10E5	1.9	26,600	T_t
$NO^+ + O_2 \rightarrow O_2^+ + NO$		$2.4 \times$ 10E13	0.41	32,600	T_t
$NO^+ + N \rightarrow N2^+ + O$		$7.2 \times$ 10E13	0	35,500	T_t
$NO^+ + O \rightarrow N^+ + O_2$		$1.0 \times$ 10E12	0.5	77,200	T_t
$O_2^+ + N \rightarrow N^+ + O_2$		$8.7 \times$ 10E13	0.14	28,600	T_t
$O_2^+ + N_2 \rightarrow N_2^+ + O_2$		$9.9 \times$ 10E12	0	40,700	T_t
$NO^+ + N \rightarrow O^+ + N_2$		$3.4 \times$ 10E13	-1.08	12,800	T_t
$NO^+ + O \rightarrow O_2^+ + N$		$7.2 \times$ 10E12	0.29	48,600	T_t
$NO + N^+ \rightarrow NO^+ + N$		$1.8 \times$ 10E12	0.57	0	T_t

These Master Equations form a set of equations which has to be solved. Depending on the radiation model, either the coupled equations are solved simultaneously as a matrix system (time dependent CR models) assuming a certain relaxation trend or it is assumed that due to the short relaxation time, $\frac{\partial n_u}{\partial t}|_{\text{atoms}} = 0$ and $\frac{\partial n_u}{\partial t}|_{\text{mol}} = 0$. The latter is the already defined Quasi-Steady State QSS assumption used in NEQAIR and many other NEQAIR-based nonequilibrium codes.

In Equation 3.57, as mentioned in the discussion above, NEQAIR does not consider any of the V-V, V-T or V-e transitions. Thus, the molecular states considered in the Master Equation of NEQAIR are states purely electronic. This means that the vibrational states are simulated for radiation using the Franck-Condon and Hoenl-London factors and the data on electronic dipole moments, despite them not explicitly entering Equation 3.57. Since many of these dominant contributions to the Master Equation in NEQAIR are determined using Equation 3.16, the selection of the rate coefficient paramaters A, n, E_a and the selection of the controlling T are crucial for accurate results. The most recent updated coefficients for the reactions relevant for Earth reentry, implemented in the newest version of NEQAIR, are shown in Table 3.2.

Rate Coefficients for Radiative Processes

Finally, the theory from Chapter 2 will be briefly revisited to indicate how the resulting population states determined from the Master Equations are used to generate nonequilibrium spectra.

Vibrational b-b transition rate coefficients for molecular transitions have already been discussed in the respective section (V-V, V-T and V-e exchange processes) and are not mentioned further.

For electronic transitions in atoms, the spontaneous emission Einstein coefficient A_{ul} is databased for each line. Then, the stimulated emission and absorption coefficient can be derived as it was in Chapter 2:

$$B_{ul} = \frac{A_{ul}\lambda_{ul}^5}{8\pi hc} \qquad B_{lu} = \frac{g_u}{g_l}\frac{A_{ul}\lambda_{ul}^s}{8\pi hc}, \tag{3.58}$$

which are already familiar expressions. Now, use can be made of the calculated upper and lower population levels n_u and n_l determined from Equations (3.56) and (3.57), from which the spectral absorptivity and emissivity are given by:

$$\alpha_{ul}(\lambda) = (n_l B_{lu} - n_u B_{ul}) \frac{h}{\lambda_{ul}} \Phi_{ul}(\lambda - \lambda_{ul}) \qquad \varepsilon_{ul}(\lambda) = n_u \frac{A_{ul}}{4\pi} \frac{hc}{\lambda_{ul}} \Phi_{ul}(\lambda - \lambda_{ul}). \tag{3.59}$$

For the b-f and f-f transitions, which create continuum radiation, the spectral intensity is typically determined using semi-empirical hydrogenic b-f and f-f transition cross sections and correcting it by the Gaunt factor $\bar{g}$, which is databased. The hydrogenic cross sections are:

$$\sigma_{h\lambda}^{b-f} = 7.9 \times 10^{7} \frac{R_y}{u^5} \lambda[\mathrm{nm}] = 7.910^{-18} \mathrm{n} (\lambda/\lambda_n)^3 \qquad \sigma_{\lambda \mathrm{H}}^{f-f} = (\mathrm{a}_1/(hc/\lambda) + \mathrm{a}_2)\, 10^{-40/\mathrm{e_p}3}, \tag{3.60}$$

in which, for the b-f cross section, u refers to the upper level index and R_y is Rydberg constant, or alternatively, n is the principal quantum number and $\lambda_n = n^2 10^8 / R_y$. For f-f cross section, hc/λ is the photon energy, and the fitting parameters a_1 and a_2 are:

$$\mathrm{a}_1 = 0.006805 - 0.00934\mathrm{e}^{-1.16 \cdot 10^{-4} \mathrm{T_e}} \qquad \mathrm{a}_2 = 0.508 + 1.046\mathrm{e}^{-5.77 \cdot 10^{-4} \mathrm{T_e}} + 1.85\mathrm{e}^{-3.43 \cdot 10^{-4} \mathrm{T_e}}. \tag{3.61}$$

Using these cross sections, both the b-f and f-f absorption coefficients can be found with the help of the Saha equation:

$$\alpha_{\lambda,b-f} = \sigma_{h\lambda} \bar{g} \frac{n^+ n_e}{2Q^+} \left(\frac{h^2}{2\pi m_e k T_e} \right)^{\frac{3}{2}} e^{-\frac{E_{ion}}{kT_e}} \qquad \alpha_{\lambda,f-f} = \sigma_{h\lambda}(1+d) \frac{n^+ n_e}{n_{tot}}, \tag{3.62}$$

in which d is another databased correction factor. Most radiation codes assume thermodynamic equilibrium for bound-free and free-free radiation, such that $\varepsilon_\lambda = \alpha_\lambda B_\lambda$, with B_λ being the Planck function. In case of nonequilibrium, the exponential term in the Planck function is replaced by n_L/n_U for b-b transitions:

$$B_\lambda = \frac{2hc^2}{\lambda^5 \left(e^{\frac{hc}{\lambda k T_e}} - 1 \right)} \xrightarrow{\text{noneq.}} B_\lambda|_{\text{noneq}} = \frac{2hc^2}{\lambda^5 \left(e^{\frac{n_l}{n_u}} - 1 \right)}. \tag{3.63}$$

The modified Planck function in Equation (3.63) still implies equilibrium at the given wavelength λ, just not over the entire spectrum. This means that all transitions generating radiation with a wavelength of λ have the same population ratio. This is implemented in NEQAIR and justified by Whiting et al. in Ref. [112] by the following statements:

- Most lines significant for reentry applications are very narrow and thus not overlapping, and so there is indeed only one n_l/n_u for the given line justifying the use of the nonequilbrium narrow Planck function.

- Even for overlapping vibrational and rotational lines of the same species, since the wavelength of the emitted radiation is the same, so are the upper and lower state energies and thus also the n_l/n_u ratio.

  In addition, even if this was not the case, the implementation of NEQAIR requires exactly 1 temperature for rotational distribution and 1 temperature for vibrational energy, implying that these equal n_l/n_u distributions are indeed the same.

- In many applications, the radiation field is close to being optically thin, in which case the exact Planck function is not that significant for intensity computation.

Whiting et al. in Ref. [112], however, admits that overlapping of atomic lines of two species in some environments can occur, and the effect of this overlapping when using a single nonequilibrium Planck function for both species is not known.

With this assumption, the ratio between the equilibrium and thermal nonequilibrium Planck function spectral intensity, assuming a two temperature model ($T_v = T_e, T_r = T_t$) can be expressed as, in the full form:

$$\frac{I_{b\eta}^{\mathrm{ne}}(T_v, T_r)}{I_{b\eta}(T_v)} = \frac{n_u}{n_l} e^{hc_0\eta/kT_v} = \frac{\left[Q_{vr,l}/Q_{vr,u}\right]^{\mathrm{ne}}(T_v, T_r)}{\left[Q_{vr,l}/Q_{vr,u}\right](T_v)} \exp\left[\frac{E_{ru} - E_{rl}}{k} \left(\frac{1}{T_v} - \frac{1}{T_r} \right) \right], \tag{3.64}$$

in which Q_{vr} refers to the rovibrational partition functions as functions of temperature and E_{ru} and E_{rl} refer to energies of upper and lower rovibrational states considered in the given transition. Thus, since E_{ru} and E_{rl} change with each spectral line, the nonequilibrium Planck function is not as smooth as its equilibrium counterpart.

The Definition of Nonequilibrium Radiation

The term "nonequilibrium" radiation has been used throughout this entire text, but not yet properly defined. Thus, the last topic in the discussion of radiation modelling will be the definition of this term and assessment of when it is significant. This is important for the thesis work since, if equilibrium can be assumed for some applications, the simulations can likely be sped up by an order of magnitude.

As radiation is created due to thermochemical processes in the gas, the term "nonequilibrium" radiation can refer to two concepts - chemical and thermal nonequilibrium. It is the thermal nonequilibrium, however, which prevents the use of simple Boltzmann distributions for internal states and which thus significantly complicates the process of radiation calculations requiring the use of QSS. Based on the time constants of the chemical and thermal processes τ_c and τ_t and the characteristic flow time scale τ_f, the regime to be considered can be determined. For chemical time scale:

- $\tau_c << \tau_f$: chemical processes are much faster than the flow → flow in chemical equilibrium.
- $\tau_c >> \tau_f$: chemical processes are much slower than the flow → flow is effectively chemically frozen.
- $\tau_c \approx \tau_f$: the time scales of chemical processes and the flow are similar → chemical nonequilibrium must be respected.

and the same approach holds for thermal time scales:

- $\tau_t << \tau_f$: thermal processes are much faster than the flow → flow roughly in thermal equilibrium.
- $\tau_t >> \tau_f$: thermal processes are much slower than the flow → flow is effectively thermally frozen.
- $\tau_t \approx \tau_f$: the thermal time scales of chemical processes and the flow are similar → thermal nonequilibrium must be respected.

The thermal time scale τ_t typically refers to relaxation time of the internal states. This relaxation time is different for each species and represents the time that the internal atomic and molecular states require to relax towards the Boltzmann distribution. The typical lifetimes of internal states can, for this purpose, be expressed as τ_e for electronic states and τ_v for vibrational states. According to Hottel and Sarofim in Ref. [46], for example, for CO, the typical lifetimes τ_e of electronic states are in the order of 10^{-6}s to 10^{-8}s and τ_v of vibrational levels of 10^{-1}s to 10^{-3}s. It is thus the vibrational nonequilibrium which is the most problematic and prevalent.

In addition, while electronic and rotational relaxation can typically be modelled well by the so-called Landau-Teller formula, which represents linear relaxation in the form of $\partial T_i / \partial t = (T - T_i)/\tau_i$, this linear relaxation in case of vibrational excitation corresponds to the harmonic oscillator case. This approximation is very inaccurate at higher temperatures were anharmonic effects are dominant. In that case, the vibrational relaxation to determine τ_v can be computed with a so-called Millikan-White formulation, or, for more complex cases, the so-called quasi-classical trajectory, which simulates interactions and transitions of particles in a Monte-Carlo fashion. For more information on these techniques, refer to Ref. [81]. For τ_v estimations prior to the simulation, taking reference values from databases are likely more practical than full calculations.

In addition, the emission of radiation will be representative of the thermal energy of the gas, in the case that the molecule has time to equilibrate with other molecules after an event such as excitation before the photon emission. In that case LTE can also be assumed, even if complete thermal equilibrium is not present. The collisional time scale τ_{col} can be determined using a collision time of $\tau_{\text{col}} \approx 10^{-10}\sqrt{(T/T_0)}p_0/p$, where T_0 and p_0 are standard pressure and temperature (can be taken according to international standard atmosphere). Thus, especially at very high pressures and small temperatures, when $\tau_{\text{col}} >> \tau_e, \tau_v$, LTE can be assumed. Otherwise, either the above mentioned QSS approximation with multiple temperature formulation must be invoked, or the internal states must be resolved using more elaborate CR approaches.

Secondly, the chemical time scale τ_c can, for the various reactions, be estimated from the reaction rate coefficients, discussed in the previous section. Chemical nonequilibrium is not necessarily a challenge for this thesis work, as long as a proper chemical mechanism is used with INCA next to the radiation solver. The HITRAN implementation will not work in chemical nonequilibrium, as will be discussed in Chapter 4, but NEQAIR will.

Finally, the flow time scale τ_f can be defined at the shock, where the nonequilibrium is the most prevalent, using the shock speed and shock thickness as for example $\tau_f = t_{\text{shock}} / V_{\text{shock}}$.

This discussion completes the description of the methodology in this thesis work. Next, the implementation of this methodology will be elaborated on.

4

Implementation

Having selected the appropriate methods, Chapter 4 aims to describe in detail how these methods are adapted in the radiation solver. First, the general ray tracing scheme and logic is discussed for non-participating media and for media with a constant κ. Afterwards, the implementation of the HITRAN and NEQAIR spectral generation is outlined, and the way the solver is coupled to INCA is touched upon. Some of the most essential implementation decisions, such as discretisation, are justified with short validation tests of the respective subroutines. The validation of the entire solver will be presented in the Chapter 5.

4.1. Photon Monte Carlo

This section discusses the logic and implementation of the core routines of the ERMC method applied, which includes handling of grey media, treatment of domain boundaries and photon ray tracing. Full derivation of the relations behind this method here shown can be found in thesis of Tesse in Ref. [108].

4.1.1. Basic Logic

The software implementation of the ERMC method proceeds as following, where for each cell in the domain:

1. Determine the cell total emission energy and energy of the photon rays
2. Compute the wavelengths at which the current cell or cell of the highest temperature in the medium emits (local vs global wavelength sampling)
3. Initialise a photon ray with assigned energy E_γ, wavelength λ_γ, random direction ϕ_γ,θ_γ and initial transmissivity τ of 1 originating from the centre of the cell
4. Determine the next cell crossing based on the ray direction
5. Compute the distance travelled, ds to the next cell boundary crossing
6. Determine the current cell absorption coefficient κ_λ at the photon ray wavelength λ_γ
7. Compute the absorptance α based on κ_λ and ds
8. Compute the change of energy of the photon ΔE_γ ray due to the absorption
9. Compute the decrease in τ of the photon ray
10. If τ < tol or a wall/ boundary is encountered, perform the proper heat transfer procedure (will be discussed below) depending on the boundary type and possibly terminate the photon ray
11. Go back to 3 until all photons rays have been traced
12. Once all photons are computed, determine the local heat source term by taking a difference between the emitted and the absorbed energy of all of the photon rays

Assuming LTE for now, the emitted energy can be computed from integrating the blackbody radiation with the pre-computed absorption spectrum. There are two ways how the initial energy is computed depending on the nature of the problem. In relatively transmissive media, the radiation in the medium will be determined by the highest temperature cells. Thus, also the wavelengths of the photons propagating through the medium will follow the emission spectrum of the highest temperature cells. $E_{\gamma,0}$ is then also computed with the temperature and Planck mean absorption coefficient of the highest temperature, $T_{\max}$, spot:

$$E_{\gamma,0} = \frac{4\kappa_p(T_{\max})T_{\max}^4\sigma}{N_\gamma}, \tag{4.1}$$

while on the other hand, in media of low transmissivity, where radiation is mostly local, the emission energy can be computed using local conditions:

$$E_{\gamma,0} = \frac{4\kappa_p T^4\sigma}{N_\gamma}. \tag{4.2}$$

The latter approach will be used in hypersonic plasma modelling, where the absorption is rather high and the photon rays typically pass only few cells before absorption. In this text, these two approaches are referred to as global and local wavelength sampling.

Once the ray enters a cell with an absorption coefficient κ, the absorptance will decrease with distance travelled through this cell as:

$$\alpha = 1 - \exp(-\kappa ds), \tag{4.3}$$

causing a drop in photon energy due to the crossing, determined by the ratio of the Planck functions of the initial emitting cell 0 and current cell 1 in which the photon ray resides:

$$\Delta E_\gamma = E_{\gamma,0}\tau\alpha\Big(\frac{I_{b,\eta,i}}{I_{b,\eta,0}} - 1\Big). \tag{4.4}$$

However, if global sampling is used and emission energy is thus determined from the highest temperature cell, this must be corrected by:

$$\Delta E_\gamma = E_{\gamma,0}\tau\alpha\Big(\frac{I_{b,\eta,i}}{I_{b,\eta,0}} - 1\Big)\frac{I_{b,\eta,0}\kappa(T_0)}{I_{b,\eta,T_{\max}}\kappa(T_{\max})}. \tag{4.5}$$

The energy E_γ of the photon ray is then decreased as:

$$E_\gamma = E_\gamma - \Delta E_\gamma, \tag{4.6}$$

as well as its transmissivity τ:

$$\tau = \tau(1-\alpha), \tag{4.7}$$

until either $\tau <$tol or the photon gets outside of the domain or hits a non-reflective boundary. The tolerance is typically set to 1e-3 according to Ref. [98].

4.1.2. Random Number Selection

The variables that have to be initiated for each emitted photon ray using random numbers in the current implementation are the emitted wavelength, λ_γ and directions θ_γ and ϕ_γ. The random numbers are generated on the scale from 0 to 1. The emitted wavelength is determined from the cumulative emission integral:

$$R_\lambda = \frac{\int_0^{\lambda_\gamma}\varepsilon_\lambda d\lambda}{\int_0^\infty \varepsilon_\lambda d\lambda} \xrightarrow{\text{LTE}} \frac{\int_0^{\lambda_\gamma}\kappa_\lambda I_{b,\lambda} d\lambda}{\int_0^\infty \kappa_\lambda I_{b,\lambda} d\lambda}, \tag{4.8}$$

or, in a wavenumber formulation:

$$R_\nu = \frac{\int_0^{\nu_\gamma}\varepsilon_\nu d\nu}{\int_0^\infty \varepsilon_\nu d\nu} \xrightarrow{\text{LTE}} \frac{\int_0^{\nu_\gamma}\kappa_\nu I_{b,\nu} d\nu}{\int_0^\infty \kappa_\nu I_{b,\nu} d\nu}, \tag{4.9}$$

and so, in an inverse fashion, upon generation of a random number, a binary search is performed to find at which wavelength the cumulative emissivity distribution (normalised by its maximum) is equivalent to the random number.

Furthermore, for photon ray velocity direction unit vector in x, y and z, v_x, v_y and v_z, the photon ray directions are defined in the current implementation as:

$$v_x = \cos(\theta_\gamma)\cos(\phi_\gamma), \qquad v_y = \sin(\theta_\gamma)\cos(\phi_\gamma), \qquad v_z = \sin(\phi_\gamma), \tag{4.10}$$

such that $\theta_\gamma \in (0, 2\pi)$ and $\phi_\gamma \in (-\pi/2, \pi/2)$. Thus, they are generated with random numbers R_θ and R_ϕ as:

$$\theta_\gamma = 2\pi R_\theta, \qquad \phi_\gamma = R_\psi \pi - \pi/2, \tag{4.11}$$

where this will later be adjusted to utilise LDS instead. For illustrative purposes, example trajectories for 12x12x12 mesh in a grey medium are shown in Figure 4.1.

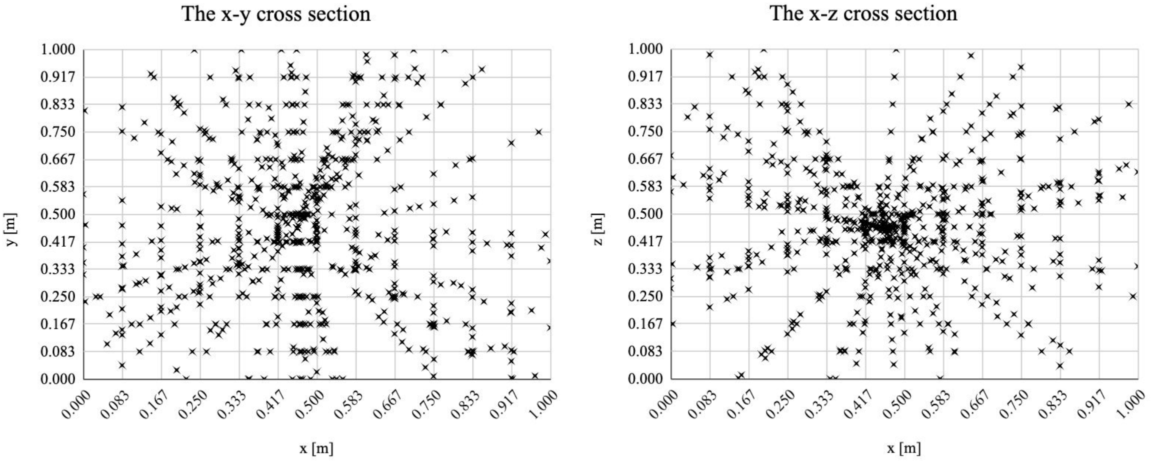

Figure 4.1: Visualisation of photon ray trajectories in a Cartesian 3D domain for illustration. The trajectories are shown at points in which a new cell is entered.

4.1.3. Discretization

So far, the generation of the emission spectrum ε_λ has not been discussed. This will be extensively elaborated on in the following sections with non-grey participating media. In case of a grey gas, a simple Planck black-body function may be used to model emission wavelengths. As discussed in Chapter 2, the Planck distribution for a black body of temperature T is given, in a λ-based formulation ($[B(\lambda, T)] = \mathrm{W/m^2 sr \mu m}$), by:

$$B(\lambda, T) = \frac{c_1}{\lambda^5 \left(e^{c_2/\lambda T} - 1\right)}, \tag{4.12}$$

with:

$$c_1 = 1.191042 \times 10^8 \left(\mathrm{W/m^2 sr \mu m^{-4}}\right) \qquad c_2 = 1.4387752 \times 10^4 (\mathrm{K\mu m}), \tag{4.13}$$

or, in a wavenumber ν formulation ($[B(\nu, T)] = \mathrm{mW\ /m^2 sr\ cm^{-1}}$):

$$B(\nu, T) = \frac{c_1 \nu^3}{e^{c_2 \nu / T} - 1}, \tag{4.14}$$

with:

$$c_1 = 1.191042 \times 10^{-5} \left(\mathrm{mW/m^2 srcm^{-4}}\right) \qquad c_2 = 1.4387752 (\mathrm{Kcm}). \tag{4.15}$$

Due to the fact that the Planck function is the weight given to the absorption coefficient when evaluating the Planck mean absorption coefficient, its spectral resolution is driving the accuracy of the emitted energy $E_{0,\gamma}$ and thus the accuracy of the results.

As a result of the shape of the Planck function, k-discretization is more suitable compared to λ-discretization (see Figure 4.2). Using the k-discretization (constant wavenumber spacing instead of constant wavelength spacing), more points are located at the steep part of the Planck curve which has a heavy contribution to the integrated emissivity and which should thus be resolved more accurately.

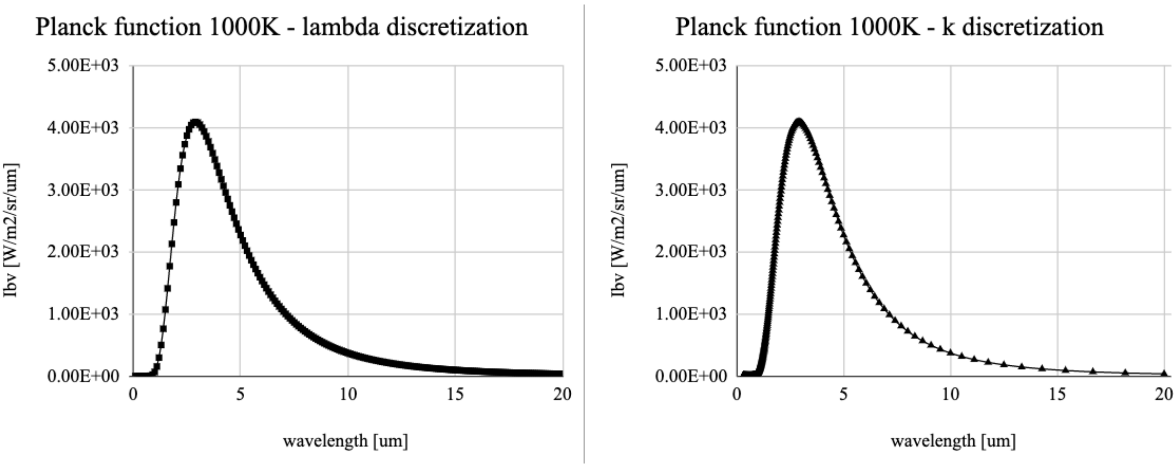

Figure 4.2: Illustration that wavenumber-based (k) discretization leads to more points located in the steep region of the Planck function unlike wavelength-based (λ) discretization, generally leading to a slightly better accuracy since majority of the radiation comes from the steep peak region.

4.1.4. Basic Flow Diagram of ERMC

The basic flow diagram of the implemented ERMC procedure is shown in Figure 4.3.

4.1.5. Boundary Conditions

In the radiation solver, four default types of boundary conditions (BCs) were implemented; wall BC, periodic BC, symmetric BC and no-initial radiance BC.

For wall boundary conditions, the temperature and reflection coefficient have to be specified, otherwise a "cold", black wall is assumed. Partly transmissive walls have not yet been implemented. For cold walls, temperature is set to -1 and in that case, the wall Planck function subroutine assigns a Planck function ratio of 0. Otherwise, the ratio of Planck functions is computed as it is for other cells, using the wall temperature.

The no-initial-radiance condition was set up for inflow and outflow boundaries. For the no-initial-radiance condition, temperature is automatically set to -2 and no heat transfer is assumed with this boundary and the photon is lost to the outside of the domain. The remaining energy is dumped back to the original cell. At a black boundary (either no-initial-radiance boundary or a black wall):

$$\Delta E_\gamma = E_{\gamma,0}\tau\Big(\frac{I_{b,\eta,i}}{I_{b,\eta,0}}-1\Big), \qquad E_\gamma = E_\gamma - \Delta E_\gamma, \qquad \tau \to 0. \tag{4.16}$$

Otherwise, if $\kappa(\text{wall}) \neq 0$:

$$\Delta E_\gamma = E_{\gamma,0}\tau\alpha\Big(\frac{I_{b,\eta,i}}{I_{b,\eta,0}}-1\Big), \qquad E_\gamma = E_\gamma - \Delta E_\gamma, \qquad \tau \to \tau(1-\kappa(\text{wall})), \tag{4.17}$$

where the reflection, changing the incoming photon vector $\boldsymbol{r}_{\gamma,0}$ to $\boldsymbol{r}_{\gamma,1}$ is computed as:

$$\hat{\boldsymbol{r}}_{\gamma,1} = \hat{\boldsymbol{r}}_{\gamma,0} - 2(\hat{\boldsymbol{r}}_{\gamma,0}\cdot\hat{\boldsymbol{n}}_{\text{wall}})\hat{\boldsymbol{n}}_{\text{wall}}. \tag{4.18}$$

Finally, in case of a periodic or a symmetric boundary, there is no additional energy transfer. In case of the former, the photon ray is simply transported to the other side of the domain with directions unchanged (e.g., if y axis is periodic and the bottom y boundary is reached, the photon is transported to the top of the domain and continues with no changes). In case of the latter, the photon is reflected off the boundary with the opposite angle to mimic symmetry with no additional heat loss.

An additional, energy-non-conserving condition was also implemented. In this case, there is no heat transfer with the boundary cell and the photon is lost outside of the domain. This condition was, however,

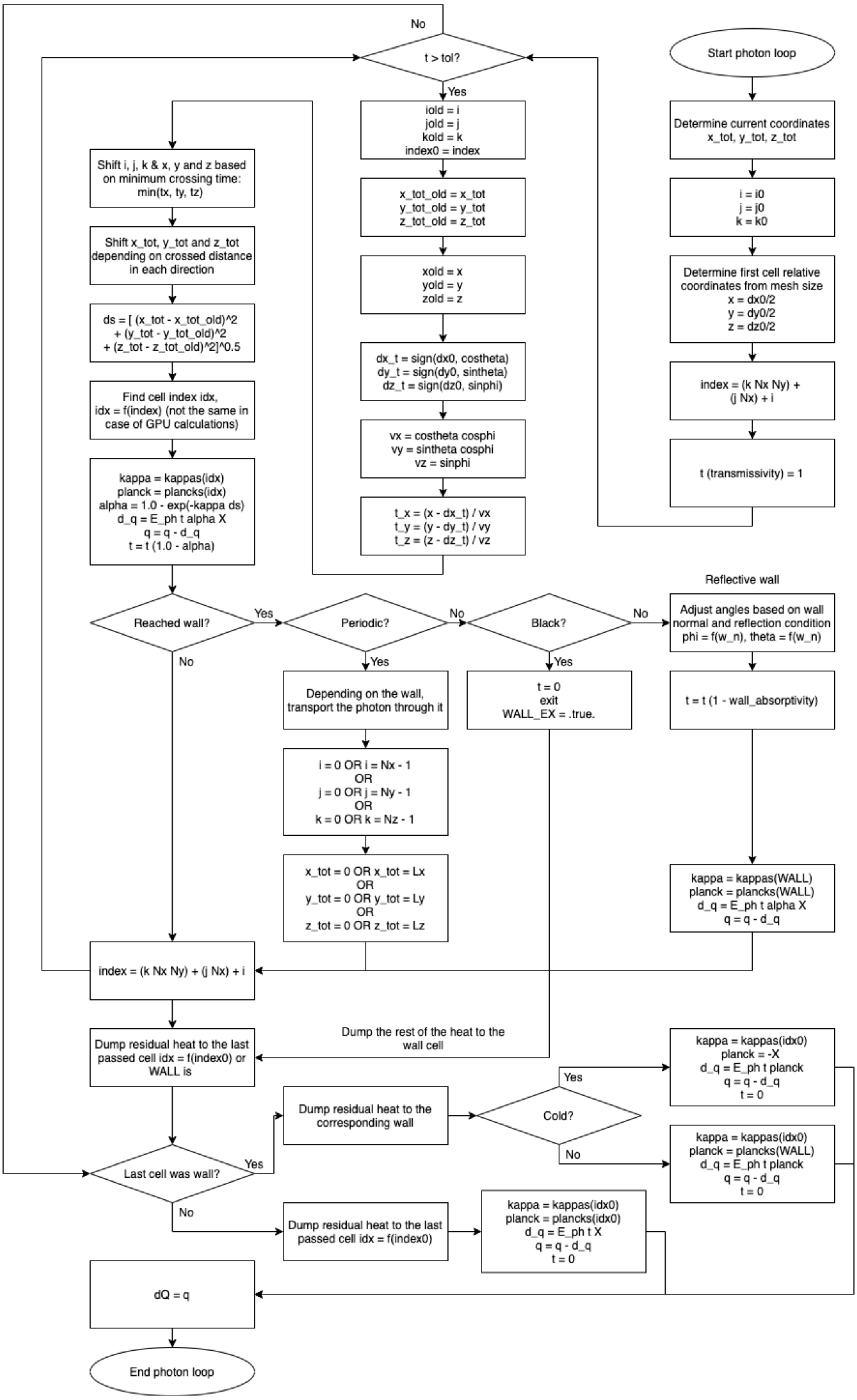
Start photon loop
Determine current coordinates x_tot, y_tot, z_tot
i = i0
j = j0
k = k0
Determine first cell relative coordinates from mesh size
x = dx0/2
y = dy0/2
z = dz0/2
index = (k Nx Ny) + (j Nx) + i
t (transmissivity) = 1
No
t > tol?
Yes
iold = i
jold = j
kold = k
index0 = index
x_tot_old = x_tot
y_tot_old = y_tot
z_tot_old = z_tot
xold = x
yold = y
zold = z
dx_t = sign(dx0, costheta)
dy_t = sign(dy0, sintheta)
dz_t = sign(dz0, sinphi)
vx = costheta cosphi
vy = sintheta cosphi
vz = sinphi
t_x = (x - dx_t) / vx
t_y = (y - dy_t) / vy
t_z = (z - dz_t) / vz
Shift i, j, k & x, y and z based on minimum crossing time: min(tx, ty, tz)
Shift x_tot, y_tot and z_tot depending on crossed distance in each direction
ds = [(x_tot - x_tot_old)^2 + (y_tot - y_tot_old)^2 + (z_tot - z_tot_old)^2]^0.5
Find cell index idx, idx = f(index) (not the same in case of GPU calculations)
kappa = kappas(idx)
planck = plancks(idx)
alpha = 1.0 - exp(-kappa ds)
d_q = E_ph t alpha X
q = q - d_q
t = t (1.0 - alpha)
Reached wall?
Yes
No
Periodic?
No
Yes
Black?
No
Yes
Reflective wall
Adjust angles based on wall normal and reflection condition
phi = f(w_n), theta = f(w_n)
t = t (1 - wall_absorptivity)
kappa = kappas(WALL)
planck = plancks(WALL)
d_q = E_ph t alpha X
q = q - d_q
Depending on the wall, transport the photon through it
i = 0 OR i = Nx - 1
OR
j = 0 OR j = Ny - 1
OR
k = 0 OR k = Nz - 1
x_tot = 0 OR x_tot = Lx
OR
y_tot = 0 OR y_tot = Ly
OR
z_tot = 0 OR z_tot = Lz
t = 0
exit
WALL_EX = .true.
index = (k Nx Ny) + (j Nx) + i
Dump the rest of the heat to the wall cell
Dump residual heat to the last passed cell idx = f(index0) or WALL is
Dump residual heat to the corresponding wall
Cold?
Yes
No
kappa = kappas(idx0)
planck = -X
d_q = E_ph t planck
q = q - d_q
t = 0
kappa = kappas(idx0)
planck = plancks(WALL)
d_q = E_ph t planck
q = q - d_q
t = 0
Last cell was wall?
Yes
No
Dump residual heat to the last passed cell idx = f(index0)
kappa = kappas(idx0)
planck = plancks(idx0)
d_q = E_ph t X
q = q - d_q
t = 0
dQ = q
End photon loop

Figure 4.3: Flow diagram of core of the Monte Carlo ray tracing code.

not tested. This concludes the description of the ray tracing. Next, the spectral additions necessary to resolve hot media spectrally, HITRAN and NEQAIR, are going to be discussed.

4.2. HITRAN

For non-grey simulations, gas spectra must be computed in the flowfield. These spectra will vary in the flowfield depending on the local conditions. Depending on the applications, two methods of spectral generation were implemented. The HITRAN database offers transition data directly, and the resulting spectra must be computed in the solver assuming LTE. NEQAIR allows non-LTE calculations, and after providing sufficient input, generates the spectra assuming the QSS assumption as discussed in the previous chapters.

4.2.1. Calculation of the Spectra from Database

Chapter 3 provided an overview and description of the parameters for each transition available in HITRAN/HITEMP; some of these are summarised in Figure 4.4. It was also mentioned that for each molecule, also the transitions for a variety of its isotopologues are presented. In the current implementation of the code, only the most naturally abundant isotopologue is considered for each species to save memory and increase speed. In the vast majority of the species, this will cause negligible difference. For example, the two most common isotopologues of H_2O and CO_2 are:

- H_2O: $H^{16}OH$ (161), nat. abundance = 99.73%, $m = 18.010565$ a. u., $Q(T_{\mathrm{ref}}) = 174.581$
- CO_2: $^{16}O^{12}C^{16}O$(626), nat. abundance = 98.42%, $m = 43.989830$ a. u., $Q(T_{\mathrm{ref}}) = 286.094$

which shows that this assumption is applicable for these species. In addition, as will be shown later, this assumption also greatly simplifies the determination of the total internal partition function needed for the calculation of the spectra.

The list of all species' isotopologues, natural abundances of the isotopologue and number of transitions in the HITRAN2012 database can be found in Appendix A. From there, it can be observed that assuming one isotopologue only might introduce errors to species such as HBr, HOBr, CH_3Br and possibly HCl, ClO, HOCl, $ClONO_2$, where the natural abundance falls below 90%. If non-neglibile errors are found, the partition functions must be pre-determined also for other isotopologues.

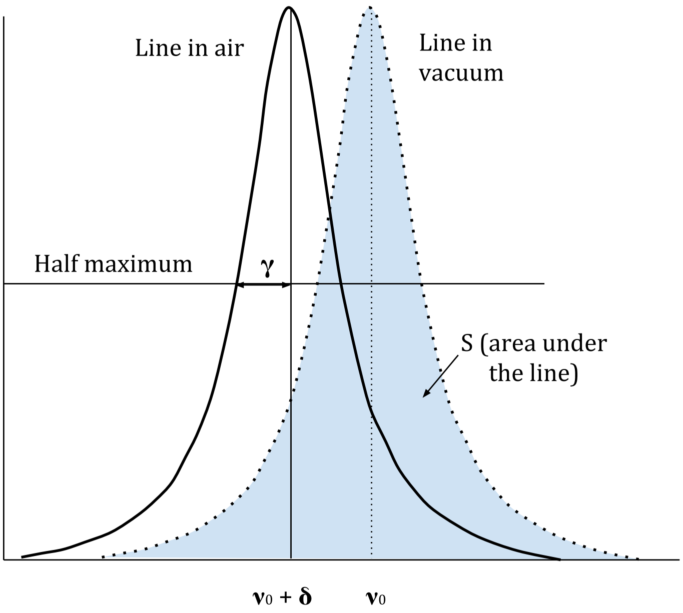

Figure 4.4: Illustration of some of the main transition parameters saved in HITRAN. S, the line strength, is the area under the line, γ is the line half width at half maximum and δ is the shift due to pressure (non-vacuum conditions).

Firstly, the line strength can be adjusted for the conditions of interest. The line strength S databased is evaluated at the reference temperature of 296K. The line strength databased in HITRAN for a given transition $i \rightarrow j$ is defined as:

$$S_{ij} = I_\mathrm{a} \frac{A_{ij}}{8\pi c \nu_{ij}^2} \frac{g' e^{-c_2 E''/T} \left(1 - e^{-c_2 \nu_{ij}/T}\right)}{Q(T)}, \tag{4.19}$$

where c_2 is 1.4387770 cm K, c is the speed of light of 2.99792458E+10 cm/s, the parameters E'', g', A_{ij} and ν_{ij} were defined in Chapter 3, and $Q(T)$ is the temperature-dependent total internal partition sum. For each energy level k, the total partition sum is:

$$Q(T) = \sum_k g_k \exp\left(-\frac{c_2 E_k}{T}\right), \tag{4.20}$$

and varies for the isotopologues of the same species. Thus, to recalculate the line strength at a new temperature $\mathrm{T_{ref}} \rightarrow \mathrm{T}$, since the Einstein A coefficient is not temperature-dependent, the following expression can be used:

$$S_{ij}(T) = S_{ij}\left(T_\mathrm{ref}\right) \frac{Q\left(T_\mathrm{ref}\right)}{Q(T)} \frac{\exp\left(-c_2 E''/T\right)}{\exp\left(-c_2 E''/T_\mathrm{ref}\right)} \frac{\left[1 - \exp\left(-c_2 \nu_{ij}/T\right)\right]}{\left[1 - \exp\left(-c_2 \nu_{ij}/T_\mathrm{ref}\right)\right]}, \tag{4.21}$$

in which everything can be extracted directly from the HITRAN data and the new conditions, apart from the ratio $\frac{Q(T_\mathrm{ref})}{Q(T)}$. This will be addressed at the end of this section.

Line Width Adjustment due to Pressure Broadening

Afterwards, the width of the line γ must be broadened accounting for pressure effects, since the HITRAN data is given for vacuum. This can be done by the following correction:

$$\gamma(p,T) = \left(\frac{T_\mathrm{ref}}{T}\right)^{n_\mathrm{air}} \left(\gamma_\mathrm{air}\left(p_\mathrm{ref}, T_\mathrm{ref}\right)\left(p - p_\mathrm{self}\right) + \gamma_\mathrm{self}\left(p_\mathrm{ref}, T_\mathrm{ref}\right) p_\mathrm{self}\right), \tag{4.22}$$

where the measured parameters n_air, γ_air and γ_self are databased. The pressure is expressed in atmospheres.

The presence of air not only broadens the line, but also shifts it. This can be corrected by the empirically determined parameters δ to allow for computation of the actual wavenumber at which the transition will be observed, ν_{ij}^*:

$$\nu_{ij}^* = \nu_{ij} + \delta\left(p_\mathrm{ref}\right) p. \tag{4.23}$$

Finally, to compute the line intensity at any wavelength due to the transition, a line profile must be assumed. Various line profiles exist, depending on which mechanism is dominant in line broadening as mentioned in Chapter 2. It was also shown in Chapter 2 that, in the majority of cases, for pressure broadened lines, the Lorentzian profile can be assumed:

$$f_\mathrm{L}\left(\nu; \nu_{ij}, T, p\right) = \frac{1}{\pi} \frac{\gamma(p,T)}{\gamma(p,T)^2 + \left[\nu - \left(\nu_{ij} + \delta\left(p_\mathrm{ref}\right) p\right)\right]^2}, \tag{4.24}$$

which is used also in the code. Otherwise, in low pressure environments, the Doppler profile should be used instead, or the Voigt profile, which is a convolution of the two profiles together. The absorption cross section, k, is then found by multiplying the profile with the line intensity S:

$$k_{ij}(\nu, T, p) = S_{ij}(T) f\left(\nu; \nu_{ij}, T, p\right), \tag{4.25}$$

and finally, the absorption coefficient is the absorption cross section multiplied by the number density N of the species:

$$\kappa_{ij} = k_{ij} N, \tag{4.26}$$

where the ideal gas law is assumed in order to arrive to the species number density:

$$N = p/(kT). \tag{4.27}$$

4.2.2. Approximation of the Total Internal Partition Function Sum

We can now return to the calculation of the ratio of the total internal partition function sums, $\frac{Q(T_{\text{ref}})}{Q(T)}$ from Equation (4.21). While various computational approaches exist to compute $Q(T)$, for the current application, where only the most commonly abundant isotopologues are assumed, Q can be considered purely as a function of temperature for the given species. Thus, to increase the performance of the code, these functions were pre-computed with the help of Ref. [2] for the available species and stored in separate text files. For quick access to the data of interest, a discretisation of 1K was used.

For the species expected to be most frequently used in the program - H_2O, CO_2 and H_2 - to avoid reading from the disk and increase speed, the pre-computed total internal partition functions were fitted using spline interpolation. The determined spline interpolation function are as follows, for H_2O:

$$f(T) = \begin{cases} 2.0688\cdot10^{-6}\cdot T^3 - 6.2065\cdot10^{-6}\cdot T^2 + 4.0258\cdot10^{-1}\cdot T + 5.9743\cdot10^{-1}, & \text{if } T \in [1,200], \\ -6.2043\cdot10^{-7}\cdot T^3 + 1.6073\cdot10^{-3}\cdot T^2 + 7.9865\cdot10^{-2}\cdot T + 2.2111\cdot10^{1}, & \text{if } T \in (200,500], \\ 4.1294\cdot10^{-7}\cdot T^3 + 5.7304\cdot10^{-5}\cdot T^2 + 8.5489\cdot10^{-1}\cdot T - 1.0706\cdot10^{2}, & \text{if } T \in (500,1000], \\ 5.2681\cdot10^{-7}\cdot T^3 - 2.8432\cdot10^{-4}\cdot T^2 + 1.1965\cdot T - 2.2093\cdot10^{2}, & \text{if } T \in (1000,1500], \\ 7.2642\cdot10^{-7}\cdot T^3 - 1.1825\cdot10^{-3}\cdot T^2 + 2.5438\cdot T - 8.9460\cdot10^{2}, & \text{if } T \in (1500,2000] \\ 9.5254\cdot10^{-7}\cdot T^3 - 2.5393\cdot10^{-3}\cdot T^2 + 5.2573\cdot T - 2.7036\cdot10^{3}, & \text{if } T \in (2000,2500], \\ 1.1053\cdot10^{-6}\cdot T^3 - 3.6852\cdot10^{-3}\cdot T^2 + 8.1222\cdot T - 5.0910\cdot10^{3}, & \text{if } T \in (2500,3000], \\ 1.5969\cdot10^{-6}\cdot T^3 - 8.1092\cdot10^{-3}\cdot T^2 + 2.1394\cdot10^{1}\cdot T - 1.8363\cdot10^{4}, & \text{if } T \in (3000,3500], \\ 5.7318\cdot10^{-7}\cdot T^3 + 2.6397\cdot10^{-3}\cdot T^2 - 1.6227\cdot10^{1}\cdot T + 2.5529\cdot10^{4}, & \text{if } T \in (3500,4000], \\ 4.6555\cdot10^{-6}\cdot T^3 - 4.6348\cdot10^{-2}\cdot T^2 + 1.7972\cdot10^{2}\cdot T - 2.3574\cdot10^{5}, & \text{if } T \in (4000,4500], \\ -1.1001\cdot10^{-5}\cdot T^3 + 1.6501\cdot10^{-1}\cdot T^2 - 7.7139\cdot10^{2}\cdot T + 1.1909\cdot10^{6}, & \text{if } T \in (4500,5000]. \end{cases}, \tag{4.28}$$

for CO_2:

$$f(T) = \begin{cases} 1.4249\cdot10^{-6}\cdot T^3 - 4.2746\cdot10^{-6}\cdot T^2 + 8.4870\cdot10^{-1}\cdot T + 3.2361\cdot10^{-1}, & \text{if } T \in [1,200], \\ 2.3117\cdot10^{-6}\cdot T^3 - 5.3637\cdot10^{-4}\cdot T^2 + 9.5512\cdot10^{-1}\cdot T - 6.7710, & \text{if } T \in (200,500], \\ 3.2301\cdot10^{-6}\cdot T^3 - 1.9139\cdot10^{-3}\cdot T^2 + 1.6439\cdot T - 1.2156\cdot10^{2}, & \text{if } T \in (500,1000], \\ 6.0464\cdot10^{-6}\cdot T^3 - 1.0363\cdot10^{-2}\cdot T^2 + 1.0093\cdot10^{1}\cdot T - 2.9380\cdot10^{3}, & \text{if } T \in (1000,1500], \\ 9.3360\cdot10^{-6}\cdot T^3 - 2.5166\cdot10^{-2}\cdot T^2 + 3.2297\cdot10^{1}\cdot T - 1.4040\cdot10^{4}, & \text{if } T \in (1500,2000], \\ 1.3551\cdot10^{-5}\cdot T^3 - 5.0453\cdot10^{-2}\cdot T^2 + 8.2872\cdot10^{1}\cdot T - 4.7757\cdot10^{4}, & \text{if } T \in (2000,2500], \\ 1.6470\cdot10^{-5}\cdot T^3 - 7.2349\cdot10^{-2}\cdot T^2 + 1.3761\cdot10^{2}\cdot T - 9.3373\cdot10^{4}, & \text{if } x \in (2500,3000], \\ 2.3962\cdot10^{-5}\cdot T^3 - 1.3977\cdot10^{-1}\cdot T^2 + 3.3989\cdot10^{2}\cdot T - 2.9565\cdot10^{5}, & \text{if } T \in (3000,3500], \\ 1.0006\cdot10^{-5}\cdot T^3 + 6.7621\cdot10^{-3}\cdot T^2 - 1.7299\cdot10^{2}\cdot T + 3.0271\cdot10^{5}, & \text{if } x \in (3500,4000], \\ 6.7372\cdot10^{-5}\cdot T^3 - 6.8163\cdot10^{-1}\cdot T^2 + 2.5806\cdot10^{3}\cdot T - 3.3687\cdot10^{6}, & \text{if } T \in (4000,4500], \\ -1.5193\cdot10^{-4}\cdot T^3 + 2.2789\cdot T^2 - 1.0742\cdot10^{4}\cdot T + 1.6615\cdot10^{7}, & \text{if } T \in (4500,5000]. \end{cases}, \tag{4.29}$$

and for H_2

$$f(T) = \begin{cases} 1.0159\cdot10^{-8}\cdot T^3 - 3.0478\cdot10^{-8}\cdot T^2 + 2.1515\cdot10^{-2}\cdot T + 9.7848\cdot10^{-1}, & \text{if } T \in [1,200], \\ -7.9164\cdot10^{-9}\cdot T^3 + 1.0815\cdot10^{-5}\cdot T^2 + 1.9346\cdot10^{-2}\cdot T + 1.1231, & \text{if } T \in (200,500], \\ 1.7632\cdot10^{-9}\cdot T^3 - 3.7043\cdot10^{-6}\cdot T^2 + 2.6606\cdot10^{-2}\cdot T - 8.6856\cdot10^{-2}, & \text{if } T \in (500,1000], \\ 6.8839\cdot10^{-10}\cdot T^3 - 4.7986\cdot10^{-7}\cdot T^2 + 2.3381\cdot10^{-2}\cdot T + 9.8797\cdot10^{-1}, & \text{if } T \in (1000,1500], \\ 8.5844\cdot10^{-10}\cdot T^3 - 1.2451\cdot10^{-6}\cdot T^2 + 2.4529\cdot10^{-2}\cdot T + 4.1404\cdot10^{-1}, & \text{if } T \in (1500,2000], \\ 5.3066\cdot10^{-10}\cdot T^3 + 7.2160\cdot10^{-7}\cdot T^2 + 2.0596\cdot10^{-2}\cdot T + 3.0363, & \text{if } T \in (2000,2500], \\ 4.2133\cdot10^{-10}\cdot T^3 + 1.5415\cdot10^{-6}\cdot T^2 + 1.8546\cdot10^{-2}\cdot T + 4.7445, & \text{if } T \in (2500,3000], \\ 3.5602\cdot10^{-10}\cdot T^3 + 2.1294\cdot10^{-6}\cdot T^2 + 1.6783\cdot10^{-2}\cdot T + 6.5080, & \text{if } T \in (3000,3500], \\ 2.8260\cdot10^{-10}\cdot T^3 + 2.9002\cdot10^{-6}\cdot T^2 + 1.4084\cdot10^{-2}\cdot T + 9.6557, & \text{if } T \in (3500,4000], \\ 4.2318\cdot10^{-10}\cdot T^3 + 1.2133\cdot10^{-6}\cdot T^2 + 2.0832\cdot10^{-2}\cdot T + 6.5870\cdot10^{-1}, & \text{if } T \in (4000,4500], \\ -2.0092\cdot10^{-10}\cdot T^3 + 9.6386\cdot10^{-6}\cdot T^2 - 1.7082\cdot10^{-2}\cdot T + 5.7530\cdot10^{1}, & \text{if } T \in (4500,5000], \\ 1.9965\cdot10^{-9}\cdot T^3 - 2.3323\cdot10^{-5}\cdot T^2 + 1.4772\cdot10^{-1}\cdot T - 2.1715\cdot10^{2}, & \text{if } T \in (5000,5500], \\ -6.4131\cdot10^{-9}\cdot T^3 + 1.1544\cdot10^{-4}\cdot T^2 - 6.1544\cdot10^{-1}\cdot T + 1.1820\cdot10^{3}, & \text{if } T \in (5500,6000]. \end{cases}. \tag{4.30}$$

The relative error of the cubic spline interpolation compared to exact data for the three species is shown in Figure 4.5. It can be seen that for temperatures of interest (higher than 500K), this error is negligible.

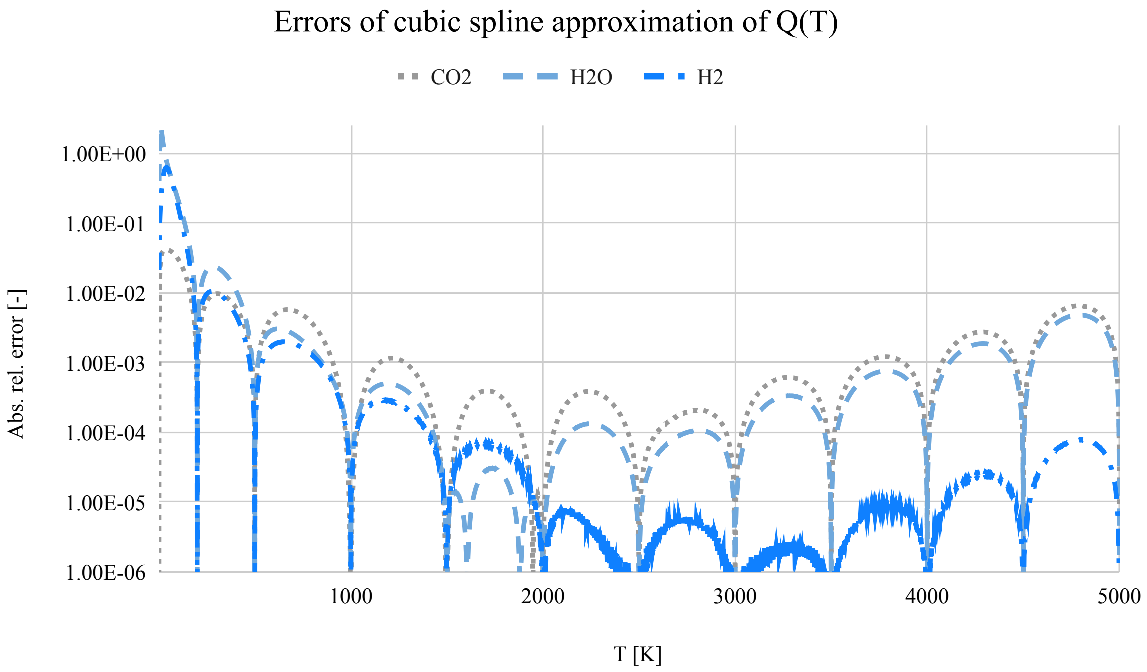

Figure 4.5: Absolute relative error in the sum of the total partition function when evaluated using cubic splines developed in Equations (4.28), (4.29) and (4.30) for H_2O, CO_2 and H_2, respectively.

4.2.3. Implementation Details

The number of transitions, even when neglecting the less abundant isotopologues, can be of hundreds of thousands for complex species such as water or carbon dioxide with dozens of rovibrational bands (see Appendix A). In addition, the lines are very narrow. This means, that to accurately resolve the spectrum including the maxima of the very strong lines, which are needed as those will be the wavelengths at which the cell will mostly emit, a very fine discretization of millions of wavelengths might be required, easily exceeding several GB required in random access and virtual memory.

To avoid the memory problems while also properly resolving the maxima of the spectra to allow for accurate integration, the spectral discretization was adjusted such that instead of following a pre-determined step in λ, the wavelengths at which the spectrum is computed are the centres of the transitions. Thus, the line intensity at those wavelengths will always correspond to the line maxima.

While this approach allows for accurate resolution of the maxima, it also artificially increases the emitted energy, since the minima are generally not resolved. This biases the integral to be higher than in reality, which projects into overestimation of the emitted energy (from the definition of the Planck mean absorption coefficient).

To resolve the maxima precisely while at the same time also accurately determining the emission integral $\int_0^\infty \kappa I_{b,\nu} d\nu$, artificial zero absorption coefficients points were added around the lines. The distance from the line centre both up and down to the zero points was calculated such that the areas below the line S and the triangular area obtained while integrating are the same. The principle is shown in Figure 4.6.

The actual implementation of this principle for an H_2O spectrum is shown in Figure 4.7. The light spectra is the original while the dark spectra is the spectra obtained by using the discretization above. The following can be deduced:

- The reduced spectrum hits the lines at their maxima in the centre as expected
- The maxima as computed in the reduced spectra of the high intensity lines are higher than those for which a constant λ spacing is used
- Apart from high intensity lines, the other lines in the reduced spectra are underestimated

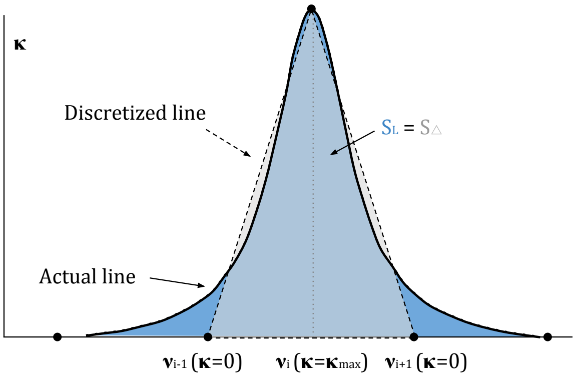

Figure 4.6: Visualisation of the discretization principle for fast HITRAN calculations of the emission spectra. Both the maximum absorption cross section as well as the area under the curve are preserved, leading to both accurate integral and κ_p as well as correct sampled emitting wavelengths.

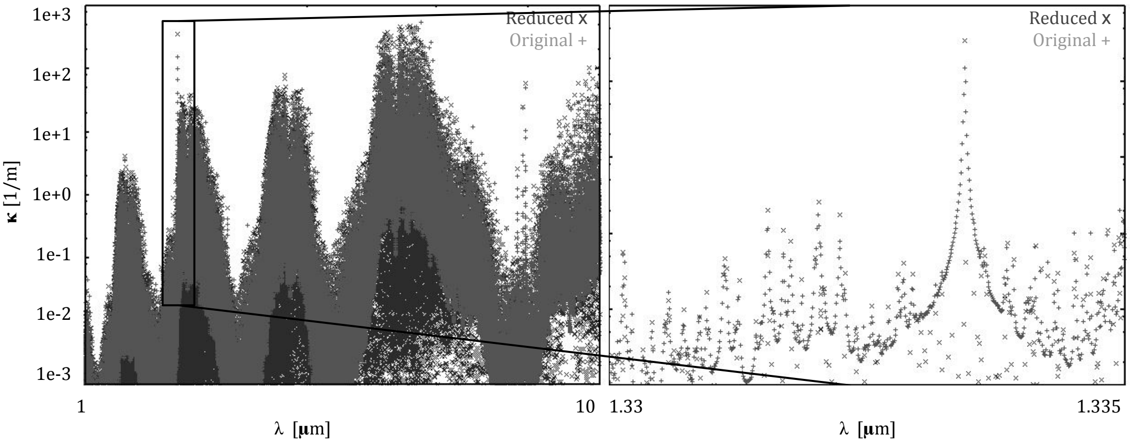

Figure 4.7: Demonstration of the principle shown in Figure 4.6 applied to a real spectrum. The light grey + data represents the original spectrum whereas the dark x data shows the reduced, fast calculation.

The reason why the maxima of the intense transitions are higher for the current implementation with non-constant spacing is the fact that the maximum is hit exactly, while in case of the spectrum with constant-spacing, it is very unlikely that the true maximum will be resolved.

For the weak lines, the resolved absorption coefficient is much lower than the actual one. That is because the surrounding line strengths are not taken into account, as correcting the peak intensity by the presence of other lines would increase the integral and make this calculation technique less accurate. This holds mainly for weak lines in close proximity to the strong lines. Since all the areas are accounted for exactly, this does not affect the emission integral and causes no error. In addition, these lines are very weak even if the presence of other lines is accounted for and would thus most likely never be selected during emission wavelength sampling. The validation of this reduced discretization is shown in Figure 4.8 for CO_2 and in Figure 4.9 for H_2O, where the computed Planck mean absorption coefficient with the reduced method (dark triangle) is compared to known data from Ref. [68] (black line) and results when using the full technique (bright diamond). The slight disagreement between the data from Ref. [68] and the obtained coefficients at very high temperature of CO_2 are most likely due to recent updates to HITRAN (from 2017), where corrections were added to some of the high temperature CO_2 lines, which were not yet implemented during the time of writing of Ref. [68]. This is thus most likely not due to the reduced technique adapted as described above, since this disagreement was also seen when the full, formal approach was used.

However, the underestimation of the weak transitions is also the reason why this technique can be only used when computing emission and not absorption. Suppose that radiation in a medium of nonhomogeneous pressure is being modelled. Pressure shift causes a slight shift of the most intense lines at which the medium emits. According to the discretization shown in Figure 4.6, the absorption coefficient decreases

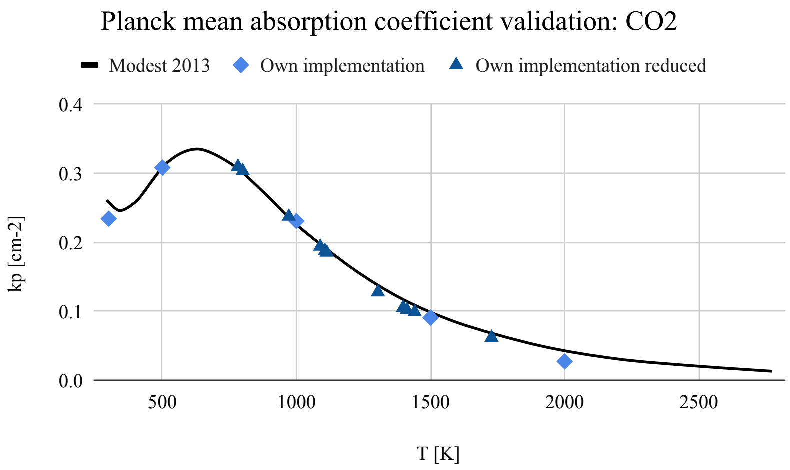

Figure 4.8: A comparison between an accurate and simulated Planck mean absorption coefficient for CO_2 with the original and the reduced spectral technique, showing an excellent agreement in the range where HITRAN is accurate despite the use of the reduction technique. Validation data from [68].

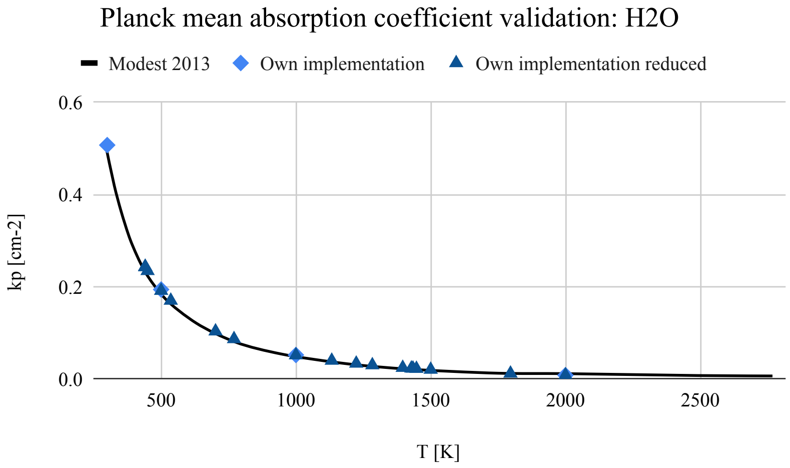

Figure 4.9: A comparison between an accurate and simulated Planck mean absorption coefficient for H_2O with the original and reduced spectral technique, showing an excellent agreement in the range where HITRAN is accurate despite the use of the reduction technique. Validation data from [68].

down to zero much faster than if the line continued in a Lorentzian/ Voigt fashion or, especially, if it was combined with a weak transition. Thus, when determining the absorption coefficient at a given wavelength during the photon ray loop, the correct shapes of the lines must be used along with accounting for the effect of the neighbouring lines, otherwise an underestimation of the absorption occurs. While this type of calculation is definitely much more time and memory consuming, the absorption coefficient must be resolved this accurately only around the target wavelengths instead of having to recreate the entire spectra as needed when computing emission.

Therefore, the reduced triangular technique is used when generating emission spectra and emission wavelengths by the cell being computed where maxima and integral must be accurate, and the proper, full approach is used when determining the absorption coefficients of the rest of the flowfield at the emitted wavelengths when the absorption coefficient needs to be accurate.

One of the reasons why the standard HITRAN API (HAPI) library was not used and an own API was developed is the fact that HAPI computes everything using the full approach. This means that compared to the method described above, where emission and absorption are computed differently, the time needed for generation is much longer with the original HAPI. The comparison between the generation of spectra of the

Table 4.1: A comparison of the performance of the standard HITRAN processing library API and own implementation. The respective speedup thanks to the developed techniques is also shown.

Species	Average HAPI time [s]	Average own t [s]	Speedup
H_2O	40	1	40x
CO_2	50	10	5x
H_2	2.5	0.007	370x

default tool HAPI set to default settings and that of the reduced spectral technique is shown in Table 4.1. The reason for much longer times to compute CO_2 compared to H_2O is the fact that it has double the number of transitions, which is also why the H_2 case took so short (as it only needed to process around 3500 lines).

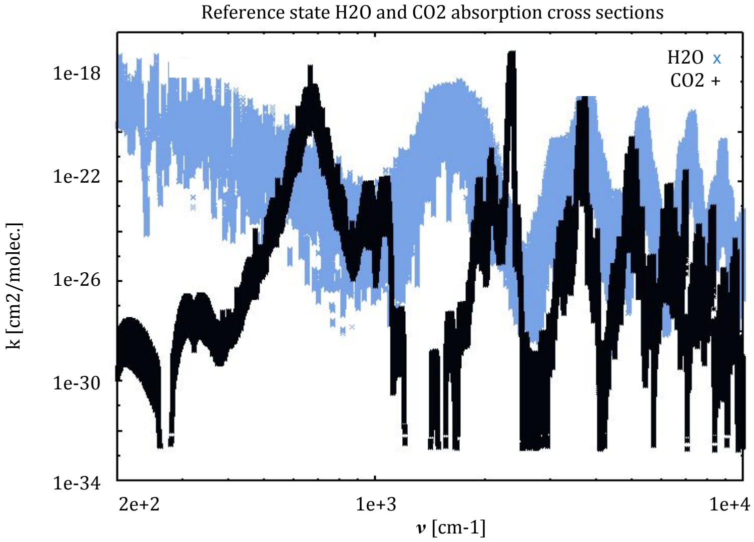

Figure 4.10: Transition cross sections for H_2O and CO_2 at reference conditions for illustration of the typical cross-section spectra.

Figure 4.10 shows the comparison of the two species cross sections at reference conditions. Despite the fact that the CO_2 spectrum looks thinner and less complex, it contains more than 2x the number of transitions. Similar species, for which the $O(10^1)$ s times can be expected, are CH_4, HNO_3, and O_3. For all other molecules, the times should be maximum of O(1)s, and for the majority, based on their database sizes, of $O(10^{-1})$s down to $O(10^{-3})$s, as seen for H_2. Table 4.1 shows that the smaller the number of transitions, the higher the expected speedup thanks to the here developed spectral reduction technique. This is most likely because for the very large files, majority of the time is spent on reading the data, which is the same for both methods.

Obviously, the easiest method to further accelerate the solution is to set appropriate lower and upper wavelengths, between which the coefficients are solved. Two cumulative emissivity distributions for water and carbon dioxide at varying temperatures were computed and are shown in Figure 4.11. These can be used for intuition when selecting the maximum and minimum wavelength limits to reduce computational time while also avoiding the introduction of unnecessary errors. The grey mode allows for calculation of these bounds directly from the Planck function and Wien's displacement law, but for HITRAN, since very strong transitions on the edges of a spectrum might compensate for a weak Planck function, this was not implemented.

Additional acceleration is achieved by an artificial cut-off. In theory, to accurately resolve the absorption coefficient, the contribution of all transitions should be considered for all resolved wavenumbers k (as the Lorentzian / Doppler or Voigt profile does not have a specific cut-off). However, since the number of transitions is very high, the resulting double loop of n_k by $n_{\text{trans.}}$ yields times of order of hundreds of seconds for the generation of a single spectrum.

Instead, a running index array j_0 is used to mark the lines at least 50 line half-widths (at T_{ref} and p_{ref}), $\gamma(p_{\text{ref}}, T_{\text{ref}})$ past the current wavelength, the lines behind which are no longer considered for calculation.

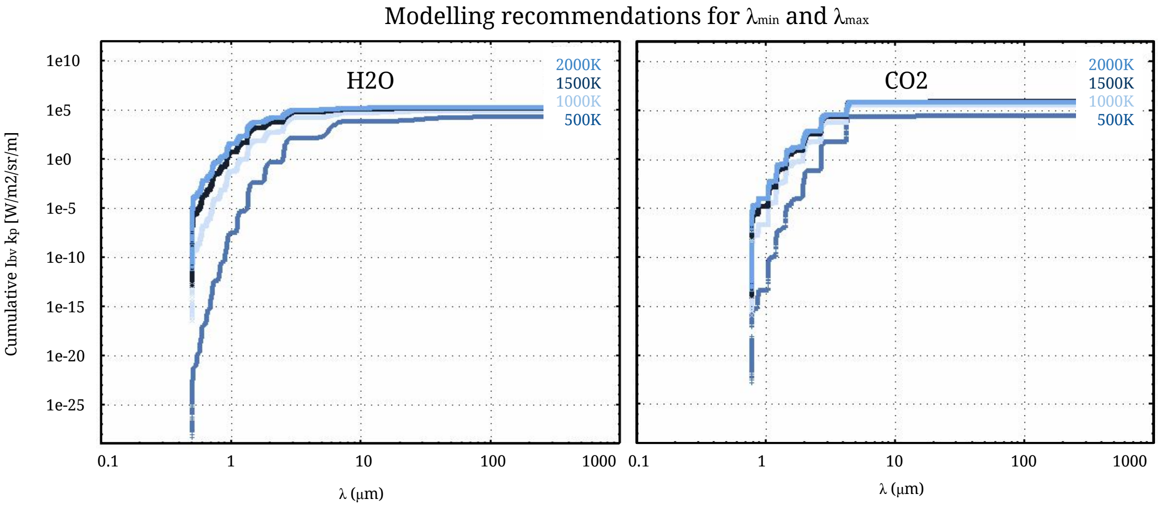

Figure 4.11: A depiction of the cumulative emissivity of H_2O and CO_2 for various temperatures to indicate the requirements for the minimum and maximum resolved wavelength.

Table 4.2: A short overview of the contents of the HITEMP database. For accuracy at high (> 3000K) temperatures, it contains 25 times more lines for CO_2 and more than 500 times the lines for H_2O.

Molecule	Number of isotopologues	Total number of transitions	Spectral Coverage [cm-1]
H_2O line list	6	114,241,164	0 - 30000
CO_2 line list	7	11,193,608	258 - 9648
CO line list	6	113,631	3 - 8465
NO line list	3	115,610	0 - 9274
OH line list	3	41,557	0 - 19268

All the other transitions within λ - 50 $\gamma(p_{\mathrm{ref}}, T_{\mathrm{ref}}) < \lambda < \lambda$ + 50 $\gamma(p_{\mathrm{ref}}, T_{\mathrm{ref}})$ are then considered for the given wavelength λ. The parameter of 50 was chosen according to the suggestions of HAPI (see Ref. [54]).

Additional speedup was achieved by saving the transition number during sampling of the emission wavelengths for faster search through the data when determining the respective absorption coefficients. For single species media at similar pressures, it is most likely that the same transition that is responsible for emission will also be the one most heavily contributing to absorption. This means that binary search through all the transitions to find the one at the correct wavelength is not necessary, and only the vicinity of the emitted transition number is quickly scanned.

The last two additional measures discussed resulted in roughly 10 times speedup in determination of the absorption coefficient.

4.2.4. HITEMP and Other Databases

The HITEMP database has the same shape and format as HITRAN, it just contains many more lines as these become dominant at high temperatures (for cases >> 1000K). The species most relevant to the potential applications of this thesis work are covered in HITEMP, databases of which should be used for high temperature simulations are summarised in Table 4.2. For example, for H_2O, the HITEMP database contains more than 200x the number of lines which are available in HITRAN. Since the computational times scale with the number of transitions, this database should only be used when truly necessary for high temperature applications.

4.3. NEQAIR

NASA's NEQAIR code was used to generate spectra for nonequlibrium applications. Since, for these cases, the Planck function is not a simple function of temperature and wavelength, both the emission and the absorption spectra have to be computed separately and, in NEQAIR, this is done using the QSS assumption. For more information about the dynamics of the collisional-radiative processes considered in NEQAIR, refer to Chapter 3. The nonequilibrium Planck function is then computed from the ratio of emissivity to the absorption coefficient.

To illustrate the difference between a close-to-equilibrium and nonequilibrium Planck function with 2kK difference between the translational and electron temperatures, refer to Figure 4.12. It is easily observed that the nonequilibrium Planck function behaves erratically and cannot be described by simple relations such as Equation (2.2).

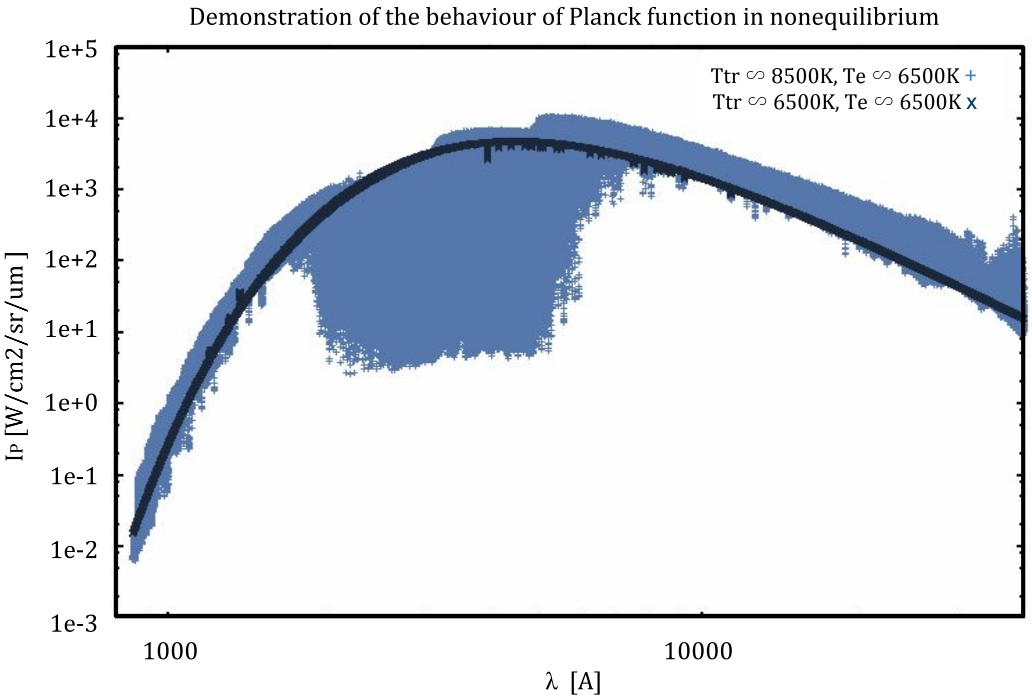

Figure 4.12: A comparison between the Planck function defined as a ratio between the emissivity and the absorption coefficient for conditions close to an equilibrium (lighter blue + data) and in a high nonequilibrium (dark x data) for a Nitrogen mixture.

4.3.1. NEQAIR Modifications and ADF

NEQAIR was written as a standalone code capable of solving the RTE using several approximate methods, such as the TS method, the spherical cap method or simple line-of-sight integration. Since in this thesis work, NEQAIR will be only used to calculate the local absorption and emission spectra, for efficiency, its main program, I/O subroutines, modules of shared variables and parallelisation scheme were rewritten to comply with the rest of the radiation code. As the release of NEQAIR is restricted, more detailed information about the internal re-structuring and re-organisation will not be published. NEQAIR as a standalone code capable of integrating the RTE using the TS method in 1D was also used to generate validation data, as will be discussed in Chapter 5.

In addition, as mentioned in Chapter 2, there were inconsistencies and outdated information in NEQAIR databases of transition data. For example, many Einstein coefficients were found to be inaccurate compared to the most recent NIST database, causing erroneous atomic radiation predictions. Similarly, the electronic transition data, such as Franck-Condon factors for many important diatomic species, were either missing or erroneous, as for example in case of NO, which is a heavy radiator. Thus, at the beginning of the thesis work, the Amsterdam Density Functional, ADF, code from Software Chemistry and Materials (see Ref. [1]) was used to recompute the Franck-Condon factors and update the Einstein coefficients based on the up-to-date databases present in ADF. However, since during the thesis work, a new version of NEQAIR was released, NEQAIRv15, with the errors corrected and updates implemented, the adaptation of the generated database computed from ADF was eventually not required.

4.3.2. Non-equilibrium Adjustments to Photon Monte Carlo Formulation

Since the two-temperature model is assumed, whenever discussing the mean temperature $\overline{T}$ in the context of nonequilibrium, the averaging $\overline{T} = \sqrt{T_{\mathrm{tr}} T_e}$ will be used. This comes from the fact that a large portion of the reaction kinetics also scales with this mean, as seen in Table 3.2.

In Equations (4.2) and (4.1), the expression for the emitted energy is derived considering the integral of the emissivity for bodies in LTE. Considering global sampling, this relationship originally comes from the following expression:

$$E_{\gamma,0} = \frac{4\kappa_P(T_{\mathrm{max}})T^4_{\mathrm{max}}\sigma}{N_\gamma} = \frac{4\pi}{N_\gamma}\int_0^\infty I_{b,\eta}\kappa(T_{\mathrm{max}})d\eta, \tag{4.31}$$

which means that in case of nonequilibrium, the emitted energy will be computed as, for local sampling:

$$E_{\gamma,0} = \frac{4\pi}{N_\gamma}\int_0^\infty \epsilon(T_{\mathrm{tr},0}, T_{\mathrm{ev},0})d\eta, \tag{4.32}$$

and for global sampling:

$$E_{\gamma,0} = \frac{4\pi}{N_\gamma}\int_0^\infty \epsilon(T_{\mathrm{tr}}(\overline{T}_{\mathrm{max}}), T_{\mathrm{ev}}(\overline{T}_{\mathrm{max}}))d\eta. \tag{4.33}$$

Since the Planck function now differs from the regular temperature-dependent Planck function $I_{b,\eta}$, it is denoted as $I^{\mathrm{noneq.}}_{b,\eta}$ and determined from the ratio of $\varepsilon_\lambda/\kappa_\lambda$. Then, the transferred energy during cell crossing will be equal to, for local sampling:

$$\Delta E_\gamma = E_{\gamma,0}\tau\alpha\Big(\frac{I^{\mathrm{noneq.}}_{b,\eta,i}}{I^{\mathrm{noneq.}}_{b,\eta,0}} - 1\Big), \tag{4.34}$$

or in case of global sampling, with the corresponding correction:

$$\Delta E_\gamma = E_{\gamma,0}\tau\alpha\Big(\frac{I^{\mathrm{noneq.}}_{b,\eta,i}}{I^{\mathrm{noneq.}}_{b,\eta,0}} - 1\Big)\frac{\int_0^\infty \epsilon(T_{\mathrm{tr},0}, T_{\mathrm{ev},0})d\eta}{\int_0^\infty \epsilon(T_{\mathrm{tr}}(\overline{T}_{\mathrm{max}}), T_{\mathrm{ev}}\overline{T}_{\mathrm{max}}))d\eta}. \tag{4.35}$$

Otherwise, the rest of the PMC procedure remains identical to the procedure for equilibrium cases. The wavelength generation using the random number R_λ is then determined directly from the emissivity cumulative distribution, instead of the product of absorption coefficient and the equilibrium Planck function (see Equation (4.8)):

$$R_\lambda = \frac{\int_0^{\lambda_\gamma} \varepsilon_\lambda d\lambda}{\int_0^\infty \varepsilon_\lambda d\lambda}, \tag{4.36}$$

where it is to be noted that while the wavenumber v or k description was applied to HITRAN and grey cases, since very hot nonequilibrum media radiates at much higher frequencies, the wavelength λ description is used now, generally given in the units of Å. This also simplifies coupling with NEQAIR. The illustration of the selection of the wavelengths from the cumulative distribution for a highly spectrally variable N + O hypersonic plasma for 100 photon rays is shown in Figure 4.13 for illustration of a typical spectrum.

4.3.3. NEQAIR Simulation Set-up Paramters

NEQAIR offers a wide range of parameters to run the simulations. A default user-independent simulation setup was generated to automate the simulation process. The following parameters were pre-set:

- Spectral region discretization
- Type of non-Boltzmann method
- Type of absorption method

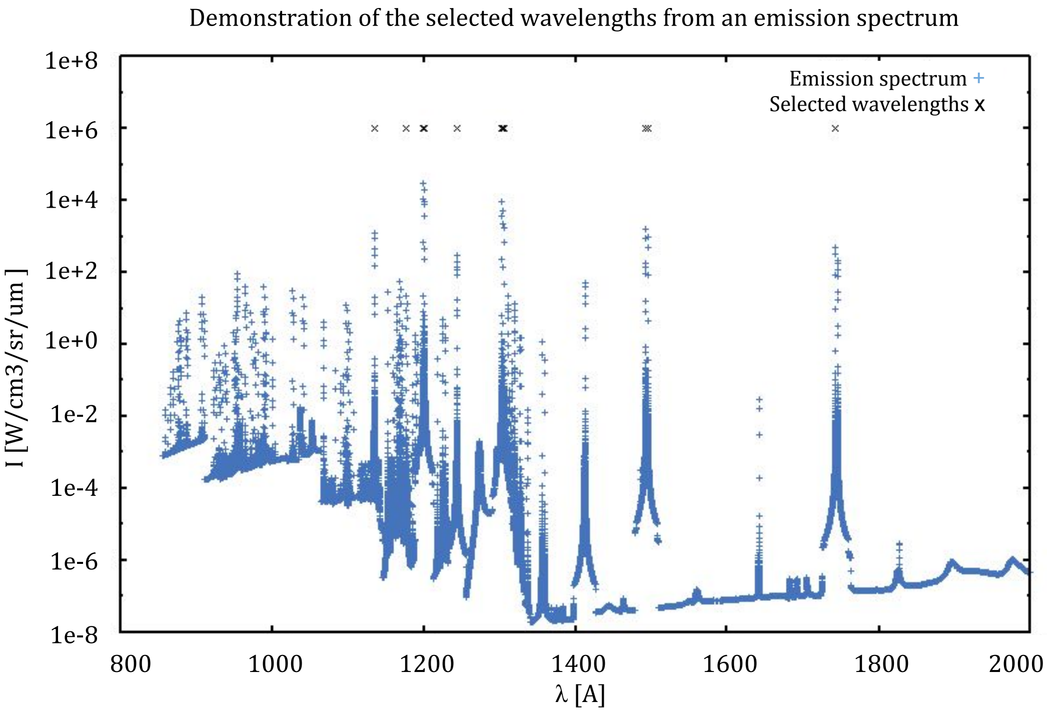

Figure 4.13: An illustration of a 100 selected wavelengths from a highly variable emission spectrum of hot air.

Table 4.3: The pre-set automatic spectral discretization used for NEQAIR subroutines.

λ_{min} [A]	λ_{max} [A]	Spacing type	Points per line	Range
855.000	2000.000	A	1-10	600
2000.00	6000.000	A	1-10	50
6000.00	12000.00	A	1-10	25
12000.0	200000.0	A	1-10	10

The other parameters required for NEQAIR, such as the type of the RTE calculation, the boundary conditions or the scanning function are not applicable, since NEQAIR is only used for spectral generation and not for solving of the actual radiation field.

In high temperature hypersonic flow, as discussed in Chapter 2, the majority of the radiation comes from the high energy region in VUV due to atomic radiation. The radiance for two typical entry cases defined in NEQAIR (Crew Exploration Vehicle and FIRE II, profiles of which will be discussed in the next Chapter) are shown in Figure 4.14, demonstrating this fact since the majority of the energy is seen to come from regions below 1000Å - 5000Å (recall that 1Å = 0.1nm).

Based on the best practices for these cases set by the authors of NEQAIR in Ref. [16], the discretization parameters set in the spectral regions are as shown in Table 4.3. The "A" spacing type means that constant spacing is not used, and instead, the discretization mode of setting the number of points-per-line (ppl) is implemented. This means that NEQAIR determines the spacing automatically, such that the given number of points for each spectral line is achieved. This is a technique similar to the HITRAN implementation mentioned earlier. The evaluation of the optimum number of ppl will be addressed in the next Chapter. "Range" determines to how far out the calculation of line broadening is performed, as a multiple of the line width. For HITRAN when determining the absorption coefficient, this was 50. Since the atomic lines are very high intensity and very narrow, for the VUV region, this number is set to very high.

As of now, a non-Boltzmann method is assumed automatically. Even though some of the regions might be in equilibrium, separate equilibrium/ nonequilibrium calculation would require separation of these regions when calling NEQAIR to compute their spectra, likely resulting in a drop in efficiency in parallelisation of this process. The only time when Boltzmann distributions are enforced is when the temperatures in the LOS data

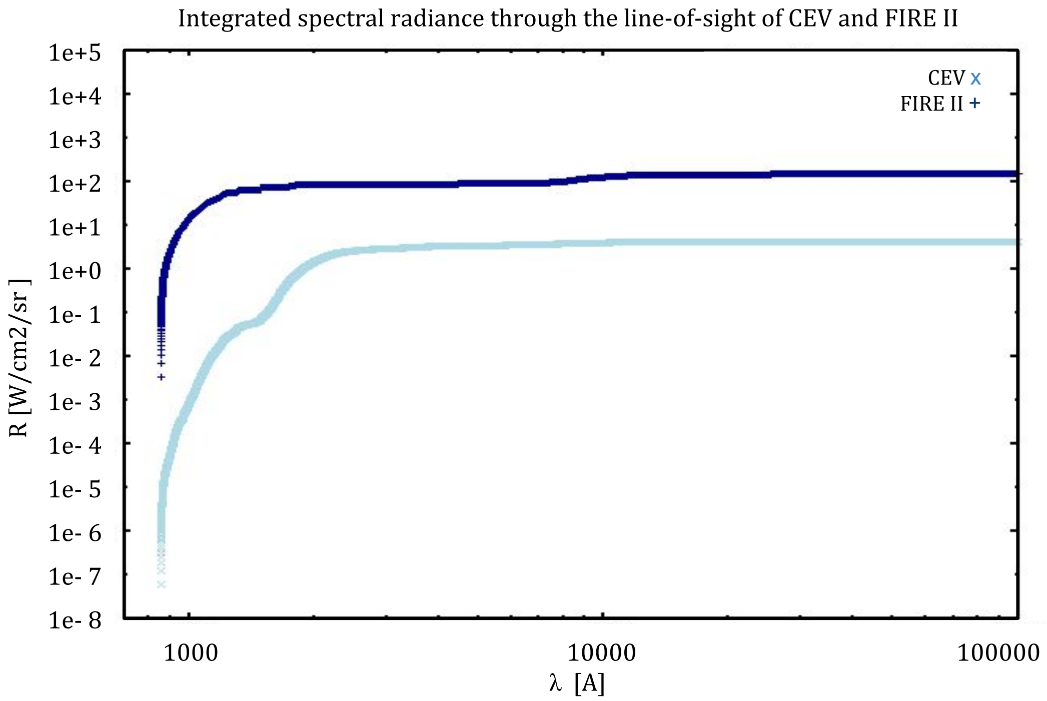

Figure 4.14: The integrated spectral radiance for two Earth reentry cases to indicate the necessary requirements on minimum and maximum wavelengths needed to be resolved to capture the essential spectral featured.

are too small. Then, an attempt to compute QSS might result in a crash of the program when inverting the QSS matrix and so enforcing equilibrium is a better option.

NEQAIR offers a wide range of choices for non-Boltzmann methods. The fastest flux-limited method recommended by the authors of NEQAIR in Ref. [16] is set as a default. In case its calculation fails, it is recommended to try a different method.

Finally, the absorption method determines how NEQAIR treats non-local transport. This refers to the fact that rates of certain excitation and de-excitation processes, which have to be accounted for when computing the local spectra, are driven by the interactions of the composition of the local gas with the radiation field from further away. The typical approach how this is handled in NEQAIR is through the definition of an escape factor Λ, as already seen in the previous Chapter. Then, the radiance is approximated using the local radiation coefficients accumulated over some distance d, which is typically in the order of the shock stand-off distance, and is a user input into the developed solver.

For example, for b-f radiation at i-th line, the absorption coefficient is given by

$$\kappa_i^{bf} = k_{ab,i} N_i - k_{st,i} N_+ N_e, \tag{4.37}$$

in which k are the absorption cross sections, and the subscript "st" refers to stimulated emission. The emission coefficient is given by:

$$\varepsilon_i^{bf} = k_{em,i} N_+ N_e. \tag{4.38}$$

From detailed balance (see previous chapters), the absorption coefficients satisfy the following relations:

$$k_{ab,i} = \sigma_{ab,i} \qquad k_{st,i} = \frac{g'}{g^+}\frac{\Lambda^3}{2}\exp\left[\frac{E_+ - E_i - hc/\lambda}{kT}\right] k_{ab,i} \qquad k_{em,i} = \frac{hc^2}{\lambda^5} k_{st,i}, \tag{4.39}$$

in which Λ is the escape factor above discussed. This can be also seen from the Master Equations (3.56) and (3.57) with Λ mentioned explicitly. From Equations (4.39), it is clear that the error in the escape factor directly translates into the error in the stimulated emission cross section, and thus also in absorption and emission coefficients.

Table 4.4: Differences in radiative surface heatflux on the CEV backshell when using various NEQAIR absorption methods.

Case	$Q_{s,\mathrm{rad}}$ [W/cm^2]
Boltzmann	2.08
Saha	291.36
Escape factor = 0	6.44
Escape factor = 1	3.62
Local	5.24
Non-local (tangent slab)	3.97
Non-local (weighted)	6.70

NEQAIR also allows for an accurate treatment of non-local transport, by solving the local spectra, integrating the radiation field, and iterating until the solution converges. This approach is needed for regions of, for example, very high nonequilibrium or strongly absorbing boundary layers (see Ref. [25] for details). However, this approach is by orders of magnitude slower and more memory consuming than the approximation with an escape factor and is thus not recommended, as it might have insignificant impact on the results. In case of high nonequilibrium or strongly absorbing boundary layers, both approaches should be evaluated before continuing the calculations with the fast, local mode. The possible differences in surface heat flux resulting from these differences, evaluated on the backshell case of CEV in high nonequilibrium, are shown in Table 4.4 from Ref. [25]. It is obvious that significant errors might arise if the chosen method is inappropriate. However, it is also clear from Table 4.4, that even with a full non-local transport considered, the solution is extremely sensitive to the chosen RTE method.

In the code developed, the non-local mode can be switched on by setting the stand-off distance d to a negative value. The non-local mode was, however, not applied in further simulation work since it usually caused insufficient-virtual-memory-related errors on the high performance cluster and was not deemed necessary. Possibly, first an approximate calculation using NEQAIR with the TS method alone could be performed to obtain an indication whether non-local calculation is needed before running such demanding calculations. Or, considering the sensitivity of these calculations to the parameters not clearly known a priori as seen from Table 4.4, even a random number generator might provide a result of a similar accuracy without the waste of computational resources.

4.4. INCA Implementation

Finally, the radiative solver must be coupled to INCA CFD. The required inputs, principles of coupling and the challenges encountered are discussed in the following subsections.

4.4.1. Required CFD Inputs

The radiation code presented above was initially developed as a standalone software which can be coupled to CFD. For a proper resolution of the radiative heat flux, each type of simulation (grey / HITRAN/ NEQAIR modes) requires a different set of input variables. The main ones are summarised in Table 4.5.

The flowfield data and boundary conditions are extracted directly from INCA. The most important information about the radiation simulation, which is the 2nd grid geometry (number of cells in each dimension), the type of simulation (1 for grey, 2 for HITRAN and 3 for NEQAIR), $\kappa_{\mathrm{const.}}$ for grey simulations and a wall reflection coefficient are part of the main `inca.inp` parameter file, along with the IDW "smoothness" exponent and type of 3rd grid spectral approximation. The rest of the simulation setup from Table 4.5 is specified in a file `radparam.inp`.

4.4.2. Implementation Principle

INCA operates such that one or several grid blocks are assigned to each processor. The processors do not have an access to the solution vector from each grid block, only to their own. In an ideal scenario, a similar principle of separation of grid blocks could be used for the radiation calculation. However, radiation is a global problem, and so if the domain was split, excessive communication between the processors would be required during the solution, most likely decreasing the efficiency of the parallelisation. Therefore the most straightforward, least error-prone method of implementation is its solution on a unified grid containing all the grid blocks with adjusted spacing. This means that a new unified grid (2nd grid) is created for radiative

Table 4.5: The input dataset required for each type of radiation simulation.

Parameter category	Parameter	Type	Grey	HITRAN	NEQAIR
2nd grid geometry					
	Domain dimension	6: real	x	x	x
	Number of cells	3: integer	x	x	x
3rd grid geometry					
	Domain dimension	6: real			x
	Number of cells	3: integer			x
Flow BCs					
	Periodicity	6: bool	x	x	x
	Wall condition + Twall	6: logical + 6: real	x	x	x
	Far field	6: logical	x	x	x
Radiative BC					
	Wall reflectivity	1: real	x	x	x
	No initial radiance	6: logical	x	x	x
	Constant kappa	1: real	x		
Flowfield data					
	Ttr	N_{cells}: real	x	x	x
	Tv	N_{cells}: real			x
	N	$N_{\text{cells}} \cdot N_{\text{species}}$: real			x
	p	N_{cells}: real		x	
	Species names	N_{species}: char(len=6)		x	x
Simulation setup					
	Temporal discretisation	1: integer	x	x	x
	No. photons	1: integer	x	x	x
	Sobol/ Random	1: logical	x	x	x
	Self absorption	1: logical	x	x	x
	Local/ global sampling	1: logical	x	x	x
	Paths to HITRAN	1: char(len=200)		x	
	Paths to NEQAIR	1: char(len=200)			x
	Radiation "dt"	1: integer	x	x	x
	NonBoltz "d"	1: real			x
	Analytic approximation	1: logical			x
	IDW "p" parameter	1: real	x	x	x

heat flux solver. The downside of this is the fact that the data has to be interpolated between the two grids using inverse distance weighting (IDW). This introduces additional performance degradation and might cause artificial smoothing of the data. The process of how the radiation is determined starting from the 1st INCA grid is the following:

1. Determine total number of cells and grid blocks present on the 1st grid
2. Determine the 2nd unified grid's dimensions
3. Extract local processor solution vector for all cells, get number density as: $N_y = N_A \rho_y \frac{R_y}{R_{\text{univ.}}}$
4. Send the processor solution vector p, T_{tr}, T_v, N of all cells to the master
5. If master, unify the solution vectors of all processors
6. Broadcast the unified solution vectors to all slaves
7. Use IDW to interpolate all values (here y) onto the 2nd grid: $y = \frac{\sum_{i=0}^{N(\text{cells})} w_i y_i}{\sum_{i=0}^{N(\text{cells})} w_i}, \quad w_i = \frac{1}{d(\boldsymbol{x}-\boldsymbol{x_i})_i^p}$
8. Check for exceptions and bad data (see the following subsection)
9. Invoke the radiation solver to obtain source term on the 2nd grid

10. Use IDW to interpolate $\nabla \cdot q_{\text{rad}}$ back to the unified grid
11. Check for potential NaNs and infinities in $\nabla \cdot q_{\text{rad}}$
12. Extract processor $\nabla \cdot q_{\text{rad}}$ from the unified grid
13. Subtract the source term from the energy equation

For the IDW process, various exponential factors were examined. While $p = 1$ gave a smooth solution, it also made it impossible to resolve shocks properly without very fine spectral resolutions. Thus, $p = 1$ or $p = 2$ is usually used, depending on the expected gradients in the problem.

While this procedure might appear straightforward, due to the universality of the CFD code (various geometries, various flow conditions etc.), several additional requirements and challenges were posed onto the solver by implementation. These will be shortly discussed next.

4.4.3. Geometry and Flow Obstructions

Initially, for validation purposes of the independent solver, only simple domains were tested with the code (box domains in 3D or simple domains in 1D). To couple the code with a CFD solver which also supports more complex geometries, it had to be assured that the code can detect walls and obstructions inside of the domain, which will then either absorb or partly reflect the photon rays, depending on their reflection coefficient or the nature of the boundary. Note that partly transmissive walls were not considered in the current implementation. In addition, INCA also supports geometries which have a shape of higher complexity than a simple box, and which are not enclosed by walls (see for example the domain tested in Chapter 5).

INCA provides the wall distance in each cell in form of a scalar field, which thus can be used to determine the actual locations of the walls. From the gradient of this field, the wall-normal unit vector can also be determined. This approach works well when walls are actually present, but is insufficient for domains which are not box-like without actual walls at these irregular boundaries. In such cases, the no-initial-radiance BC is applied to this boundary, or a wall of a reflective coefficient of 1 is considered if these boundaries are symmetry planes.

To determine whether an irregularity in the geometry is present, the 2nd (radiation) and 1st grid are compared. The 2nd grid is always regular and box-like, but can be filled with no-radiance or wall obstructions cells which are not computed and to which the photon rays never enter. An example of such a problem containing a domain with a step (white regions without 1st grid cells) and the currently implemented method of determination of these obstructions is shown in Figure 4.15.

Gaps or endings on the 1st grid are detected while evaluating cell distances for the IDW process. It is found in which axis the nearest cell lies, and if this nearest 1st grid cell distance is larger than half of the 2nd grid cell dimension in the respective axis, the 2nd grid cell is regarded to be outside of the 1st grid domain. This is illustrated in Figure 4.15 for both aligned and misaligned grids (2nd radiation grid if shown in blue dashed lines and 1st INCA grid in black lines). The resulting grid geometries after detection are, for each case, shown on the right side. Obviously, grid misalignment means that the end of the domain will be shifted such that it corresponds to the borders of the radiation cells.

This also means that if said obstruction is smaller than the 2nd grid cell dimension, it will not be detected. This should be respected when deciding upon the dimensions of the radiation mesh and problem geometry.

4.4.4. Flow Related Implementation Challenges

According to the NEQAIR guide in Ref. [16], NEQAIR should not be used for temperatures below 500K. Many CFD solutions, however, also include the pre-shock freestream and far fields, which can get as low as 40 - 50K. Especially during the solution convergence, some of these temperatures might get even lower. For temperatures below 400-500K, the nonequilibrium models might fail to converge when computing and inverting the QSS condition, resulting in the crash of the program.

However, it is still necessary to compute the spectra in these cells at least approximately, since these cells will be absorbing and transmitting the radiation from the shock region. Thus, if a certain line of sight includes such very low temperature cells, Boltzmann calculation is used instead, which does not result in crashing. The spectral solution might include values defined as NaN, but these are then subsequently filtered out and replaced with continuum values. Examples of such bad spectra at low temperatures for a general air mixture (N, O and NO), computed assuming Boltzmann distribution, is shown in Figure 4.16. It is obvious that these spectra are not very accurate even when resolved with legitimate values instead of NaNs, but since these cells

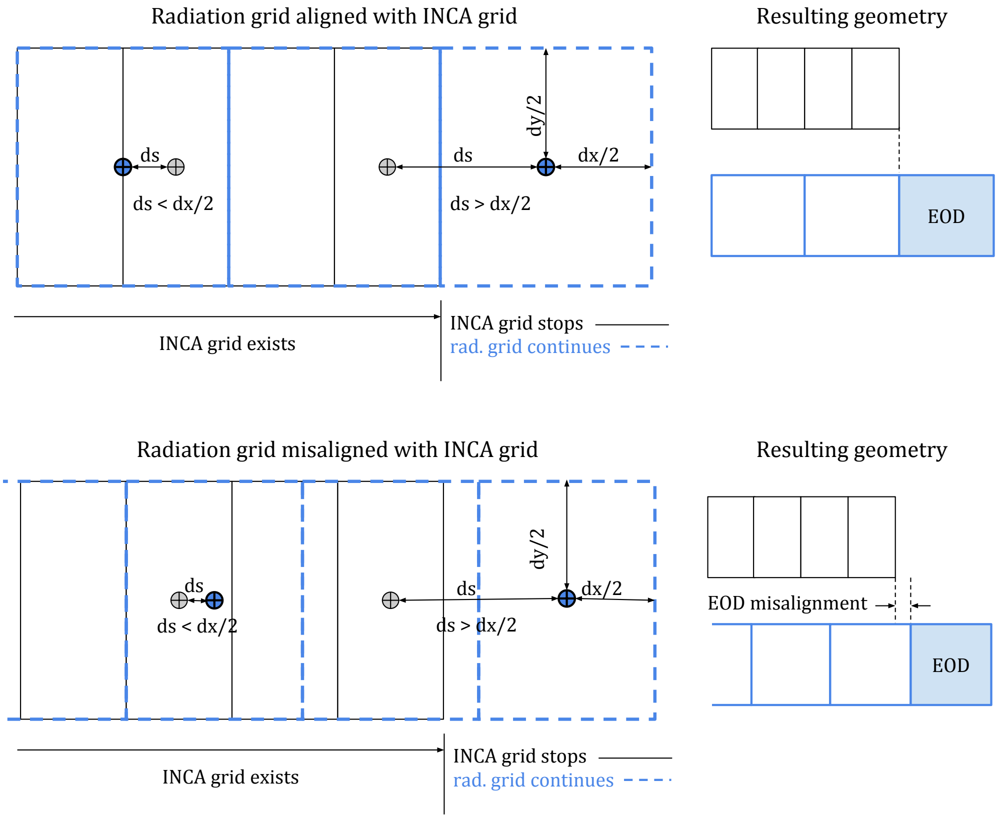
Radiation grid aligned with INCA grid
Resulting geometry
ds
ds < dx/2
ds
dy/2
dx/2
ds > dx/2
EOD
INCA grid exists
INCA grid stops
rad. grid continues
Radiation grid misaligned with INCA grid
Resulting geometry
ds
ds < dx/2
ds
dy/2
dx/2
ds > dx/2
EOD misalignment
EOD
INCA grid exists
INCA grid stops
rad. grid continues

Figure 4.15: An illustration of the principle of detection of the end of a computational domain (EOD) from INCA. On the upper part of the Figure, a case of aligned grids is shown. The right radiation cell (in blue dashed lines) is outside of the INCA grid (black thin lines). This is detected by the comparison of the distance ds of the radiation cell centroid (blue) to the nearest INCA cell centroid (grey). Since this distance is larger than half of the dimension of the radiation cell in the axis where the nearest INCA cell is located (x-axis, dx), the radiation cell is considered outside of the domain. For the left radiation cell, the nearest centroid is less than $dx/2$ away, and thus this cell is a part of the domain. The same scenario is illustrated on the lower half for non-aligned grids, showing the source of the misalignment in the domain boundaries as a result. In case the nearest cell was located in the y axis, ds would be compared to $dy/2$.

will not be radiating a lot compared to the high temperature region, it is believed that no significant error will be introduced to the solution. In addition, with the analytic adjustment technique adapted for spectral approximation on the 2nd grid, as will be discussed in Chapter 6, these spectra can be re-adjusted back down according to their real temperatures. For the future development of the program, it is suggested that a separate library is used to resolve cold cell spectra instead of NEQAIR, such as a HITRAN routine adjusted for mixtures. This would increase accuracy, save time and also save memory.

In addition, in the current state, INCA has not been configured to work with ionised mixtures with free electrons. This means that b-f and f-f radiation might not be accurately resolved in case the transport of electrons and ions is not computed properly. The computation of b-f and f-f contribution is skipped completely in case electrons and ions are omitted from the mixture.

As a result of the above, the following problem cases are currently implemented in INCA to prevent program crash during radiation calculation (and a warning is thrown to the radiation output file):

- If $\max(T) < 500$K: NEQAIR radiation calculation skipped
- If $\mathrm{any}(T) \leq 0$K: radiation calculation skipped
- if $\mathrm{any}(T) = \mathrm{NaN}$: radiation calculation skipped
- If $\mathrm{any}(T) < 500$K: LTE assumed, applied Boltzmann modelling

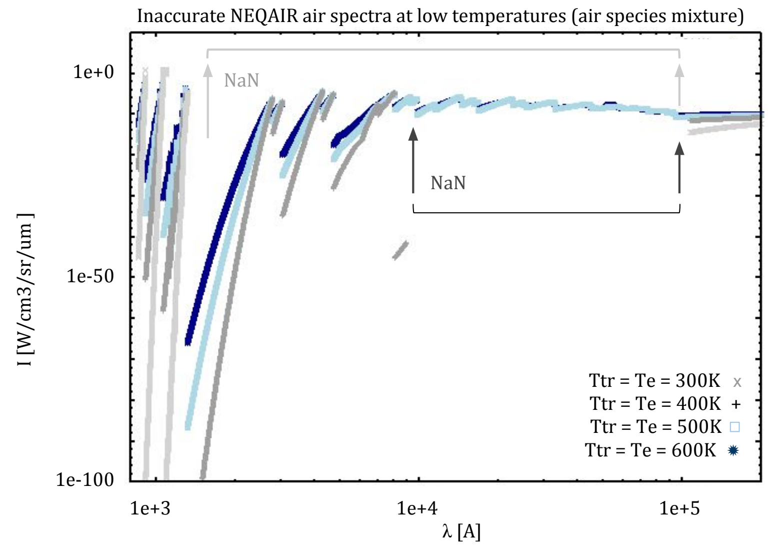

Figure 4.16: Illustrations of the problematic results obtained when using NEQAIR for flow at low temperatures. The missing section for temperatures of 300K (grey x signs) and 400K (dark grey plus signs) represents the regions where the values which come from NEQAIR are undefined. The values for 500K (light blue squares) and 600K (dark blue stars) are resolved without errors.

- If N(E-) or N(ions) missing: NEQAIR f-f and b-f radiation calculation skipped
- If any(N) = NaN: NEQAIR radiation calculation skipped
- If any(N) < 0cm^{-3}: NEQAIR radiation calculation skipped
- If any(p) < 0Pa: HITRAN radiation calculation skipped
- If none of the species recognised: NEQAIR and HITRAN radiation calculation skipped
- If $\kappa_{\text{const.}} < 0$: grey radiation calculation skipped

Since HITRAN calculations are currently implemented such that only temperature was considered variable, a warning is also thrown if large pressure fluctuations are detected, and only the average pressure is used. To make HITRAN calculations practical from the perspective of speed, the parallelisation is done in such a way that the processors pre-calculate the spectra at the temperature conditions given and only load them later during ray tracing (see the user manual). Thus if the pressure was also considered to be variable, this pre-calculation would have to be done in a two dimensional way - for both pressure and temperature. In general, pressure changes cause the pressure shift of the lines, broadening of the lines in the spectra and the magnitude of the absorption coefficient (since the cross section is multiplied by the number density to obtain the absorption coefficient). For relatively small pressure variations of a couple of percent, when pressure broadening and shifting effect is not very significant, the same spectra can be used everywhere, recomputed with the local pressure ratio. For an indication of how strong the effect of pressure broadening is, the spectra of H_2O at reference temperature (296K) and at 0.2atm, 1atm and 5atm are shown in Figure 4.17.

While it is clear from Figure 4.17 that relatively large pressure variations must be present to significantly alter the spectra and to require complete recomputing, the specific value for which this has to be done depends on the species and temperature and thus cannot be given. Figure 4.17 should rather act as an illustrative example of these differences, and any HITRAN cases with pressure larger variations than 10% - 20% without adjusted pre-databasing should be treated with caution in the current solver configuration.

4.4.5. Coupling Frequency

The second to last aspect of implementation with INCA to discuss before moving onto the results is the selection of the coupling frequency based on the intended application.

As already mentioned in Chapter 2, while close coupling is recommended for TRI studies in combustion flows (update of the radiation field with each CFD iteration), this coupling does not need to be so tight for

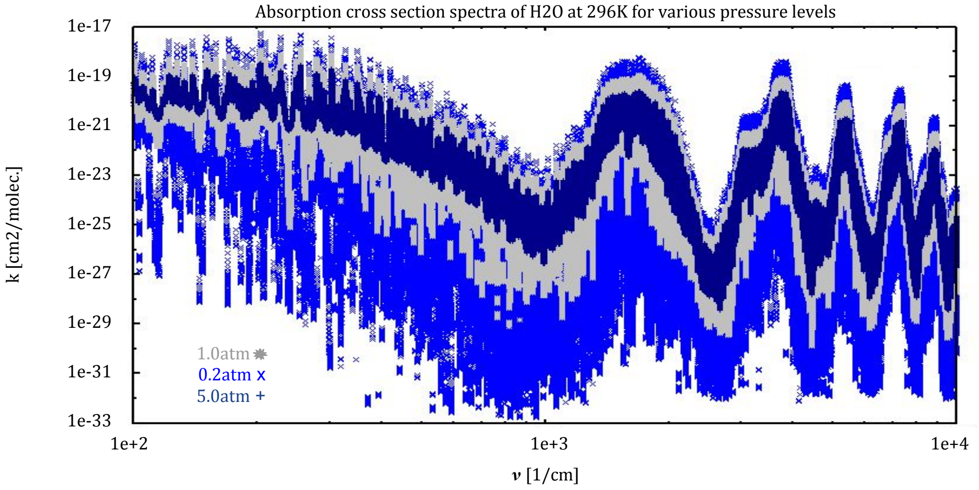

Figure 4.17: The effect of pressure broadening for H_2O at reference temperature (296K) for pressure levels of 0.2, 1.0 and 5.0 atmospheres. As can be seen, for small variations in pressure (10-100%), the spectra should not differ significantly and the absorption coefficient can be recomputed by the pressure ratio.

many hypersonic flows in which radiation is not the main contributor to heat flux and where spectral generation is an especially complex task due to nonequilibrium.

The definition of the Goulard number, expressing the significance of the effects of radiation on the overall heat flux was defined by Goulard in Ref. [39] in 1961 as:

$$\Gamma = \frac{2q^R_{unc}}{\frac{1}{2}\rho_\infty V^3_\infty}, \tag{4.40}$$

where q^R_{unc} is the uncoupled radiative heat flux. Depending on the Goulard number, the following coupling regimes are usually defined (see for example Ref. [78]):

- Close/ tight coupling, $\Gamma > 0.01$
- Loose coupling, $\Gamma \approx 0.01$
- Uncoupling, $\Gamma \ll 0.01$

Close coupling requires radiation to be recomputed after every iteration of the flowfield. Loose coupling requires iteration every N iterations of the flowfield, ranging from 10 to 1000 depending on the case. Complete decoupling is possible for conceptual studies, but was found to show significant errors if Goulard number is not much smaller that 0.01 (as can be seen from, e. g., studies of Titan entry by Wright et al. in Ref. [117]). The significance of radiation on the overall energy budget should be monitored during the initial CFD calculations and the coupling frequency adjusted accordingly.

The figure of 0.01 comes originally from the Stardust trajectory, in which the radiation accounted for less than 10% of the total heat flux, corresponding to $\Gamma \approx 0.01$. It was seen that loose coupling could be applied without a very significant reduction in accuracy (see e.g. Ref. [64]). According to the study of Tauber and Wakefield in 1971 (see Ref. [107]), for conceptual estimations, the ratio of the coupled to uncoupled heat flux can be also estimated using:

$$\frac{q^R_{\text{coup}}}{q^R_{\text{unc}}} = \frac{1}{1+\text{const.}\Gamma^{0.7}}, \tag{4.41}$$

where a constant of 0.345 is suggested for air and 0.3 for Jovian entry. The Γ in various (re)entry environments will be discussed further to give the reader an intuition of what level of coupling can be expected depending on the (re)entry environment.

Relatively small Goulard numbers can be expected for Earth entry with relatively small nose radii such as Stardust or Orion CEV (0.01 to 0.02). For Stardust, the coupling requirements were as low as once in 1000-2000 iterations (see Ref. [30]) to keep the errors insignificant. Similar findings were obtained for Mars Science

Laboratory entry where coupling of once in 2000 iterations was found sufficient by Palmer et al. (see Ref. [78]) for a Goulard number of 0.0002 - 0.009.

For higher nose radius Martian entry (Orion CEV) with Goulard number > 0.02, a coupling of once every 10 iterations was necessary at the peak heat flux point as found in Ref. [31]. The largest Goulard numbers are found for optically thick atmospheres such as Jovian entry or Titan entry. Full coupling was required for Goulard number of 0.4 for Titan entry simulations performed by Wright et al. in Ref. [117].

4.4.6. Coupling with Nonequilibrium PMC

Finally the energy source term application should be discussed for the case of nonequilibrium. The application in case of equilibrium is straightforward, where the divergence of the heat flux is subtracted from the energy budget. In nonequilibrium simulations however, several energy budgets are present for the various internal modes, as well as for the global energy. In a 4T model, the energy equations solved are the global energy conservation, electronic/ electron energy conservation and vibrational energy conservation.

As discussed in Chapter 2, three radiative mechanisms are present in the plasma; b-b transitions, b-f (f-b) transitions and f-f transitions. The logic followed by Park in Ref. [81] and from personal communication with Dr. Karl from the Institute of Aerodynamics and Flow Technology, DLR, Goettingen is outlined below.

B-b transitions are mostly dominated by electronic transitions and thus affect primarily electronic energy. While rovibrational bands are also present and included in b-b transitions, these states rather broaden the spectral line in a way mostly symmetric around the central electronic spectral line. Thus, the probability that the vibrational energy increases is similar to the one that it decreases, resulting in a net zero vibrational energy addition.

There are pure vibrational bands included in b-b transitions, but as discussed in previous chapters, these are usually located in far IR and thus do not have a very significant contribution to the energy budget.

F-f transitions mostly concern free electrons. Since four and two temperature models are typically considered, where it is assumed that the electronic temperature of the heavy particles is the same as that of free electrons ($T_{el} = T_e$), this will also only affect the budget of the electronic energy, not the vibrational one.

F-b (b-f) transitions, similarly to the case above, concern free electrons and electronic states of the heavy particles. The same reasoning can thus be applied as in the case above, in that it concerns the electronic energy budget and not the vibrational energy equation.

Based on the arguments above, the radiative heat flux is accounted for in the electronic and total energy conservation equations. Since E_e is not yet implemented in INCA, only the total energy budget is modified.

This discussion concludes the description of the implementation. With an overview given about how the solver works, the next Chapter will show its performance when compared to validation data and its computational requirements when coupled with CFD.

5

Validation Results

While validation and verification details of some subroutines of the solver were already given in Chapter 4, it is still necessary to confirm the correct function of the entire code covering all its parts together. This Chapter aims to summarise the validation cases and the respective results and estimate the errors where appropriate. It also aims to assess the performance of the code when coupled with INCA. Firstly, the testing logic is presented, followed by grey test cases, HITRAN test cases and finally, NEQAIR test cases. The Chapter is concluded by a demonstration of a simulation coupled with INCA CFD.

5.1. Test Selection

As discussed in the previous Chapter, the code consists of the following main routines:

- Definition of geometry of the radiation grid layer(s)
- Spectral generation
- Calculation of emission spectrum and wavelength sampling routines
- Calculation of absorption coefficients and Planck function ratios for heat transfer routines
- Ray tracing routine including boundary condition implementation and possible wall reflections

To ensure that all these routines are confirmed to work correctly, the following tests were to be carried out:

1. Test of a grey medium at $\kappa = 1$ m^{-1} in 1D to determine whether basic PMC scheme works in a black wall enclosure and with periodic domains
2. Test of a grey medium at $\kappa \neq 1$ m^{-1} in 1D to determine the correct operation of emission wavelength sampling and absorption/ Planck function ratio calculations
3. Test of a grey medium at $\kappa \neq 1$ m^{-1} in 3D to determine the correct calculation of 3D heat transfer
4. Test of any media with variable domain dimensions to prove correct mesh operations and resizing
5. Test of any media with a partly reflective wall to determine correct treatment of non-black walls
6. Test of at least two non-grey participating media at LTE to confirm correct implementation of HITRAN
7. Test of at least two non-grey non-LTE hypersonic cases to confirm the correct implementation of NEQAIR

These tests allowed to verify at least twice the correct operation of every essential portion of the code, and were, in different combinations, carried out by 14 different validation test cases. The description of these test cases and the respective results will be discussed in the sections following. The cases are summarised in Table 5.1. The boundary conditions are given in the order of x_{front}, x_{back}, y_{top}, y_{bottom}, z_{left}, z_{right}. "W" in the boundary conditions stands for a wall (either black or reflective, hot or cold), "P" stands for a periodic boundary condition and "N" stands for the no-initial-radiance condition, as defined in the Chapter 4.

Table 5.1: The summary of the validation cases.

Case	Name	Spectral	Boundaries	Dim.	Source	Comments
1	Grey #1	$\kappa = 1\ \mathrm{m}^{-1}$	W, W, P, P, P, P	1D	Ref. [98]	
2	Grey #2	$\kappa = 1\ \mathrm{m}^{-1}$	W, W, P, P, P, P	1D	Ref. [98]	
3	Grey #3	$\kappa = 5\ \mathrm{m}^{-1}$	W, W, W, W, W, W	3D	Ref. [92]	
4	Grey #4	$\kappa = 0.5\ \mathrm{m}^{-1}$	W, W, W, W, W, W	3D	Ref. [92]	
5	HITRAN #1	H_2O	W, W, P, P, P, P	1D	Ref. [52]	
6	HITRAN #2	H_2O	W, W, P, P, P, P	1D	Ref. [52]	Resized x-axis domain
7	HITRAN #3	CO_2	W, W, P, P, P, P	1D	Ref. [23]	
8	HITRAN #4	CO_2	W, W, P, P, P, P	1D	Ref. [23]	Partly reflective walls
9	NEQAIR #1	NLTE mixture	W, W, P, P, P, P	1D	NEQAIR	Equilibrium only
10	NEQAIR #2	NLTE mixture	N, W, P, P, P, P	1D	NEQAIR	Nonequil. only
11 a, b	NEQAIR #3	NLTE mixture	N, W, P, P, P, P	1D	NEQAIR	l0cm and 1cm scales
12 a, b	NEQAIR #4	NLTE mixture	N, W, P, P, P, P	1D	NEQAIR	lcm and 0.1cm scales

The reasoning behind the different scales simulated for the two NEQAIR test cases is the fact that the media are fairly opaque in some regions and the photon rays are typically absorbed within a couple of cell passages, especially if the scales are large (10-100cm). This means that even if there were minor errors which would show only for heat transfer between cells of very different temperatures, these might not be revealed in large scale cases where the photons would never make it to those regions. Similarly, if the heat flux divergence was driven by the heat transfer between cells with very high temperature differences, larger scale cases would allow the photons to be absorbed much earlier before these regions are reached and reveal how the heat transfer behaves between cells of similar conditions.

5.2. Discretisation and Convergence

In the validation cases, it was observed that already a fairly coarse spatial, angular and spectral discretization produced relatively accurate results. For all domains apart from the nonequilbrium cases, 10-20 cells along each dimension were sufficient, typically with requirements of 1000-5000 photons to reach accurate agreement. Since these calculations served for testing of the code and thus very high accuracy and convergence studies were not required as the actual solutions were known, the calculations were stopped when the differences between successive runs in the divergence of heat flux were below roughly 5%. This was set to 10% for the 3D domains since these, due to their three dimensional nature, required many more cells to be resolved compared to the periodic cases. For 1D domains, the heat flux was averaged along the periodic boundaries. Example convergence plots for some of the grey cases will be presented in the next Chapter.

For the nonequilibrium cases, the mesh was made to roughly match the mesh of the 1D technique, preset in the test cases library of NEQAIR for the two entry cases 11 and 12. For the other two cases 9 and 10, 16 and 17 data points were chosen, both for PMC as well as for NEQAIR. Due to high gradients and a fairly coarse mesh considering these gradients, 10000-20000 photons were used for these cases after which the divergence of the heat flux would stay typically within 10% at each location. This was deemed sufficient, as similar errors are expected in the spectral generation by NEQAIR, and since the computational time requirements scale in proportion to the number of photons.

As for the spectral discretization, for grey cases, 100 000 wavelengths were evaluated for the emission spectrum, starting from 1/1000th of the wavelength of maximum emission computed according to Wien's displacement law. For HITRAN, all transitions in the range from 0.01μm to 20000μm were considered and the discretization of the emission spectrum followed the reduction technique introduced in the previous Chapter. The obtained κ_P was verified with literature as shown in Figure 4.8 and 4.9.

Finally, as will be justified in the following Chapter, 1 point per line was selected for the NEQAIR cases and with the spectral band parameters as given in Table 4.3.

5.3. PMC Implementation and HITRAN Spectral Generation

For verification and validation of the code in the equilibrium mode, 8 cases were considered following Ref. [98]. In all the cases below, sampling from the highest temperature cell in the domain (global sampling) was applied, since the absorption coefficients are relatively low, making this sampling physical.

5.3.1. Case 1 and Case 2: Basic PMC Principles in 1D

The first two cases focused on testing the basic PMC procedures such as photon ray tracing, wavelength sampling and heat transfer. The validation data were based on analytical solutions in 1D from Ref. [98]. Thus the code developed implemented periodic boundary conditions and averaging across the periodic dimensions was applied when evaluating the total heat transfer. Case 1 was defined with a linear temperature profile:

$$T_m = 500 + 1000x[\mathrm{K}], \quad T_{w1} = 500[K], \quad T_{w2} = 1500[\mathrm{K}], \tag{5.1}$$

and with a constant absorption coefficient of $\kappa = \kappa_P = 1\ \mathrm{m}^{-1}$. The second case was computed with the same absorption coefficient and parabolic temperature distribution:

$$T_m = 500 - 2000x^2 + 2000x[\mathrm{K}], \quad T_{w1} = T_{w2} = 500[\mathrm{K}]. \tag{5.2}$$

Figure 5.1 and 5.2 show a very good agreement with the analytical solutions already for 100 photon rays and fairly coarse meshes, validating the adapted approach.

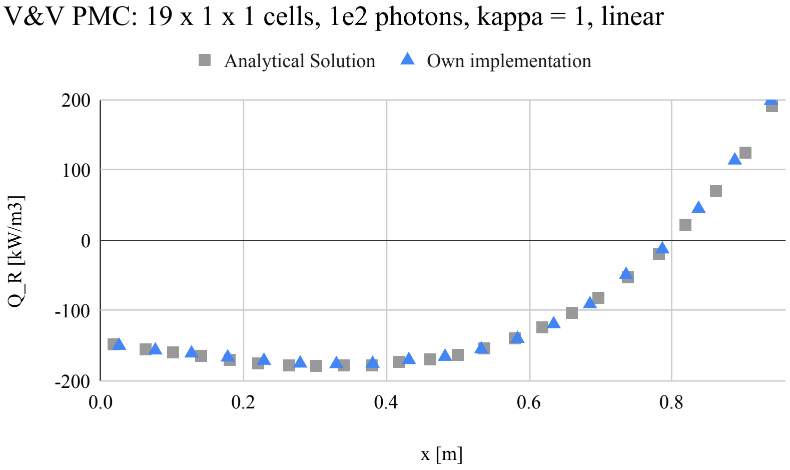

Figure 5.1: The radiative source term for the 1st test case: 1D domain with a constant absorption coefficient of 1 m^{-1} and black walls, linear profile. Validation data from Ref. [98].

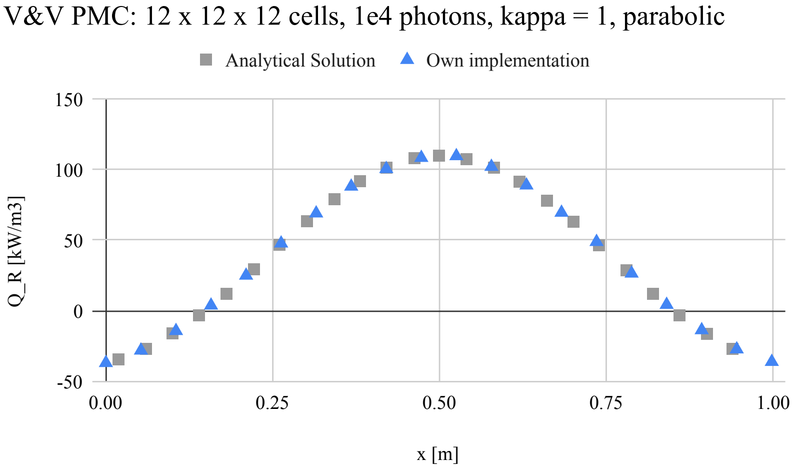

Figure 5.2: The radiative source term for the 2nd test case: 1D domain with a constant absorption coefficient of 1 m^{-1} and black walls, parabolic profile. Validation data from Ref. [98].

5.3.2. Case 3 and Case 4: Heat Transfer Mechanisms in 3D

With the basic PMC principles tested, cases 3 and 4 focused on testing the behaviour of the heat transfer for varying absorption coefficients and in a 3D domain. The validation data was taken again from Ref. [98]. The sinusoidal temperature profile:

$$T_m = (\sin\pi x \cdot \sin\pi y \cdot \sin\pi z \cdot \pi/\sigma)^{0.25}[K] \tag{5.3}$$

was applied to both cases, with the absorption coefficient of 5 m^{-1} for case 3 and 0.5 m^{-1} for case 4. The high absorption coefficient can help reveal problems in local heat transfer calculations since the photons are quickly absorbed, while the low absorption case can reveal global effects, such as the treatment of the wall heat transfer.

The results are shown in Figures 5.3 and 5.4. Since 3D domains were used, more photon rays were required for convergence compared to Cases 1 and 2, though the total number of photon rays needed was still relatively low. Similarly to the previous two cases, precise match with the validation data is obtained.

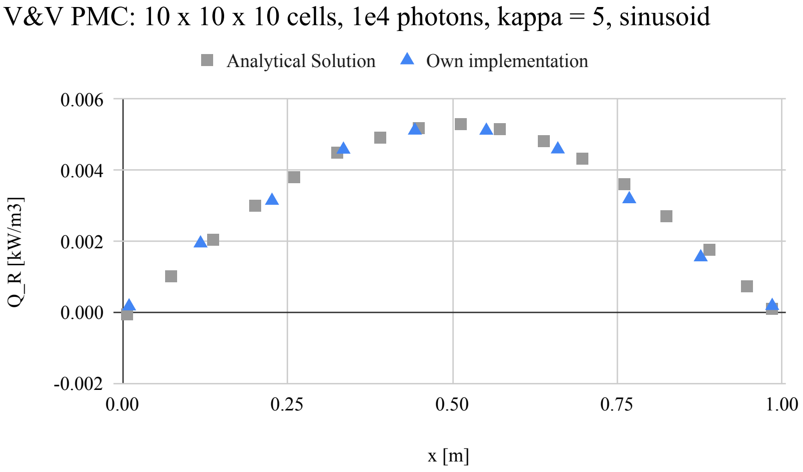

Figure 5.3: The radiative source term for the 3rd test case: 3D domain with a constant absorption coefficient of 5 m^{-1} and black walls and sinusoid profile. Validation data from Ref. [98].

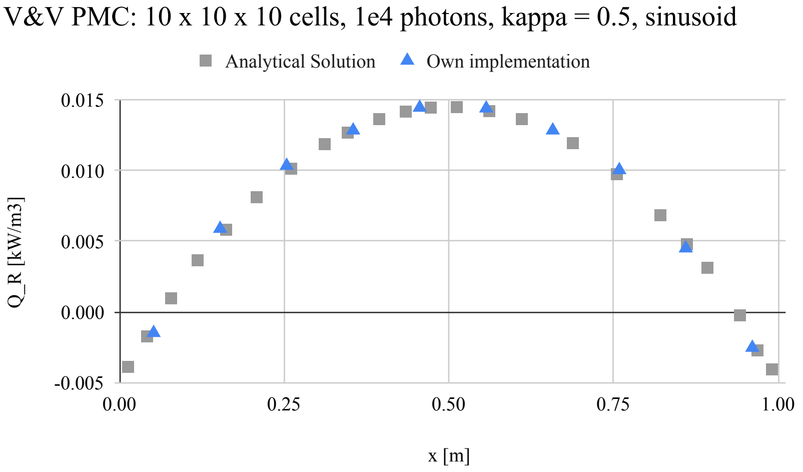

Figure 5.4: The radiative source term for the 4th test case: 3D domain with a constant absorption coefficient of 0.5 m^{-1} and black walls and sinusoid profile. Validation data from Ref. [98].

5.3.3. Case 5 and Case 6: HITRAN Implementation for H2O and Variable Domain

To test the implementation of the HITRAN subroutine, the constant temperature cases 5 and 6, filled with H_2O with cold walls in 1D, were computed and compared to the validation data from Ref. [98] as before:

$$T = 1000[\mathrm{K}], \quad T_{\mathrm{w1}} = 0^* K, \quad T_{\mathrm{w2}} = 0^* K, \tag{5.4}$$

where obviously, T = 0K would result in an infinite value of the Planck function, and thus a very small value for temperature was used instead (1e-8K).

In addition, Case 6 was scaled down in the x direction from 1m to 0.1m to verify the geometry and meshing. The results are shown in Figures 5.5 and 5.6, and confirm the correct computation of spectra using the HITRAN database as well as mesh resizing.

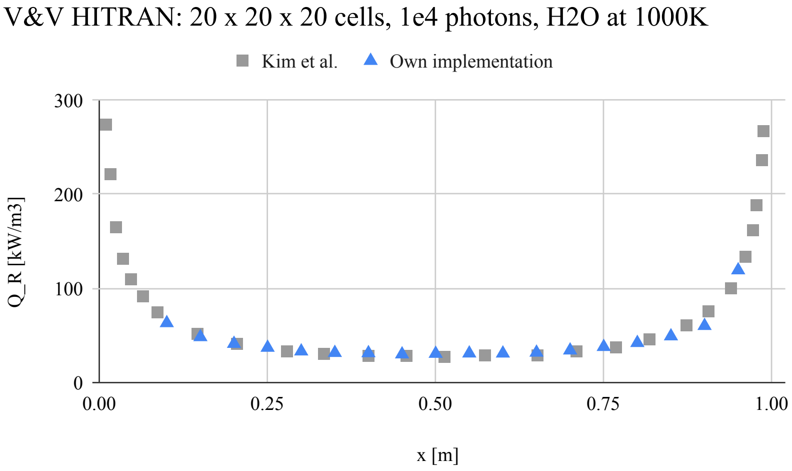

Figure 5.5: The radiative source term for the 5th test case: 1D domain filled with H_2O at constant 1000K and black walls. Validation data from Ref. [98].

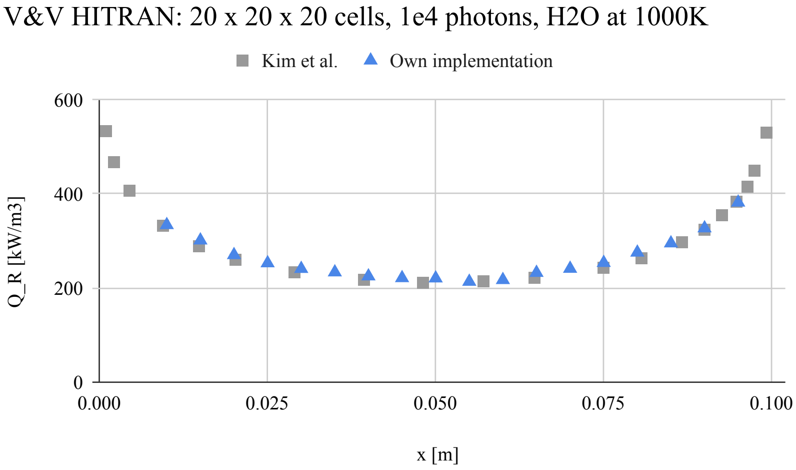

Figure 5.6: The radiative source term for the 6th test case: 1D, downsized domain filled with H_2O at constant 1000K and black walls. Validation data from Ref. [98].

5.3.4. Case 7 and Case 8: HITRAN Implementation for CO2 and Non-black Walls

Finally, two last HITRAN Cases 7 and 8, tested the implementation of the spectral computation with HITRAN for a medium with a temperature gradient and with non-black walls with validation data, again following Ref. [98]. The emissivity of the two walls in Case 8 were set to 0.1. The temperature profile in both cases followed:

$$T = 295 + 10x[\mathrm{K}], \quad T_{\mathrm{w1}} = 295K, \quad T_{\mathrm{w2}} = 305K, \tag{5.5}$$

where the participating gas was CO_2. The Figures 5.7 and 5.8 show the correct calculation of the spectra as well as correct implementation of a non-black wall condition.

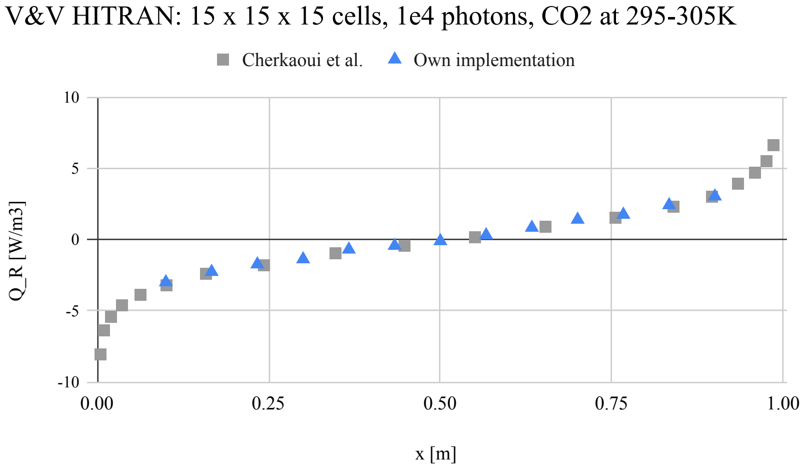

Figure 5.7: The radiative source term for the 7th test case: 1D domain filled with CO_2 with black walls at a linear profile. Validation data from Ref. [98].

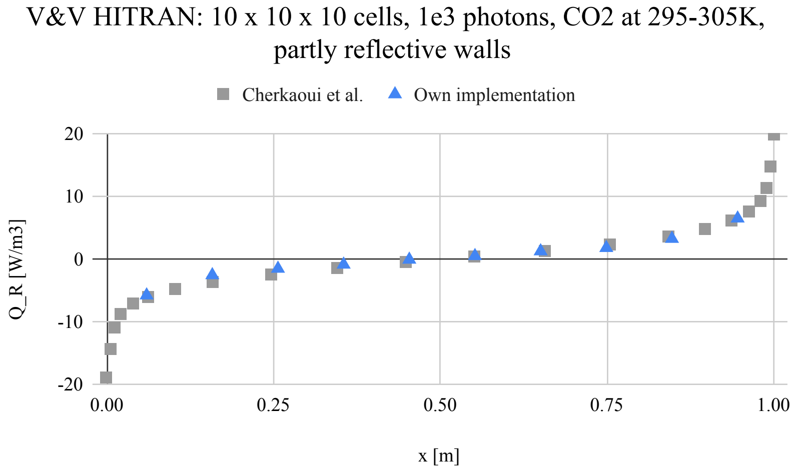

Figure 5.8: The radiative source term for the 8th test case: 1D domain filled with CO_2 with black wall and partly reflective at a linear profile. Validation data from Ref. [98].

5.4. NEQAIR Verification and Validation Procedures

For the nonequilibrium mode and implementation of NEQAIR subroutines, the validation cases were obtained directly from NEQAIR's 1D RTE solution. The correct operation in 3D was already verified in Cases 3 and 4, and it was thus deemed sufficient to validate the NEQAIR implementation in 1D only. This accelerated the testing process significantly, since the 1D calculations could be accurately performed with the original NEQAIR directly and the convergence of the developed solver was much faster.

The first case ran with NEQAIR was in complete equilibrium - a mixture of N and O (1e17/cm^3) at 8kK enclosed by black walls of 5kK - which assisted with verifying the correct coupling with the NEQAIR subroutines. The NEQAIR results were obtained with the same spectral and population calculation settings as used by default for the radiation code (set in Chapter 4). The results are shown in Figure 5.9. Convergence within 5% was achieved already for 2000 photons at 20 cell mesh. Figure 5.9 thus demonstrates correct implementation of NEQAIR to the code, at least for $T_{tr} = T_{ev}$.

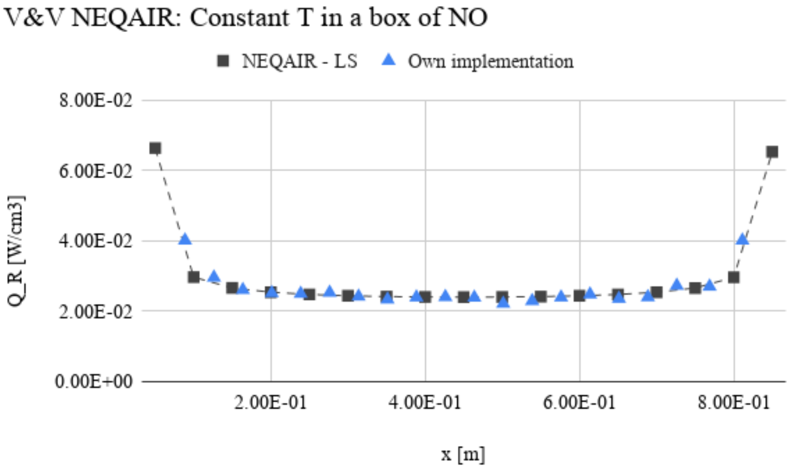

Figure 5.9: The radiative source term for the 1st NEQAIR case: A box of a N and O mixture at 8000K enclosed by black walls at 5000K. Validation data directly from NEQAIR.

In all of the following NEQAIR test cases, the boundary conditions were set to no-initial-radiance at $x = 0$ and black wall at $x = x_w$ to mimic the NEQAIR test cases.

The cases were used directly from NEQAIR's test case library. The discretization of NEQAIR is set according to the so-called LOS points which span across the line-of-sight from the shock to the vehicle wall. While each LOS point has a different spacing (starting from the shock and ending at the body), since the code developed considers Cartesian mesh only, for validation purposes, the NEQAIR mesh was stretched such that the spacing between the LOS points was constant. This obviously resulted in very significant stretching of the boundary layer. NEQAIR was then re-run to resolve the heat transfer on this new profile. In this adjusted setting, the LOS profile no longer represents the actual physical LOS profile encountered during entry. However, the ranges of temperatures, nonequilibrium and species number densities encountered are still the same, which allows for a full validation nevertheless. In addition, in this setting, excessively fine mesh is not required allowing for a quick code development and debugging.

The real LOS spacing (with 0cm starting at the shock) for the two investigated entry cases is shown in Figure 5.10. It can be seen that the majority of the points are located in the boundary layer right in front of the wall (where the distance x stops growing). This is mainly due to the fact that the temperature and species number density gradients are the steepest here, requiring fine resolution.

5.4.1. CEV Entry

The first validation case is the front of the Crew Exploration Vehicle. The translational-rotational and electronic-vibrational temperatures on the stagnation line are shown in Figure 5.11.

Figure 5.11 shows that the temperatures range from roughly 2.5kK to about 9kK, including a small nonequilibrium region at the beginning of the profile, where T_{tr} exceeds T_{ev} by 2.5kK.

The species number densities for each LOS point considered in the calculation are shown in Figure 5.12.

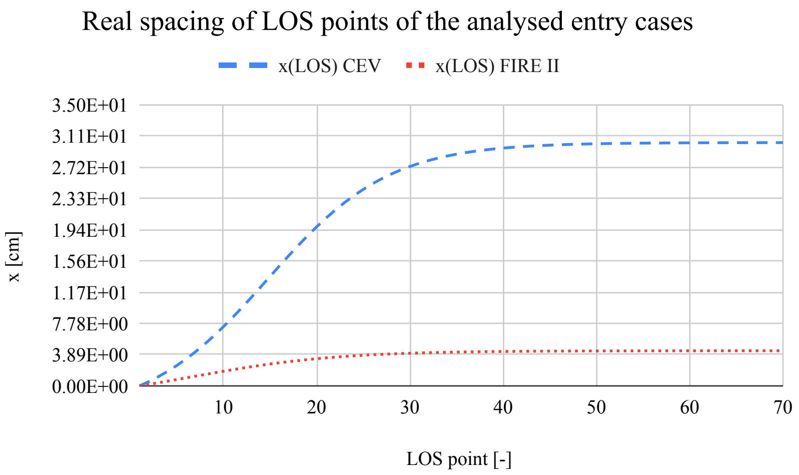

Figure 5.10: The real spacing between the line-of-sight points of the NEQAIR test cases. Fire II spacing shown in red, CEV spacing in blue.

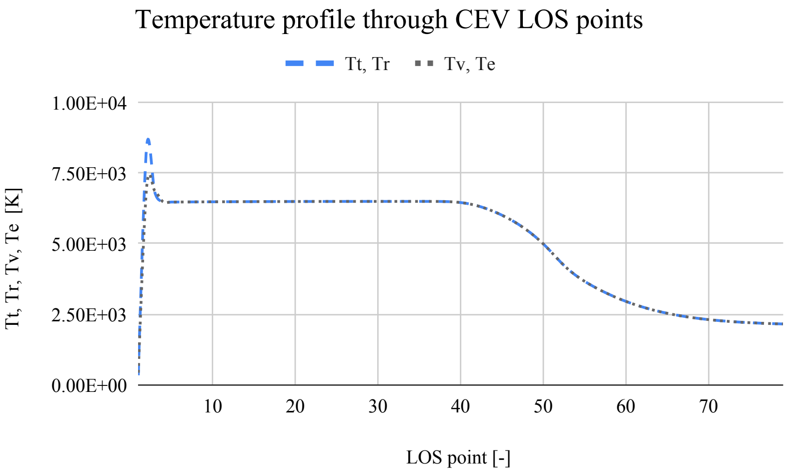

Figure 5.11: Profiles of translational, electron, vibrational and rotational temperatures through the LOS points of the Orion Crew Entry Vehicle stagnation line.

Despite the fact that O_2^+ is shown, it is not a part of NEQAIR calculation (the species data is not currently available, and thus calculation is not possible). It can be seen that the species number densities have a very wide range from below 1000 per cm^3 to almost 1e19 per cm^3, which is optimal for validation as this causes very large differences in the neighbouring spectra.

As already mentioned, since stretching of the LOS data to achieve Cartesian mesh changes the scale of the problem, two different scales were examined to reveal possible inaccuracies in global (small scale) and local (large scale) heat transfer calculation. The results for the large scale (on scale of 1m) simulation compared to the NEQAIR results are shown in Figure 5.13, in which 20000 photon rays were used for the simulation. A general agreement with the validation data can be seen, including the nonequilibrium region at the beginning of the LOS point.

Same conclusion can be drawn about the simulation on the small scale (of 0.1m) shown in Figure 5.14. Compared to the large scale result agreement, it can be seen that there is a general small under-prediction in the first part of the LOS. This is most likely due to the nature of ERMC and will be discussed towards the end of this section in much more detail.

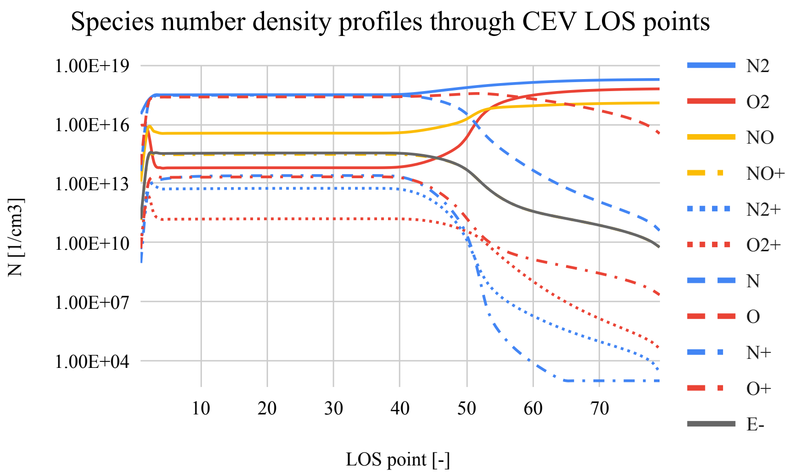

Figure 5.12: Species number density profiles through the LOS points of the Orion Crew Entry Vehicle stagnation line

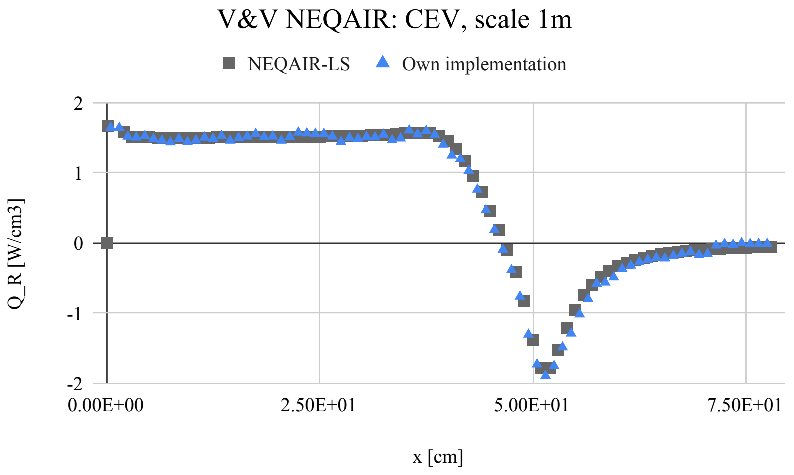

Figure 5.13: A comparison between the 1D results for the radiative source term of the large scale CEV simulation produced by NEQAIR and by own radiation solver (grey squares and blue triangles, respectively).

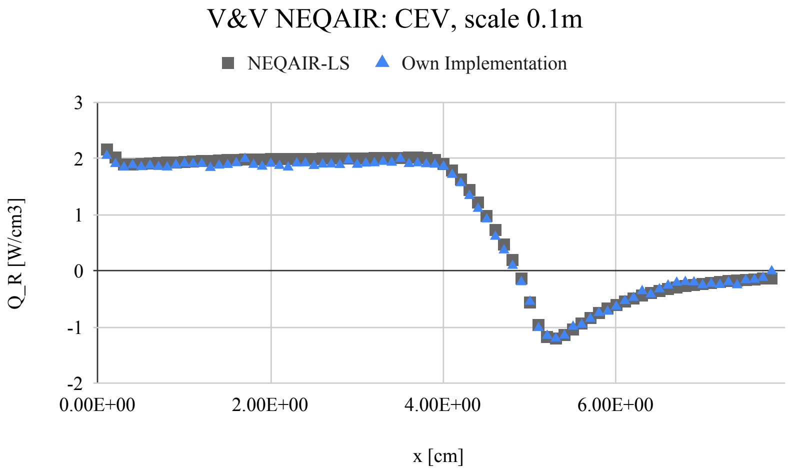

Figure 5.14: A comparison between the 1D results for the radiative source term of the small scale CEV simulation produced by NEQAIR and by own radiation solver (grey squares and blue triangles, respectively).

5.4.2. FIRE II Entry

The second validation case chosen was the FIRE II entry, where, similarly to the previous case, the LOS data was stretched to match the Cartesian grid. The temperature profile on the stagnation line is shown in Figure 5.15. In this case, two nonequilibrium regions are present, and the temperature range is much larger spanning almost 12kK.

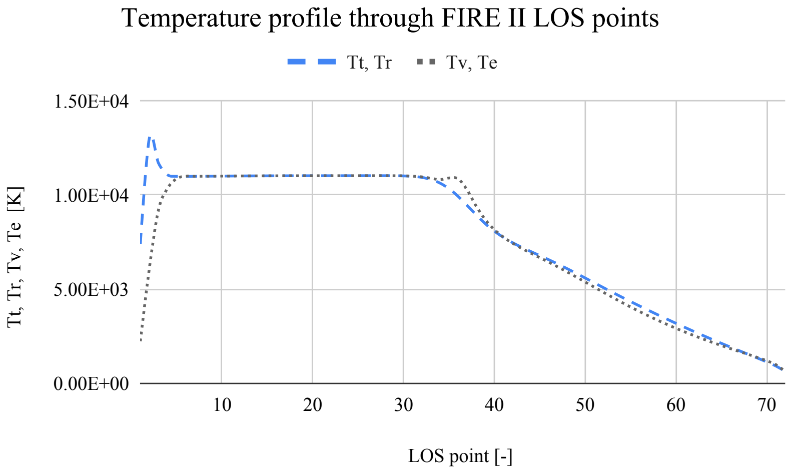

Figure 5.15: Profiles of translational, electron, vibrational and rotational temperatures through the LOS points of the FIRE II stagnation line.

The species number densities have a similar range to the CEV profile and are shown in Fiugre 5.16.

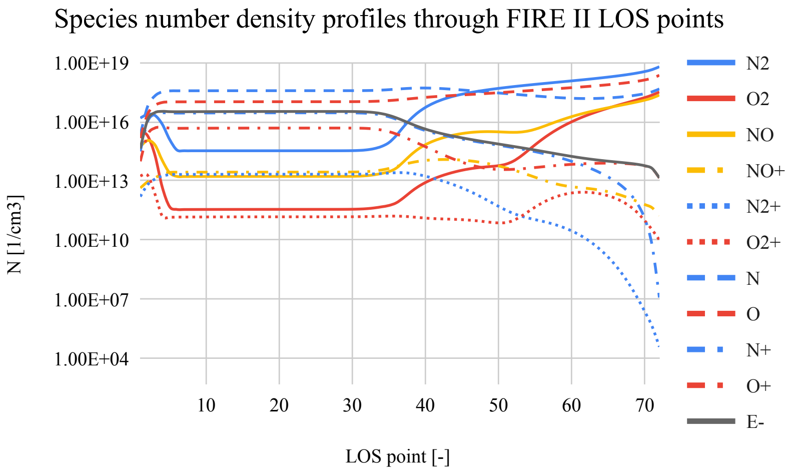

Figure 5.16: Species number density profiles through the LOS points of the FIRE II stagnation line.

Similarly to the CEV test case, two different scales were investigated. In case of FIRE II, since the shock detachment region is smaller than in case of CEV (refer to Figure 5.10), the scales of 10cm and 1cm were analysed.

The results for the larger scale are in Figure 5.17. Since the shock region source term is very high compared to the rest of the flowfield, the close-up is shown in Figure 5.18 for easier assessment.

In general, a good agreement is obtained. Both the nonequilibrium shock part and the flowfield right after the shock are slightly underestimated, which is the same observation as was made in the CEV case. The same holds for the smaller scale, shown in Figures 5.19 and 5.20.

While there exists a likely reason why the regions right behind the shock are underestimated as will be discussed in the next subsection, it is believed that the underestimation of the hot region at the shock is

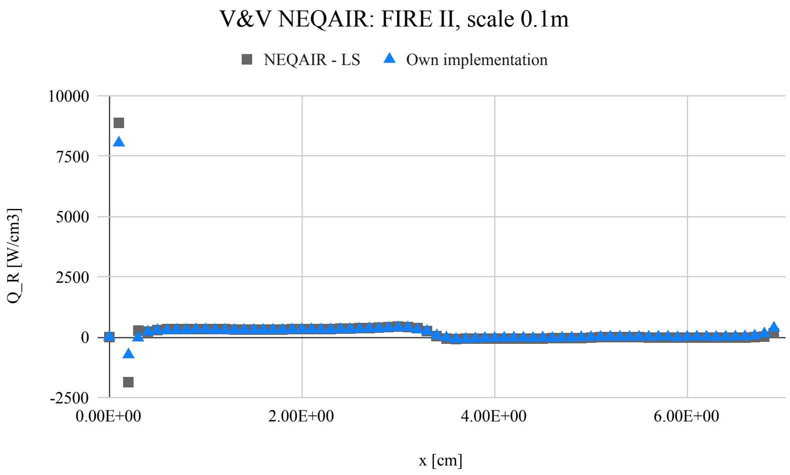

Figure 5.17: A comparison between the 1D results for the radiative source term of the large scale FIRE II simulation produced by NEQAIR and by own radiation solver (grey squares and blue triangles, respectively).

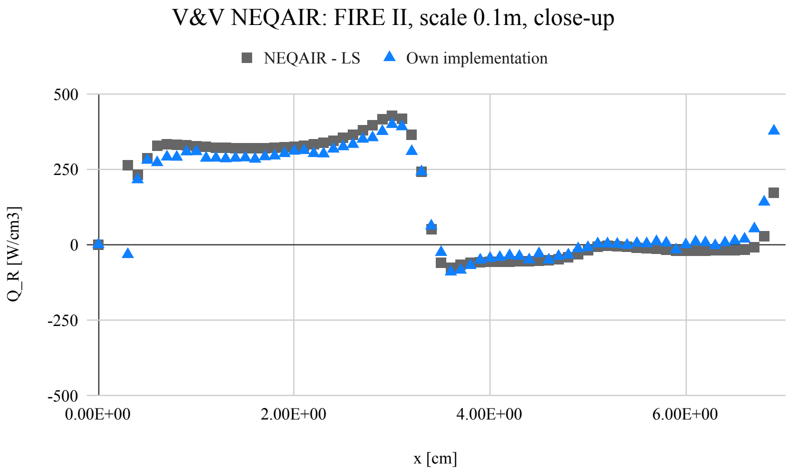

Figure 5.18: A magnification of Figure 5.17 without the high temperature region to show the rest of the profile.

mostly likely due to its location right at the no-initial-radiance boundary. The boundary conditions of the line-of-sight integration method used by NEQAIR and the applied PMC are defined in a different way. For NEQAIR, setting initial radiance to 0 is straightforward and means that there is no interaction between the boundary point and the highest temperature point following right after. In PMC formulation, the photons still lose some energy before escaping the domain to the no-radiance region due to self-absorption. Indeed, when self-absorption was excluded, the divergence of heat flux at the highest temperature point increased noticeably. This is, however, a non-physical adjustment to PMC and results in very significant errors in the rest of the flowfield.

To evaluate whether this is the case and whether the shock would otherwise be accurately resolved if further away from the boundary, an artificial shock was modelled. The electron and vibrational temperature was maintained at 7kK throughout the profile, while the translational and rotational temperature was increased from 7kK at 0.2cm to 10kK and brought back to 7kK at 1.4cm in a linear fashion. The maximum was reached at x = 0.85cm. The same species gradients were used as for the shock region of FIRE II. Figure 5.21 shows the comparison between the PMC and NEQAIR 1D evaluation.

From Figure 5.21, it is clear that even the nonequilibrium region (spanning from 0.2 to 1.4cm) is well resolved, with the match at the centre of the shock being exact, confirming the code's ability to accurately model also nonequilibrium conditions, and supporting the theory that the under-estimation in Figures 5.19

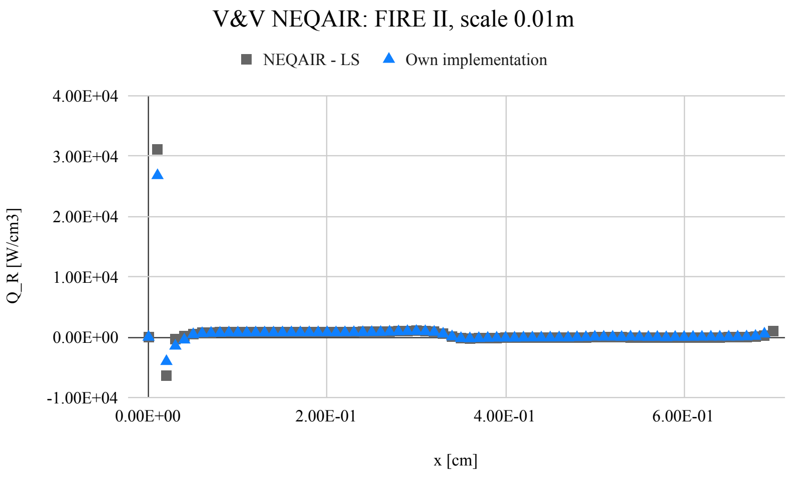

Figure 5.19: A comparison between the 1D results for the radiative source term of the large scale FIRE II simulation produced by NEQAIR and by own radiation solver (grey squares and blue triangles, respectively).

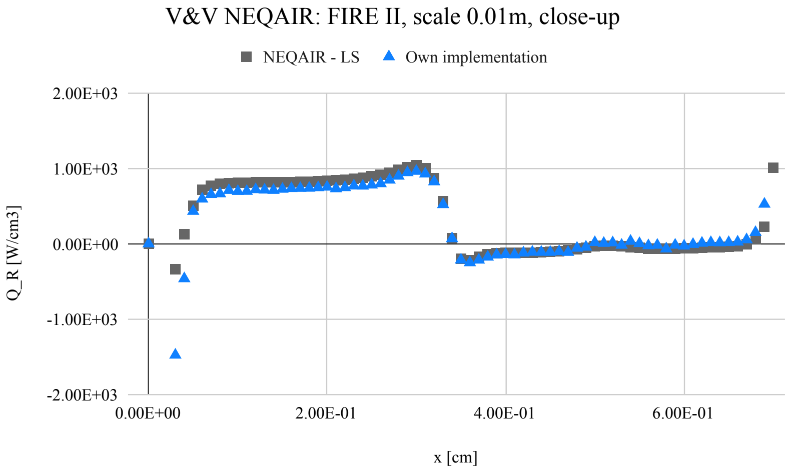

Figure 5.20: A magnification of Figure 5.19 without the high temperature region to show the rest of the profile.

and 5.17 at the shock hot spot was due to BCs.

The rest of the shock also shows a slight underestimation, with the error decreasing further away from the shock centre. This is consistent with the findings from the previous two cases and the origin of this error is debated in the next subsection.

5.4.3. Local vs Non-local Emission Wavelength Sampling

As discussed in previous Chapter, hypersonic plasma can be very absorptive, and thus local sampling was chosen when evaluating the photon ray wavelengths for each cell. This assumption can affect cells which are in close proximity to heavily radiating regions. In such close proximity, it is likely that the radiation in these places is still dominated by the highly radiating hot spots, but local sampling is used anyway as it is in the rest of the plasma. This could be the reason why in general, the energy source term around the highly radiating spots might be underestimated, as observed in the NEQAIR test cases.

The case of FIRE II was thus run with global sampling, meaning that the photons were all sampled from the high temperature nonequilibrium region at the very beginning of the line-of-sight. Comparison with the benchmark NEQAIR data and the local sampling method are shown in Figure 5.22.

It is clear from Figure 5.22 that global sampling allowed for a more accurate resolution of the post-shock region with the previously observed under-estimation no longer present (diamond shaped light blue data).

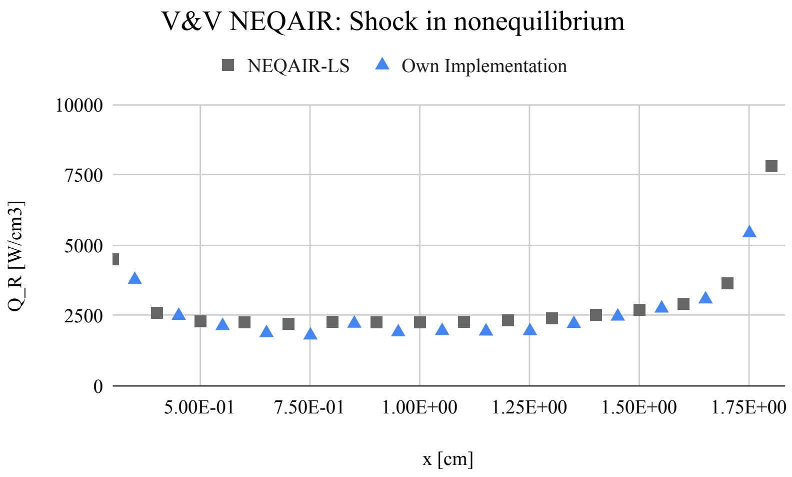

Figure 5.21: A comparison between the results for the radiative source term of NEQAIR and own solver for a simple nonequilibrium case (grey squares and blue triangles, respectively).

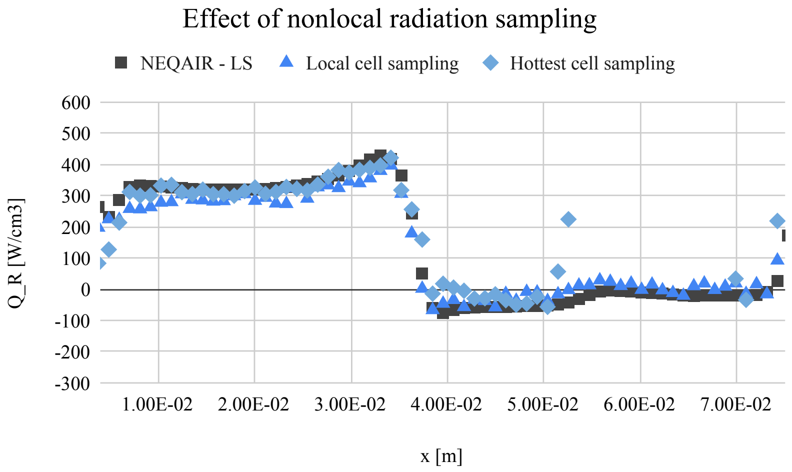

Figure 5.22: Difference between the divergence of the heat flux for the large scale FIRE II case (see Figure 5.17 and 5.18) when using local (blue triangle) and global (light blue diamond) wavelengths sampling compared to validation data (grey squares).

However, in the regions far away from the shock, the distance of which is too large for the high energy photon rays to propagate to, global sampling resulted in a nonphysical solution.

A possibility would be to run the solver twice to determine which regions need local sampling and set up a certain "domain of influence" for each cell. The first run could be used to determine this region of influence, and then the hottest cell from this domain would be used to generate the photons (type of a limited global sampling). However, since this would double the computational time required and since the observed errors were not considerable, this approach was not investigated further. Another possibility would be to measure the domain of influence while also evaluating the heat flux, and use that information when determining the domain during the next CFD radiation iteration.

Obviously, the most straighforward solution would be to switch to the forward MC formulation, which could, however, hinder the future GPU parallelisation potential of the code.

5.4.4. Standard Deviations Compared to NEQAIR

The final STDEVs of the evaluated cases are presented in Table 5.2. Due to the fact that, as discovered above, most likely the boundary condition formulation caused large errors for the FIRE II case, the results for this case are also presented not taking the points close to the boundary (first three) into account. This causes the

STDEV value to drop by one order of magnitude.

Table 5.2: Standard deviation and average (absolute) heat flux for comparison, and the ratio of the two for the nonequilibrium cases evaluated using data from the 1D NEQAIR technique. For FIRE II, since majority of the STDEV came from the edge, shock region thanks to the boundary conditions, the figures are also stated not taking these boundary condition points into account.

Case	Identification	STDEV [W/cm3]	Average (abs) [W/cm3]	Ratio [-]
9	Box of N and O	0.00161	0.03025	0.0533
10	Nonequilibrium	272.286	2654.74	0.1025
11 a	CEV large	0.08673	1.05209	0.0824
11 b	CEV small	0.07533	1.31399	0.0665
12 a	FIRE large	175.664	315.691	0.5564
	- no BC points	37.9263	167.926	0.2259
12 b	FIRE small	624.122	932.743	0.6691
	- no BC points	68.5028	416.552	0.1645

The remaining STDEV is believed to be mostly caused by the problems with the local sampling, as outlined above. However, since the majority of the remaining errors remain within 5-10%, and since correcting it would almost definitely result in a performance decrease, a correction to this method was not implemented. Considering the actual estimated accuracy of NEQAIR, which will be assessed next, errors of 5-10% are acceptable since similar errors can also be expected from NEQAIR itself. Thus, this correction, if implemented, might not even improve the result accuracy.

5.4.5. A Note on NEQAIR Accuracy and Convergence Requirements

The final aspect which should be discussed and which should also be taken into account when selecting the number of photon rays for convergence is the expected overall error of the simulation. With sufficient domain, angular and spectral discretization, as discussed in Chapter 2, forward PMC can be considered exact. The same can be said about ERMC when local or global sampling is completely physically sound.

However, attempting to remove the stochastic PMC error down to very low tolerances by excessive convergence demands will not necessarily drastically improve the accuracy of the simulation when evaluating the radiative heat transfer, at least for the complex cases such as hypersonic plasma. This is due to the fact that, as already mentioned in Chapter 2 when discussing Ref. [26], NEQAIR is not always accurate itself in its spectral calculations. As an example for this argument, Table 5.3 shows how the radiative heating on the wall differs for three different cases depending on the version of NEQAIR and depending on the discretisation settings. The differences between these versions stem mostly from improvements to reaction rates thanks to papers such as Ref. [26] where NEQAIR spectral results are compared to data from facilities such as EAST.

Table 5.3: Evolution of test case results with NEQAIR version. From Ref. [25].

Radiative Heating, W/cm2	CEV Afterbody	CEV front	FIREII
2009v8		19.4	609.0
v13.1		19.4	606.6
v13.1r2			
v13.2		20.4	660.7
v14.0	5.45	20.9	669.3
v15.0 (v14.0 inputs)		20.9	680.1
v15.0 (all bands, Auto)	14.44	22.8	703.4
v15.0 (all bands, Fast)	14.50	22.7	707.0
Percent Difference:			
v14.0 ->v15.0 (v14.0 inputs)		-0.1%	1.6%
v14.0 ->v15.0 (all bands)	62.2%	8.0%	4.8%
v15.0 (Auto) ->v15.0 (Fast)	0.4%	-0.1%	0.5%

From Table 5.3 it can be inferred that between the version 14 and 15 alone, the overall heating increased by 8% for the CEV case, 5% for the FIRE II case and more than 60% when resolving the FIRE II afterbody. Even with perfected transition rates and databases, NEQAIR and NEQAIR-based models might still be very far off from the actual plasma state, as was for example shown by Cai et al. in Ref. [17] when comparing it to StS results.

Thus, since this is indicative of the still existing errors and uncertainties in the thermochemical calculations of NEQAIR, it is not reasonable to demand better than 5% accuracy from the PMC scheme, the computational effort of which directly scales with convergence demands. This is also the reason why only 10000 - 20000 photon rays with a very coarse mesh were used above, and why this setting is deemed acceptable for the normal operating mode of NEQAIR as implemented in the developed radiation code.

5.5. Results with INCA

Finally, to demonstrate compatibility with INCA and indicate the performance which could be expected from this coupling, a simple hypersonic flow of Nitrogen plasma was simulated. The aim of the simulation was to test the most essential routines of coupling such as the extraction and interpolation of the flow conditions, detection of internal obstructions and translation of flowfield BCs to radiative BCs. In addition, it was also intended to measure how long a loosely coupled simulation takes, and what CPU portion is occupied by the radiative solver. It is expected that this figure would be around 95 - 99%, similar to values reported by other researches (see for example Ref. [75] where figure of 97% was reported).

5.5.1. Case 1 Setup

Firstly, a basic simulation of a wall-bounded hot supersonic Nitrogen flow plasma was made. The walls were set to 900K and bounded the y-dimension both on the top and bottom. The inflow condition and Neumann condition were used to bound the x domain, translated to the no-initial-radiance BCs conditions for the radiative domain. The z-domain was set to periodic. The variety in boundary conditions (periodic, walls and inflows/ outflows with assumed no-initial-radiance) were used in both cases to test all boundary possibilities and their correct extraction from the INCA flowfield data.

The domain dimensions were set to 0.5m x 0.3m x 0.1m and the INCA mesh is shown in Figure 5.23. The radiative 2nd grid was set to 50 x 30 x 1 cells, making it double the size of the INCA mesh. The spectral grid was set only to 15 x 15 x 1. The concept of the spectral grid will be introduced in the next Chapter when discussing acceleration techniques. Briefly, it represents the grid where the spectra are actually resolved and used to approximate spectra on the 2nd grid.

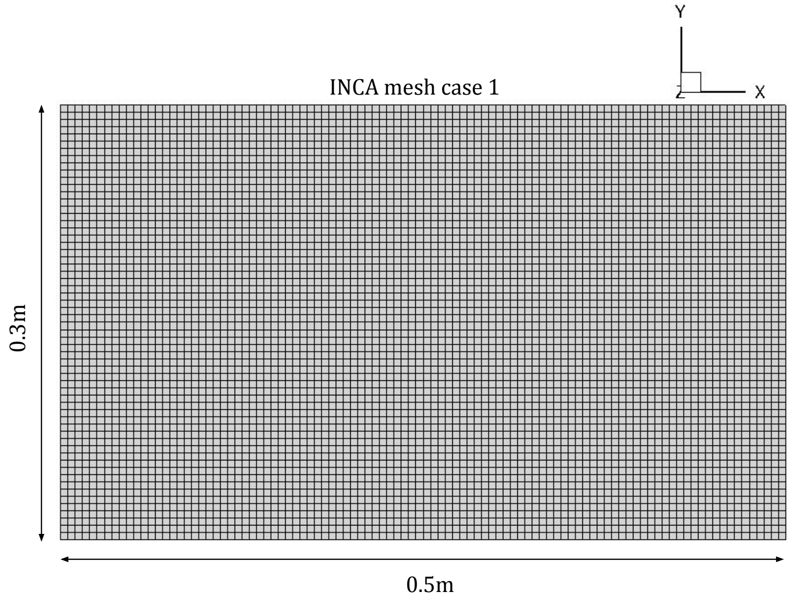

Figure 5.23: An illustration of the INCA grid for the first case. The overall domain dimension is 0.5m x 0.3m x 0.1m.

The INCA mesh, despite the presence of walls, was a simple homogeneous mesh with no scaling or obstructions. While, obviously, this will not resolve the boundary layer and make the solution somewhat nonphysical, the presence of the walls was important not from the flowfield standpoint, but to test radiative

Table 5.4: Thermodynamic parameters and number species densities of the hot, non-reacting Nitrogen flow case simulated with INCA.

	Case 1				Case 2			
L_{ref}	0.5 m				0.03 m			
T_{ref}	1500.0 K				600.0 K			
T_{w}	900.0 K				500.0 K			
ρ_{ref}	2.0E-3 kg/m3				2.0E-3 kg/m3			
Re	90000				1500			
M	2.5				5.0			
	N2	N	N+	e-	N2	N	N+	e-
X_i	0.510	0.489	4.08E-5	5.68E-4	0.510	0.489	4.08E-5	5.68E-4

Table 5.5: An overview of the simulated cases with INCA and the performance of the radiation code for varying discretisation levels.

	Case [-]	1st grid [-]	2nd grid [-]	3rd grid [-]	N_γ [-]	Coupling [1/iter]	Time per proc [s / proc]
Run 1	1	6000	50 x 30	15 x 15	10000	1/1000	≈ 1200 / 15
Run 2	2	5200	15 x 15	15 x 15	10000	1/1000	≈ 700 / 12
Run 3	2	5200	20 x 20	20 x 15	10000	1/1000	≈ 750 /12
Run 4	2	5200	30 x 30	25 x 20	10000	1/1000	≈ 1550 /12

transfer. It was expected that the radiative source term will, in general, follow the temperature and density profile, and would be enhanced near the walls (as can be for example seen in validation cases 5 and 6).

The initial number species density conditions were taken from beginning of the Orion CEV stagnation line. A non-reacting hot Nitrogen flow was considered consisting of N, N+, E- and N_2. This will not affect the quality of the testing method, since although the mole fractions throughout the flow remain the same, the spectra will still differ depending on the local total number density and temperature. The full thermodynamic setup of the simulation is shown in Table 5.4 as case 1.

The CFL number was set to 1.0 and a 3 step Runge-Kutta scheme was used with time from 0 to 0.001 seconds.

5.5.2. Case 2 Setup

Afterwards, a more complex case was set up, with more variable boundary conditions, more complex temperature and density fields and an internal obstruction. The thermodynamic parameters of the simulation are shown as case 2 in Table 5.4.

Similarly to the previous case, the CFL number was set to 1.0 and a 3 step Runge-Kutta scheme was used with time from 0 to 0.001 seconds. In this case, the spectral and radiative discretisation was varied to analyse its impact on the necessary CPU time. Compared to the first case, there was an internal step obstruction at $0.01 < x < 0.03$ and $y < 0.01$. For clarity, the INCA mesh used for this simulation is shown in Figure 5.24. The Neumann boundary condition was used for the right boundary, and the inflow at the left and outflow at the upper and lower boundaries, respectively. This time, the inviscid walls of the step were modelled using symmetric boundary conditions at the respective edges. The z-direction was again set to periodic.

5.5.3. Case Results and Performance

The overview of the simulation runs is in Table 5.5. The spatial resolution is indicated on the first INCA grid, 2nd radiation grid (where the radiative source term is resolved) and 3rd spectral grid. N_γ indicates the number of photon rays used.

From the initial runs of the two cases, it was determined that for the majority of the cells, the radiative heat flux was at or below 1-5% of the convective heat flux. Thus, according to Goulard number analysis (see Equation (4.40) and the respective discussion), loose coupling of 1/1000 iterations was chosen. The simulations were run on 15 and 12 processors Intel(R) Xeon(R) CPU E5-2640v4 and took between 12 to 40 hours. The accurate CPU time percentage is not shown here, as, for practicality reasons, radiative calculations were invoked only once the flowfield was fully developed. The radiative simulations took between 700 to 1600s for the cases examined, which would make it approximately 94 - 99% of the CPU time if radiation simulation was invoked from t = 0s, as expected based on the literature study. It is likely that if reactions were

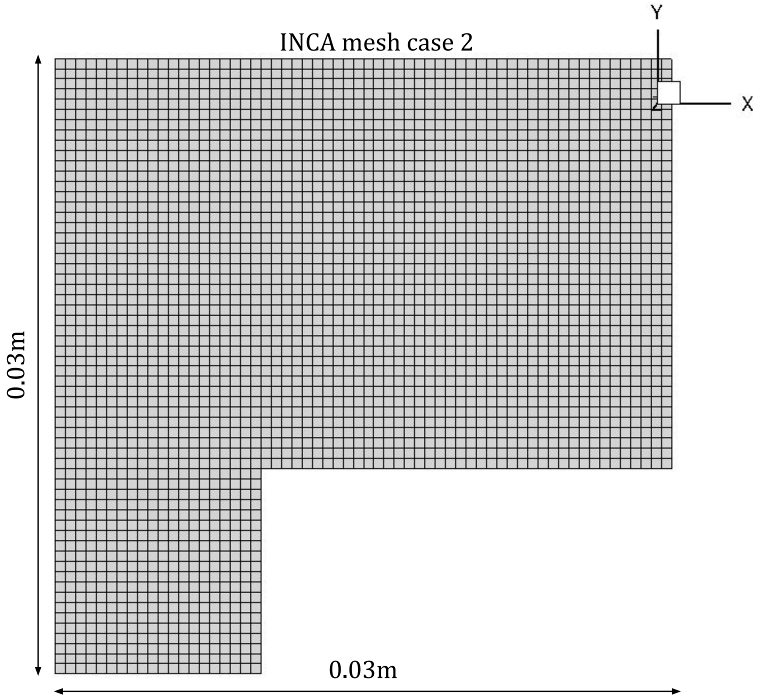

Figure 5.24: An illustration of the INCA grid for the second case. The overall domain dimension is 0.03m x 0.03m x 0.01m. The step if 0.01m tall and 0.02m wide.

included, the total time of the simulation would increase noticeably and the CPU time % of the radiation solver would decrease.

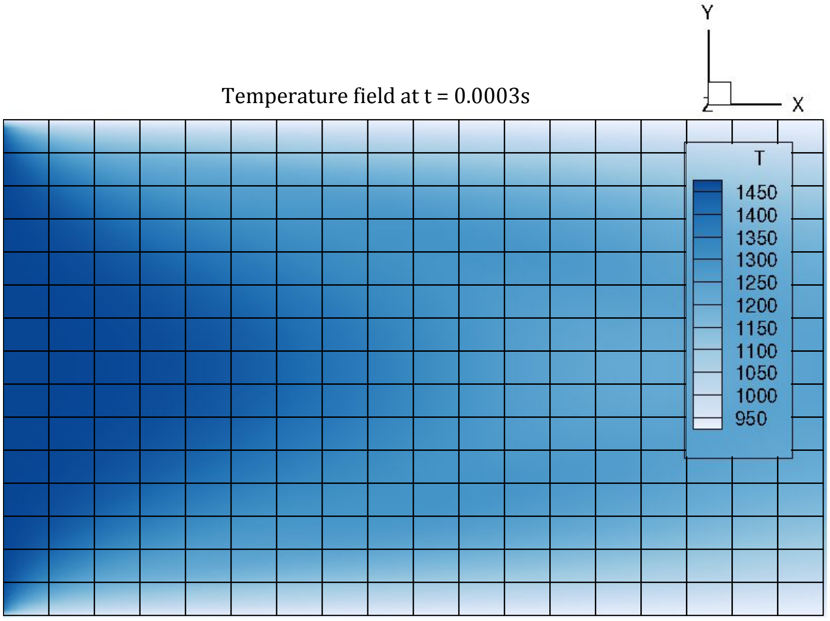

Figure 5.25: The temperature field of the INCA CFD test case 1 at 0.003s. The black lines show the spectral discretisation. Temperature in K.

As for the results, first the case 1 run is discussed. The velocity and density profiles at 0.0003s, after the flow became fully developed, are shown in Figures 5.25 and 5.26. As mentioned above, these profiles are not expected to be physical, since the walls bounding the y-dimension were not properly resolved with sufficient mesh (as the mesh was homogeneous without any refinement in the y axis). The walls were added merely to

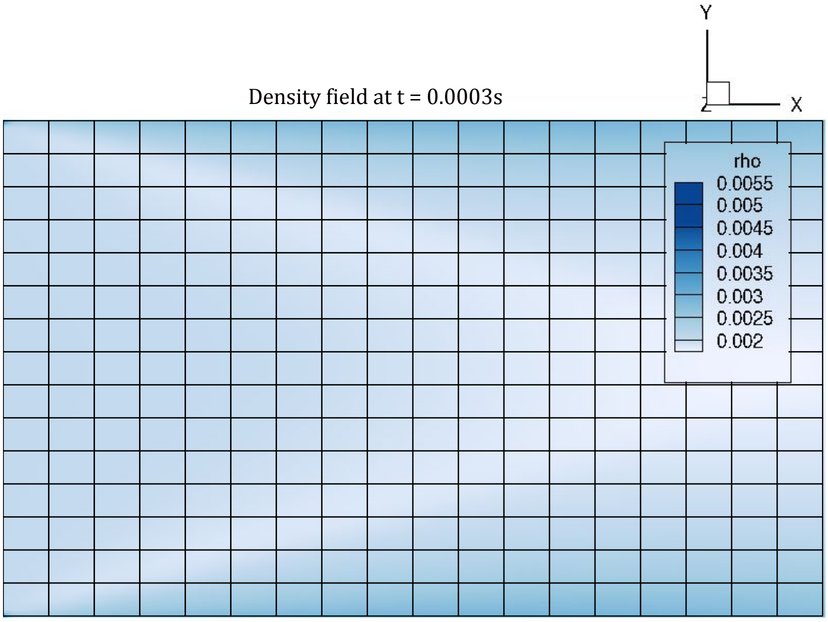

Figure 5.26: The density field of the INCA CFD test case 1 at 0.003s. The black lines show the spectral discretisation. Density in kg/m^3.

create a flowfield structure and provide a symmetrical radiative heat transfer mechanism.

The resulting radiative source term from case 1 is shown in Figure 5.27. It is clear that, despite the coarse spectral grid discretisation, the expected profile is obtained, i.e., following the temperature and density profiles and being enhanced at the walls. The source term is also somewhat amplified at the x boundaries, which is due to the no-initial-radiance boundary conditions at inflow and outflow. For better spectral discretisation, these spots became slightly more uniform, but where still present due to the BCs. Apart from these regions, as expected, the profile of the source term is symmetric around the horizontal mid-line.

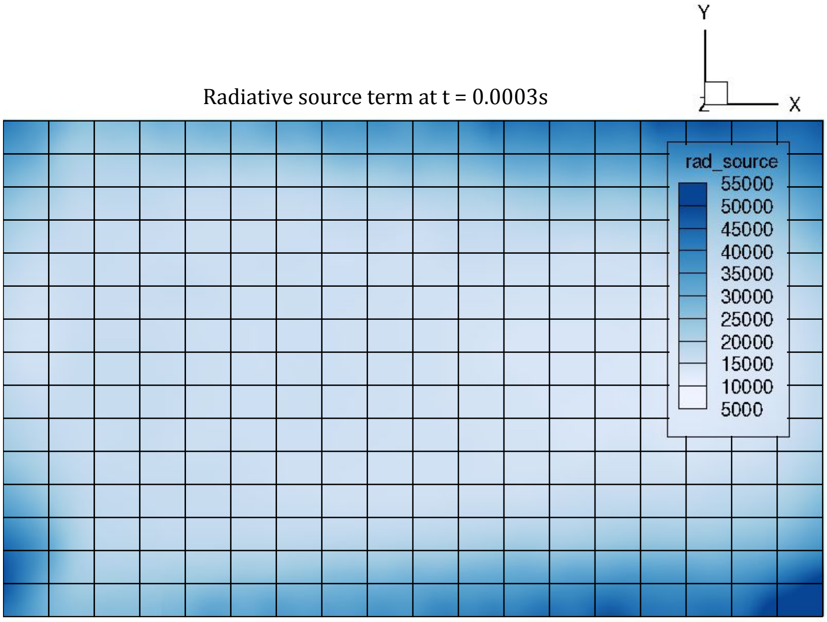

Figure 5.27: The radiative source term of case 1 at 0.003s. The black lines show the spectral discretisation. The radiative source is given in W/m^3.

From the case 2 runs, further analysed was the case with the finest 3rd grid resolution (25 in x and 20 in y at the 3rd grid and 30 in x and 30 in y at the 2nd grid), run 4 at t = 0.0007s when the flow was fully developed.

The distributions of temperature and density are shown in Figures 5.28 and 5.29, with the spectral grid shown in black lines for illustrative purposes. The flow is fairly under-resolved as can be seen especially from Figure 5.28 as due to time constraints, a finer mesh could not be applied. It can be seen that the hot, high density shock and post-shock regions are fairly narrow, spanning two or three spectral cells. Similarly to the previous case, it is expected that the radiative term profile will directly follow the profiles of density and temperature as these are the factors (next to boundary conditions) determining the spectra.

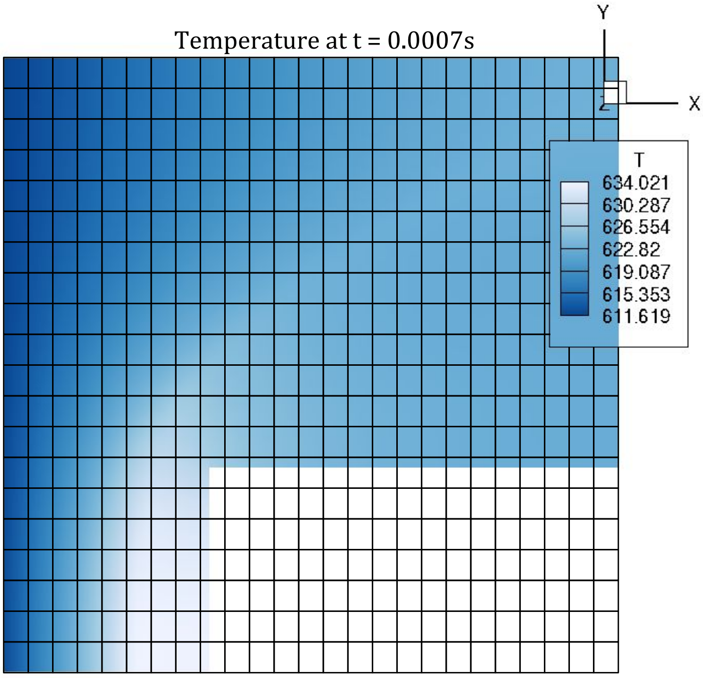

Figure 5.28: The temperature field of the INCA CFD test case 2 at 0.007s. The black lines show the spectral discretisation. Temperature in K.

For purposes of verification, sample spectra at three different locations with different conditions (density and temperature) were compared. While the mole fraction of the species is the same, meaning that the structure of the spectra should also be the same, the spectra themselves will differ in magnitude, as they scale with the density and the Planck function (temperature) in the case of the emission spectrum. The spectra were taken at the 1st, 7th and 9th i-point at j = 1 (vertically at the bottom of the domain, in front of the symmetry step).

The three pairs of spectra (both emissive and absorptive) are shown in Figure 5.30. It is clear that the absorption spectra follow the number density distribution (highest number density at the right-most point, smaller at the middle point and even smaller at point on the left). The same holds for the emission spectra, also taking into account the effects of temperature making the differences between the spectra slightly larger. The radiative source term resulting from these spectra and the respective BCs as resolved by the radiation solver is shown in Figure 5.31, after being smoothed using a second order filter. The shock region seems fairly diffused. Firstly, this is due to the diffused temperature field. Secondly, it is likely thanks due to relatively coarse discretisation - both from the perspective of the number of cells (radiative and spectral) in each dimension as well as number of photons. Finally, it is also due to the settings of the IDW interpolation - the lower the value of the exponent, the smoother but also the more diffused the flowfield is. In this manner, IDW smooths both the input data (temperature and density fields) into the radiation solver as well as the output radiative source term. The IDW exponent should thus be tweaked for each application depending on the desired smoothness and depending on the gradients existing in the field which are to be preserved. In this case, since the temperature variation in the flow was so small, there were no easily noticeable changes to the flowfield once the source term was applied.

The contributions of the different parts of the radiation solver to the total computational time are evaluated for the 1st run in Table 5.6. The ranges are present since the computational demands depend on factors such as temperature and number density. The higher the two, the stronger the transitions (on average, not for

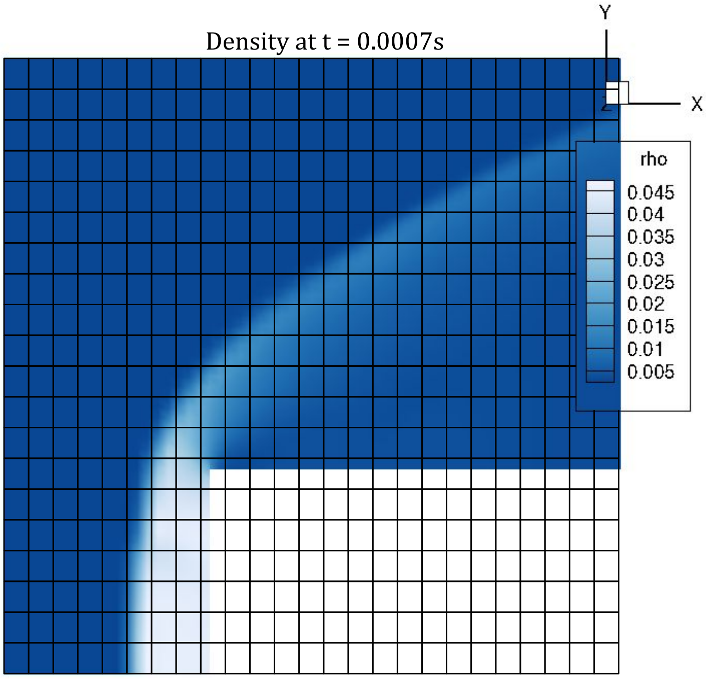

Figure 5.29: The density field of the INCA CFD test case at 2 0.007s. The black lines show the spectral discretisation. Density in kg/m^3.

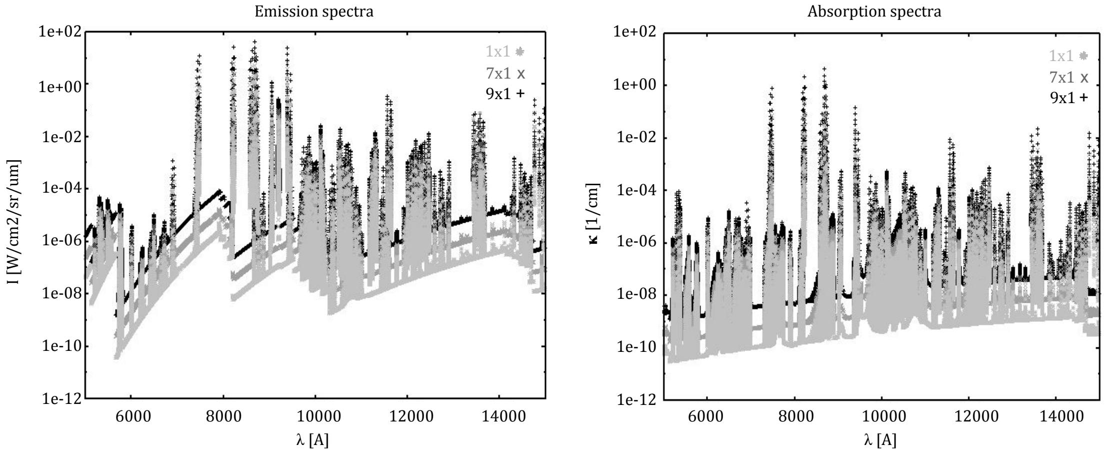

Figure 5.30: Emission and absorption spectra from case 2 from three different regions in the domain along the bottom line. The spectrum at point 9 (black) is from the hottest, highest density region close the the symmetry wall. The middle grey spectrum is roughly in the middle of the domain, and the light-grey spectrum comes from the left side of the domain with lowest temperatures and number densities.

all transitions), meaning higher complexity and size of the spectra, which in turn increases the times needed for the spectral reading and handling operations as well as for the NEQAIR generation process. For the other runs, the 1st to 2nd and 2nd to 1st grid IDW scales in proportion to the size of the 1st and 2nd grids as expected, since the loop which has to be carried out is N(1st grid) x x N(2nd grid) twice. These times were, however, still fairly small considering their contribution to the total time. The generation time of the spectra scales linearly with the size of the 3rd grid as long as the conditions are sufficiently different on that grid (the spectra are not produced for cells with repeated condition entries to save time and memory). Finally, the radiation solution time scales with the number of photon rays used for computation and with the second grid size. In case of the former, this scaling is linear since the spectral handling procedures and ray tracing must be carried out for each photon ray separately. As for the latter, the time required scales with N(2nd grid)^2, as for each photon ray from each cell on the second grid, all the properties in all of the second grid cells must

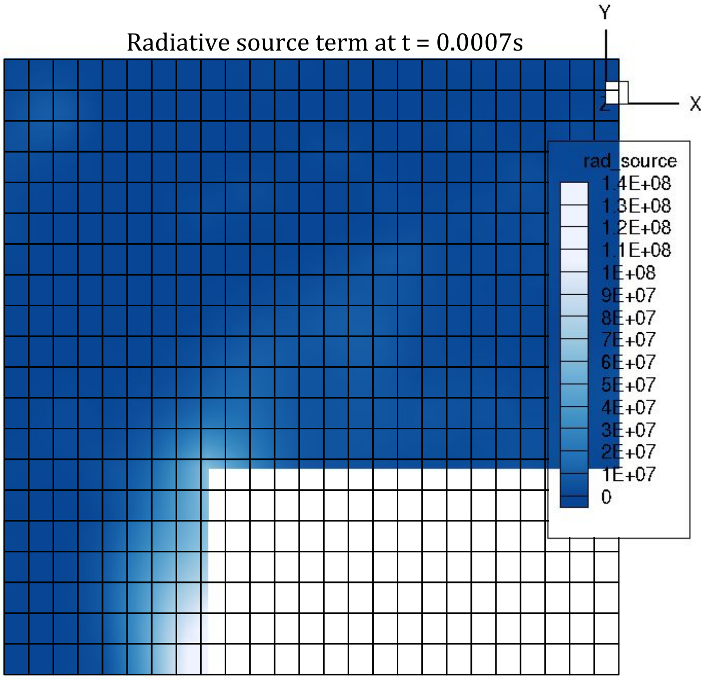

Figure 5.31: The radiative source term of case 2 at 0.007s. The black lines show the spectral discretisation. The radiative source given in W/m^3.

Table 5.6: Contributions of various parts of the radiative solver to the total computation time, for the 3rd run from Table 5.5.

Process (proc = processor)	Average Time Ranges [s]	Solution time [%]
Initial processing in INCA (all procs)	0.01 - 1.0	<0.1
IDW 1st to 2nd (all procs)	1 - 10	≈ 1
Generation of spectra (200 / 15 proc)	150 - 300	≈ 15 - 25
Reading of spectra (all procs)	200- 250	≈ 15 - 25
Radiation solution (1500 / 15 proc)	800 - 1000	≈ 50 - 70
IDW 2nd to 1st (all procs)	0.1 - 1	<0.1
Total	1200 - 1300	100

be determined. This procedure is parallelised with CPU, and thus can be significantly accelerated if more processors are in use.

From Table 5.6, it is clear that vast majority of the time is spent on the core of the solver (excluding the spectral generation and reading), the majority of which is spent on the determination of emission wavelength, emission energy, and absorption coefficients and the respective nonequilibrium Planck function ratios for heat transfer calculations in the rest of the flowfield. Thus, to speed the solver up, these are the routines which should be of primary focus, further hinting to the potential improvements with methods such as MBOB. This will be further elaborated on in the discussion section.

This case concludes the discussion of the main results. Since from the last section it is clear that acceleration techniques might be necessary to make the computations more practical, especially when coupled with CFD more tightly, further acceleration techniques were developed and adapted in the radiation code, analysis of which follows in the next Chapter.

6

Further Acceleration Efforts

This Chapter elaborates on the techniques applied to improve the performance of the solver besides the methods already presented in Chapter 4. Firstly, acceleration using the Sobol quasi-random sequence is analysed, which can be applied to all spectral modes. Afterwards, for nonequilibrium simulations specifically, an explanation is given on how to improve speed while maintaining an acceptable error, using various spectral discretization techniques, as well as approximation and databasing approaches for local spectral generation.

6.1. Acceleration using Sobol Sequences

Firstly, an implementation of a low discrepancy sequence, LDS, for photon ray directions was analysed. While the stochasticity of PMC is one of its main advantages compared to other methods, random number generators might result in omitting certain directions of emission, leading to a slower convergence. For this reason, an application of a pseudo-random LDS has been analysed before as potential means of convergence acceleration, as discussed in Chapter 2.

The Sobol sequence is a type of a pseudo-random sequence which has a low discrepancy. The derivation below can be found for Example in Ref. [59] in more detail. Assume that a low discrepancy distribution in an s-dimensional hypercube has to be found. For each of the dimensions, one firstly chooses primitive polynomials p_1 to p_s of respective degrees s_1 to s_s:

$$p(j) = x^{s_j} + a_1 x^{s_j-1} + a_2 x^{s_j-2} \ldots\ldots + a_{s_j-1} x + 1, \tag{6.1}$$

in which the coefficients a_1 to a_{s_j-1} are either 0 or 1. This polynomial is said to be primitive if it has the order $2^{sj} - 1$. For example, the primitive polynomials for the first few dimensions are:

- $s_j = 1: \quad 1 + x$
- $s_j = 2: \quad 1 + x + x^2$
- $s_j = 3: \quad 1 + x + x^3, 1 + x^2 + x^3$
- $s_j = 4: \quad 1 + x + x^4, 1 + x^3 + x^4$
- $s_j = 5: \quad 1 + x^2 + x^5, 1 + x + x^2 + x^3 + x^5, 1 + x^3 + x^5, 1 + x + x^3 + x^4 + x^5, \ldots$

Afterwards, an initial set of initialisation numbers $m_i(s) - m_1, m_2, m_3, \ldots m_{s_j}$ is determined randomly, provided that they are odd and satisfy $m_{k,j} < 2^k$ where $k = 1 \ldots s_j$. The rest is then computed as:

$$m_k = 2a_1 m_{k-1} \oplus 2^2 a_2 m_{k-2} \oplus \ldots \oplus 2^{s_j-1} a_{s_j-1} m_{k-s_j+1} \oplus 2^{s_j} m_{k-s_j} \oplus m_{k-s_j}, \tag{6.2}$$

in which $\oplus$ is the bit wise XOR operation. Then, based on m's, the so-called direction numbers can be determined according to:

$$v_{k,j} := \frac{m_{k,j}}{2^k}. \tag{6.3}$$

In the original implementation of the Sobol sequence from Ref. [100], $x_{i,j}$, the j-th component of the i-th point in a Sobol sequence, is determined by:

$$x_{i,j} := i_1 v_{1,j} \oplus i_2 v_{2,j} \oplus \cdots , \tag{6.4}$$

where i_k is the k-th digit from the right when i is written in binary $i = (\ldots i_3 i_2 i_1)_2$. This method allows for computation of any number in the Sobol sequence.

A faster method was developed by Antonov and Saleev in Ref. [8], which works if all numbers from the sequences are to be computed in order. If c_i is the index of the first 0 from the right in the binary expression of $i = (\ldots i_3 i_2 i_1)_2$, then, having computed the number x^n (where the first x is determined using Equation (6.4)), the next number can be resolved using:

$$x^{n+1} = x^n \oplus v_{cn}. \tag{6.5}$$

This operation is repeated for all dimensions, each of which has a different primitive polynomial.

The ACM TOMS 659 (Association for Computing Machinery, Transactions on Mathematical Software) implementation freely available was used to generate Sobol sequences in the code to determine photon ray directions. A comparison between the default FORTRAN random number generator and the Sobol number generator for 1000 and 10000 photon rays is shown in Figure 6.1. It is clearly observable that the Sobol sequence has a much lower discrepancy.

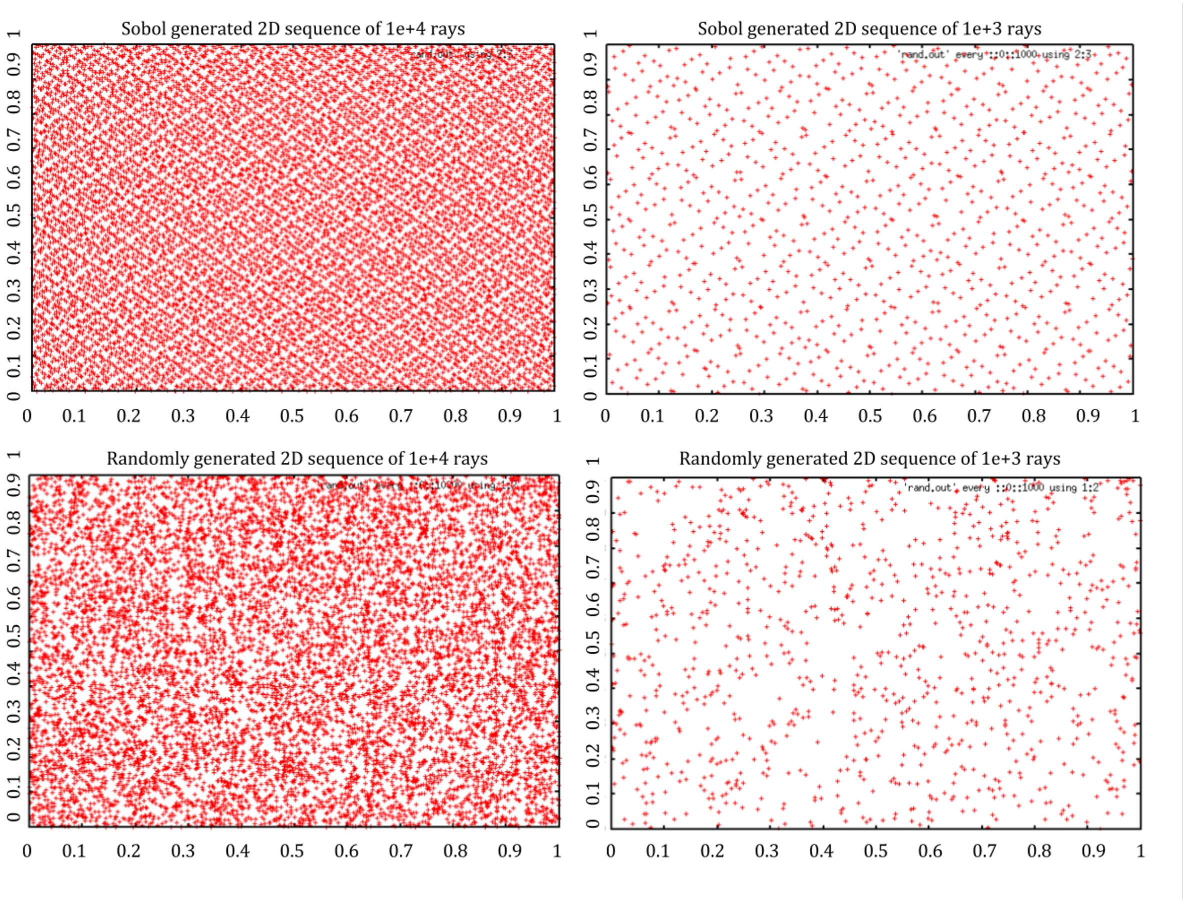

Figure 6.1: A comparison between a 2D Sobol sequence for 10000 (top, left) and 1000 (top, right) realisations and a 2D random number sequence generated using a built-in generator for 10000 (bottom, left) and 1000 (bottom, right) realisations.

The lower discrepancy in theory means faster convergence of the code to the desired solution as fewer photon rays have to be emitted to span the entire domain. Due to the complexity of the generation of Sobol sequences, as outlined in Equations (6.4) and (6.5), generation of the sequences also takes more time compared to the generation of random numbers. Thus, whether the implementation of a Sobol sequence with the purpose to accelerate the radiation calculation is useful depends on the balance between these two aspects.

It was measured that the Sobol sequence code used takes roughly 10x longer to generate a random number compared to a default random number generator.

The performance of a Sobol-aided PMC and default PMC was evaluated for two validation cases - case 1 and case 3, and the relative error was evaluated in the middle of the domain. These two cases were selected since considering the middle of the domain, case 1 is highly anisotropic while case 3 is far more isotropic. It is expected that for the anisotropic case, the performance improvement thanks to use of the Sobol sequences will be appreciably higher, as proper covering of the entire spatial domain by the photons is more essential.

The error of the radiative source term in the middle of the domain with respect to the baseline in case of the nearly isotropic field is shown in Figure 6.2 as a function of number of rays. It can be seen that the performance of the two PMC versions is almost the same, as can be expected as the actual directions of the photon rays do not play a significant role in the resulting heat flux. The benefits of the Sobol sequence can only be seen for the very coarse simulations (in order of 10 photon rays), but are within the bounds of the uncertainty.

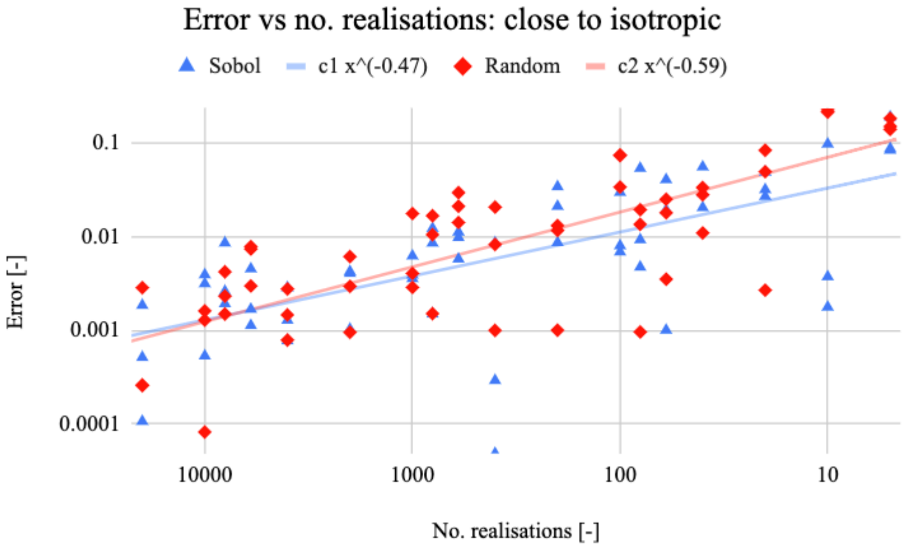

Figure 6.2: Convergence of PMC using Sobol and built-in random number generators for case 3 with number of realisations.

For the very anisotropic case, the same parameters are shown in Figure 6.3. It is easily observed that the use of the Sobol sequence in this case leads to much smaller errors compared to the default built-in random number generator. For example, already at 500 photon rays, the Sobol-sequence-aided PMC has the same average relative error as the default PMC with 12000 photon rays.

The most useful parameter to accelerate radiation calculations is, however, not the number of realisations, but the total time the simulation takes. As mentioned, since generation of the Sobol sequences takes roughly 10x longer than generation of random numbers using the built-in functions, the results from Figures 6.2 and 6.3 were corrected by this time difference, assuming that the ray tracing time is negligible. The results are shown in Figure 6.4 for the nearly isotropic case and in Figure 6.5 in the highly anisotropic case.

For case 3, accounting for the difference in the generation time actually offsets the small performance benefit (though statistically insignificant) of Sobol sequences that was observed in Figure 6.2 for coarse simulations. From Figure 6.4, it can be concluded that for highly isotropic problems, there is no significant gain from the use of Sobol sequences, unless a much faster code is developed to generate them or pre-database them.

As for highly anisotropic cases, Figure 6.5 shows that there are still substantial benefits of using the LSD, though not as large as shown if the generation time is not accounted for. The results above presented are for relatively transparent media, with several tens to hundreds of cell passes before absorption. In highly absorptive media, the initialisation of the photon ray takes up a much larger portion of the overall simulation time since only a few cell passes are expected. Thus, in these cases, it is likely that the impact of the generation time will be even more pronounced.

However, these conclusions can be formulated for grey simulations only and cannot be applied to conclu-

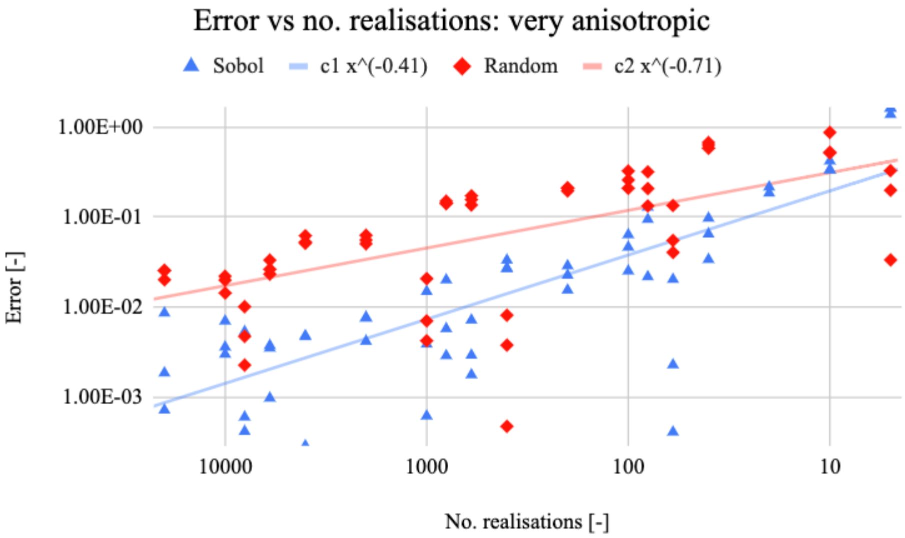

Figure 6.3: Convergence of PMC using Sobol and built-in random number generators for case 1 with number of realisations.

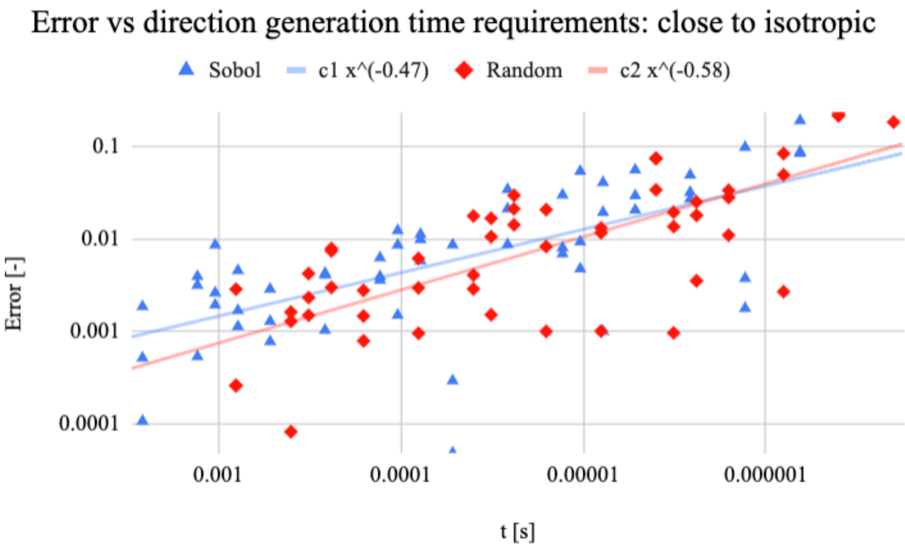

Figure 6.4: Convergence of PMC using Sobol and built-in random number generators for case 3, adjusted by the higher Sobol number generation time.

sions for non-grey media. In applications such as hypersonic plasma or even combustion flows with participating media, in which the medium has complex absorption and emission spectra, the majority of the time of PMC is not spent on photon tracing or direction generation, but on the characterisation of the flowfield at the selected photon wavelengths (determination of the absorption coefficients, Planck functions and further handling of the spectra). The complexity of these processes scales linearly with the number of realisations. Thus, even though these media are typically highly absorptive, the impact of higher generation time of Sobol sequences is completely negligible, and fewer realisations needed as a result of faster convergence might lead to noticeable speed improvements.

For example, case 6 was ran, and the average time required for each photon loop was measured (photon loop being defined to start with the calculation of total emissive energy, generation of directions and wavelengths and end with the known heat flux source contribution). This time was measured for both Sobol direction generation and for a random direction generation. The results are shown in Figure 6.6. It is clear that the times are almost identical, with the small differences being statistically insignificant. Thus, even though

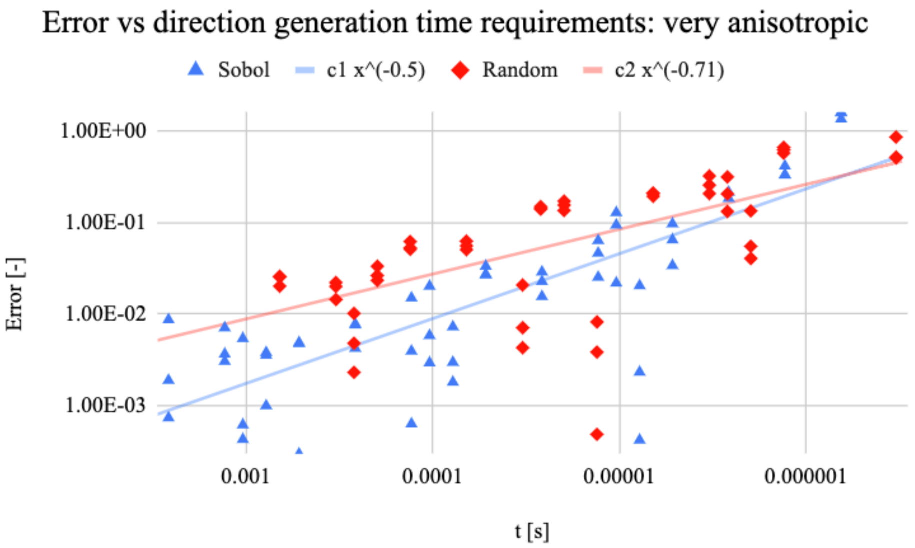

Figure 6.5: Convergence of PMC using Sobol and built-in random number generators for case 1, adjusted by the higher Sobol number generation time.

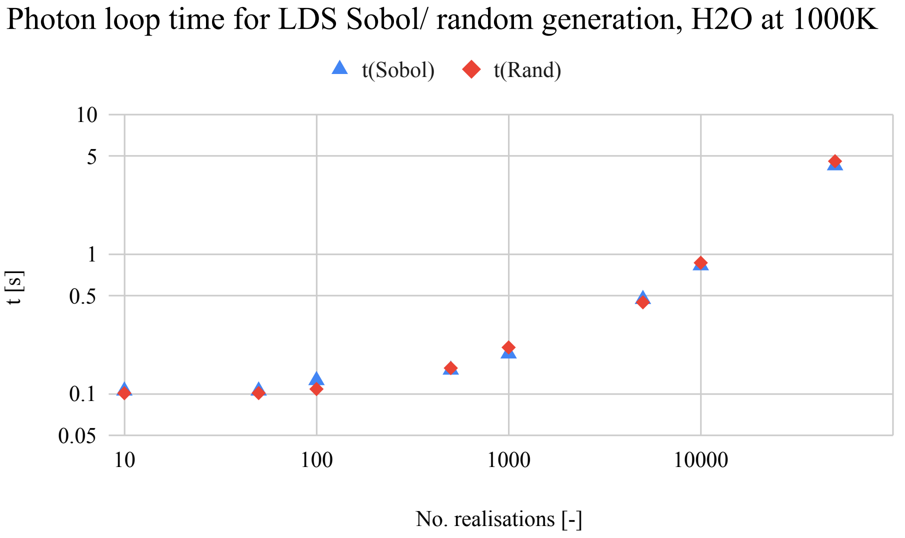

Figure 6.6: Photon loop times for a HITRAN case of H_2O at 1000K with Sobol direction and random direction generation, demonstrating that the effect of Sobol generation time is completely negligible when complex spectra are involved.

the case of H_2O at 1000K is close to isotropic, since the majority of the time is spent on handling the spectra, use of Sobol LDS does not cause any noticeable under-performance. Thus, the use of Sobol LDS for non-grey media, especially when high anisotropy is present, is definitely advantageous.

6.2. Acceleration by Optimising Discretisation Style

Especially for nonequilibrium calculations, the major concerns are the required memory and resulting computational time, since the sizes of the generated spectra are extremely large. When generating spectra with NEQAIR, it is up to the user to select either an automatic or a constant spacing grid. As discussed with the HITRAN implementation in Chapter 4, an automatic grid, which assigns points based on the position of transitions, is in general a more cost effective solution. In case of HITRAN, it was shown that one point per line, if possibly neighboured by zero points preventing a significant increase in the emissive power, still provided accurate emission spectra while reducing the time by up to two orders of magnitude.

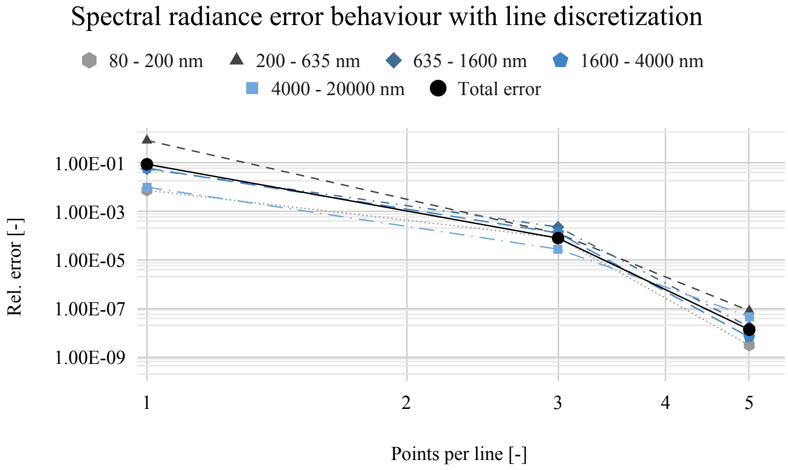

Figure 6.7: The relative error in spectral radiance (W/cm^2/sr) for various spectral bands as a function of line discretization.

For NEQAIR, the emission and absorption spectra must have the same size. In addition, in a high temperature gas, there are not only the discrete b-b transitions, but also b-f and f-f transitions causing continuum contributions, making the definition of the number of points-per-line (ppl) somewhat vague. Therefore, to determine what ppl discretisation is needed for NEQAIR spectra to be accurate in a more straightforward fashion, the full CEV profile was computed with spectra ranging from 10 ppl, which was considered to be the exact solution, down to 1 ppl. The emissive power at each LOS point was evaluated, since this is the factor driving the accuracy of the resulting radiative source. Then, the standard deviation over the entire LOS was computed and compared to the reference 10 ppl data for 5 spectral bands separately. This spectral division was made in order to allow for this ppl setting to be determined based on application. The results are shown in Figure 6.7. Since in most cases in hypersonic flows, the most dominant region of emission is the 80-200nm region where the majority of the atomic emission occurs (see for example Figure 4.14), the accuracy of 1 ppl was deemed sufficient considering memory savings (as these scale linearly with ppl). Possibly, for slower shocks at lower altitudes where molecular radiation might prevail in the 200-635nm range, 3 ppl might be needed to keep the error low.

The automatic ppl discretisation has to be respected while generating the spectra in the first place. Once the spectra are generated, further downsampling techniques can be used to reduce the total size. The two approaches analysed and applied in this work are what will be referred to as "regular downsampling" and "cumulative downsampling". The principles are shown in Figure 6.8.

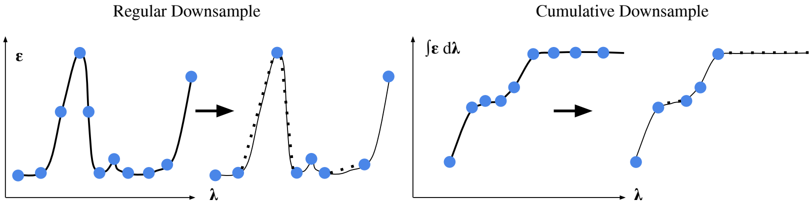

Figure 6.8: Principles of the two downsampling methods adapted and investigated.

Regular downsampling is a technique also already built in NEQAIR. It considers three points, and if a certain point can be within a certain tolerance (relative) represented by a linear fit between the two edge points, it is removed. Down to the tolerance of 1e-5, it is already implemented during NEQAIR calculations. Here, it was investigated whether further downsampling could be beneficial.

The cumulative downsampling is based on a similar principle, but the linear fitting check is made for the cumulative distribution instead of the regular spectrum. The reasoning behind this is the fact that it is the cumulative distribution which determines the emitted energy and is thus also the major component of the total error. Unlike the regular downsampling, the cumulative downsampling also removes very weak lines, which might introduce additional error when evaluating the absorption coefficient.

The CEV LOS simulation was ran with varying tolerances for the downsampling techniques above. Similarly to the case with ppl discretisation, the STDEV was computed. Since in this case, the memory savings do not decrease linearly as in case of ppl, an average size per spectrum in GB is also presented. The results for regular downsampling are shown in Figure 6.9 and for cumulative downsampling in Figure 6.10.

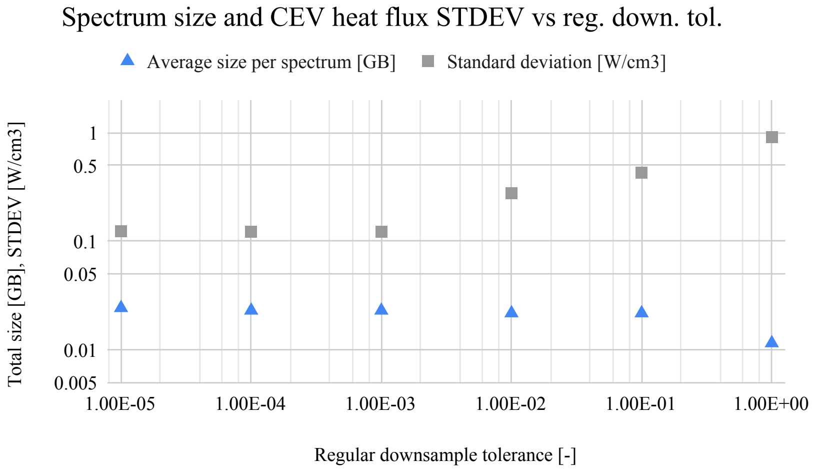

Figure 6.9: The performance of the regular downsampling technique in terms of the STDEV and spectrum size with tolerance.

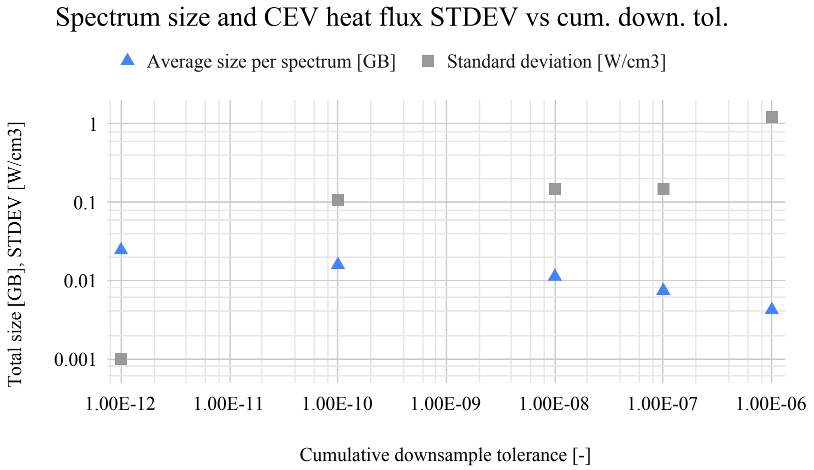

Figure 6.10: The performance of the cumulative (integral) downsampling technique in terms of the STDEV and spectrum size with tolerance.

Since regular downsampling did not significantly decrease the spectra size and only increased the time due to the necessity of handling of the spectra, it was not further used in simulations. The presented results are used to justify the application of a 1e-7 tolerance for cumulative downsampling. With the standard deviation in the order of 0.1 - 0.2 W/cm^3, the average relative error still remained below 1% for this particular study case.

6.3. Acceleration Using Three Grid Configurations

Now, we can return to the discussion of the three grid system introduced in the INCA simulations in the previous Chapter. However, the spectra of neighbouring cells might oftentimes be very similar, especially if there are no significant gradients in species concentrations and temperature, whereas the actual radiative heat source varies by an order of magnitude. Consider, for example, the test case 9, where despite the same spectrum everywhere, the divergence quadrupled due to the presence of walls on the edges. Also when examining the stagnation line profiles, as for example shown in Figure 5.12 and Figure 5.16 for number species densities and Figure 5.11 and 5.15 for temperatures, it is clear that over a large portion of the stagnation line, the spectra are going to look very similar. For this reason, another uniform grid layer was added for the radiation calculation. While the radiative heat flux is resolved on the 2nd grid, the spectra is computed on the 3rd grid. Thus, to summarise the configuration:

- 1st CFD grid is the grid where flowfield data exist in their original form
- 2nd radiation grid is the grid where the divergence of the heat flux is computed from ray tracing
- 3rd spectral grid is the grid where spectra are computed and used for approximation on the 2nd grid

How exactly this approximation of the spectra onto the second grid takes place is the focus of this section. Various avenues have been explored and the respective performance in terms of speed and error have been compared. Two families of methods have been formulated:

- Averaging/ adjustment: where spectra from the 3rd grid are retained and modified in some way for estimation of the spectra on the 2nd grid
- Interpolation / regression: where the dependence of the absorption and emission coefficients at a given wavelength are approximated as functions of local state vector with certain coefficients, and the spectra on the 2nd grid are computed from these coefficients and their local state vector

The details of these two principles and respective methods are discussed in the following subsections with their performance comparison following after that.

6.3.1. Solution on a Coarser Mesh and IDW

The simplest techniques to reduce computational requirements is to solve the spectra on the coarsest 3rd mesh and use these spectra to directly approximate the spectra on the 2nd grid by either direct copying or interpolation. One of the techniques tested was thus to find the closest resolved spectra and use these spectra for the cell on the 2nd grid with no modifications. Alternatively, a second technique evaluated resolved spectra which were the closest to the given cell, and created average spectra using the respective distances with IDW to the reference cells. The distances were evaluated using the difference in thermal conditions (T_{tr} and T_{ev}) rather than the physical distance, as temperature is the main factor (next to species concentration) affecting emission (as the Planck function scales with T^4). Then, the emission and absorption coefficients at a given wavelength λ are, from the two reference spectra:

$$\varepsilon_{i,\lambda} = w_{\text{ref}\,1}\varepsilon_{\text{ref}\,1,\lambda} + w_{\text{ref}\,2}\varepsilon_{\text{ref}\,2,\lambda}, \tag{6.6}$$

$$\kappa_{i,\lambda} = w_{\text{ref}\,1}\kappa_{\text{ref}\,1,\lambda} + w_{\text{ref}\,2}\kappa_{\text{ref}\,2,\lambda}, \tag{6.7}$$

where the weights are found from the inverse distances:

$$w_{\text{ref}\,1} = \frac{1/d_1}{1/d_1 + 1/d_2}, \qquad w_{\text{ref}\,2} = \frac{1/d_2}{1/d_1 + 1/d_2}. \tag{6.8}$$

This approach is straightforward and fairly stable, in that as long as the reference spectra are accurate, there will be no significant overshoots or negative/ illegitimate values in the spectra obtained. However, this technique cannot adjust for any potential minima or maxima or other fluctuations which might occur between the neighbouring cells, and thus will not work accurately unless careful attention is paid to how the 3rd grid geometry is set up. Only actual physics-based methods could, to some extent, correct for such gradients and fluctuations and will be discussed next.

6.3.2. Spectral Interpolation and Regression

Firstly, an approach using interpolation was assessed. The dependent variables, in general, are the number species densities and the two considered temperatures. If, say, we consider a model consisting of T_t, T_r, E-, N+, O+, N, O, N_2, O_2 and NO, 10 weights are required, and the system to be solved to obtain the spectral interpolation coefficients w is:

$$\begin{bmatrix} f\left(\left\|T_{tr,1}-T_{tr,0}\right\|\right) & f\left(\left\|T_{ev,1}-T_{ev,0}\right\|\right) & \dots & f\left(\left\|N_{O_2,1}-N_{O_2,0}\right\|\right) \\ r\left(\left\|T_{tr,2}-T_{tr,0}\right\|\right) & f\left(\left\|T_{ev,2}-T_{ev,0}\right\|\right) & \dots & f\left(\left\|N_{O_2,2}-N_{O_2,0}\right\|\right) \\ \vdots & \vdots & \vdots & \vdots \\ f\left(\left\|T_{tr,10}-T_{tr,0}\right\|\right) & f\left(\left\|T_{ev,10}-T_{ev,0}\right\|\right) & \dots & f\left(\left\|N_{O_2,10}-N_{O_2,0}\right\|\right) \end{bmatrix} \begin{bmatrix} w_{0,\varepsilon} \\ w_{1,\varepsilon} \\ \vdots \\ w_{10,\varepsilon} \end{bmatrix} = \begin{bmatrix} \varepsilon(x_1) \\ \varepsilon(x_2) \\ \vdots \\ \varepsilon(x_{10}) \end{bmatrix} \tag{6.9}$$

This means that 10 spectra are needed to evaluate these dependencies. The configuration of the grids and the weights are then defined for the regions as shown in Figure 6.11. However, this approach does not work in such a straightforward manner in practice.

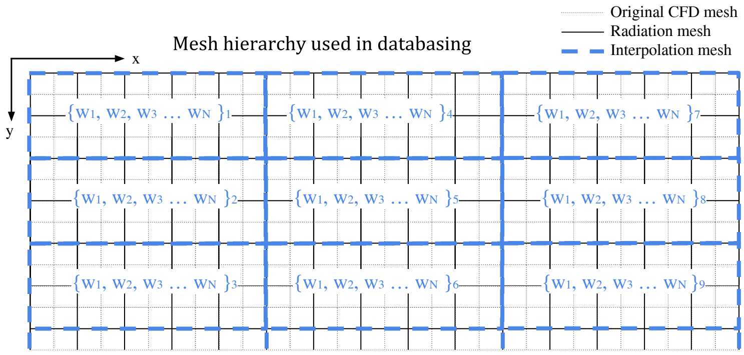

Figure 6.11: The setup of the primary, secondary and tertiary grid with illustration where the interpolation weights used for 2nd grid spectral approximation are defined.

Interpolation of this sort would require actually independent variables to provide accurate weights. Even though locally, in nonequilibrium, very large differences of order of thousand K may exist between $T_t = T_r$ and $T_e = T_v$, a large portion of the flowfield can usually be in LTE. This means that in these zones of LTE, the two temperatures are not independent, and their inclusion will only worsen the conditioning of the system, oftentimes leading to exploding spectral weight values.

In addition, since the interpolation is computed spectrally, the approach of Equation (6.9) implies that the absorption / emission coefficient at each wavelength depends on all species densities, which is not the case. For example, at a wavelength where an atomic O line peaks, this peak coefficient will be almost completely independent of, for example, the number species density of NO or N_2 and almost exclusively dependent on density of O. In case of interpolation, this would lead to oftentimes extreme and nonphysical values for these coefficients, just as for the two temperatures in LTE. Thus, regression instead of interpolation was used further, where the number of dimensions can be altered depending on the location in the spectrum and in the flowfield.

6.3.3. Spectral Approximation and Regression

With regression, only a certain state vector entries would be used to obtain the spectral gas state weights. The temperature (or two of them for nonequilibrium) would be one of them, along with electron number density. Then, depending on the spectral location, the correct species would be selected, depending on whether this species has some transition in close proximity to that region affecting the absorption/ emission cross section. The preliminary distinction that was formulated to indicate which species are considered in which spectral regions based on absorption spectrum analysis of each species separately is shown in Table 6.1. If none of the species was present, it was considered as a part of the continuum and ion species number densities were used instead.

Table 6.1: The specification of the spectral regions defined for the species considered for regression.

atomic N systems

λ_{min} [A]	λ_{max} [A]
864	867
868	871
872	878
883	890
903	915
950	957
959	961
962	967
979	981
989	992
999	1001
1062	1072
1082	1083
1089	1107
1129	1140
1159	1181
1184	1215
1222	1231
1241	1244
1307	1322
1325	1329
1335	1338
1410	1413
1478	1505
1735	1752
3816	3837
3885	3895
4131	4157
4645	4675
7422	7425
7440	7445
7465	7471
7982	7918
8161	8171
8181	8192
8199	8202
8209	8226
8240	8245
8566	8569
8592	8597
8625	8633
8653	8658
8676	8690
8700	8705
8708	8715
8716	8721
8727	8731
8746	8749
9025	9032
9044	9067
9382	9399
9458	9463
9858	9875
10091	10167
10469	10566
10619	10655
10705	10726
11220	11327
11560	11572
12069	12386
12455	12480
13570	13635

atomic O systems

λ_{min} [A]	λ_{max} [A]
877	880
921	922
924	928
929	933
935	940
947	953
970	980
988	991
999	1000
1023	1029
1038	1040
1041	1042
1151	1153
1217	1218
1294	1310
1641	1642
3945	3949
4363	4372
7766	7780
8443	8451
9254	9275
11279	11294

NO systems

λ_{min} [A]	λ_{max} [A]
1459	3000

N2 systems

λ_{min} [A]	λ_{max} [A]
920	1500
2500	2000

O2 systems

λ_{min} [A]	λ_{max} [A]
1800	4500

N2+ systems

λ_{min} [A]	λ_{max} [A]
1550	2330
3000	5000

Then, for regression, the method of least squares (LS) was used, formulated as:

$$\text{minimise} \, \| b - Ax \|_2, \tag{6.10}$$

which, in full formulation with coefficients w would be the following problem:

$$\text{minimise} \left\| \begin{bmatrix} \varepsilon_1 - \varepsilon_0 \\ \varepsilon_2 - \varepsilon_0 \\ \vdots \\ \varepsilon_{10} - \varepsilon_0 \end{bmatrix} - \begin{bmatrix} f\left(T_{tr,1} - T_{tr,0}\right) & f\left(T_{ev,1} - T_{ev,0}\right) & \dots & f\left(N_{O_2,1} - N_{O_2,0}\right) \\ f\left(T_{tr,2} - T_{tr,0}\right) & f\left(T_{ev,2} - T_{ev,0}\right) & \dots & f\left(N_{O_2,2} - N_{O_2,0}\right) \\ \vdots & \vdots & \vdots & \vdots \\ f\left(T_{tr,10} - T_{tr,0}\right) & f\left(T_{ev,N} - T_{ev,0}\right) & \dots & f\left(N_{O_2,N} - N_{O_2,0}\right) \end{bmatrix} \begin{bmatrix} w_{1,\varepsilon} \\ w_{2,\varepsilon} \\ \vdots \\ w_{N,\varepsilon} \end{bmatrix} \right\|, \tag{6.11}$$

where N is the number of samples. To invert this system, the freely available LAPACK library was used. This technique was sometimes found to produce negative emission and absorption coefficients due to incorrect determination of the weights w. The method considered so far only assumed the dependencies to be linear, which is definitely not physically accurate especially for larger state vector differences (see for example Chapter 2 for the actual physical description). Thus, an alternative of non-negative least squares, NNLS, was also tested:

$$\text{minimize} \, \| b - Ax \|_2, \qquad x > 0. \tag{6.12}$$

Whereas NNLS is even more nonphysical than LS and, in general, has a worse agreement if the original spectrum is recomputed from the weights at the resolved points (since the coefficients are forced to be positive), it also does not result in negative emission or absorption coefficients in case the differences between the state vectors of the resolved and unresolved cells are too large. The applied algorithm was the freely available NNLS solver for High Energy Solar Spectroscopic Imager by NASA (see Ref. [94]).

In both cases, after having determined the weights w, the spectral coefficients are found by:

$$\varepsilon_{i,\lambda} = \varepsilon_{0,\lambda} + \sum_{j=1}^{\text{dim}} w_{j,\varepsilon} f_j, \tag{6.13}$$

$$\kappa_{i,\lambda} = \kappa_{0,\lambda} + \sum_{j=1}^{\text{dim}} w_{j,\kappa} f_j \tag{6.14}$$

,
where f was considered as the linear difference of the local variables (e.g. $T_{t,\text{unresolved}} - T_{t,\text{resolved}}$).

Obviously, more sophisticated methods could be developed to make this regression more physically sound, but as will be shown towards the end of this Chapter, these methods ended up being so computationally expensive, that even them having better accuracy would most likely not be a sufficient justification for their use.

6.3.4. Analytic Approach

Finally, the last technique examined follows the physics of radiation more accurately. The absorption coefficient at a given wavelength would be proportional to the absorption cross section and the number density of the respective species causing the transition. For emissivity, this would be also proportional to the value of the (non)equilibrium Planck function.

The actual value of the Planck function in nonequilibrium cannot be quickly computed. In this simplified approach however, it is assumed that for two neighbouring points in the flowfield with similar conditions and spectra and close to LTE, the ratio between their nonequilibrium Planck functions at a given wavelength will be similar to the ratio of their equilibrium Planck functions if LTE was present. For demonstration, Figure 6.12 shows the nonequilibrium and equilibrium Planck functions in a heavily nonequilibrium region in the CEV afterbody (case taken from the NEQAIR test suite). The radiation field was solved assuming both nonequilibrium, as well as equilibrium. While the actual values of the Planck functions differ significantly, the ratio between them for the neighbouring LOS points with similar conditions is comparable.

This might not hold for spectral regions where there is strong emission, such as those close to the atomic lines (in Figure 6.12, only continuum is shown). An example of such a case is the highly emitting region at the N line, the region around which is shown in Figure 6.13. In this particular case, the difference is caused due to a 10% drop in N number density from LOS point 26 to 27. This drop does not show in the case of a Boltzmann

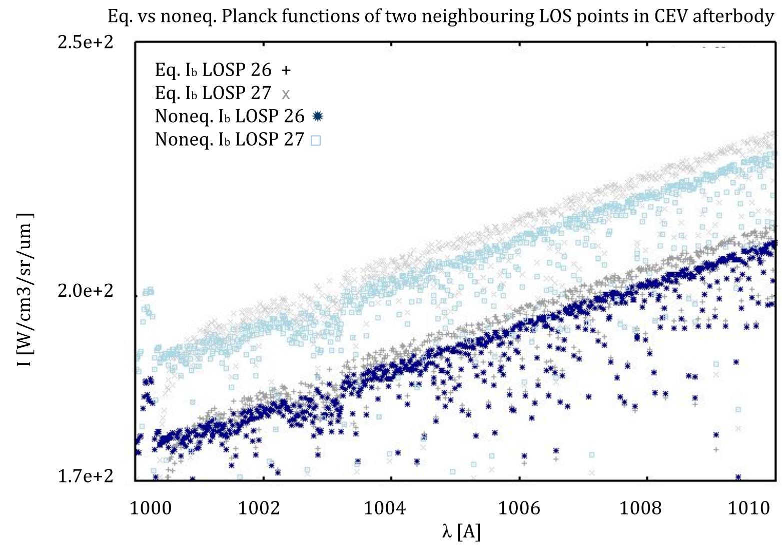

Figure 6.12: Strong nonequilibrium Planck functions (dark and light grey) at two consecutive LOS points in the CEV Afterbody test case in a spectral region relatively far away from strong transitions. Equilibrium Planck functions (dark and light blue) shown for comparison, illustrating the Planck function ratio assumption.

distribution results since there the Planck function is not dependent on species number densities. The emission and absorption in case of nonequilibrium are, however, computed using QSS, the results of which are directly affected by number species densities. Therefore, this drop is projected on the nonequilibrium Planck function where, as a result, the emission with lower N number density is much smaller, with the largest differences occurring at the peak of the line. This is problematic, since these regions contribute most heavily to the emitted energy. Thus, the developed technique can work also for nonequilibrium, as long as the differences in species number densities of the cells are not too large. Otherwise, a different approximation technique should be chosen.

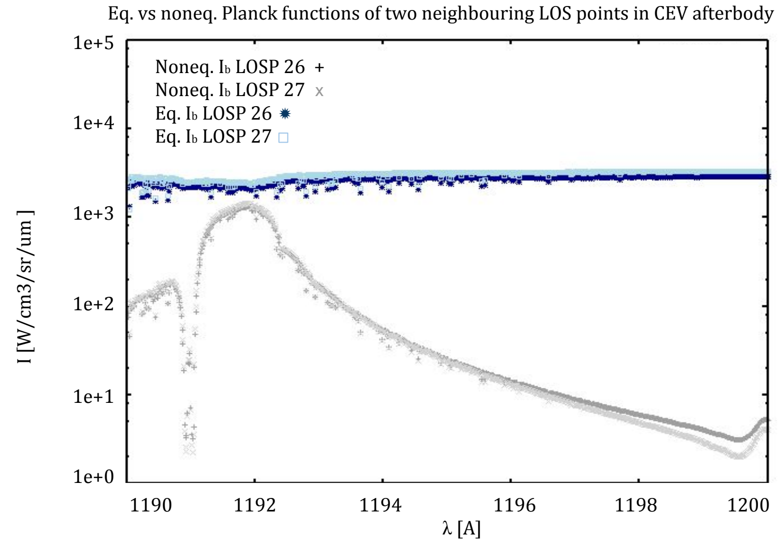

Figure 6.13: Strong nonequilibrium Planck functions (dark and light grey) at two consecutive LOS points in the CEV Afterbody test case in a spectral region at strong transition lines showing that the Planck function ratio assumptions cannot be made. Equilibrium Planck functions (dark and light blue) shown for comparison, illustrating the Planck function ratio assumption.

It is believed however that an approximation technique such as this one would be mostly needed for boundary layers with steep gradients, where the thermal conditions are close to LTE. For the other regions,

Table 6.2: The summary of the gas conditions of the 4 LOS points selected for analysis of the analytic adjustment method.

n	x	Tt, Tr	Tv, Te	E-	N+	O+	O	N
2	1.00E-01	1.30E+04	6.13E+03	1.24E+16	1.02E+16	2.18E+15	2.44E+16	5.96E+16
3	2.00E-01	1.17E+04	9.21E+03	2.90E+16	2.42E+16	4.79E+15	6.67E+16	2.04E+17
50	4.90E+00	5.59E+03	5.38E+03	7.38E+14	6.42E+14	3.81E+13	2.95E+17	2.86E+17
51	5.00E+00	5.33E+03	5.10E+03	6.44E+14	5.60E+14	3.76E+13	3.13E+17	2.67E+17

one of the other presented alternatives might be more suitable.

Since this will in the end be the preferred method of choice, the FIRE II spectra were taken to demonstrate the principle of this analytic adjustment and its limitations. Strong nonequilibrium exists next to the shock as observed in Figure 5.15. On the other hand, the boundary layer region on the left half is mostly in LTE. Thus, these two regions were used for demonstration. The differences in gas conditions in these 4 points are summarised in Table 6.2.

From the equilibrium region, LOS point 50 was selected, spectra of which were readjusted to represent spectra at LOS point 51. Between these two cells, the temperatures differ by 260K and the species number densities vary in the range of 1% to 35%, with the most dominant atomic species roughly 6%. The emission spectrum was approximated from the spectrum at 50, and all three spectra; the original, the estimated and the actual, are shown in Figure 6.14.

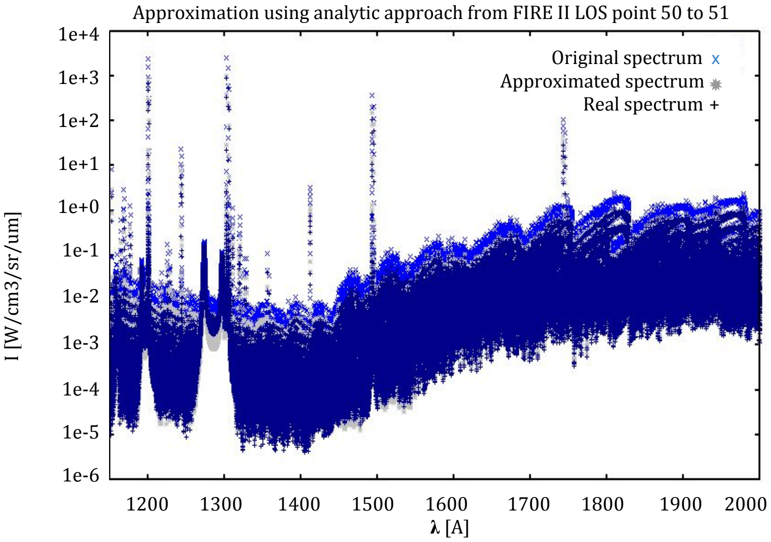

Figure 6.14: A demonstration of the accuracy of the analytical approach when LTE can be assumed. The original spectrum is in bright blue x, the approximated result in grey * and the real spectrum for comparison in dark +.

Figure 6.14 was further magnified into the region of the strong atomic radiation from which the majority of the intensity originates, as shown in Figure 6.15. From this example, it is self-evident that this analytic readjustment can offer a fast spectral approximation with a fairly good performance. On most places, the approximated and real spectra overlap almost to the point that they cannot be told apart.

However, this cannot be said about nonequilibrium. Spectrum from LOS point 3, following the region of maximum intensity, was selected as base spectra to estimate the spectra at the region of maximum nonequilibrium and radiative intensity at LOS point 2. The difference of translational temperature between these two points is 1.3kK and approximately over 3kK in vibrational temperature, with the two temperatures evolving with a different trend. The resulting approximation attempt is shown in Figure 6.16.

As could be seen from Figure 6.13, especially around the strong atomic lines, the assumption of the constant equilibrium Planck function ratio is not accurate. For this reason, the magnified atomic radiation region in Figure 6.17 shows a very large discrepancy, with the approximated spectrum indicating orders of magnitude lower intensity. Even though these regions are fairly narrow, they are the main contributors to radiation, and so this disagreement cannot be ignored. At best, in the regions of strong atomic radiation, the code can

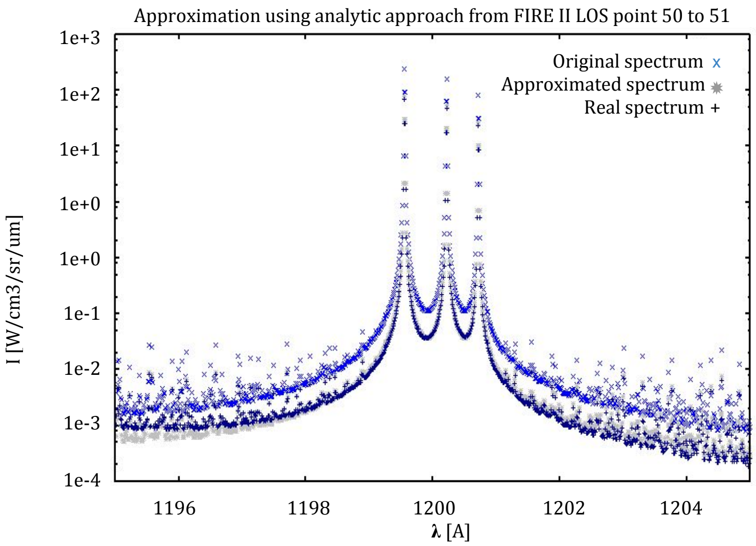

Figure 6.15: A demonstration of the accuracy of the analytical approach around the region of strong atomic emission when LTE can be assumed. The original spectrum is in bright blue x, the approximated result in grey * and the real spectrum for comparison in dark +.

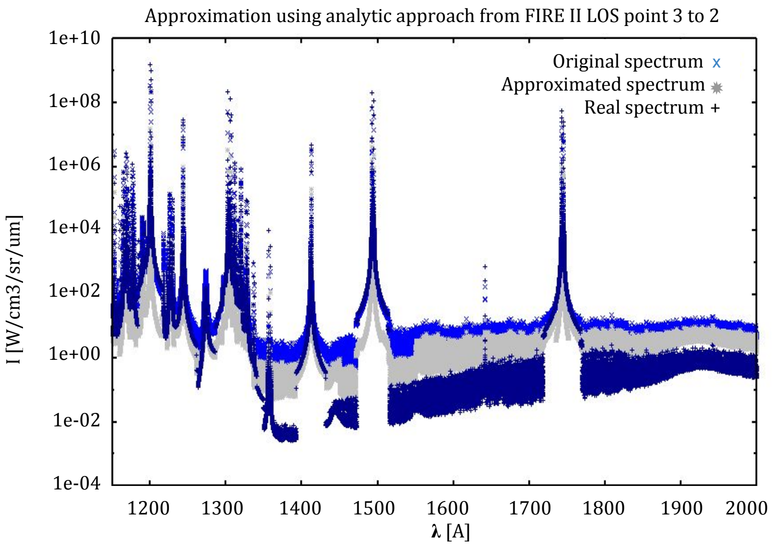

Figure 6.16: A demonstration of the inaccuracy of the analytical approach in nonequilibrium. The original spectrum is in bright blue x, the approximated result in grey * and the real spectrum for comparison in dark +.

be made to ignore any adjustments to spectral emissivity as a result of the Planck function.

Thus, this technique should be used in conditions close to LTE. Taking this assumption into account, at each wavelength, the emissivity can be recomputed using the Planck function ratio from the known reference spectrum as:

$$\varepsilon = \varepsilon_0 \frac{c_1}{\lambda^5 \left(e^{c_2/\lambda T} - 1\right)} \frac{\lambda^5 \left(e^{c_2/\lambda T_0} - 1\right)}{c_1} = \varepsilon_0 \frac{\left(e^{c_2/\lambda T_0} - 1\right)}{\left(e^{c_2/\lambda T} - 1\right)}, \tag{6.15}$$

and both the emissivity and the absorption coefficient with the ratio of the species densities:

$$\varepsilon = \varepsilon_0 \frac{N_i}{N_{0,i}}, \qquad \kappa = \kappa \frac{N_i}{N_{0,i}}, \tag{6.16}$$

that are considered to be emitting at that particular wavelength. This is tricky, however, since absorption

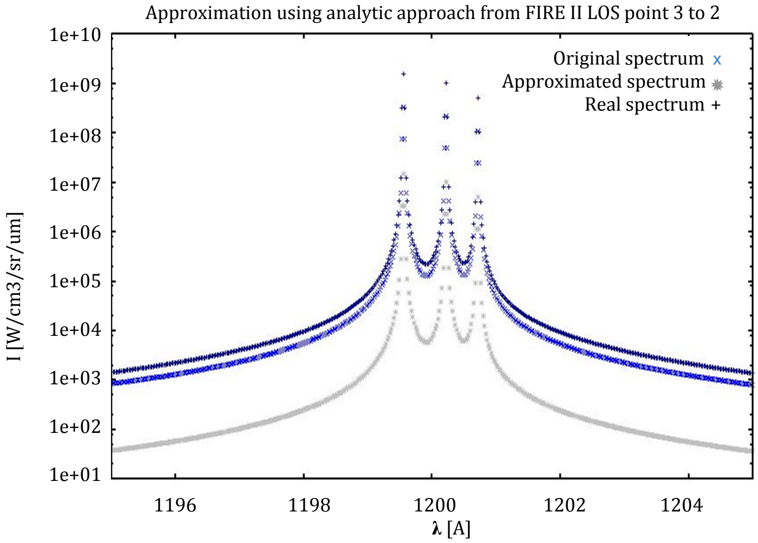

Figure 6.17: A demonstration of the inaccuracy of the analytical approach in nonequilibrium around the region of strong atomic emission. The original spectrum is in bright blue x, the approximated result in grey * and the real spectrum for comparison in dark +.

coefficient is not multiplicative when multiple species contribute to it:

$$\kappa \neq \kappa_0 \prod_{i=1}^{N_{\text{species}}} \frac{N_i}{N_{i,0}}. \tag{6.17}$$

Since storing information about to what extent each species contributes to each wavelength in each cell would require a lot of computational memory, only the strongest emitters are always considered, following Table 6.1. For example, from the 6 main species in air, the highest priority is given to the atomic emitters, then N_2^+, NO, N_2 and then O_2.

Now, the performance of all of these techniques when applied to an actual radiative problem will be discussed.

6.3.5. Performance Comparison

The techniques formulated above were assessed by considering the CEV Orion (small scale) case. The original spectral discretization of 78 points was decreased down to 30 points and 15 points, and the rest of the spectra were recomputed using the techniques above. Then, the profile of the radiative source term was compared to the original. In addition, the required time for computation was compared. Table 6.3 shows the results, were N_f refers to the number of cells where spectra were generated and $N_{x,0}$ is the initial number of cells (78). As can be seen from the Table, when these two numbers are the same, as expected, the averaging and analytic techniques are exact, since the actual spectra are retained.

Next to these techniques, 3 regression techniques were tested, using both LS and NNLS, as well as a varying number of dimensions. The reason why lower dimensional regression analyses were included is the fact that, from Figure 5.12, it is clear that the profile of many species is similar in nature, just not in magnitude, and therefore could, in a way, be considered to be dependent. Reducing the number of dimensions should, in theory, be beneficial, as then more samples can be used with same 3rd grid spectral discretization level (lower dimensional regression requires fewer samples), and the accuracy could increase. Thus, 4 dimensional methods were also tested.

The source term that results when attempting to recreate the radiative heat flux divergence over the CEV stagnation line, with 30 known spectra on the 3rd grid, are shown in Figure 6.18 for regression techniques and in Figure 6.19 for the rest. All techniques performed well over the first half of the profile, where significant species and temperature gradients are not present. Especially the region between LOS point 50 to 60 was difficult for most methods to properly reproduce. For all simulations, 20000 photon rays were used.

The same test but with 15 spectra was then performed with the results shown in Figure 6.20 for regression techniques and in Figure 6.21 for the rest. The only two methods which could follow the steep decrease in

Table 6.3: A comparison of standard deviations of the radiative heat flux divergence for the different spectral approximation techniques tested. (NN)LS stands for (non-negative) least squares with the number of regression dimensions indicated.

	STDEV [W/cm^3]		
Technique	$N_f = N_{x,0}$	$N_f = 30$	$N_f = 15$
NNLS, 4 dim	0.25	0.20	0.49
NNLS, 10 dim	0.04	>1	0.06
LS, 4 dim	0.02	>1	>1
Closest match	0.00	0.02	0.17
2 Point averaging	0.00	0.03	0.13
Analytic adjustment	0.00	0.02	0.04

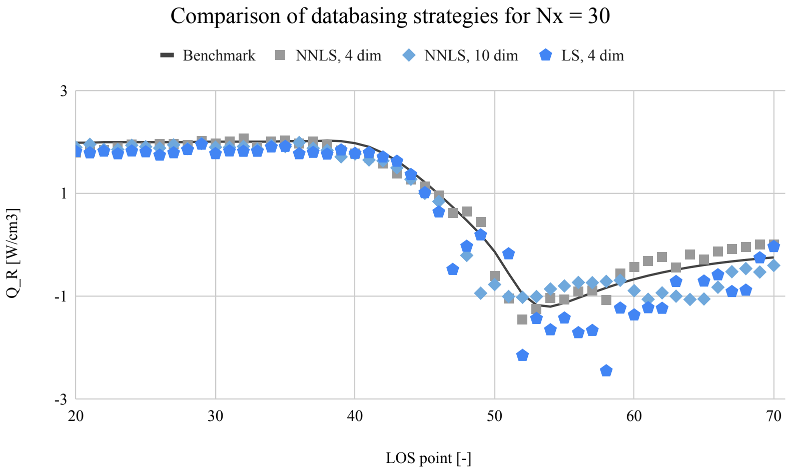

Figure 6.18: Performance of the spectral regression methods for a 3rd grid adjusted from 78 cells to 30. LS stands for least square regression and NNLS for non-negative least squares regression.

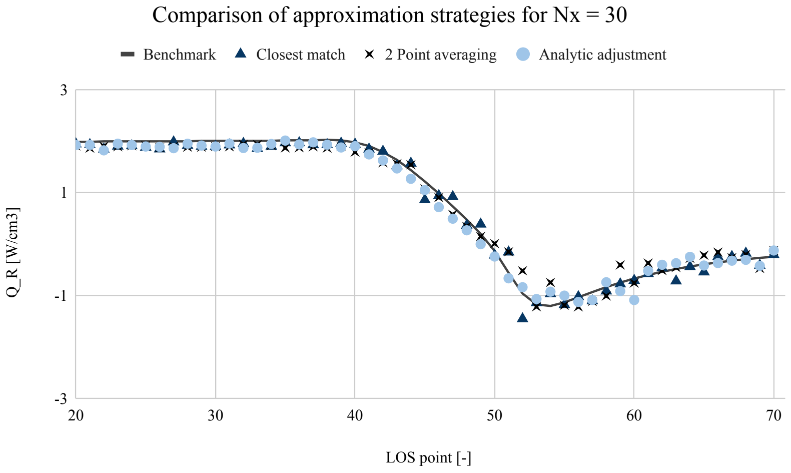

Figure 6.19: The performance of spectral approximation methods for a 3rd grid adjusted from 78 cells to 30.

the source term were the full 10D non-negative least squares regression method and the analytic adjustment method.

It is curious to see that the regression techniques were, in many regions, worse than simply taking the nearest known spectrum. For the LS method, bad conditioning of the system combined with inaccurate physical representation (linear differences in the state vectors) would oftentimes result in extremely large,

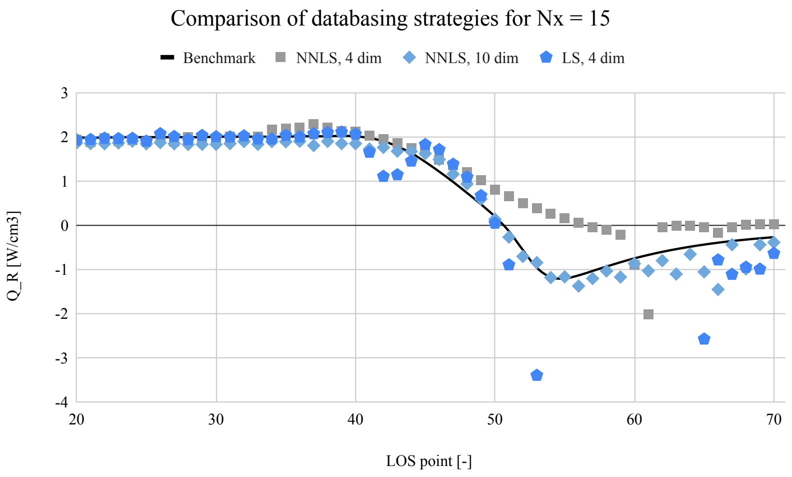

Figure 6.20: The performance of spectral regression methods for a 3rd grid adjusted from 78 cells to 15. LS stands for least square regression and NNLS for non-negative least squares regression.

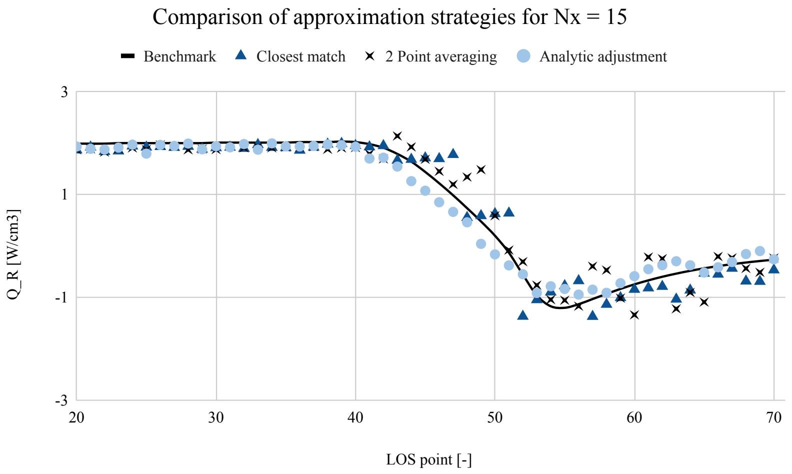

Figure 6.21: the performance of spectral approximation methods for a 3rd grid adjusted from 78 cells to 15.

sometimes negative, coefficients, which also caused the solution to explode in the coarse case in the boundary layer portion of the LOS. The NNLS performed better, but forcing positive coefficients further devalued any physical meaning that could be behind the regression approach.

In addition to the error, also the computational requirements are of importance since the sole purpose of this effort is to reduce the simulation time. The time required for these methods, and how it scales with increasing the number of photons (N_γ), number of 3rd grid cells (N_f) and second grid cells (N) is shown in Tables 6.4 through 6.6, respectively. It is clear that the simple techniques without regression are much faster.

Further effort could definitely be put to improve the accuracy of the regression techniques by more elaborate filtering of the dependent variables and making the calculation of the gas state differences more sophisticated. Then, most likely, the errors observed in Figures 6.20 and 6.18 could be reduced dramatically. However the purpose of this approximation process is to improve speed, and, based on the results, the simple techniques are faster by an order of magnitude when compared to regression. Since the analytic technique was found to have the best match, it was selected as a default method. For problems with strong nonequilibrium regions, the technique of 2-averaging (interpolation from 2 spectra) can be selected instead by the user in the code.

Table 6.4: The time required for the tested acceleration schemes for the two 3rd grid discretisation levels (N_f) with doubling in photon ray number N_γ. N is the number of the 2nd grid cells.

Technique	Mesh 1 $N = 70$, $N_f = 70$ $N_{\gamma,1} = 1e4$	Mesh 1 $N = 70$, $N_f = 70$ $N_{\gamma,2} = 2e4$	$\frac{t_{N_{\gamma,2}}}{t_{N_{\gamma,1}}}$	Mesh 2 $N = 70$, $N_f = 15$ $N_{\gamma,1} = 1e4$	Mesh 2 $N = 70$, $N_f = 15$ $N_{\gamma,2} = 2e4$	$\frac{t_{N_{\gamma,2}}}{t_{N_{\gamma,1}}}$
2-Averaging	875 s	1045 s	1.19x	487 s	297 s	1.64x
Closest m.	785 s	871 s	1.11x	322 s	231 s	1.39x
10D NNLS	3618 s	4056 s	1.12x	2730 s	2324 s	1.17x
4D NNLS	2639 s	2877 s	1.09x	1623 s	1147 s	1.41x
4D LS	2925 s	3156 s	1.08x	1730 s	1363 s	1.27x
Analytic	575 s	741 s	1.29x	-	-	-

Table 6.5: The time required for the tested acceleration schemes for two 3rd photon ray discretisation levels (N_γ) with refining the 3rd grid N_f. N is the number of the 2nd grid cells.

Technique	Mesh 1 $N = 70$, $N_\gamma = 2e4$ $N_{f,1} = 15$	Mesh 2 $N = 70$, $N_\gamma = 2e4$ $N_{f,2} = 70$	$\frac{N_{f,2}}{N_{f,1}}$	Mesh 1 $N = 70$, $N_\gamma = 1e4$ $N_{f,1} = 15$	Mesh 2 $N = 70$, $N_\gamma = 1e4$ $N_{f,2} = 70$	$\frac{N_{f,2}}{N_{f,1}}$
2-Averaging	487 s	1045 s	2.15x	297 s	875 s	2.95x
Closest m.	322 s	871 s	2.70x	231 s	785 s	3.40x
10D NNLS	2730 s	4056 s	1.49x	2324 s	3618 s	1.56x
4D NNLS	1623 s	2877 s	1.77x	1147 s	2639 s	2.30x
4D LS	1730 s	3156 s	1.82x	1363 s	2925 s	2.15x
Analytic	-	-	-	-	-	-

Table 6.6: The time required for the tested acceleration schemes with increasing number of 2nd grid cells. N_f stands for the number of the cells on the 3rd grid and N_γ for the number of photon rays.

Technique	Mesh 1 $N_f = 15$, $N_\gamma = 1e4$ $N = 35$	Mesh 2 $N_f = 15$, $N_\gamma = 1e4$ $N = 70$	Mesh 3 $N_f = 15$, $N_\gamma = 1e4$ $N = 140$	$\frac{t_{N_2}}{t_{N_1}}$	$\frac{t_{N_3}}{t_{N_2}}$
2-Averaging	141 s	297 s	1188 s	2.11x	4.00x
Closest m.	104 s	177 s	620 s	1.70x	3.50x
10D NNLS	758 s	2324 s	8366 s	3.07x	3.60x
4D NNLS	458 s	1192 s	4089 s	2.60x	3.43x
4D LS	462 s	1363 s	4406 s	2.95x	3.23x
Analytic	110 s	232 s	-	2.11x	-

This concludes the analysis of the acceleration methods examined. The use of Sobol sequences is preferred, especially for highly anisotropic media. The downsampling and discretisation tolerances were pre-set to maximise the speed and minimise the memory needed, while avoiding the introduction of significant errors. A 3rd grid layer was added to the nonequilibrium calculations from which spectra are approximated to the much finer 2nd grid.

7

Discussion

This Chapter aims to summarise and evaluate the main findings, such that conclusions and recommendations for improvement can be formulated afterwards. The various portions of the code are discussed separately.

7.1. Performance of the Core of the RTE Solver

The implementation of the core of the RTE solver (ERMC formulation) is the same as the one adapted in Ref. [98], which was also demonstrated when the results were compared for the grey validation cases 1 through 4 (see Figures 5.1 to 5.4). Example convergence plots (error as a function of number of realisations) for two of these cases were shown in Figures 6.2 and 6.3. Compared to the solver presented in Ref. [98], GPU paralellisation was not yet employed. Unlike the implementation from Ref. [98], due to the necessity of proper coupling with CFD and of applicability to a wide range of cases, the current solver also supports the presence of reflective boundaries, internal (possibly reflective) obstructions such as walls, as well as no-wall boundaries for inflow, outflow and symmetry.

The solver also supports the use of Sobol sequences when convergence performance is critical. As shown in Figure 6.3, for anisotropic cases, the same error can be achieved with an order of magnitude smaller number of realisations, if an LSD is used. The time required to generate a Sobol sequence was found to be roughly 10 times longer than that with the default random number generator, but as shown in Figure 6.6, this time, in general, is completely negligible for cases with complex spectra.

The performance of the solver from Ref. [98] for CPU adaptation was reported for a case of H_2O at 1000K. The k-distributions of H_2O for that solver are, however, pre-databased as the solver was made for LTE cases only with pre-determined temperatures. Therefore, since the spectral generation and handling is the most time consuming portion of the solver, a fair comparison of the two solvers cannot be made based on this data alone.

7.2. Performance of the HITRAN Spectral Generator

The implementation of the HITRAN database was in detail discussed in Chapter 4. It was shown that compared to the HAPI standard for spectral generation, a speed up of one to two orders of magnitude was obtained depending on the number of transitions available for the particular species. This was thanks to the reduced (triangular) spectral discretization (see Figure 4.6), as well as the pre-databasing of the partition functions (see Equations (4.28), (4.29) and (4.30)) using spline interpolation. Despite this sped-up generation with a reduced number of lines, it was shown in Figures 4.8 and 4.9 that the integrated mean Planck coefficients were accurate, with only a small discrepancy at certain temperatures for CO_2, most likely caused by recent updates to HITRAN not accounted for in the validation data. Demonstration of the accuracy of the HITRAN implementation along with the rest of the PMC solver is shown in Figures 5.5, 5.6, 5.7 and 5.8, further confirming the accuracy of the developed method.

And yet, even though the implemented routine for HITRAN is performance-wise superior to the standard HAPI routines, the time to generate spectra is still not negligible, if they are to be resolved for hundreds to thousands of cells and if the absorption coefficients and Planck ratios should be computed for ten thousands to hundred thousands of photon rays. Thus, it is recommended that, if a certain case is to be studied with fine radiation refinement and repeatedly, especially when coupled with CFD, the k-distributions for the particular species are pre-databased for the expected thermodynamic conditions as in Ref. [98], so that the spectra do not have to be generated on-the-fly. Alternatively, for simpler radiative problems, other spectral models (such as EWB or the box model) can be used.

7.3. Performance of the NEQAIR-Based Spectral Generator

The accuracy of the NEQAIR implementation was shown in Figures 5.9 through 5.21 both for flows in equilibrium and strong nonequilibrium. Since in this case, the convergence to accurate results could not be guaranteed unlike the LTE cases based on Ref. [98], the standard deviation when compared to the 1D NEQAIR integration was computed and presented in Table 5.2. For all of the evaluated cases, a relatively high standard deviation was found compared to the LTE cases, especially for the FIRE II simulations.

As was discussed in Chapter 5, two main explanations for the observed discrepancies were formulated. The first one, in case of the FIRE II shock, is the different formulation of the no-initial-radiance boundary condition in the 1D LS integration and in PMC. Since the error at the shock was removed when this shock was moved closer to the middle of the domain with same temperatures (see case 10 and Figure 5.21), data for STDEV without the boundary points for FIRE II was also presented, dropping by an order of magnitude.

The second explanation for the under-prediction of regions close to the hot spots is the local wavelength sampling used for hypersonic cases, instead of the global wavelength sampling. When global wavelength sampling was used, the under-prediction disappeared (as shown in Figure 5.22), but the computation blew up for regions further away, which the photon rays from the hottest cell would not reach. This points at a challenge which could be solved either by reformulation of the code to forward MC or by solving for radiation twice, to determine the domains of influence and to select from where to sample the wavelengths.

In practice, this was not attempted due to the additional increase in the required computational resources. Apart from the FIRE II case, the resulting error remained within the 5-10% range, and as it could be seen from Table 4.4, that is also the magnitude of error that could be expected from NEQAIR due to inaccuracies in the spectral generation. Thus, reducing this error by the method suggested above might not make the simulation more accurate, and would definitely result in more computational cost, which is already high as it is.

In Chapter 6, several acceleration techniques were presented to speed up the computation in the NEQAIR mode. Trade-offs between error and spectrum size were presented when filtered using various downsampling techniques, shown in Figures 6.9 and 6.10. It was also shown that, for fast simulations, a 1 to 3 point-per-line discretisation is typically sufficient, depending on whether it is the atomic or molecular radiation that is mostly prevalent.

Afterwards, techniques to approximate the spectra from another grid layer were shown. Three types of techniques were tested - simple weighing, multivariate regression and analytic adjustment considering LTE. The methods were tested by taking the original CEV stagnation line and coarsening the spectral mesh from the original mesh of 78 spectra down to 30 and 15 spectra, with the results shown in Figures 6.18 and 6.19 for the former case and Figures 6.20 and 6.21 for the latter. It was pointed out that due to the time constraints, only a very primitive regression principle was used with linear functions, leading to difficulties when used for flow sections with high gradients, sometimes having the source completely blow up. From the comparison of the techniques when it came to the computational time (see Tables 6.6, 6.4 and 6.5), it became clear that even if the regression approach could be made far more accurate with more sophisticated methods, it would still require an order of magnitude higher time for computation compared to other techniques. Thus, it was suggested that for problems close to equilibrium, the analytic approach is used, and for problems in nonequilibrium, since the analytic approach could lead to much worse estimates than simple averaging (see for example the discussion around Figure 6.17), a 2-point averaging should be applied instead.

The single most effective technique which should be applied to lower the computational demands further remains the use of some of the spectral processing methods, such as MBOB. While these do sometimes require a fair amount of pre-databasing and their setup is typically case specific, which is the reason they were not used in this thesis work, the LBL processing remains the most computationally demanding method of all.

7.4. Coupling and Performance with INCA

After the solver was tested as a standalone software, it was coupled with INCA CFD. Chapter 4 summarised the required inputs to allow for this coupling and specified how this data is converted from the INCA grid to the radiation grid.

The conversion is mainly done through the inverse distance weighting. This introduces a loop of N(1st grid) x N(2nd grid) twice, which might consume significant resources should the two grids be very fine. The smoothness of the final solution depends on the IDW exponent, and thus attention must be paid to its selection for flows with sharp gradients, where a small exponent might lead to an artificial diffusion.

To test this coupling, a case was set up with a Nitrogen plasma at a Mach number of 2.5 and 5. Reaction kinetics was not considered, but since the number density of the flow constituents varied anyway thanks to the variations in total density, this did not discredit this testing method. Cases of varying discretisation were run levels to assess the computational needs of the radiation solver with respect to those of INCA.

For the simulation cases described in Chapter 5, the radiation calculation took between 94 to 98% of the total simulation, as expected according to the literature study. This figure might drop by a couple of percentage points if the reaction kinetics is properly accounted for, due to the fact this routine takes additional time, as solving for the stiff ODE systems might be computationally heavy in many flow problems.

In the analysed cases, the applied discretisation varied roughly between 5 - 25% of the 1st grid for the 2nd grid and 4 - 10% of the 1st grid for the 3rd grid. Since the contribution of the radiative heat flux for this case was found to be relatively small (below 1% in a majority of the domain), loose coupling was applied.

In Table 5.6, the times of the various portions of the radiation solver were compared. It was found that up to 70% of the total time was spent on the Monte Carlo procedures, which is dominated by spectral handling (calculation of emission wavelengths and absorption coefficients with Planck function ratios in the rest of the flowfield). This means that the most significant acceleration could be achieved if these operations were simplified (e.g. using spectral simplification techniques, such as MBOB or k-distributions), as discussed in the previous section. The techniques which could be further used to accelerate these computationally heavy portions are thus discussed next.

7.5. Recommended Acceleration Methods

Having seen that the vast majority of CPU time is invested into radiation solving, several methods can be proposed to accelerate this procedure based on both the performed literature study, as well as observations made when assessing the performance of the code. These are discussed below.

7.5.1. On-the-Fly Calculation of QSS with Databasing Schemes

A technique which would not require pre-calculation of all spectra and thus possibly allowing also for a straightforward GPU adaptation would be the use of the pre-databasing system proposed by Sohn et al. in Ref. [101]. Refer to Chapter 2 for more information about this technique. If the absorption and emission spectra could be relatively quickly computed on-the-fly, memory problems with the GPU would be avoided completely. However, it is still questionable whether the databasing scheme from Ref. [101] would actually result in significant increase in performance compared to if NEQAIR was invoked each time a coefficient was required, especially if molecular radiation is involved, since with diatomic species, a speed up of only 3x was measured. If a typical NEQAIR spectral generation takes 200 - 300s, with this speedup, it is clear that this approach with on-the-fly calculation would still be completely impractical. Further investigation on this method and on additional possible simplifications and approximations would thus be appreciated.

7.5.2. Use of LBL Alternatives

For LTE problems, for repeated calculations coupled to CFD and cases without large ranges of pressures and temperatures, pre-databased k-distributions or even simpler models, such as EWB or the box model for single species media, would definitely make the radiation calculations more affordable. Since these usually require pre-databasing, they would have to be implemented on the case-specific basis. Judging from the very high speed of the k-distribution-based solver from Ref. [98], the investment of this additional effort would definitely be compensated by the increase in performance, especially if the simulations were to be done repeatedly for the same or similar cases.

An acceleration would be possible also for nonequilibrium with methods such as (multiple-band) opacity binning (see e.g. Ref. [51]). Firstly, an analysis would be necessary to evaluate how many bands and bins are required for accurate results and in which cases such a method can be implemented. Depending on the technique, quite some effort might be needed to create all the databases required before the start of the computation, similarly to the LTE problems with simpler models.

7.5.3. Other Recommended Acceleration Methods

Apart from the pre-databasing of the k-distributions in case of LTE and approximation/ databasing techniques for non-LTE, and besides the possible GPU parallelisation, which will be discussed in the following subsection, there are still several portions of the code which could be improved. These are, for example, the following:

- Detection of repetition in photon wavelength: Especially in regions dominated by strong atomic radiation, it was observed that many emitted photons shared the same wavelengths (in the centre of these transitions). Thus, if 10000 of photons rays are computed, from which 1/10th has the same wavelength, it would be beneficial to detect that the wavelength repeats so that the absorption coefficients in the rest of the flow field do not have to be re-computed. Since determination of the absorption coefficient is computationally as heavy as the emitting process (and even more for larger number of cells and photons), depending on the case, this could save a lot of solution effort.

- Generation of a multigrid around the emitting cell: Another approach, which was also tested by Silvestri and Pecnik in Ref. [98], is to use a grid, the size of which increases further away from the cell. This is due to the fact that those photon rays which will be quickly absorbed, will do so close to the cell where the grid is still fine, whereas the rest that will travel far away will be traced much faster due to the coarser mesh.

- Use of binary files: In the current implementation, all the files generated are in ASCII. This was mainly for the purposes of easy verification and validation. Use of binary files can halve their size, which also means faster processing such as reading and writing.

- Use of more appropriate spectral boundaries: Currently, to conform to all possible simulation cases, the spectra generated are very wide to not miss any important transitions. However, when the composition and temperature ranges of the media are known a priori, the spectral bounds (lower and upper resolved wavelength/ wavenumber) could be readjusted, for example by following the modelling advice shown in Figure 4.11, or by defining the threshold according to the Planck function shape and Wien's displacement law.

- Use of HITRAN for cold NEQAIR cells: Lastly, when NEQAIR has problems to solve the spectra due to low temperatures (assuming LTE), HITRAN could be invoked instead. The HITRAN spectral generation is much faster and, in cold cells, also more reliable than NEQAIR. This would, however, mean that the HITRAN subroutine would have to be configured for mixtures and made compatible with the subroutines of NEQAIR to combine the results, while still processing everything in an MPI parallel fashion. This was considered to be outside of the scope of the thesis work, since a major reconstruction of the code would be necessary.

Finally, even application of Graphical Processing Units could be beneficial for this type of the reciprocity Monte Carlo formulation, which is the main reason this approach was selected. This is briefly touched upon in the following subsection.

7.5.4. Recommendations for a Possible GPU Adaptation

Due to time constraints, this work was not extended to GPUs. However, planning for a possible extension to GPU has been performed nevertheless, and thus will be discussed here briefly as a starting point for a potential future work.

As discussed by Silvestri and Pecnik in Ref. [98], the ERMC formulation is ideal for GPU. The heat flux in each cell can be computed independently, and thus for equilibrium cases, where each spectrum can be relatively quickly computed from local temperature, gas composition and pressure, only these field variables need to be transferred to the GPU memory. Memory transfer and communication is essential for working with GPUs, since the slow CPU to GPU memory transfer is the biggest drawback of using GPUs, in addition to their relatively small memory size (typically ranging from 8 to 24GB). In this case, for HITRAN and grey simulations, the parallelisation can be performed in the same way as it was done in Ref. [98], without significant challenges and with comparable expected performance increase. Obviously, if spectra are generated from HITRAN directly and not read from k-distributions as in Ref. [98], the efficiency of GPU parallelisation will likely suffer.

For nonequilibrium, however, this process is far more complicated, and is the reason why GPUs were in the end not yet implemented. The slow operation of NEQAIR and the way in which it is parallelised (one spectrum per processor) means that the spectra should be pre-computed for maximum efficiency, as it is done in the current configuration. Also, during pre-computation of these spectra, even CPU sometimes struggles with insufficient memory, indicating that use of GPU for this task would be inappropriate.

This means that, in theory, the spectra of the entire domain would have to be transferred to the GPU memory. Even if in a binary format, this would mean more than 1GB per 100 spectral cells (considering real 8). That means that larger problems could not be fitted onto the GPUs, at least until significant technological leaps in GPU storage (and memory transfer time) are made.

Two possible GPU parallelisation approaches were formulated in the beginning of the thesis work:

1. Cell per thread parallelisation
2. Photon ray per thread parallelisation

In case of the former, the approach is the same as in Ref. [98]. The memory problem remains, since to resolve a cell, all the spectra of the cells in the flowfield where the photon ray can wander must be known. An adjustment to this was formulated, were only the spectra of the neighbouring cells would be transferred to GPU such that they would fit onto it. This is a reasonable remedy, but only for the highly absorptive regions. Then, in case a photon escapes this transferred domain, it is retraced by the CPU after the GPU threads have finalised their calculations and added to the statistics. Both approaches will be discussed below in more detail.

Firstly, the latter option will be discussed. The second approach appears simpler and faster when it comes to memory operations, since only the absorption coefficients and Planck function ratios of all cells at the already known emission wavelengths must be transferred, which is in order of tens of MBs. However, this transfer still costs time, and thus of crucial importance to performance estimation is to determine whether the combined time of ray tracing and this memory transfer to and from GPU is shorter than the tracing time by the CPU alone.

To estimate how many iterations are made in the ray tracing "for" loop, the average number of cells crossed in the CEV Orion case was computed. The results are shown in Figure 7.1. Obviously, these numbers may very depending on the case, but, in general, the absorption coefficients in the centre of these hot gasses and indeed very large, so the expected order of magnitude remains the same.

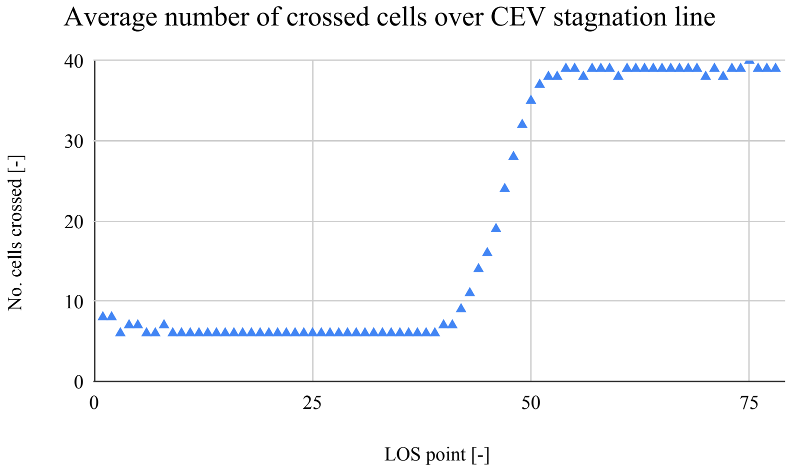

Figure 7.1: The average number of cell crossings over the Orion CEV stagnation line. The higher number corresponds to the more transmissive boundary layer region.

For a typical photon tracing loop in a domain of 1000 cells, it was measured that one loop takes approximately 1e-6s by CPU. A typical memory transfer of 10-100MB takes, regardless of the transfer method and device, in the range of 1 to 100ms (see e.g. Ref. [34]). From Figure 7.1, it is thus clear that this approach is not efficient and will only degrade the performance. From these estimates, this approach would only be beneficial if the number of iterations per photon ray exceeded 1000 - 100 000 depending on the device and transfer method, which might happen only in very, very transmissive problems. Thus, for this approach to work efficiently:

- The medium should be very transmissive: to allow for (hundred-) thousands cell passages while tracing
- The 3rd spectral grid domain should be relatively small: to limit the memory transfer time

It is therefore clear that the first approach of GPU thread per cell is more practical for nonequilibrium problems from the two here analysed. However, the obstacle of memory transfer time and GPU storage must be resolved. The storage problem could be tackled by the technique of transferring only a certain portion of the domain and re-tracing the escaping photon rays by CPU. As for the transfer time problem, typical GPUs nowadays have CPU to GPU memory transfer speed of 5-10GB/s (see e.g. Ref. [34]). For the investigated nonequilibrium cases, for 10000 photons and a domain of a 100 cells, one cell loop was found to take between 1 - 5 seconds. Doubling of cells in the domain caused roughly doubling of this time. This time is not known for GPU as it was not measured, but despite the fact that several "if" statements are present, for the sake of the argument, let us assume that its duration is negligible compared to the time required for CPU. Under these circumstances, for this approach to be beneficial:

- The medium should be very opaque: so that re-tracing by CPU is not frequently needed and smaller spectral domains can be transferred
- The 2nd grid domain should be relatively large, ideally >> 1000 cells: so that the cell loop on GPU gives much better performance than on CPU and overshadows the 1-2s memory transfer time

Should the two above conditions not be met, it is unlikely that parallelisation with GPU would provide significant performance increase, unless other possible GPU implementation approaches, not here formulated, are developed instead.

8

Conclusions and Outlook

The aim of this thesis work was to implement radiation modelling to INCA to model hypersonic and combustion flows, while aiming for an optimum balance between accuracy of the solution and computational resources required. This aim led to the development of a solver which would have to be both sufficiently accurate for potential studies of turbulent-radiation interaction in combustion flows, as well as capable of handling nonequilibrium conditions in hypersonic plasma. Additional requirements on this code included compatibility with INCA, and suitability for a wide variety of problems without additional effort.

After a thorough literature study on the topics of hypersonic radiation, combustion flows and turbulence-radiation interaction and, after a trade-off of the available avenues, it was decided to develop a code based on the stochastic method of Monte Carlo, based on the emission reciprocity formulation. This solver would use the HITRAN database for problems at local thermodynamic equilibrium (LTE) and subroutines from NASA's NEQAIR for nonequilibrium problems, to generate spectra.

The code was developed in Fortran 90 and was parallelised using Message Passing Interface. The implementation of the Monte Carlo technique along with the HITRAN and NEQAIR libraries has been tested with 14 test cases to cover all main subroutines of the code. The cases included grey media, hot LTE H_2O and CO_2 media, as well as adjusted nonequilibrium stagnation line profiles of the FIRE II vehicle and Orion Crew Exploration Vehicle during reentry. In addition, the implementation of features such as partly reflective walls and periodic boundary conditions was verified. The validation results revealed good convergence and accurate operation of the code, at least for the operation in LTE. Errors were present at the very high intensity shock region in the FIRE II test case, but this was attributed to the formulation of the no-initial-radiance boundary conditions. When this shock was placed into the middle of the domain, far away from the boundaries and with sufficient discretization, the error was no longer present.

Coupling with NEQAIR and evaluation of the test cases of the reentry vehicle stagnation lines showed that the emission reciprocity formulation might lead to an under-prediction in the radiative heat flux divergence. This was associated to the fact that the emission-based reciprocal formulation uses sampling either from the hottest cell in the domain, or from the local cell, depending on the optical thickness of the medium. In hypersonic plasma, which can be locally highly absorptive compared to, e.g., combustion flows, local sampling was found to generally lead to more accurate results. However, local sampling might not be accurate for cells close to very high-intensity, high-temperature regions, where the majority of the radiation in these cells comes from the neighbouring hot spots.

Future work might investigate ways to overcome this problem. An obvious solution would be the shift to the forward Monte Carlo formulation, which would, however, make the possible GPU implementation less favourable. An alternative is to run the radiative code once in the beginning to determine the average length that the photon rays reach to determine a zone of influence and then sample the wavelengths from the hottest region in that zone. However, this doubles the computational requirements. Another option is to use this average path length information from the previous radiation iteration. Since the resulting inaccuracies matched the inaccuracies in spectral generation by NEQAIR, and thus likely not introduced large additional errors to the solution, none of these techniques was applied yet.

Several challenges when coupling the nonequilibrium calculation to INCA CFD were outlined. NEQAIR does not work well with low temperature cells, especially when in the nonequilibrium mode. Thus, for low temperatures, radiation is either skipped or the Boltzmann equilibrium mode is used.

A CFD run with a 2D nitrogen plasma flow with a step wall obstruction revealed that, as expected, 94% to 98% of the CFD calculation was spent on radiation modelling, even though the radiation mesh was coarser than the CFD mesh (ranging between 10% to 50% of the 1st grid cells).

Several attempts were made to accelerate the routines implemented. One of the most basic ones, which became an integral part of the code, was triangular discretization of the spectral lines during computation of HITRAN emission spectra, which led to insignificant errors in the evaluation of the Planck mean absorption coefficient and sampled wavelengths, while also resulted in the generation times dropping by one to two orders of magnitude compared to the conventional HITRAN library. This was aided by the computed spline interpolation and pre-databasing of the total internal partition function sums for the species. Additional adjustments to the resolution of the absorption spectrum led to further 10x speed up.

In addition to the use of triangular emission spectral approximation, it was also investigated whether the Monte Carlo solver convergence can be improved with the use of low discrepancy Sobol sequences. It was found, for grey media, that while this is the case for cases when the temperature field is not isotropic, the performance of a random sequence and pseudo-random sequence was comparable for media close to isotropic conditions, as could be expected. The overall performance, taking into account the generation time for the Sobol numbers, was even worse than the random operation for close to isotropic media. However, in cases of participating media with spectrally highly variable absorption coefficient, the generation time of the (pseudo)random directions is negligible compared to the time required for handling of the spectra, and hence the use of Sobol sequences are expected to improve or at least match the convergence performance in any conditions.

The most demanding function of the radiation code is the generation and handling of the nonequilibrium spectra, as NEQAIR itself takes quite a while to generate them, and as their sizes are very large. First of all, it was investigated how many points per spectral line are generally required for the cases investigated, and how this selection affects the error of the solution. Depending on whether it is atomic or molecular radiation that dominates the problem, the suggestion of 1 to 3 points per line was formulated. It was also inspected to what extent the spectra can be downsampled (from the perspective of both the regular absorption coefficient as well as its integral) and what the resulting errors and memory savings are. Cumulative downsampling with a tolerance of 1e-7 allowed to bring down the size of spectra to a half, without the introduction of non-negligible errors.

To make coupling with computational fluid dynamics (CFD) possible and faster, a concept of 3 grid-layered mesh was developed. The CFD solutions are available on the first grid. These are interpolated onto the second grid using inverse distance weighting interpolation. The second grid is the basic grid for the radiation code, and the final divergence of the radiative heat flux, necessary for CFD coupling, is computed on this grid layer. The spectral discretization is performed on the third grid layer. In case the third and second grid layers do not coincide, various techniques have been investigated to approximate the spectrum on the unresolved cells. These included various forms of regression, estimates using the nearest spectra and also analytic recalculation (assuming LTE). The accuracy and performance of these techniques was compared and it was suggested that the recalculation is used if nonequilibrium is not too strong and is outside of spectral atomic line regions; otherwise the averaging of the spectra is preferred. The radiative source term on the second grid is then inverse-distance-weighted onto the first grid, such that it can be used by the CFD solver for the energy budget.

Since only line-by-line spectra were used in the code, it is suggested that, to further accelerate the nonequilibrium simulations, for example the opacity binning approach from Ref. [51] be implemented. The adaptation of spectral processing methods will require a slightly different approach to the solution method, depending on whether grey/HITRAN mode or NEQAIR mode is used, and most likely initial pre-databasing, which are the reasons why such techniques were not yet implemented in the code. In addition, for faster generation of the spectra, a pre-databasing system such as that suggested by Sohn et al. [101] could be used and the QSS could be computed on-the-fly, especially for atomic-radiation-dominated simulations. It is questionable whether this would be practical for cases where molecular radiation is more prevalent and must be included.

Finally, for HITRAN calculations, where memory is not a problem, a GPU parallelisation could be implemented, which should be a straightforward process due to the nature of the emission-based reciprocity Monte Carlo formulation, following the approach of Silvestri from Ref. [98]. For NEQAIR, since the spectra of several hundreds of MB in each cell must be transferred to each thread, a separate technique must be developed to reduce these memory requirements. It was hypothesised that, if each cell is computed by one GPU thread, provided that the plasma is sufficiently absorptive, only the spectra of the neighbouring cells would be transferred to the corresponding thread. In case the photon escaped the transferred domain, it would be retraced by the CPU. This approach was, however, not tested in practice.

The developed code was shown to produce accurate data for both combustion flows as well as flows in thermal nonequilibrium. In addition, the line-by-line formulation in combination with the adapted stochastic Monte Carlo method has been shown to be sufficiently accurate to study turbulence radiation interaction in literature (see Chapter 2). The solver was also developed to be compatible and capable of functioning alongside INCA CFD. To improve its performance, MPI parallelisation and several acceleration techniques have been proposed, developed, applied and evaluated. Finally, thanks to the almost universally applicable techniques selected for the code (Monte Carlo with LBL spectral generation), no case-specific pre-databasing or additional effort is necessary to run various radiation problems. It is therefore believed that the requirements set for the radiation solver in Chapter 1 have been principally met, along with the thesis goals.

Bibliography

[1] Amsterdam Modeling Suite 2019.3. *Software for Chemistry and Materials*, 2019. Available at `https://www.scm.com/doc/ADF/_downloads/75dfd572a16fa2583e20d37f1034ae31/ADF.pdf`.

[2] Hitran On The Web. Date of Access: March 2020. Available at `http://hitran.iao.ru/`.

[3] W. S. Rigdon and R. B. Dirling and M. Thomas. Stagnation point heat transfer during hypervelocity atmospheric entry. *NASA CR-1462*, 1970.

[4] J. D. Anderson. An Engineering Survey of Radiating Shock Layers. *AIAA*, 7(9):1665 – 1675, 1969. doi:10.2514/3.5373.

[5] D. A. Andrienko, S. T. Surzhikov, and J. S. Shang. Spherical Harmonics Method Applied to the Multi-Dimensional Radiation Transfer. *Computer Physics Communications*, 184:2287 – 2298, 2013. doi:10.1016/j.cpc.2013.05.015.

[6] D. A. Andrienko, P. G. Huang, S. T. Surzhikov, and J. Shang. A Computational Approach for Hypersonic Nonequilibrium Radiation Utilizing Space Partition Algorithm and Gauss Quadrature. *Journal of Computational Physics*, 266:1 – 21, 2014. doi:10.1016/j.jcp.2014.02.007.

[7] D. A. Andrienko, S. Surzhikov, and J. Shang. View-Factor Approach as a Radiation Model for the Reentry Flowfield. *Journal of Spacecraft and Rockets*, 53(1):74 – 83, 2016. doi:10.2514/1.A33305.

[8] I. A. Antonov and V. M. Saleev. An Economic Method of Computing LPtau-Sequences. *USSR Computational Mathematics and Mathematical Physics*, 19(1):252 – 256, 1979. doi:10.1016/0041-5553(79)90085-5.

[9] J. Bacri and A. Medani. Electron diatomic molecule weighted total cross section calculation: I. Principles for calculation. *Physica B+C*, 101(3):399 – 409, 1980. doi:10.1016/0378-4363(80)90037-6.

[10] A. Bansal, D. A. Levin, and M. F. Modest. Correlated-k Distribution Method for Atomic Radiation in Hypersonic Nonequilibrium flows. *47th AIAA Aerospace Sciences Meeting 5-8 January 2009, Orlando, Florida, AIAA 2009-1027*, 2009. doi:10.2514/6.2009-1027.

[11] A. Bansal, D. A. Levin, and M. F. Modest. Multi-Scale k-Distribution Model for Gas Mixtures in Hypersonic Nonequilibrium Flows. *Journal of Quantitative Spectroscopy and Radiative Transfer*, 112(7):1213 – 1221, 2011. doi:10.1016/j.jqsrt.2010.09.012.

[12] A. Bansal, A. Feldvick, and M. F. Modest. Simulation of Hypersonic Flow and Radiation over a Mars Reentry Vehicle Using OpenFOAM. *50th AIAA Aerospace Sciences Meeting, 9-12 January 2012, Nashville Tennessee, AIAA 2012-0650*, 2012. doi:10.2514/6.2012-650.

[13] P. E. Bernath. *Spectra of Atoms and Molecules.* Oxford University Press Inc., 3rd edition, 2016. ISBN 978–0–19–938257–6.

[14] J. Bonin and C. Mundt. Full Three-Dimensional Monte Carlo Radiative Transport for Hypersonic Entry Vehicles. *Journal of Spacecraft and Rockets*, 56(1):1 – 9, 2019. doi:10.2514/1.A34179.

[15] D. Bose and M. J. Wright. View-Factor-Based Radiation Transport in a Hypersonic Shock Layer. *Journal of Thermophysics*, 18(4):553 – 555, 2000. doi:10.2514/1.8817.

[16] A. M. Brandis and B. A. Cruden. NEQAIRv14.0 Release Notes. *NASA Technical Report 20150000832*, 2014.

[17] J. Cai, S. Lei, A. Dasgupta, M. F. Modest, and D. C. Haworth. High fidelity radiative heat transfer models for high-pressure laminar hydrogen–air diffusion flames. *Combustion Theory and Modelling*, 18(6):607 – 626, 2014. doi:10.1080/13647830.2014.959060.

[18] J. C. Camm, B. Kivel, R. L. Taylor, and J. D. Teare. Absolute Intensity of Non-equilibrium Radiation in Air and Stagnation Heating at High Altitudes. *Journal of Quantum Spectroscopy and Radiative Transfer*, 1(1):53 – 75, 1961. doi:10.1016/0022-4073(61)90011-5.

[19] G. Candler and C. Park. The Computation of Radiation of Nonequilibrium Hypersonic Flows. *23rd Thermophysics, Plasmadynamics and Lasers Conference, 27 - 29 June 1988, San Antonio, California, AIAA-88-2678*, 1988. doi:10.2514/6.1988-2678.

[20] L. A. Carlson. Approximations for Hypervelocity Nonequilibrium Radiating, Reacting, and Conducting Stagnation Regions. *Journal of Thermophysics*, 3(4):380– 388, 1989. doi:10.2514/3.28764.

[21] M. Cernetic, A. I. Shapiro, V. Witzke, N. A. Krivova, S. K. Solanki, and R. V. Tagirov. Opacity Distribution Functions for Stellar Spectra Synthesis. *Astronomy and Astrophysics*, 627(A157), 2019. doi:10.1051/0004-6361/201935723.

[22] L. H. Chamber. Predicting Radiative Heat Transfer in Thermochemical Nonequilibrium Flow Fields: Theory and User's Manual for the LORAN Code. *NASA-TM-4564*, 1994.

[23] M. Cherkaoui, J. Dufresne, R. Fournier, J. Grandpeix, and A. Lahellec. Monte Carlo Simulation of Radiation in Gases with Narrow-Band Model and a Net-Exchange Formulation. *Journal of Heat Transfer*, 118(2):401 – 407, 1996. doi:10.1115/1.2825858.

[24] P. J. Coelho. A Theoretical Analysis of the Influence of Turbulence on Radiative Emission in Turbulent Diffusion Flames of Methane. *Combustion and Flame*, 160(3):610 – 617, 2013. doi:10.1016/j.combustflame.2012.11.009.

[25] B. A. Cruden and A. M. Brandis. Updates To The NEQAIR Radiation Solver. 2014. Available at `https://ntrs.nasa.gov/archive/nasa/casi.ntrs.nasa.gov/20150022164.pdf`.

[26] B. A. Cruden and A. M. Brandis. Measurement of Radiative Nonequilibrium for Air Shocks Between 7 and 9 km s. *Journal Thermophysics and Heat Transfer*, pages 1 – 28, 2019. doi:10.2514/1.T5735.

[27] L. Duan, M. P. MArtin, I. Sohn, D. A. Levin, and M. F. Modest. Study of Emission Turbulence–Radiation Interaction in Hypersonic Boundary Layers. *49th AIAA Aerospace Sciences Meeting, 4 - 7 January 2011, Orlando, Florida, AIAA 2011-749*, 2011. doi:10.2514/6.2011-749.

[28] J. Farmer. Development of a Quasi-Monte Carlo Method for Thermal Radiation. *Master Thesis, Marquette University*, 2009.

[29] J. Farmer and S. Roy. A quasi-monte carlo solver for thermal radiation in participating media. *Journal of Quantitative Spectroscopy and Radiative Transfer*, 242, 2020. doi:10.1016/j.jqsrt.2019.106753.

[30] A. M. Feldick and M. F. Modest. An Improved Wavelength Selection Scheme for Monte Carlo Solvers Applied to Hypersonic Plasmas. *Journal Thermophysics and Heat Transfer*, 112(8):1394 – 1401, 2011. doi:10.1016/j.jqsrt.2011.01.028.

[31] A. M. Feldick and M. F. Modest. A Spectrally Accurate Two Dimensional Axisymmetric, Tightly Coupled Photon Monte Carlo Radiative Transfer Equation Solver for Hypersonic Entry Flows. *Journal Thermophysics and Heat Transfer*, 134(2):122701, 2012. doi:10.1115/1.4007069.

[32] A. M. Feldick, L. Duan, M. P. Martin, D. A. Levin, and M. F. Modest. Influence of Interactions Between Turbulence and Radiation on Transmissivities in Hypersonic Turbulent Boundary Layers. *48th AIAA Aerospace Sciences Meeting, 04 - 07 January 2010 Orlando, Florida, AIAA 2010-1185*, 2010. doi:10.2514/6.2010-1185.

[33] R. M. Frost, P. Awakowicz, H. P. Summers, and N. R. Badnell. Calculated Cross Sections and Measured Rate Coefficients for Electron-Impact Excitation of Neutral and Singly Ionized Nitrogen. *Journal of Applied Physics*, 84(6):2989 – 3003, 1998. doi:10.1063/1.368452.

[34] Y. Fujii, T. Azumi, N. Nishio, S. Kato, and M. Edahiro. Data Transfer Matters for GPU Computing. *19t International Conference on Parallel and Distributed Systems 15-18 December 2013, Seoul, Korea*, 1989. doi:10.1109/ICPADS.2013.47.

[35] T. A. Gally, L. A. Carlson, and D. Green. Flowfield Coupled Excitation and Radiation Model for Nonequilibrium Reacting Flows. *Journal of Thermophysics and Heat Tansfer*, 7(2):285 – 293, 1993. doi:10.2514/3.418.

[36] S. Ghosh and R. Friedrich. Effects of Radiative Heat Transfer on the Turbulence Structure in Inert and Reacting Mixing Layers. *Physics of Fluids*, 27(5):055107, 2015. doi:10.1063/1.4920990.

[37] R M. Goody and Y. L. Yung. *Atmospheric Radiation: Theoretical Basis*. Oxford University Press, Inc, 2nd edition, 1989. ISBN 0-19-510291-6.

[38] J. P. Gore, S. M. Jeng, and G. M. Faeth. Spectral and Total Radiation Properties of Turbulent Hydrogen/Air Diffusion Flames. *Journal of Heat Transfer*, 109(2):339 – 345, 1987. doi:10.2514/3.9627.

[39] R. Goulard. The Coupling of Radiation and Convection in Detached Shock Layers. *Journal of Quantitative Spectroscopy and Radiative Transfer*, 1(3-4):249 – 257, 1961. doi:10.1016/0022-4073(61)90025-5.

[40] W. L. Grose and J. E. Nealy. Estimates of Nonequilibrium Radiation for Venus Entry. *AIAA*, 13(4):421 – 424, 1975. doi:10.2514/3.49723.

[41] M. Gryzinsky. Classical Theory of Electronic and Ionic Inelastic Collisions. *Physical Review*, 115(2):374 – 383, 1958. doi:10.1103/PhysRev.115.374.

[42] A. Gupta, M. F. Modest, and D. C. Haworth. Large-Eddy Simulation of Turbulence-Radiation Interactions in a Turbulent Planar Channel Flow. *Journal of Heat Transfer*, 131(6):016704, 2009. doi:10.1115/1.3085875.

[43] L. C. Hartung. Development of a Nonequilibrium Radiative Heating Prediction Method for Coupled Flowfield Solutions. *Journal Thermophysics and Heat Transfer*, 6(4):618 – 625, 1992. doi:10.2514/3.11542.

[44] W. Hayek, M. Asplund, M. Carlsson, R. Trampedach, R. Collet, B. V. Gudiksen, V. H. Hansteen, and J. Leenaarts. Radiative Transfer with Scattering for Domain-Decomposed 3D MHD Simulations of Cool Stellar Atmospheres: Numerical Methods and Application to the Quiet, Non-Magnetic, Surface of a Solar-Type Star. *Astronomy and Astrophysics*, 517(A49), 2010. doi:10.1051/0004-6361/201014210.

[45] H. Hoshizaki and K. H. Wilson. Convective and Radiative Heat Transfer During Superorbital Entry. *NASA-CR-584*, 1966.

[46] H. C. Hottel and A. F. Sarofim. *Radiative Transfer*. McGraw-Hill, Inc, 1st edition, 1967.

[47] C. O. Johnston. Nonequilibrium Shock-Layer Radiative Heating for Earth and Titan Entry. *Dissertation at Virginia Polytechnic Institute and State University*, 2006.

[48] C. O. Johnston and A. Mazaheri. Impact of Non-Tangent-Slab Radiative Transport on Flowfield–Radiation Coupling. *Journal of Spacecraft and Rockets*, 55(4):899 – 913, 2018. doi:10.2514/1.A34072.

[49] C. O. Johnston, A. Sahai, and M. Panesi. Comparative analysis of reduced-order spectral models and grouping strategies for non-equilibrium radiation. *International Journal of Thermophysics and Heat Transfer*, 32(3), 2018. doi:10.2514/1.T5349.

[50] S. Karl, D. Potter, and M. Lambert. Numerical rebuilding of viking afterbody radiative heating with the dlr tau code. *5th International Workshop on Radiation of High Temperature Gases in Atmospheric Entry, 16th - 19th October 2012, Barcelona, Spain.*, 2012.

[51] S. Karl, D. Potter, M. Lambert, and K. Hannemann. Computational Analysis of Radiative Heat Loading on Hypervelocity Reentry Vehicles. *Journal of Spacecraft and Rockets*, 52(1):63 – 75, 2015. doi:10.2514/1.A32791.

[52] T. Kim, J. Menart, and H. Lee. Nongrey Radiative Gas Analyses Using the S-N Discrete Ordinates Method. *International Journal of Heat Transfer and Mass Transfer*, 41(14):2227–2236, 1991. doi:10.1016/S0017-9310(97)00267-6.

[53] B. Kivel. Radiation From Hot Air and Its Effect on Stagnation-Point Heating. *Journal of Aerospace Sciences*, 28(2):96 – 102, 1961. doi:10.2514/8.8883.

[54] R. V. Kochanov. HITRAN Application Programming Interface (HAPI). *Harvard-Smithsonian Center for Astrophysics*, 2019. Available at `https://hitran.org/static/hapi/hapi_manual.pdf`.

[55] M. E. Kounalakis, J. P. Gore, and G. M. Faeth. Turbulence/ Radiation Interactions in Nonpremixed Hydrogen/ Air Flames. *22nd Symposium (International) on Combustion 22nd - 27th July 1990, Orleans, France*, 22, 1989. doi:10.1016/S0082-0784(89)80139-0.

[56] title = Assessment of Randomized Quasi-Monte Carlo Method Efficiency in Radiative Heat Transfer Simulations L. Palluotto and N. Dumont and P. Rodrigues and O. Gicquel and R. Vicquelin. *Journal of Quantitative Spectroscopy and Radiative Transfer*, 236:106570, 2019. doi:10.1016/j.jqsrt.2019.07.013.

[57] A. A. Lacis and V. Oinas. View Factors between Disk/Rectangle and Rectangle in Parallel and Perpendicular Planes. *Journal of Geophysical Research*, 96 (5), 1991. doi:10.1029/90JD01945.

[58] A. Lemal. Prediction of Air Nonequilibrium Radiation with a Collisional-Radiative Model: Application to Shock-Tube Conditions Televant to Earth Reentry. *Dissertation at Ecole Centrale Paris, NNT : 2013ECAP0044. tel-01175651*, 2013.

[59] C. Lemieux. *Monte Carlo and Quasi-Monte Carlo Sampling*. Springer Science+Business Media, 5th edition, 2009. ISBN 978-0-387-78165-5. doi:10.1007/978-0-387-78165-5.

[60] D. A. Levin, G. V. Candler, R. J. Collins, P. W. Erdman, P. Espy, C. Howlett, and E. Zipf. Comparison of Theory with Experiment for the Bow Shock Ultraviolet Rocket Flight. *26th Thermophysics Conference 24 - 26 June 1991, Honolulu, Hawaii, AIAA-91-1411*, 1973. doi:10.2514/6.1991-1411.

[61] D. A. Levin, G. V. Candler, R. J. Collins, P. W. Erdman, P. Espy, C. Howlett, and E. Zipf. Examination of Theory for Bow Shock Ultraviolet Rocket Experiments — I. *Journal of Thermophysics and Heat Transfer*, 8(3):447 – 452, 1994. doi:10.2514/3.563.

[62] D. A. Levin, G. V. Candler, R. J. Collins, P. W. Erdman, P. Espy, C. Howlett, and E. Zipf. Examination of Theory for Bow Shock Ultraviolet Rocket Experiments — II. *Journal of Thermophysics and Heat Transfer*, 8(3), 1994. doi:10.2514/3.564.

[63] J. Li, H. Huang, and N. Kobayashi. Hydrogen Combustion as a Thermal Source. *Energy Procedia*, 142: 1083 – 1088, 2017. doi:10.1016/j.egypro.2017.12.360.

[64] Y. Liu, D. Prabhu, K. A. Trumble, D. Saunders, and P. Jenniskens. Radiation Modeling for the Reentry of the Stardust Sample Return Capsule. *Journal of Spacecraft and Rockets*, 47(5):741 – 752, 2010. doi:10.2514/1.37813.

[65] Y. Liu, M. Panesi, A. Sahai, and M. Vinokur. General Multi-Group Macroscopic Modeling for Thermo-Chemical Non-Equilibrium Gas Mixtures. *The Journal of Chemical Physics*, 142(13):134109, 2015. doi:10.1063/1.4915926.

[66] S. Mazumder and M. F. Modest. Turbulence-Radiation Interactions in Nonreactive Flows of Combustion Gases. *Journal of Heat Transfer*, 121(3):726 – 729, 1999. doi:10.1115/1.2826041.

[67] M. F. Modest. The Weighted-Sum-of-Gray-Gases Model for Arbitrary Solution Methods in Radiative Transfer. *Journal of Heat Transfer*, 113(3):650 – 656, 1991. doi:10.1115/1.2910614.

[68] M. M. Modest. *Radiative Heat Transfer*. Elsevier, Inc, 3rd edition, 2013. ISBN 978-0-12-386944-9.

[69] S. Moreau, C. O. Laux, D. R. Chapman, and R. W. MacCormack. A More Accurate Nonequilibrium Air Radiation Code - NEQAIR Second Generation. *23rd Plasmadynamics and Lasers Conference, 06 - 08 July 1992 Nashville, Tennessee, AIAA 92-2968*, 1992. doi:10.2514/6.1992-2968.

[70] J. N. Moss, C. W. Boltz, and E. C. Anderson. Aerothermal Environment for Jovian Entry Probes. *11th Thermophysics Conference, 14 - 16 July 1976, San Diego, California, AIAA-76-469*, 1976. doi:10.2514/6.1976-469.

[71] H. Nakamura and M. Shindo. Effects of Radiation Heat Loss on Laminar Premixed Ammonia/Air Flames. *Proceedings of the Combustion Institute*, 37:1 – 8, 2019. doi:10.1016/j.proci.2018.06.138.

[72] W. E. Nicolet. Prediction Method for Calculating Radiation Transport in Ablation Product Contaminated, Hypersonic Boundary Layers. *NASA-CR-1656*, 1970.

[73] W. B. Olstadt. Stagnation-Point Solutions For Inviscid Radiating Shock Layers. *NASA-TN-D-5792*, 1970.

[74] D. Olynick, Y. K. Chen, , and M. E. Tauber. Aerothermodynamics of the Stardust Sample Return Capsule. *Journal of Spacecraft and Rockets*, 36(3):442 – 462, 1999. doi:10.2514/2.3466.

[75] T. Ozawa, D. A. Levin, and M. F. Modest. Spectral Module for Photon Monte Carlo Calculations in Hypersonic Nonequilibrium Radiation. *ASME*, 132(2):023406, 2010. doi:10.1115/1.4000242.

[76] T. Ozawa, A. Wang, D. A. Levin, and M. F. Modest. Development of Coupled Particle Hypersonic Flowfield-Photon Monte Carlo Radiation Methods. *International Journal of Thermophysics and Heat Transfer*, 24(3):612 – 622, 2010. doi:10.2514/1.44645.

[77] S. I. Pai and A. I. Speth. Shock Waves in Radiation-Magneto-Gas Dynamics. *The Physics of Fluids*, 4 (10): 1232 – 1237, 1961. doi:10.1063/1.1706201.

[78] G. Palmer, G. Allen, C. Tang, and J. Brown. Coupled Fluids-Radiation Analysis of a High-Mass Mars Entry Vehicle. *42nd AIAA Thermophysics Conference, 27 - 30 June 2011, Honolulu, Hawaii, AIAA-2011-3495*, 2011. doi:10.2514/6.2011-3495.

[79] C. Park. Calculation of Nonequilibrium Radiation in AOTV Flight Regimes. *22nd Aerospace Sciences Meeting, 09 - 12 January 1984, Reno, Nevada, AIAA-84-0306*, 1984. doi:10.2514/6.1984-306.

[80] C. Park. Assessment of Two-Temperature Kinetic Model for Ionizing Air. *Journal of Thermophysics and Heat Transfer*, 3(3):233 – 244, 1989. doi:10.2514/3.28771.

[81] C. Park. *Nonequilibrium Hypersonic Aerothermodynamics*. John Wiley and Sons, Inc, 1st edition, 1990.

[82] D. Paschchenko. Comparative Analysis of Hydrogen/Air Combustion CFD-Modeling for 3D and 2D Computational Domain of Micro-Cylindrical Combustor. *International Journal of Hydrogen Energy*, 42(49):29545 – 29556, 2017. doi:10.1016/j.ijhydene.2017.10.070.

[83] L. C. Pierrot, C. O. Laux, and C. H. Kruger. Vibrationally Specific Collision-Radiative Model for Nonequilibrium Nitrogen Plasmas. *29th AIAA, Plasmadynamics and Lasers Conference, 15 June 1998 - 18 June 1998, Albuquerque, New Mexico, AIAA 98-2664*, 1999. doi:10.2514/6.1998-2664.

[84] L. C. Pierrot, C. O. Laux, and C. H. Kruger. Collisional-Radiative Modeling of Nonequilibrium Effects in Nitrogen Plasmas. *30th Plasmadynamic and Lasers Conference, 28 01 July 1999, Norfolk, Virginia, AIAA 99-3478*, 1999. doi:10.2514/6.1999-3478.

[85] J. Pomerantz. The Influence of Absorption of Radiation in Shock Tube Phenomena. *Journal of Quantum Spectroscopy and Radiative Transfer*, 1:185 – 248, 1961. doi:10.1016/0022-4073(61)90024-3.

[86] N. R. Richardson. Project FIRE Instrumentation for Radiative Heating and Related Measurements. *NASA-TN-D-3646*, 1966.

[87] M. Roger, C. B. Da Silva, and P. J. Coelho. Analysis of the Turbulence–Radiation Interactions for Large Eddy Simulations of Turbulent Flows. *International Journal of Heat and Mass Transfer*, 52(9-10):2243 – 2254, 2009. doi:10.1016/j.ijheatmasstransfer.2008.12.004.

[88] S. Ghosh and R. Friedrich and M. Pfitzner and C. Stemmer and B. Cuenot and Mouna El-Haf. Effects of radiative heat transfer on the structure of turbulent supersonic channel flow. *Journal of Fluid Mechanics*, 677:417 – 444, 2011. doi:10.1017/jfm.2011.92.

[89] R. G. Sachs. Some Properties of Very Intense Shock Waves. *Physical Review Letters*, 69 (10):514 – 522, 1946. doi:10.1103/PhysRev.69.514.

[90] A. Sahai, C. O. Johnston, B. Lopez, and M. Panesi. Flow-Radiation Coupling in CO2 Hypersonic Wakes Using Reduced-Order Non-Boltzmann Models. *Physical Review of Fluids*, 4:093401, 2019. doi:10.1103/PhysRevFluids.4.093401.

[91] A. Sahai, C. O. Johnston, B. Lopez, and M. Panesi. Comparative Analysis of Reduced-Order Spectral Models and Grouping Strategies for Non-Equilibrium Radiation. *Journal of Quantitative Spectroscopy and Radiative Transfer*, 1:106752, 2020. doi:10.1016/j.jqsrt.2019.106752.

[92] A. Sakurai, T. Song, S. Maruyama, and H. Kim. Comparison of Radiation Element Method and Discrete Ordinates Interpolation Method Applied to Three- Dimensional Radiative Heat Transfer. *Numerical Heat Transfer*, 48 (2):259 – 264, 2005. doi:10.1299/jsmeb.48.259.

[93] P. D. Santos and A. Lani. An Object-Oriented Implementation of a Parallel Monte Carlo Code for Radiation Transport. *Computer Physics Communications*, 202:233 – 261, 2016. doi:10.1016/j.cpc.2015.12.017.

[94] E. Schmahl. NNLS: A New Imaging Algorithm for HESSI. 2002. Available at `https://hesperia.gsfc.nasa.gov/~schmahl/nnls/`.

[95] M. J. Seaton. The Theory of Excitation and Ionization by Electron Impact. *Pure and Applied Physics*, 13: 364 – 420, 1962. doi:10.1016/B978-0-12-081450-3.50015-1.

[96] H. K. Sen and A. W. Guess. Radiation Effects in Shock-Wave Structure. *Physical Review Letters*, 108 (3): 560 – 564, 1957. doi:10.1103/PhysRev.108.560.

[97] S. Silvestri and R. Pecnik. A Fast GPU Monte Carlo Radiative Heat Transfer Implementation for Coupling with Direct Numerical Simulation. *Journal of Computational Physics*, 3, 2019. doi:10.1016/j.jcpx.2019.1000322.

[98] S. Silvestri, A. Patel, D. J. E. M.Roekaerts, and R. Pecnik. Turbulence Radiation Interaction in Channel Flow with Various Optical Depths. *Journal Fluid Mechanics*, 834:359 – 384, 2017. doi:10.1017/jfm.2017.738.

[99] S. Silvestri, D. J. E. M.Roekaerts, and R. Pecnik. Assessing Turbulence-Radiation Interactions in Turbulent Flows of Non-Gray media. *Journal of Quantitative Spectroscopy and Radiative Transfer*, 233:134 – 148, 2019. doi:10.1016/j.jqsrt.2019.05.018.

[100] I. M. Sobol. Distribution of Points in a Cube and Approximate Evaluation of Integrals. *USSR Computational Mathematics and Mathematical Physics*, 7, 1967.

[101] I. Sohn, D. A. Levin, A. Bansal, and M. F. Modest. Advanced Radiation Calculations of Hypersonic Reentry Flows Using Efficient Databasing Schemes. *International Journal of Thermophysics and Heat Transfer*, 24(3):623 – 637, 2012. doi:10.2514/1.45085.

[102] L. Soucasse, J. B. Scoggins, P. Riviere, T. E. Magin, and A. Soufiani. Flow-Radiation Coupling for Atmospheric Entries Using a Hybrid Statistical Narrow Band Model. *Journal of Quantitative Spectroscopy and Radiative Transfer*, 180:55 – 69, 2006. doi:10.1016/j.jqsrt.2016.04.008.

[103] S. E. Strom and R. L. Kurucz. Statistical Procedure for Computing Line-Blanketed Model of Stellar Atmospheres with Applications to the F5 IV Star Procyon. *Journal of Spectroscopy and Radiative Transfer*, 6(5):591 – 607, 1966. doi:10.1016/1-s2.0-002240736690048-3.

[104] S. T. Surzhikov. Electronic Excitation in Air and Carbon Dioxide Gas. *NATO Report RTO-EN-AVT-162 7 - 1*, 2009.

[105] J. T. Suttles. Comparison of the Radiation Flux Profiles and Spectral Detail from Three Detailed Nongray Radiation Models at Conditions Representative of Hypervelocity Earth Entry. *NASA TMX-2447*, 1972.

[106] K. Sutton. Characteristics of Coupled Nongray Radiating Gas Flows with Ablation Product Effects About Blunt Bodies During Planetary Entries. *NASA-TM-X-72078*, 1973.

[107] M. E. Tauber and R. C. Wakefield. Heating Environment and Protection during Jupiter Entry. *Journal of Spacecraft*, 8(6):630 – 636, 1971. doi:10.2514/3.59703.

[108] L. Tesse, F. Dupoirieux, B. Zamuner, and J. Taine. Radiative Transfer in Real Gases using Reciprocal and Forward Monte Carlo Methods and a Correlated-k Approach. *International Journal of Heat and Mass Transfer*, 45(13):2797 – 2814, 2002. doi:10.1016/1-s2.0-S001793100200009-1.

[109] J. T. Vanderslice and S. Weissman. On the Theory of Vibrational Energy Exchange. *The Journal of Chemical Physics*, 37(10):2247 – 2279, 1962. doi:10.1063/1.1732993.

[110] R. Vicquelin, Y. F. Zhang, O. Gicquel, and J. Taine. Effects of Radiation in Turbulent Channel Flow: Analysis of Coupled Direct Numerical Simulations. *Journal of Fluid Mechanics*, 753:360 – 401, 2014. doi:10.1017/jfm.2014.368.

[111] E. E. Whiting and R. W. Nicholls. Reinvestigation of Rotational-Line Intensity Factors in Diatomic Spectra. *Astrophysical Journal Supplement*, 27:1 – 19, 1974. doi:10.1086/190286.

[112] E. E. Whiting, C. Park, Y. Liu, J. O. Arnold, and J. A. Paterson. NEQAIR96, Nonequilibrium and Equilibrium Radiative Transport and Spectral Program: User's Manual. *NASA Reference Publication 1389*, 1996.

[113] K. H. Wilson. Evaluation of One-Dimensional Approximations for Radiative Transport in Blunt Body Shock Layer. *NASA Contractor Report, NASA-CR-1990*, 1972.

[114] A. A. Wray, J. F. Ripoll, and D. Prabhu. Investigation of the opacity binning approach for solving the shock-generated radiation of the apollo as-501 re-entry. *Center for Turbulence Research, Proceedings of the Summer Program*, 2006.

[115] A. A. Wray, J. F. Ripoll, and D. Prabhu. Opacity distribution functions applied to the cev reentry. *39th AIAA Thermophysics Conference, 25 - 28 June 2007, Miami, Florida, AIAA 2007-4542*, 2007.

[116] K. L. Wray, J. D. Teare, B. Kivel, and P. Hammerling. Relaxation Processes and Reaction Rates Behind Shock Fronts in Air and Component Gasses. *Symposium on Combustion*, 8 (1):328 – 339, 1961. doi:10.1016/S0082-0784(06)80520-5.

[117] M. J. Wright, D. Bose, and J. Olejniczak. Impact of Flowfield–Radiation Coupling on Aeroheating for Titan Aerocapture. *Journal of Thermophysics and Heat Tansfer*, 19(1):17 – 27, 2005. doi:10.2514/1.10304.

[118] X. Yang, Z. He, S. Dong, and H. Tan. Prediction of Turbulence Radiation Interactions of CH4-H2/air Turbulent Flames at Atmospheric and Elevated Pressures. *International Journal of Hydrogen Energy*, 43(32):15537 – 15550, 2018. doi:10.1016/j.ijhydene.2018.06.060.

[119] L. Yu, L. C. Pierrot, C. O. Laux, and C. H. Kruger. Effects of Vibrational Nonequilibrium on the Chemistry of Two-Temperature Nitrogen Plasmas. *Plasma Chemistry and Plasma Processing*, 21(4):483 – 503, 2001. doi:10.1023/A:1012073800284.

[120] H. Zhang and M. F. Modest. A Multi-scale Full-spectrum Correlated-k Distribution for Radiative Heat Transfer in Inhomogeneous Gas Mixtures. *Journal of Quantitative Spectroscopy and Radiative Transfer*, 73(2-3):349 – 360, 2002. doi:10.1016/S0022-4073(01)00220-5.

A

HITRAN Database

This appendix presents the species isotopologues available in the database of HITRAN, along with the natural abundance of the isotopologues, spectral coverage and the number of transitions.

Molecule	Isotopologue	Natural Abundance	Spectral Coverage (cm-1)	Number of Transitions
(1) H2O	161	9.973E-1	0 - 25711	142 045
	181	1.999E-3	0 - 19918	39 903
	171	3.719E-4	0 - 19946	27 544
	162	3.107E-4	0 - 22708	13 237
	182	6.230E-7	0 - 3825	1 611
	172	1.158E-7	1234 - 1599	175
(2) CO2	626	9.842E-1	345 - 12785	169 292
	636	1.106E-2	406 - 12463	70 611
	628	3.947E-3	0 - 9558	116 482
	627	7.340E-4	0 - 9600	72 525
	638	4.434E-5	489 - 6745	26 737
	637	8.246E-6	583 - 6769	2 953
	828	3.957E-6	491 - 8161	7 118
	827	1.472E-6	626 - 5047	821
	727b	1.368E-7	535 - 6933	5187
	838b	4.446E-8	4599 - 4888	121
(3) O3	666	9.929E-1	0 - 6997	261 886
	668	3.982E-3	0 - 2768	44 302
	686	1.991E-3	1 - 2740	18 887
	667	7.405E-4	0 - 2122	65 106
	676	3.702E-4	0 - 2101	31 935
(4) N2O	446	9.903E-1	0 - 7797	33 074
	456	3.641E-3	5 - 5086	4 222
	546	3.641E-3	4 - 4704	4 592
	448	1.986E-3	542 - 4672	4 250
	447	3.693E-4	550 - 4430	1 705
(5) CO	26	9.865E-1	3 - 8465	1 019
	36	1.108E-2	3 - 6279	797
	28	1.978E-3	3 - 6267	770
	27	3.679E-4	3 - 6339	728
	38	2.223E-5	3 - 6124	712
	37	4.133E-6	1807 - 6197	580
(6) CH4	211	9.883E-1	0 - 11502	336 830
	311	1.110E-2	0 - 11319	72 420
	212	6.158E-4	7 - 6511	54 550
	312	6.918E-6	959 - 1695	4 213
(7) O2	66	9.953E-1	0 - 15928	1 787
	68	3.991E-3	1 - 15853	875
	67	7.422E-4	0 - 14538	11 313
(8) NO	46	9.940E-1	0 - 9274	103 701
	56	3.654E-3	1609 - 2061	699
	48	1.993E-3	1602 - 2039	679
(9) SO2	626	9.457E-1	0 - 4093	72 460
	646	4.195E-2	0 - 2501	22 661
(10) NO2	646	9.916E-1	0 - 3075	104 223
(11) NH3	4111	9.959E-1	0 - 7000	45 302
	5111	3.661E-3	0 - 5180	1 090
(12) HNO3	146	9.891E-1	0 - 1770	903 854
	156	3.636E-3	0 - 923	58 108
(13) OH	61	9.975E-1	0 - 19268	30 772
	81	2.000E-3	0 - 329	295
	62	1.554E-4	0 - 332	912
(14) HF	19	9.998E-1	24 - 46985	10 073
	29	1.557E-4	13 - 47365	24 303
(15) HCl	15	7.576E-1	8 - 34250	11 879
	17	2.423E-1	8 - 34240	11 907
	25	1.180E-4	5 - 33284	29 994
	27	3.774E-5	5 - 33258	29 911

Molecule	Isotopologue	Natural Abundance	Spectral Coverage (cm-1)	Number of Transitions
(16) HBr	19	5.068E-1	13 - 16034	3 039
	11	4.931E-1	13 - 16032	3 031
	29	7.894E-5	7 - 8781	1 455
	21	7.680E-5	7 - 8778	1 455
(17) HI	17	9.998E-1	10 - 13908	3 161
	27	1.557E-4	5 - 7625	1 590
(18) ClO	56	7.559E-1	0 - 1208	5 721
	76	2.417E-1	0 - 1200	5 780
(19) OCS	622	9.374E-1	0 - 4200	15 618
	624	4.158E-2	0 - 4166	6 087
	632	1.053E-2	0 - 4056	3 129
	623	7.399E-3	0 - 4164	2 886
	822	1.880E-3	0 - 4046	1 641
(20) H2CO	126	9.862E-1	0 - 3100	40 670
	136	1.108E-2	0 - 117	2 309
	128	1.978E-3	0 - 101	1 622
(21) HOCl	165	7.558E-1	1 - 3800	8 877
	167	2.417E-1	1 - 3800	7 399
(22) N2	44	9.927E-1	11 - 9355	1 107
	45	7.478E-3	11 - 2578	161
(23) HCN	124	9.851E-1	0 - 3424	2 955
	134	1.107E-2	2 - 3405	652
	125	3.622E-3	2 - 3420	646
(24) CH3Cl	215	7.489E-1	0 - 3198	107 642
	217	2.395E-1	0 - 3198	104 854
(25) H2O2	1661	9.950E-1	0 - 1731	126 983
(26) C2H2	1221	9.776E-1	604 - 9890	12 613
	1231	2.197E-2	613 - 6589	285
	1222	3.046E-4	1 - 789	7 512
(27) C2H6	1221	9.770E-1	706 - 3001	43 592
	1231	2.195E-2	725 - 919	6 037
(28) PH3	1111	9.995E-1	0 - 3602	22 189
(29) COF2	269	9.865E-1	696 - 2002	168 793
	369	1.108E-2	686 - 815	15 311
(30) SF6	29	9.502E-1	580 - 996	2 889 065
(31) H2S	121	9.499E-1	2 - 11330	36 561
	141	4.214E-2	5 - 11227	11 352
	131	7.498E-3	5 - 11072	6 322
(32) HCOOH	126	9.839E-1	10 - 1890	62 684
(33) HO2	166	9.951E-1	0 - 3676	38 804
(34) O	6	9.976E-1	68 - 159	2
(35) ClONO2	5646	7.496E-1	763 - 798	21 988
	7646	2.397E-1	765 - 791	10 211
(36) NO+	46	9.940E-1	1634 - 2531	1 206
(37) HOBr	169	5.056E-1	0 - 316	2 177
	161	4.919E-1	0 - 316	2 181
(38) C2H4	221	9.773E-1	701 - 3243	18 097
	231	2.196E-2	2947 - 3181	281
(39) CH3OH	2161	9.859E-1	0 - 1408	19 897
(40) CH3Br	219	5.010E-1	794 - 1706	18 692
	211	4.874E-1	796 - 1697	18 219
(41) CH3CN	2124	9.739E-1	890 - 946	3 572
(42) CF4	29	9.889E-1	594 - 1313	60 033
(43) C4H2	2211	9.560E-1	0 - 758	124 126
(44) HC3N	1224	9.633E-1	0 - 760	180 332

Molecule	Isotopologue	Natural Abundance	Spectral Coverage (cm-1)	Number of Transitions
(45) H2	11	9.997E-1	15 - 36024	4 017
	12	3.114E-4	3 - 36406	5 129
(46) CS	22	9.396E-1	1 - 2586	1 088
	24	4.168E-2	1 - 1359	396
	32	1.056E-2	1 - 1331	396
	23	7.417E-3	1 - 156	198
(47) SO3	26	9.434E-1	0 - 2778	10 881

B

Code Description

B.1. Brief Developer Guide

Here, the operating logic of the code will be discussed in more detail from the software perspective. In this case, it will be discussed in the context of INCA. The code can also be run separately from INCA. To preserve the structure, a routine `INCA_simulator.f90` is available, where all data, which would be extracted from INCA, can be set. The format must comply with the INCA internal data format.

When iteration step from INCA matches the desired coupling, as described in Chapter 4, the flowfield is unified on a mesh and the necessary data for radiation computation is communicated to the entire MPI communication world. If the data passes tests (e.g. minimum temperature requirements for NEQAIR etc.), the radiation interface routine `rad_interface` is invoked.

In this interface routine, the INCA information is translated to input radiation data. The boundary conditions are saved in two arrays: `wall_periodicity` and `wall_noradiance`. If wall is detected at a particular edge, both of these array entries at the given index are false. Same holds for symmetry boundaries, but in this case, the wall reflection coefficient is set to 1. Currently, the code cannot operate with different reflection coefficients at different boundaries. Thus, this means that also all other walls inside the domain or at the boundary will be fully reflective. If this is not desired, instead, either a no-initial-radiance condition or a periodicity condition should be applied. The place where this can be done in the code is explicitly shown.

Afterwards, the species are translated to a form that the radiation solver can understand. Note that as mentioned in the thesis, HITRAN cannot operate with more than one species right now, meaning that only the first species recognised by the code will be used. In case species are present that are not defined (both in HITRAN and NEQAIR), a warning is thrown and this species are ignored. If none of the species are recognised, radiation calculation is skipped. The allowed names for ions in INCA are e.g. `N+`, the allowed electron names are `E-` and `e-`. These can be adjusted in the `electron_names` and `ion_names` arrays in `rad_convert_species_neq`.

The code can recognise the species as electrons and ions in any order, and reorders them to match the desired internal structure. For NEQAIR subroutines, since a lot of information is necessary for flowfield calculations, most of the time, the information is stored in a structure `database_entry` or equivalent. This entry has the following components:

1. Translational and rotational temperature
2. Electron and vibrational temperature
3. Electron number density
4. Number densities of ions in sequence that is indicated in the `ion_names` array
5. Number densities of species in the following sequence: N, O, N2, O2, N2+, NO, C, H, Ar, He, C2, H2, CN, CO, OH, NH, CH, H2O, CO2

Since there are typically 2 ions present, 19 species and 3 other parameters, the size of the entry is 24. Even higher or lower number of ions, however, will not make the calculation crash.

After recognition of the species, IDW is applied along with the obstruction detection mechanism described in Chapter 4. If everything proceeds correctly, the main radiation solver is invoked. After this, the radiation calculation cannot be stopped, and is stopped only in case of a NEQAIR crash. After heat flux divergence is resolved, outliers are detected. Typically, there are no problems, but in case the random number distribution results in a for example extremely energetic photon being emitted, which impacts a very cold wall, with 10-20k photon rays only, this might result in significant local overestimation. To remove these errors without having to use 100-1000k photon rays, an algorithm is in use that detects these extreme values based on the values of the regions around.

The next piece to discuss is the main radiation code. The code can function in 2 different input modes - the `FROM_INCA` mode and its opposite. If this boolean is set to false, all the inputs will be ignored and a test case can be simulated by setting the desired test case as true. However, since the arrays are allocated still using either INCA or `INCA_simulator`, the array dimensions must still match to those from INCA even if all the rest of the input data is ignored. If the dimensions do not match, a warning will be thrown. This choice is suitable for validation of the code. The parameters of the validation cases can be found in the `CASE DEFINITION` portion of the code. The geometry and additional subroutines to allow for the set up of these cases is in the portion called `CASE SETUP` along with he definition of wall temperatures.

Most of the choices and input is self-explanatory, or explained in the comments in the code. The type of the approximation from the 3rd grid to 2nd grid can be set using the `NEQAIR_DIRECT` or `NEQAIR_DATAB`. With the former, the following additional options can be set - `NEQAIR_SIMPLE_ITPR` for 2 point averaging and `NEQAIR_ANL` for analytic adjustments. If `NEQAIR_DATAB` is selected, the regression technique is invoked, with dimensions based on which of the `USE_SPCS`, `USE_IONS_ONLY` and `USE_TTR_ONLY` options is selected. Finally, if the spectra are already computed and saved from the previous run, `NEQAIR_GENERATE` can be set to false to save time. Then, NEQAIR will not be invoked and the spectra will be simply loaded in.

Additional information is then read from the `radparam.inp`, but this can be ignored if the boolean `READ_PARAMS_FROM_FILE` is set to false, such as in validation runs.

In addition to the settings of these simulation parameters and modes, the input values are checked and if necessary, warnings about illegal data or inaccurate results predicted are thrown. The number species density for NEQAIR is converted to appropriate units, since NEQAIR needs to operate in $1/\mathrm{cm}^3$. The pressure for HITRAN is converted to atmospheres, as those are the units used for HITRAN calculation procedures.

HITRAN simulation parameters can be altered in the `hcallprms` structure, where the minimum and maximum wavelength for spectral resolution is set. Despite the fact that λ step and N is included, these are no longer used, since the reduced technique is applied and since N is computed from pressure using the perfect gas law. They were kept there however anyway, if it is in future desired to switch to a standard, full routine for spectral generation (not based on the reduced technique) which requires this data.

Variables and arrays which seem to be redundant in the current implementation are `nocellspassedx`, `nocellspassedy` and `nocellspassedz`, along with the `cellsselected` and `cellspassedidxs` arrays. These were set up since initially, GPU implementation was planned. Thus, as described in Chapter 7, only certain number of cells and data was supposed to be passed to the GPU threads. These variables and arrays can be used for this purpose later during GPU adaptation. Right now, these variables are set to the total number of cells in all directions to fill these arrays completely.

MPI is defined next. In the radiation code, the conventional `MPI_COMM_WORLD` is used for all communication, and `mpirank` is the name of the current node. For NEQAIR and grey calculations, the number of nodes does not matter for the solution - it just makes the calculation either faster or slower. NEQAIR subroutines are invoked depending on the type of NEQAIR simulation. Each of the spectral approximation techniques - closest match / averaging/ regression or analytical adjustment - requires a slightly different set up and treatment of the variables. In all cases, the third grid is formed, the NEQAIR routines are invoked on this third grid, and then the information from the third grid is linked to the second grid, typically through the structure `which_entry`, indicating to the 2nd grid cells which spectra from the 3rd grid should be used for further manipulation. The `a_ws`, `a_ks` and `a_es` arrays contain the actual spectra in case of the direct techniques, databased as [spectrum number, spectral coefficient at given index]. For the regression method, `a_ws_w`, `a_ks_w` and `a_es_w` contain the spectral weights in the same form. Also note that while regression works with original NEQAIR units for better stability and conditioning (cm-1, W/cm2/um/sr), the direct approaches convert this data to SI units.

As for the spectral generation with NEQAIR, its principle is shown in Figure B.1. Most of the steps are self-explanatory, some additional useful details though follow in the paragraphs below. The most complex part is the spectral regression, but since this is unlikely to be used again, it will not be elaborated on here in more detail.

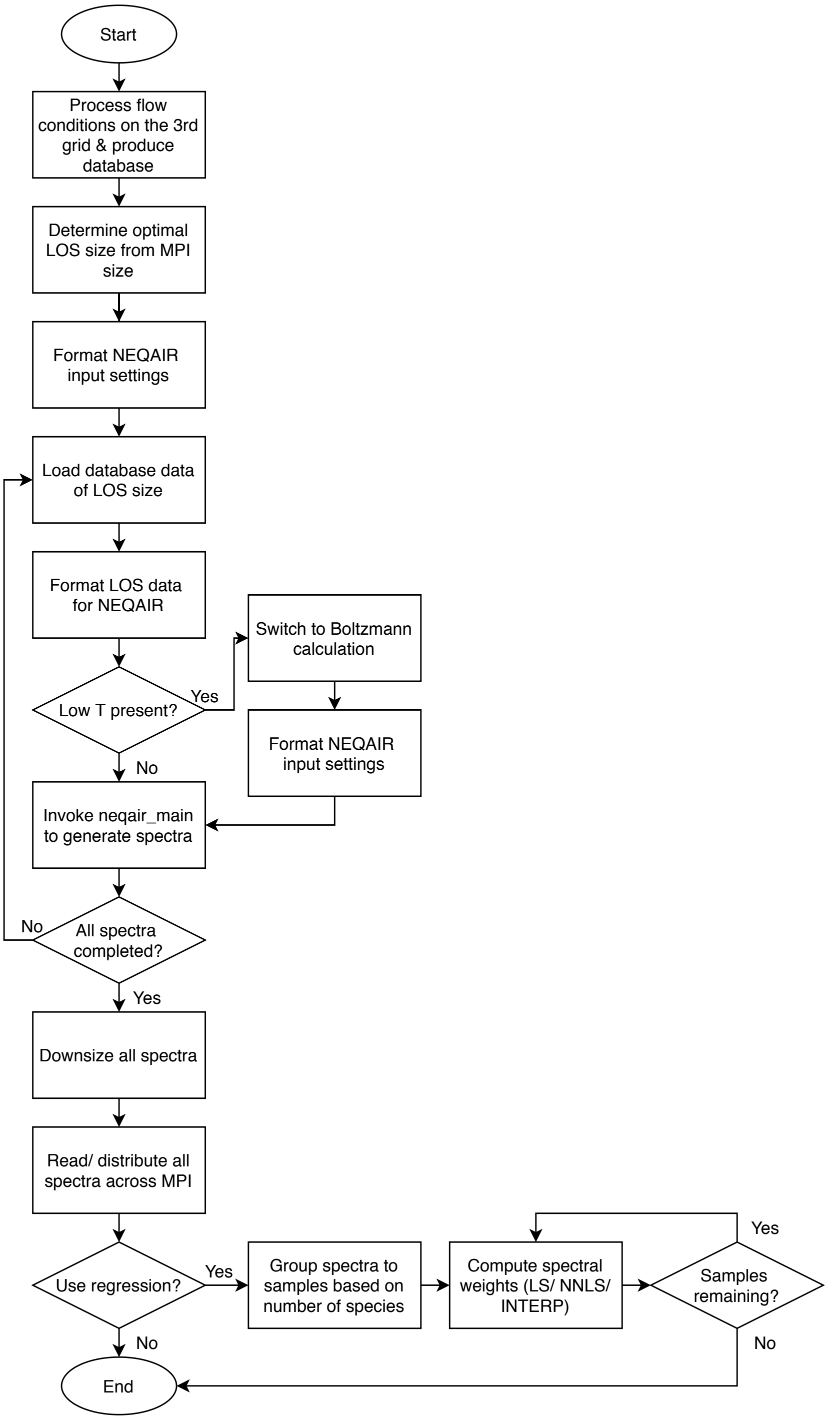
Start
Process flow conditions on the 3rd grid & produce database
Determine optimal LOS size from MPI size
Format NEQAIR input settings
Load database data of LOS size
Format LOS data for NEQAIR
Low T present?
Yes
Switch to Boltzmann calculation
Format NEQAIR input settings
No
Invoke neqair_main to generate spectra
All spectra completed?
No
Yes
Downsize all spectra
Read/ distribute all spectra across MPI
Use regression?
Yes
Group spectra to samples based on number of species
Compute spectral weights (LS/ NNLS/ INTERP)
Samples remaining?
Yes
No
No
End

Figure B.1: Basic logic of the subroutine used for NEQAIR spectral generation.

It should be noted that to save time, if there are repeated conditions in the 3rd grid field (two or more cells have the same properties), these cells are skipped. This skipping is automatic and presents no problems for linking to the 2nd grid, as all the information about this is saved to the `which_entry` array. This can be also set to a certain tolerance instead of an exact match for additional speedup.

In addition, NEQAIR does not resolve the first LOS point provided, as it considers it to be a boundary condition. Thus, the database sent to NEQAIR in this routine has a dummy first entry, which is the copy of the actual first entry. This in no way influences the calculation of the entries or hinders performance, it just means that the NEQAIR-generated spectra start from `ae.2`, which actually denotes the 1st point on the grid.

Furthermore, if there are more nodes than provided NEQAIR LOS data, NEQAIR crashes. To prevent this, when we have say additional 5 LOS points to resolve but 12 processors available, another 7 dummy LOS points are added with 0 in their conditions to occupy the processors in some way and have NEQAIR not crash. These spectra will be written as the rest, they will just contain 0 bytes.

When it comes to the routines within NEQAIR itself that had to be modified, they were modified in a way that the changes can be easily tracked. Most of the heavily modified routines contain the name `_brch` so that they can be easily located (for the fact that the combination of these consonants from author's name is unique and used nowhere in the original code, the author thanks to their Slavic ancestry). In addition, deallocation of all the arrays used in NEQAIR was added to avoid crush upon repeated call.

The formatting of the NEQAIR settings, which would typically come from the `neqair.inp` file is done using a large structure `inp_data_brch`, where the default settings for the various NEQAIR booleans are pre-set in the subroutine `get_default_sim_setup`. The LOS data in the correct format such that they can directly enter the modified NEQAIR routines are stored in `los_data_brch`.

Despite the best efforts to skip radiation calculation in case it is suspected that NEQAIR might crash, NEQAIR can surprisingly still sometimes manage to crash anyway. The most common ways of crashing are:

- Insufficient memory and allocation problems: try un-limiting the stack and heap space
- Problems with calculation of molecular levels: typically due to "problematic" difficult-to-compute species such as N2+. Try removing these species to see if this is the cause of the error. If yes, some conditions in the flow may prevent from proper calculation of this species radiation, and in these regions, these species might have to be ignored. Sometimes this might also be due to insufficient memory
- NaNs from QSS: typically due to low temperatures or other conditions causing the inversion of the master Eq. matrices to be impossible. Try switching to Boltzmann
- Forever computation or out of memory: typically when nonlocal calculations are attempted
- Cannot compute automatic spacing: this typically happens at low temperature when there are simply no significant transitions in the given region. One might attempt to increase the region size

Since the regression routines will not be discussed, this concludes the summary of the NEQAIR generation procedure.

For HITRAN, to enhance the performance, the current configuration is made such that the temperature range is discretised based on the number of nodes available, each of which computes the absorption spectra for one of the temperatures. Obviously, having only 2-3 nodes will thus lead to very coarse spectral discretisation. This can be easily adjusted if needed by adding an additional loop for the processors to make more than one spectrum depending on the desired discretisation, it was just not necessary for the cases tested with the code. The HITRAN absorption spectra are pre-databased this way, and then just used for interpolation on-the-fly.

This pre-calculation starts with the master reading the `.par` files for the given species from `HITRAN_path`. The transition data loaded from this par file are saved in the `hitdata` structure. The master broadcasts this data to the entire communication space. Based on the temperature discretisation style, the processor determines for which temperature it should pre-compute the absorption spectra from this HITRAN data. After completion of this spectra, it is sent to the master, which then broadcasts it to the rest of the slaves again.

This concludes the data preparation routine in the main radiation program just before the photon loop starts. All of this is summarised in Figure B.2.

Afterwards, the photon loop begins. The processor determines which cell to compute next, and in case this cell is an internal obstruction (end of domain or a wall), calculation is skipped. Then, depending on the simulation mode (grey/ HITRAN/ NEQAIR) and for NEQAIR, depending on the type of spectral approximation, the emission spectrum is obtained and wavelengths are selected and saved in the `gnrtd_wvlngths` array. These routines also compute the required emission energy for NEQAIR mode, saved in `emi_max` in case global sampling is used and `neq_int` for local sampling. The emission energy for all the photon rays is then computed.

If Sobol LDS is used, the directions are computed next. In case this is not desired, the directions were already pre-computed before the start of the photon loop. Afterwards, the number of cells passed to the possible GPU thread in each dimension is determined. As explained, this feature is not needed for CPU

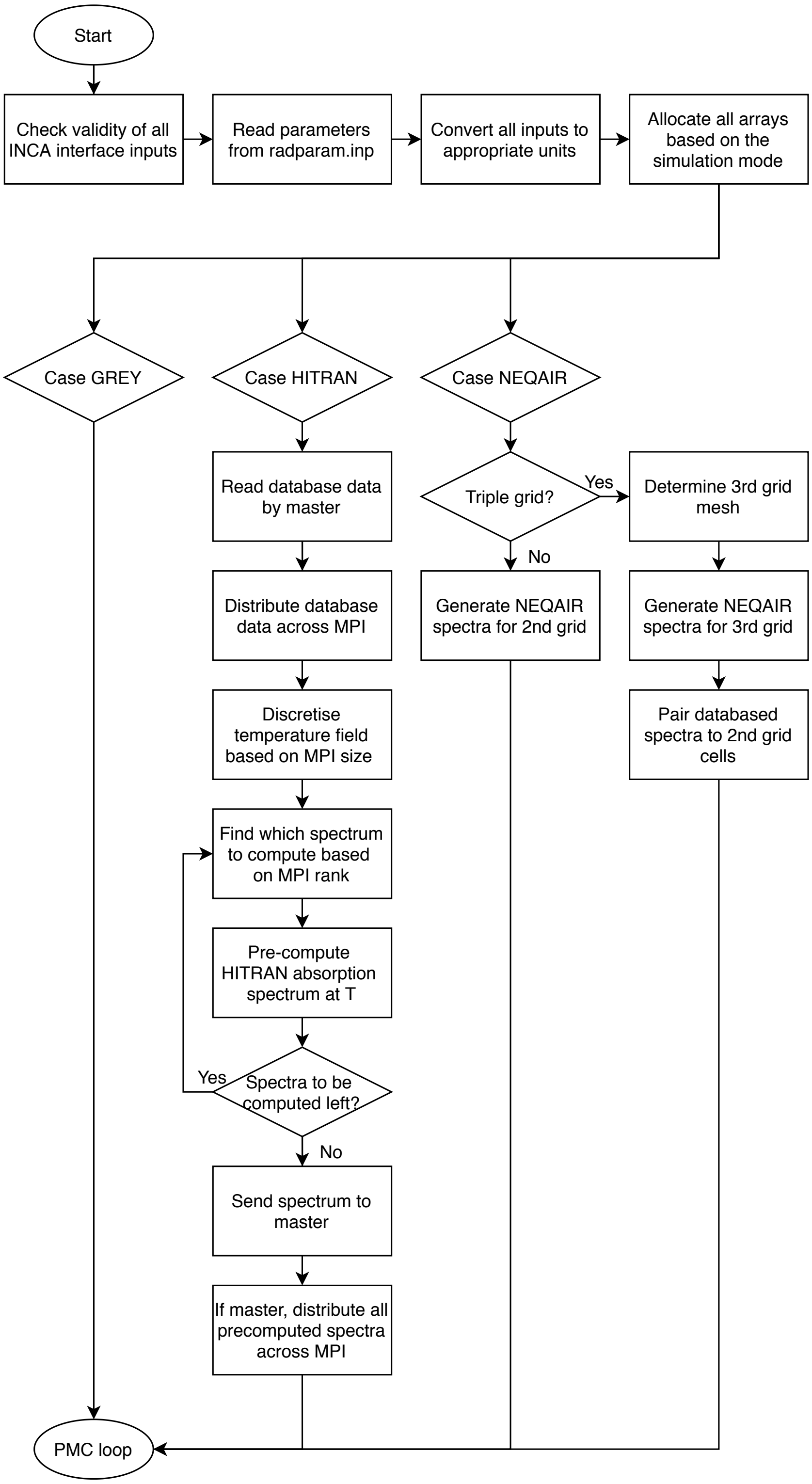
Start
Check validity of all INCA interface inputs
Read parameters from radparam.inp
Convert all inputs to appropriate units
Allocate all arrays based on the simulation mode
Case GREY
Case HITRAN
Case NEQAIR
Read database data by master
Distribute database data across MPI
Discretise temperature field based on MPI size
Find which spectrum to compute based on MPI rank
Pre-compute HITRAN absorption spectrum at T
Spectra to be computed left?
Yes
No
Send spectrum to master
If master, distribute all precomputed spectra across MPI
Triple grid?
Yes
No
Determine 3rd grid mesh
Generate NEQAIR spectra for 2nd grid
Generate NEQAIR spectra for 3rd grid
Pair databased spectra to 2nd grid cells
PMC loop

Figure B.2: The principle of spectral data preparation in the main radiation routine before photon loop is started, depending on the type of simulation.

implementation. Depending on the simulation mode and NEQAIR approximation technique, for each of the photon wavelengths, a subroutine is invoked to determine the absorption coefficient in the entire flowfield in the array `absorptions`. The same is done with the Planck function ratios in the array `allplancks`. Finally, also the wall Planck function ratios are computed, with the subroutines again differing depending on the simulation mode and spectral approximation technique in the array `planck_walls`. Finally, for all photons, the `PMC` routine is called to ray trace the photon ray. The output `q_i` is added to the total cell `Q` sum. After the end of the loop, the processors send the radiative source term results for the cells that they resolved to the master, which then broadcasts them all back.

This information is returned to the `rad_interface` routine, which uses IDW to compute the heat flux back on the 1st grid. NaN or infinite values are checked for, and if all values are valid, the `inca_radiation` routine adds the radiation source term to the energy budget. This marks the end of the radiation calculation.

B.2. Brief Description of Subroutines

Next, to aid future development of the code, the purpose of the most essential subroutines is described below.

`subroutine: PMC`

This subroutine processes the ray tracing data, switches to python indexing (starting from zero) in which the ray tracing procedure was tested and transfers all the data to the respective arrays which the ray tracing can work with, such as absorption coefficients in the flowfield, Planck function ratios and directions of the photons. Invoked by rad_main for each photon.

`subroutine: RTM`

RTM is invoked by the PMC subroutine. It assigns the origin to the photon ray and transmissivity of 1 and ray traces it until transmissivity is below tolerance. All radiative BCs such as domain edges and internal (partly) reflective walls are implemented here. To avoid infinite loops and stalling of the code for completely transmissive media, if more than 1e6 cell crossings are made, the photon ray is terminated. If at any point the heat flux becomes NaN, a message is thrown at the user along with the information where this happened.

`subroutine: neqair_grid_transform`

To connect the 2nd and 3rd grid, the so-called `which_entry` array exists which dictates which spectrum index (3rd grid) should be used for which cell on the 2nd grid. This subroutine determined this pairing using a simple distance function.

In addition, not all 3rd grid cells have their own unique spectra. If the conditions are almost the same at two points (tolerance can be set in the spectral generating routine), the spectra are not computed again. Instead, the `which_entry` array points to the previous spectrum.

`subroutine: neqair_grid_transform_doub`

Similarly to the `neqair_grid_transform`, this subroutine determines the pairing. However, this subroutine is made for a 2-point averaging approach to approximation. It finds the two closes spectra (spatially) and then determines their respective weights for IDW using the differences in their temperatures. These weights are then used when re-creating the spectra on the fly.

In addition, not all 3rd grid cells have their own unique spectra. If the conditions are almost the same at two points (tolerance can be set in the spectral generating routine), the spectra are not computed again. Instead, the `which_entry` array points to the previous spectrum.

`subroutine: make_a_box`

This subroutine acts as a simple internal mesh generator, creating a domain enclosed by wall structures. The walls are represented the boundary cells.

`subroutine: make_no_box`

This subroutine acts as a simple internal mesh generator, creating a domain enclosed not enclosed by walls explicitly (the walls can still be set, just are defined right outside of the domain).

`subroutine: rad_main`

The main radiation routine. This routine is invoked from the interface routine in case the flow conditions and user settings are judged to be suitable to prevent any errors in radiation calculation. This main routine performs the entire process, from the domain setup, through invoking the subroutines for spectral generation and ray tracing. Comments provided inside this routine can be insightful to understand the exact operation in more detail. For a general description of the logic, refer to Figure 4.3.

`subroutine: hitran_interp_kappa`

This subroutine uses pre-databased absorption spectra from HITRAN to interpolate the absorption coefficient at a given wavelength for given conditions. IDW in 2D (temperature and wavelength) is used to determine the resulting absorption coefficient.

`subroutine: make_sobol_directions`

In this subroutine, the Sobol number generator is invoked (for each cell separately), returning the vector of Sobol numbers for each photon ray. The integer specifying the dimensionality of the vector from the Sobol generator (in this case 2, one for θ and one for ϕ) must be an 8-integer for the Sobol library to work.

`subroutine: hitran_getabsorption`

While this subroutine is not used in the current version (currently, the absorption coefficient is determined from the pre-calculated spectra via 2D interpolation), this routine can accurately compute the absorption coefficient for given conditions around a given wavelength without having to compute the entire spectrum. The range in which transitions are taken into account around this central wavelength (wavemin and wavemax) are right now 1μm, but can be adjusted to optimise speed.

`subroutine: grey_getabsorption`

This subroutine simply returns the grey absorption coefficient.

`subroutine: getPlanck`

Here, the Planck ratios for calculation of the heat transfer are computed for the entire flowfield for HITRAN and grey simulations. The Planck factor is the expression:

$$\mathrm{PF} = \left(\frac{I_{b,\eta,1}}{I_{b,\eta,0}} - 1\right) R_i \tag{B.1}$$

where R_i is the correction factor in case of global wavelength sampling.

`subroutine: getPlanckWalls`

This subroutine calculates heat transfer Planck factors for the implicit domain walls. This means walls implied at the boundaries (defined in `Twall`), but not part of the actual domain. For internal walls such as obstructions, the Planck factors are computed as for all the other flow cells with the subroutine above.

`subroutine: hitr_make_spectrum_and_emirnd`

This subroutine invoked HITRAN's subroutine to generate an emission spectrum for a gas at given conditions and with the pre-defined number of photon rays, generate the photon ray wavelengths. The number density is computed from pressure assuming ideal gas law. The `transj` array is created, indicated where approximately (which transition index) these emissions occurred for easier search for the absorption coefficient in this vicinity. The parameters for spectral generation such as minimum and maximum wavelength are saved in the `hcallprms` type, defined in `rad_main`. The `hitdata` type contains all the transition information read for the particular species from the database (reading of this database is also invoked in the `rad_main` routine). The Planck mean absorption coefficient is also computed.

`subroutine: grey_make_spectrum_and_emirnd`

Here, black body emission spectrum is generated for grey simulations and random emission wavelengths are generated. The Planck means absorption coefficient is set to the constant absorption coefficient. The minimum and maximum wavelength are pre-set based on Wien's displacement law.

`subroutine: hitran_getmaxlinewidth`

This subroutine was meant to obtain the maximum line width present in the spectrum to aid the determination of maximum and minimum wavelength ranges in the absorption coefficient determination for HITRAN. It can be used in conjunction with `hitran_getabsorption`.

`subroutine: makemesh3d`

Here, a 3D Cartesian mesh for the 2nd grid is made based on the dimensions of the domain and desired number of cells. All information about the grid, also used everywhere throughout the code, is stored in the `cells(ncell, 6)` array. This contains the i, j, k indices of the respective cell as the first three entries and centroid location x, y, z as the second three entries.

`subroutine: makearandomfield`

This subroutine is meant mostly for testing, or potentially TRI studies. Using minimum and maximum limits on flowfield variables, it generates a random fluctuating flowfield in the domain.

`subroutine: makecase`

All the `makecase` routines generate the flowfield according to the respective validation cases. For NEQAIR cases, n is added proceeding the number of the case. The `makencasefromLOS` allows the user to create a case from any NEQAIR-LOS formatted data.

`subroutine: neqair_convert`

This subroutine converts the NEQAIR spectra to SI units. The default units in which spectra are generated are Angstroms for wavelength, 1/cm for the absorption coefficient and $\mathrm{W/cm^2/sr/\mu m}$ for emissivity. This is converted to m, 1/m and $\mathrm{W/m^3/sr}$.

`subroutine: interpolate`

Here, a basic 1D interpolation is performed using a binary search.

`subroutine: database_filter`

This subroutine creates the 3rd grid mesh, denoted by `_f` (as filtered). The data from the nearest cell on the 2nd grid are used.

`subroutine: lorentzian`

This is a simple HITRAN subroutine returning the Lorentzian line shape. For a given position in the spectrum and line data, the line intensity is returned.

`subroutine: translate_molecule_identifier` and `get_molecule_identifier`

These HITRAN subroutines transfer back and forth between the molecular IDs from HITRAN needed to load the correct database file and the actual name of the species.

`subroutine: calculate_absorb_xsec`

This HITRAN subroutine computes the absorption cross section spectrum (which, if multiplied by number density, gives the absorption spectrum). This routine is made to provide accurate absorption coefficient around transition lines (all maxima are properly resolved), but the integral would be overestimated, so it cannot be used for emission calculation. The considered lines when computing the cross section are all within 50 line half widths.

`subroutine: calculate_emiss_xsec`

With this HITRAN subroutine, the absorption cross section spectra appropriate for emission calculations are generated. The reduced triangular approach from Figure 4.6, resulting in accurate determination of the important maxima and accurate emission integral is used. This routine should not be used for calculation of cross sections for absorption spectra, since for weaker transitions, the cross sections are underestimated, see the discussion in Chapter 4.

`subroutine: read_hitran2012_parfile`

This subroutine determines which database file to use and loads all the transition data to the `data_cur` structure, which in the main program is referred to as `hitdata`.

`subroutine: get_emiss_spctr`

This HITRAN subroutine calls the `calculate_emiss_xsec` subroutine with the corrected input data. Depending on the molecule computed, the dimensions arrays in which the neighbouring transitions are stored are set.

`subroutine: get_absorb_spctr`

This HITRAN subroutine calls the `calculate_absorb_xsec` subroutine with the corrected input data. Depending on the molecule computed, the dimensions arrays in which the neighbouring transitions are stored are set.

`subroutine: get_kappa`

This HITRAN subroutine calls `get_absorb_spctr` with a given range to determine the absorption coefficient from the absorption cross sectional data (can be called by `hitran_getabsorption` is interpolation is not used). This is done by multiplying with the number species density. Coefficient is returned for a given wavelength.

`subroutine: get_full`

This HITRAN subroutine is used to compute the full absorption spectra during their pre-databasing in `rad_main` along with computation of the Planck mean absorption coefficient. It calls `get_absorb_spctr` to generate cross sectional data and multiplies them with the species density.

`subroutine: make_rnd_emit`

This HITRAN subroutine computes the emission spectra for the cell and generates random wavelength from its cumulative distribution. It calls `get_emiss_spctr` to produce the cross sectional data and multiplies them with number species density and Planck function. It accurately computed also the Planck mean absorption coefficient. Besides the computation of the generated wavelengths, it also saves the index of the transitions where these emissions occurred to accelerate the determination of the absorption coefficient.

`subroutine: get_partition_sum`

This HITRAN subroutine calculates the total internal partition function sum considering the first (naturally most abundant) isotopologue from the pre-computed spline interpolation functions for H_2O, CO_2 and H_2. It returns its ratio to the reference internal partition function sum. For other species, databased functions are used in `return_Q_ratio`.

`subroutine: return_Q_ratio`

This HITRAN subroutines interpolates the total internal partition function sum ratio for other species than H_2O, CO_2 and H_2. These were pre-databased with 1K resolution for fast access and are in the adjusted HITRAN database folder under `partfun/`.

`subroutine: neqair_main`

This is the main NEQAIR subroutine rewritten to adjust the NEQAIR program into a callable subroutine. It functions the same way as the original NEQAIR program with adjusted inputs, outputs and MPI communication. For more information about the function of NEQAIR, refer to the NEQAIR use manual in Ref. [16].

The NEQAIR inclusion means that all the NEQAIR subroutines were modified such that allocatable arrays are deallocated before allocation to enable repeated calling of the routine. Apart from that, since the inputs are determined directly from the radiation solver, the initialisation `readLOS` and `read_neqair_input` were rewritten to be compatible. Output routines were also adjusted. To allow for tracing of all the major changes to NEQAIR, the additional variables and structures have the addition of `_brch` at the end.

`subroutine: read_ae`

This NEQAIR subroutine reads the databased spectra.

`subroutine: downsize`

This NEQAIR subroutine performs the cumulative downsampling shown in Figure 6.8 according to predefined tolerance. The regular downsampling is a part of the original NEQAIR program and can be found as `downsample`.

`subroutine: get_neqair_spectra`

This is the main NEQAIR subroutine. Firstly, from the 3rd grid, it determines the database for which the spectra must be solved and removed repeated entries. Then, the flowfield data and simulation settings are transoformed into structures using `get_default_sim_setup` and `formal_los` which are read by the modified NEQAIR `readLOS` and `read_neqair_input` subroutines. The `neqair_main` is then called to invoke the rest of the NEQAIR subroutines to compute the spectra.

After computation of the spectra, the spectra is checked for possible errors such as inf and NaN values and downsized using the cumulative downsampling in `downsize`.

In case regression is used as an approximation technique, the spectra are then processed to determine the corresponding weights using the `getweights` subroutine.

`subroutine: get_default_sim_setup`

This NEQAIR subroutine determines NEQAIR simulation settings. Some of them (e.g. characteristic distance of nonBoltzmann calculations, database path) are extracted from radiation input files, while the rest is either defined within the subroutine as specified in Chapter 4 (e.g. spectral resolution, type of nonBoltzmann model) or computed form the flow field data (e.g. whether Boltzmann or nonBoltzmann modelling is used).

`subroutine: format_los`

In this NEQAIR subroutine, the database entries from the 3rd grid are transformed and organized into an input which NEQAIR can process as if it was read from the original `LOS.dat` file, normally necessary for operation of NEQAIR. This LOS structure is adjusted according to the number of available nodes. The spacing in this LOS structure is not physical and neither is the order of the points. Correct spacing and order are only required when the RTE is to be integrated by NEQAIR. Since this is not done with NEQAIR as only the absorption and emission spectra are generated, the arbitrary spacing and order do not have an influence on the calculations.

In addition, NEQAIR requires a first initial point which determines the origin of the system and might serve as a boundary condition when integrating the RTE. Neither of these functions is needed in current implementation, but to avoid having to heavily modify the structure of NEQAIR, this dummy point is inserted there anyway, as a repeated entry of the actual first database entry. The spectrum is not solved for this point, thus causing no added use of computational resources. This is also the reason why the spectra begin with `ae.2`, and not `ae.1`.

`subroutine: get_neqair_maxPlanck` and `get_neqair_maxPlanck_datab`

These NEQAIR subroutines determines the maximum emissivity for the use of global wavelength sampling, according to the highest mean temperature $\sqrt{T_t T_e}$. The outputs are both the Planck mean absorption coefficient as well as integrated emissivity $\int_0^\infty \varepsilon d\lambda$. Only the integrated emissivity is, however, used for calculations when NEQAIR is involved due to nonequilibrium; the output of the κ_p in this context is only for informative purposes.

Since the spectra are generated in a different way for ordinary operation (spectra as simply saved in the memory) and for regression approximation (the spectral weights are saved in the memory), the subroutine `get_neqair_maxPlanck_datab` is used when regression approximation is applied.

`subroutines: neq_make_spectrum_and_emirnd`, `neq_make_spectrum_and_emirnd_anl`, `neq_make_spectrum_and_emirnd_doub` and `neq_make_spectrum_and_emirnd_datab`

All these NEQAIR subroutines in some way compute the NEQAIR emission spectrum for the cell, determine the total emissive power and generated wavelengths of the photon rays. The basic routine is applicable anytime the spectra directly resolved from NEQAIR is used without any modification. The `_anl` subroutines refer to the use of the analytic adjustment method, where the nearest spectrum from the 3rd grid is recomputed using local data and assuming constant ratio of equilibrium Planck functions. The `_doub` subroutines refer to 2 point averaging, where two nearest spectra from the 3rd grid are used and weighted according to their differences in temperature with respect to the cell being computed. Finally, the `_datab` subroutines recompute the local spectra using the local weights determined from regression of the spectra on the 3rd grid. These subroutines are separated, since in each case, the spectrum is stored and handled completely differently.

In case global sampling is used, instead of the local cell, the hottest cell in the domain according to $\sqrt{T_t T_e}$ is used to define the emissive power and sampled wavelengths.

In case of regression techniques, though not currently employed, in case negative values are obtained somewhere in the spectrum due to non-physical spectral weights, the data from the nearest spectrum are used instead.

`subroutines: neqair_get_kappa`, `neqair_get_kappa_anl`, `neqair_get_kappa_doub` and `neqair_get_kappa_datab`

These NEQAIR subroutines determine the absorption coefficient at a given wavelength from the stored spectral information. Similarly to the case of the `neq_make_spectrum_and_emirnd` subroutines, since the spectral information is stored differently depending on the approximation technique, these subroutines are separated and function differently.

In case of the regression techniques, even though they are currently not in use to their time consumption, if a negative κ is obtained due to non-physical spectral weights somewhere in the spectrum, the next wavelengths are searched until the absorption coefficient becomes physical.

`subroutines: neqair_getPlanck`, `neqair_getPlanck_anl`, `neqair_getPlanck_doub` and `neqair_getPlanck_datab`

Just as for NEQAIR emission and absorption spectra, these NEQAIR subroutines compute the Planck factors from Equation (B.1) depending on the approximation technique used. Since division is involved, the absorption coefficients can never be zero. If a NaN Planck function ratio is produced, PF is set to -1. The PF is computed depending on whether local or global wavelength sampling is adapted.

`subroutines: neqair_getPlanckWalls`, `neqair_getPlanckWalls_anl`, `neqair_getPlanckWalls_doub` and `neqair_getPlanckWalls_datab`

Finally from NEQAIR main subroutines, these subroutines compute the Planck factor for implicit walls (walls just behind the end of the domain, which are not in actual cells). The explicit walls and inner obstructions are computed using the `neqair_getPlanck` subroutines. Similarly to the `neqair_getPlanck` subroutines, the actual calculation depends on whether local or global wavelength sampling is used.

`subroutine: write_neqair_database`

This NEQAIR subroutine creates a `database_ae.txt` in which the conditions for the generated spectra are saved. This is mainly useful for postprocessing, when it is desired to know which conditions were considered where in the domain for spectral generation.

`subroutine: output_spectra`

If regression is used as an approximation technique, this subroutine allows the user to output the resulting spectrum at given conditions from the spectral weights to check for their validity.

`subroutine: recalc_analytic_coeff`

This NEQIAR subroutine is used for calculation of absorption coefficients whenever the analytic adjustment method is used for spectral approximation. The input reference absorption coefficient at input reference conditions is here recalculated for desired conditions using the ratio of species number density and the spectral database from Table 6.1 using the subroutine `spectral_datab`.

`subroutine: recalc_analytic`

Similarly to `recalc_analytic_coeff`, this subroutine recalculates the spectrum using reference conditions and desired conditions. In this case, the entire reference emission spectrum is provided and the desired recalculated emission spectrum is produced. The calculation is done using equilibrium Planck function ratio as well as the spectral database from Table 6.1 using the subroutine `spectral_datab`.

When it comes to spectral regression, as mentioned in Chapter 6, it is not suggested for use in the current configuration due to time consumption and sometimes inferior performance compared to the alternatives. However, it is possible that if more effort is put into perfecting these techniques, they could still be useful and advantageous in the future if adjusted. Thus also the description of some of the most essential subroutines made for this calculation technique is provided below.

`subroutine: getweights`

The databasing subroutine takes a sample of the absorption and emission spectra for the use of regressions. The NNLS boolean determines whether non-negative least squares or ordinary least-squares will be used. Note that for ordinary least squared, use of the LAPACK libraries is needed and in the current form, without LAPACK, the invocation of the respective subroutines from LAPACK (`DGELS`, `DGETRF`, `DGECON`) is commented out. The INTERPOLATE boolean, if set to true, finds the weights use matrix inversion, not LS regression and uses only as many samples, as there are dimensions. This approach is however very unstable due to frequent nonphysical behaviour. The theory about how these weights are obtained is explained in Chapter 6.

`subroutine: getcondition`

This is a subroutine for databasing which computes the condition matrix of the system. This can be useful when determining whether regression should be used in the first place or not (when the condition number is very low, the weights will most likely be unphysical and negative emission and absorption coefficients might be obtained).

`subroutine: get_spectra_from_weights`

This subroutine uses the databased spectral weights from the 3rd grid and reference 3rd grid conditions to produce emission spectra for a cell on the second grid with the desired conditions. If it is found that negative emission or absorption coefficient is obtained due to non-physical weights, the coefficient from the original spectrum is used instead. This, however, generally does not happen, at least not when NNLS is used.

`subroutine: get_coeff_from_weights`

This is a subroutine similar to `get_spectra_from_weights`, but the calculation is only made for one absorption and emission coefficient to save time, such as for the purposes of determining the Planck function for `rad_main`.

`subroutine: spectral_datab`

This subroutine is used for the purposes of regression and analytic adjustment. It defined the ranges where various species absorb/emit, so that the number densities of said species in these regions can be used to recalculate the absorption and emission coefficients. This database was so far built only for N, O, NO, N_2, O_2 and N_2+.

B.3. Example Radiation Input File

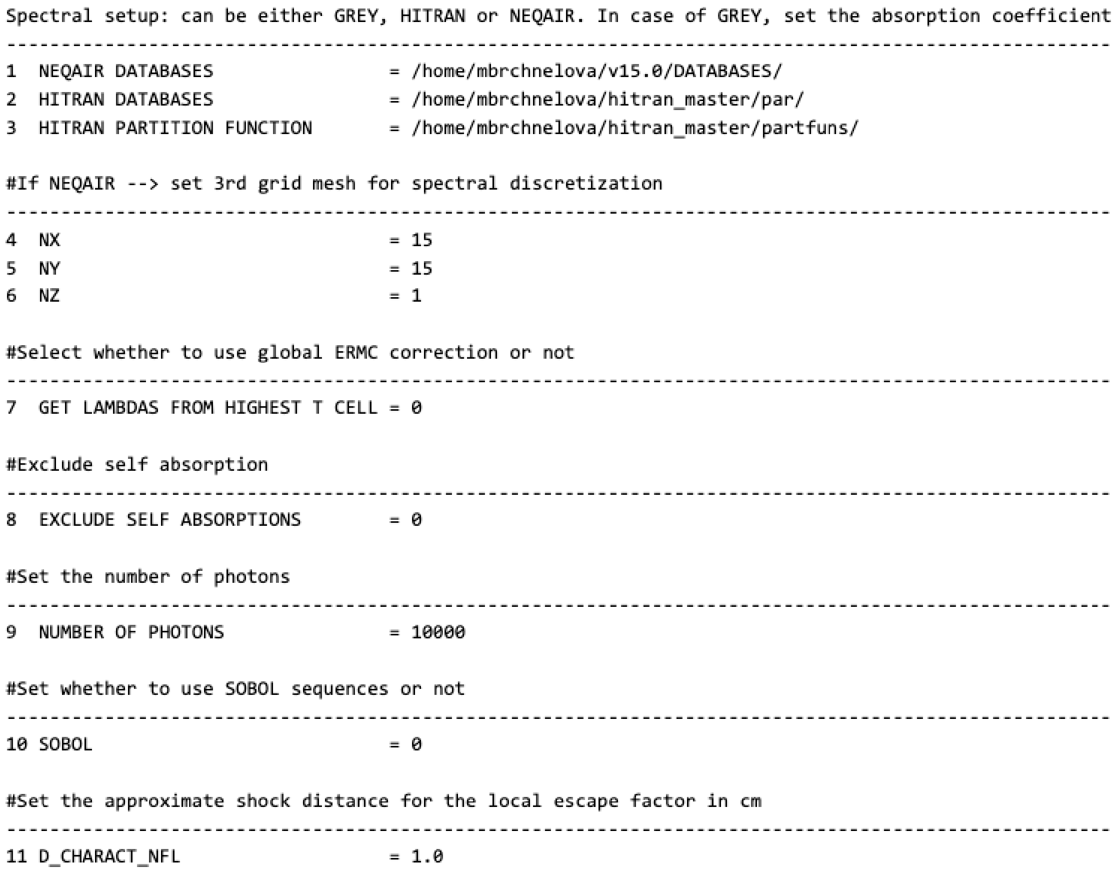

```
Spectral setup: can be either GREY, HITRAN or NEQAIR. In case of GREY, set the absorption coefficient
-----------------------------------------------------------------------------------------------------
1  NEQAIR DATABASES                = /home/mbrchnelova/v15.0/DATABASES/
2  HITRAN DATABASES                = /home/mbrchnelova/hitran_master/par/
3  HITRAN PARTITION FUNCTION       = /home/mbrchnelova/hitran_master/partfuns/

#If NEQAIR --> set 3rd grid mesh for spectral discretization
-----------------------------------------------------------------------------------------------------
4  NX                              = 15
5  NY                              = 15
6  NZ                              = 1

#Select whether to use global ERMC correction or not
-----------------------------------------------------------------------------------------------------
7  GET LAMBDAS FROM HIGHEST T CELL = 0

#Exclude self absorption
-----------------------------------------------------------------------------------------------------
8  EXCLUDE SELF ABSORPTIONS        = 0

#Set the number of photons
-----------------------------------------------------------------------------------------------------
9  NUMBER OF PHOTONS               = 10000

#Set whether to use SOBOL sequences or not
-----------------------------------------------------------------------------------------------------
10 SOBOL                           = 0

#Set the approximate shock distance for the local escape factor in cm
-----------------------------------------------------------------------------------------------------
11 D_CHARACT_NFL                   = 1.0
```

Figure B.3: Example radparam.inp file.